Modelling of Ice Crystal Icing in Turbofan Engines

Liam Parker

Mansfield College

University of Oxford

Supervised by: Prof. M. McGilvray & Prof. D.R.H Gillespie

A thesis submitted for the degree of

Doctor of Philosophy

Hilary 2024

for Grandad

Acknowledgements

Firstly, I would like to thank my supervisors, Prof. Matthew McGilvray and Prof. David Gillespie for their support, guidance and excellent teaching throughout the years of this work. Their collective knowledge and experience helped form the unique and exciting work in this area.

Thank you to the staff at the Rolls Royce Engine Environmental Protection Team. Thank you Geoff, Rory, Ben, Donald, Hiren and Henrik for their excellent project management, insight, guidance and expertise.

Thank you to my colleagues both current and past in the Particle Deposition Group for the brilliant technical discussions, lunch meet ups and occasional memes.

Thank you to the wider community at OTI both past and present. Thank you to fellow D.Phil's, research staff and support staff for friendship, endless interesting discussions, conference trips, lunches, end of week socials and support both professionally and socially.

Thank you to my friends both in Oxford and beyond for all the good and bad times we have shared throughout. Between kayaking, golf, concerts, dinners, formals, bops, pub trips, holidays, board games and listening to me rant you have all been there in many amazing ways.

Thank you to my family who have supported me in every way throughout, celebrated the milestones with me and helping me to get this far. Thank you Mum, Issy and Jay.

And thank you to Jericho Coffee Traders, for your unwavering support throughout the execution of this project.

Sponsorship

I would like to thank Oxford University, Rolls Royce plc. and Innovate UK for the funding, studentship, management and oversight of this D.Phil and the wider DE-ICER project. It has been incredibly interesting, challenging and enjoyable to be directly involved in a multi-disciplinary turbofan engine icing research project and to see the developments and technical advances in knowledge and capability realised.

Abstract

Turbofan engine icing threatens compressor operation and service life. Ice crystal ingestion during cruise and descent phases of flight results in smaller, partially melted crystals entering the engine core. Here, crystals can stick to stationary surfaces driven by the presence of a water film, and evaporative and melting heat exchange with the mixed-phase crystals. Modelling of the ice crystal cloud conditions is needed to understand threat areas within the core and operating envelope and to provide a reliable basis for ice accretion modelling at solid surfaces. This thesis, therefore, enhances the accuracy and fidelity of ice crystal icing modelling for turbomachinery applications.

The particular emphasis of the model development was in three-dimensional particle transport and accretion, especially in the context of compressor ice crystal icing. Traditionally, icing models have relied on simplified two-dimensional cases or complex three-dimensional studies lacking validation or accuracy assessments. This work bridged this gap by advancing the individual models relevant to icing and examining three-dimensional transport and accretion data.

Specifically, warmed substrate accretion was modelled. This is characteristic of compressor ice crystal icing with through casing or through vane heat transfer. Existing codes were extended to three dimensions with turbophoresis and two-way mass energy coupling were introduced along with novel methods to capture the accretion shape and size. These enhancements were shown to be necessary to accurately simulate real-world turbomachinery representative geometry and test conditions, characterised by wall-bounded, highly turbulent, and accelerating flows. The results showed that incorporating turbophoresis and two-way coupling significantly improves the accuracy of transport model predictions, particularly when the melting rates of smaller particulates are considered. Particle melting is known to be a major influencer of accretion initiation.

The study also significantly improved numerical integration and modelling of ice crystal icing particles interacting with the gas-phase and surfaces. A dual time stepping method was employed for particle tracking to enable unsteadiness in the gas-phase along the particle residence time. A literature-based stochastic bounce model was introduced to represent roughened surfaces, resulting in appreciable changes in mass and melting distribution after a single impact event. A multi-zone modelling scheme was developed to efficiently model the farfield flows typical of complex experimental test rigs in altitude

icing facilities, while allowing test geometries of interest to be independently modelled based on derived boundary conditions.

Simulation results of mixed-phase warmed substrate accretion were compared against representative compressor stator vane icing experiments. The findings highlighted the importance of considering wall conditions, as excess accretion on stator vane roots suggested inadequacies in current sticking models or the omission of downstream water and ice sliding along walls. The influence of runback water energy recovery and substrate conduction was characterised.

The work advances the understanding of individual physical processes involved in ice crystal icing, providing an improved route to tackle turbofan compressor icing threats, mitigate maintenance costs, engine damage, and design inefficiencies.

While the final model is not yet capable of modelling full rotating stages, most icing accretion occurs on stationary components. Thus it is still able to provide predictive insight into engine sub-systems and provides a route to engine certification by analysis in the future.

Nomenclature **ix**

1 Introduction **1**
1.1 Motivation 1
1.2 Aims 5
1.3 Publications 7
1.4 Thesis Contribution 8

2 Literature Review **9**
2.1 Background 10
2.2 Ice Crystal Icing Conditions 11
2.3 Particle Transport 18
2.4 Particle Heat Transfer and Phase Change 26
2.5 Particle Surface Impact 28
2.6 Ice Crystal Icing Accretion 34
2.7 Ice Crystal Icing Modelling 37
2.8 Numerical Ice Accretion Models 39
2.9 Summary 46

3 Model Development **47**
3.1 Overview 48
3.2 Continuous Phase Modelling 53
3.3 Discrete Phase Modelling 54
3.4 Particle - Gas Coupling 69
3.5 Thermodynamic Accretion Models 71
3.6 Topography Update 78
3.7 Summary 80

4 Computational Methodology **81**
4.1 Continuous Phase Modelling 82
4.2 Particle Cloud Seeding 89
4.3 Vapour Mixture Specification 90
4.4 Particle Transport 92
4.5 Accretion 94
4.6 Summary 96

5 Previous Ice Crystal Icing Experiments **97**
5.1 Ice Crystal Icing Experiments 98
5.2 Working Section Measurements 99
5.3 Test Articles 104
5.4 Ice Accretion 105
5.5 Test Matrices 107

6 Validation of Particle Transport Model Enhancements Against Previous RATFac Experiments **109**
6.1 Overview 110
6.2 Validation Test Case 111
6.3 Numerical Arrangement 111
6.4 Particle Stream Spatial Convergence 114
6.5 Model Assessment 118
6.6 Combined Transport Model 129
6.7 Summary 140

7 Evaluation of Surface Response Model Against Previous Fundamental Conical Experiments at RATFac **142**
7.1 Overview 143
7.2 Numerical Arrangement 143
7.3 Model Assessment 144
7.4 Summary 148

8 Evaluation of Transport and Accretion Models against previous LP Compressor Stator Vane Experiments at RATFac **150**
8.1 Overview 151
8.2 Numerical Arrangement 151
8.3 Particle Cloud Properties 154
8.4 Volume Extrusion 157
8.5 Heat Transfer 157
8.6 Accretion Adhesion Conditions 163
8.7 Comparison to Ice Thickness Data 164
8.8 Summary 172

9 Thesis Summary **176**
9.1 Conclusions 176
9.2 Further Work 179

Appendices

List of Figures **182**

List of Tables **194**

A Experimental Conditions **196**
A.1 Experimental Readings 196
A.2 Centreline Distributions of TWC and MR 199

B Ice Crystal Icing Experiments **200**
B.1 Ice Crystal Icing Experiments 200

References **207**

Nomenclature

Acronyms

AIWT Altitude Icing Wind Tunnel

CFD Computational Fluid Dynamics

EASA European Union Aviation Safety Agency

EGV Exit Guide Vane

EHWG Engine Harmonization Working Group

EMM (-C) Extended Messinger Model (- Crystals)

FAA Federal Aviation Administration

HAIC High Altitude Ice Crystals

HIWC High Ice Water Content

HP High Pressure

HPC High Pressure Compressor

HPT High Pressure Turbine

ICI Ice crystal icing

ICICLE Ice Crystal Icing ComputationaL Environment

IDW Inverse Distance Weighting

IGV Inlet Guide Vane

IP Intermediate Pressure

IPC Intermediate Pressure Compressor

IPT Intermediate Pressure Turbine

IWC Ice Water Content

IWT Icing Wind Tunnels

LP Low Pressure

LWC Liquid Water Content

MAD Mean Absolute Difference

MMD Median Mass Diameter

NASA National Aeronautics and Space Administration

NRC National Research Council

OGV Outlet Guide Vane

ONERA Office National d'Etudes et de Recherches Aérospatiales

PSD Particle Size Distribution

RATFac Research Altitude Test Facility

SLD Supercooled Large Droplets

SLW Supercooled Liquid Water -

TWC Total Water Content

USQ University of Southern Queensland

Roman

$\mathcal{L}$	Dimensionless Impact Energy Coefficient	$-$
B	Height of ice	m
c	Specific heat capacity	J kg $^{-1}$ K $^{-1}$
C_d	Coefficient of drag	-
C_f	Skin Friction Coefficient	
C_p	Coefficient of pressure	-
E	Aspect Ratio	-
e	Eccentricity	-
e_σ	Surface Energy	J
g	Acceleration due to gravity	m s^{-2}
H	Heat Transfer Coefficient	W m $^{-2}$ K $^{-1}$
h	Height of water film	m

k	Conductivity	W m^{-1} K^{-1}
L_f	Latent Heat of Fusion	kJ kg $^{-1}$
L_v	Latent Heat of Vaporisation	kJ kg $^{-1}$
MMD_{eq}	Median Mass Diameter - Equivalent (Non-Spherical)	m
P	Pressure	Pa
q	Heat flux	W m^{-2}
R	RMS Roughness Height	m
r	Specific Gas Constant	J kg^{-1} K^{-1}
RH	Relative Humidity	$\%$
T	Temperature	K
t	Time	s
U	velocity	m s^{-1}
V	Volume	m^3
Y_D	Mass Fraction	-
z	Ice/Water extrusion direction	m
$\dot{m}$	Mass flux	kg m^{-2} s^{-1}
m	Mass	kg

Dimensionless Groups

Bi	Biot number	hL/k
Le	Lewis number	$\alpha/\mathcal{D}_{1,2}$
M	Mach number	$u/\sqrt{\gamma RT}$
Nu	Nusselt number	hL/k
Pr	Prandtl number	ν/α
Re	Reynolds number	uL/ν
Sc	Schmidt number	$\nu/\mathcal{D}_{1,2}$
Sh	Sherwood number	hD/L
St	Stokes number	τ_p/τ_g

We	Weber number	uL/ν

Greek

α	Under-relaxation coefficient	-
$\Delta(x)$	Change in quantity x	-
ϵ	Turbulent Kinetic Energy Dissipation	$m^2\ s^{-3}$
ϵ_{xy}	Coefficient of restitution	–
γ	Virtual Wall Normal Angle	$^\circ$
γ_a	Isentropic Expansion Factor	c_p/c_v
μ	Dynamic Viscosity	Pa· s
ν	Kinematic viscosity	$m^2\ s^{-1}$
ω	Vapour Mass Fraction	-
ϕ	Sphericity	-
ρ	Density	$kg\ m^{-3}$
τ	Relaxation Time	s
τ_w	Wall Shear Stress	Pa
θ	Water temperature	K

Superscripts and Subscripts

$\bar{x}$	Mean
∞	Free stream value
$\phi_\perp$	Crosswise Sphericity
x	Axial
x'	Fluctuation
0	Total/Stagnation Conditions
a	Air
aero	Aerodynamic
conv	Convective
d	Drag

evap	Evaporation
g	Gas
i	Ice
in	Inlet Conditions
int	Internal Layer
kin	Kinetic
L	Latent
max	Maximum Diameter
melt	Melting
n	Normal
p	Particle
s	Surface Area
sens	Sensible
subl	Sublimate
subs	Substrate
surf	Surface Layer
t	Tangential
turb	Turbophoresis
vap	Vapour
vap,sat	Vapour at Saturation
vXX	Median Volume Diameter - XXth Percentile
w	Water
wb	Wet Bulb

1 Introduction

1.1 Motivation 1
1.2 Aims 5
1.3 Publications 7
1.4 Thesis Contribution 8

1.1 Motivation

Ice crystal icing (ICI) is known to have caused engine events resulting in power loss and damage since the mid-1990's. Lawson et al. [85] identified a trend in 10 engine rollback events. Mason et al. [95] identified 42 power loss events through the Engine Harmonization Working Group (EHWG) , Mason concluded that small ice particle ingestion in convective cloud systems leads to ice crystal icing on warm engine core components at air temperatures above freezing. Through repeated flight tests and weather analyses, Boeing compiled a database comprising 174 ice crystal icing events [18]. These events occur primarily in conditions of high ice water content (HIWC) , in oceanic convective cloud at altitudes between 20,000 and 40,000ft at this altitude.

An ICI certification envelope was developed by EASA and the FAA based upon known events and the prevalence of oceanic convective cloud at cruise altitudes being the main cause of these [17, 18]. Figure 1.1 illustrates the events compiled by Boeing and the EHWG. A high number of events occur in the tropics, where convective storms and HIWC conditions are more frequent. Given the population density of South-East Asia, these conditions put a large number of flights at risk.

Figure 1.1: Engine powerloss events from Boeing database as of Jan 2019 [17].

Ingestion of ice crystals into the engine core leads to warming and partial melt of particles. Fully frozen particles are not likely to stick to surfaces but within a specific band of particle melt ratio and local wet bulb temperature [23, 39], particles will stick to compressor surfaces forming a film of water. This water film improves the adhesion forces upon impinging particles. A sufficient impinging mass flux of ice crystals at HIWC conditions will transfer heat from the surface and cool it sufficiently to enable ICI accretion to occur. Before entering the engine core, the fan causes centrifuging effects and will mill the ice crystals entering the core stages. Figure 1.2 illustrates the Ultrafan geared turbofan design from Rolls Royce plc. The red box illustrates areas where ICI accretion is common.

ICI events recorded in the Boeing database [17] due to engine flameout, surge or stall during flight formed the initial motivation to study ICI conditions. Pilots often reported rain appearing on the wind-shield despite flying at altitudes where liquid water could not exist (> 22000ft) [95]. Some ICI events have been documented and evidence of damage to components and downstream stages has been released.

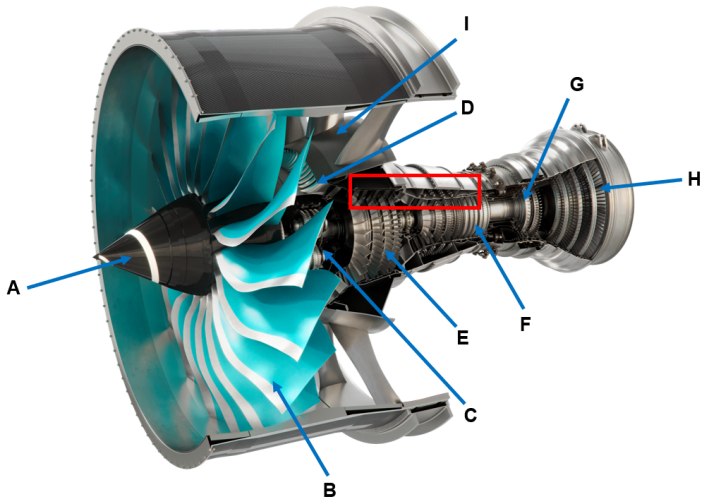

Figure 1.2: Ultrafan turbofan schematic, red box shows the likely ICI sites adapted from [119].

Table 1.1: Ultrafan Turbofan Schematic Labels and Descriptions

Label	Description
A	Spinner
B	Fan
C	Gearbox/Low Pressure Compressor (LPC)
D	Splitter Lip/Core Inlet Guide Vane (IGV)
E	Intermediate Pressure Compressor (IPC)
F	High Pressure Compressor (HPC)
G	High Pressure Turbine (HPT)
H	Intermediate Pressure Turbine (IPT)
I	Bypass/Outlet Guide Vane (OGV)

In service events of the BAe146, involving multiple engine rollback of the Lycoming ALF502 geared high-bypass turbofan led to a flight testing campaign and full engine rig test [14, 54, 103, 104]. The ALF502 engine is a geared turbofan system, leading to slower fan speeds and warmer forward components due to the gearbox. Downstream of the intake a booster stage was prone to icing and this was reproduced in the NASA PSL3 facility. The flight test campaign was conducted by Honeywell to reproduce an ICI envelope and record engine and atmospheric conditions for the ALF502 [103]. T_{wb} was varied from $-10°C$ - $3.5°C$ and accretion and rollback was observed across the entire wet bulb temperature range [145].

Shedding of accreted ice can further lead to flame-out or damage to downstream

stages. ICI appears to affect older turbofan designs and newer high-bypass ratio engine designs [95].

The current FAR14 Part 33 Appendix-D ICI certification envelope, shown in Figure 1.3, provides a regulation framework for engine operation conditions. In-flight testing, full engine rig testing and part component testing in Icing Wind Tunnels (IWT) is costly. Testing in IWT can be limited by operating altitude and Mach number making scaling and matching test conditions difficult. Additionally, recreating ice crystals is challenging and matching conditions at the fan is limited.

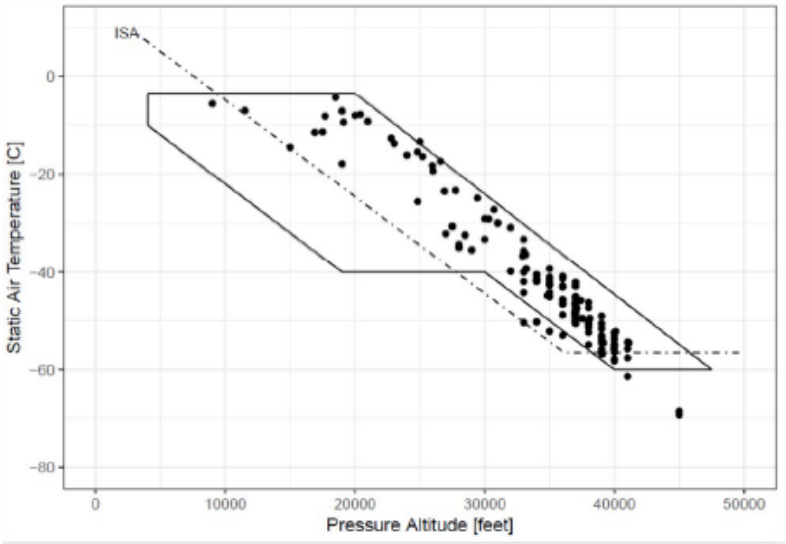

Figure 1.3: Ice crystal icing FAR14 Part 33 Appendix D certification envelope.

Certification of new engine architecture operating within this envelope requires validation and testing of the compressor geometry. Modern turbofan designs comprise large bypass ratios, reduced fan blade counts and fan-compressor gearboxes which can increase operating efficiency whilst causing an increase in ice ingestion into the core. A lower fan blade tip speed and fan blade count [84] can reduce milling and centrifuging effects upon the particles. The primary aim of researchers, government and industry is to demonstrate that icing conditions are well understood and engine operations are robust. The following summarises the framework necessary to achieve engine operability improvements of current and future engine designs. It also details the strategy informing the research gap specifically point number 5. This works towards a more complete understanding of ICI physics and associated risks.

1. Improved ICI detection and avoidance procedures developed by engine manufacturers and operators.

2. Core engine design approaches limiting ice accretion. Employing bleed air and high cruise power settings may offer simpler methods to limit accretion but will reduce operating efficiency.

3. Full engine and sub-section testing to observe and characterise operating conditions leading to accretion and shed. This provides an empirical yet costly approach.

4. Fundamental physics rig testing. Generating sub-models of the physical processes involved in ICI.

5. Numerical model and simulation development. Generating models for ice crystals, mass transport, heat transfer and impact and accretion physics is vital in understanding the results obtained in empirical and fundamental ICI testing.

1.2 Aims

The D.Phil project focused on the final 2 steps in the ICI risk reduction approaches. The initial work summarised in this report comprised the investigation and design of a modification and update to the existing in-house ice crystal icing accretion and particle tracking code ICICLE at the Oxford Thermofluids Institute. The existing code design provides a 2D planar/axisymmetric throughflow modelling suite which combines the following [22],

- Test body and bounding domain meshes.
- Steady state continuous phase viscous flow solution.
- Gas - Fluid heat exchange/melt model
- Lagrangian discrete phase non-spherical water-ice particle tracking model.
- Mixed phase impact, stick and fragmentation model.
- Stefan heat transfer problem and ice accretion model (extended Messinger model)

The work in this thesis project involved a novel 3D ICI meshing and simulation framework which simulated the highly coupled 3D flows found around accreted ice and across Low/Intermediate Pressure (LP/IP) compressor stages. Compressor icing conditions are complex to replicate and a numerical simulation capability reduces the need for reliance on purely testing. The numerical tool development aimed to predict ICI accretion shapes informed by experiments. This can help to understand particulate dynamics and accretion risk within compressor architecture.

The primary goal over the D.Phil was to generate time resolved ice accretion distributions across compressor sub-components and partial stage geometries in comparison to rig and component testing conducted in altitude icing wind tunnel (IWT) experiments.

This involved a new implementation of the heat transfer and ice accretion energy-mass balance at the surface generated by Bucknell et al. [24] in 3D accounting for water runback, conduction across the span or radial direction of the stage and implementation of a mesh morphing method to the existing panel discretisation and ice layer growth.

Lastly, investigation and analysis of the particle-surface interaction at impact was conducted to improve the accuracy and capability of the physical model. This involved characterising the surface roughness, water runback and ice initiation upon the overall accretion. Altitude wind tunnel testing to examine the effects of ice particle impact upon roughened compressor and outer ice layer surfaces provided the empirical background for this model.

1.3 Publications

The author generated the following publications from this body of work.

1. Liam Parker, Matthew McGilvray, and David Gillespie. "Modelling and Simulation of Mixed Phase Ice Crystal Icing in Three-Dimensions". In: *SAE Technical Paper Series* 1 (June 2023). DOI: 10.4271/2023-01-1475

2. Liam Parker, Matthew McGilvray, David R. H. Gillespie, and Geoffrey Jones. "Numerical Simulations of Ice Particle Transport at Representative Turbofan Compressor Conditions". In: *ASME Turbo Expo 2024, Turbomachinery Conference and Exposition* (Aug. 2024). DOI: 10.1115/GT2024-121461

3. Liam Parker, Matthew McGilvray, David R.H. Gillespie, and Geoffrey Jones. "Numerical simulations of ice particle transport at representative turbofan compressor conditions". In: *Journal of Turbomachinery* (Apr. 2025), pp. 1–14. DOI: 10.1115/1.4068485

In addition, the author contributed in part to the following works.

1. Jonathan Paul Connolly, Matthew McGilvray, David Gillespie, Alex Bucknell, Liam Parker, Geoffrey Jones, and Benjamin Collier. "Two-Way Flow Coupling in Ice Crystal Icing Simulation". In: *SAE Technical Papers* June (June 2019). DOI: 10.4271/2019-01-1966

2. Alexander Bucknell, Matthew McGilvray, David Gillespie, Liam Parker, Peter Forsyth, Hassan Saad Ifti, Geoffrey Jones, Benjamin Collier, and Alasdair Reed. "Experimental Study and Analysis of Ice Crystal Accretion on a Gas Turbine Compressor Stator Vane". In: *SAE Technical Papers* 2019-June.June (June 2019). DOI: 10.4271/2019-01-1927

3. Natan Zawadzki, Thomas Cross, Liam Parker, James Farmborough, Matthew McGilvray, and David Gillespie. "Wall Heat Transfer Measurements in a Turbomachinery Environment Subject to Ice Crystal Icing". In: *AIAA AVIATION FORUM AND ASCEND 2024*. Reston, Virginia: American Institute of Aeronautics and Astronautics, July 2024. DOI: 10.2514/6.2024-3848

1.4 Thesis Contribution

This thesis identified a gap in understanding and modelling concerning ice crystal icing accretion in three-dimensions on above freezing temperature surfaces. Particle phase modelling in three-dimensions inclusive of non-spherical particle transport, heat transfer and phase change was compared against conditions created in altitude icing wind tunnel experiments.

An assessment of the state of the art, found the following gaps in understanding from literature and existing models.

1. Spatially resolved three-dimensional simulated ice accretion shapes.
2. Measurements of convective heat flux on complex compressor surfaces subject to ice crystal icing.
3. Particle size distribution measurements for ice crystal icing after interacting with a test article.
4. Turbophoretic effects relating to particle mass and melt distribution.
5. Surface roughness effects on impact physics, melting and mass distribution of ice crystal icing.
6. Engine representative geometry modelled/simulated in ice crystal icing conditions.

For this body of work, it was pertinent to focus on (1) and (4) - (6). This established the direction from the initial assessment of the art.

2
Literature Review

This chapter summarises the background and critical evaluation of conditions and literature pertaining to ice crystal icing. The focus was specifically on turbofan compressor icing and the conditions, models, experiments and codes relevant to the ICI problem. Compressor gas paths have accelerating flows, highly turbulent boundary layers and rotating components. This required an assessment of models and their applicability to these conditions.

2.1 Background 10
2.2 Ice Crystal Icing Conditions 11
2.2.1 Evaporative Cooling 11
2.2.2 Altitude 12
2.2.3 Particle Shape 13
2.2.4 Particle Size Distribution 15
2.3 Particle Transport 18
2.3.1 Flow Conditions 18
2.3.2 Particle Forces 20
2.3.3 Gravity and Buoyancy 22

2.3.4 Drag . . . 22
2.3.5 Lift . . . 23
2.3.6 Turbophoresis . . . 23
2.3.7 Inter-Particle Collisions . . . 25
2.4 Particle Heat Transfer and Phase Change . . . 26
2.5 Particle Surface Impact . . . 28
2.5.1 Stick . . . 29
2.5.2 Bounce . . . 30
2.5.3 Fragmentation . . . 31
2.5.4 Erosion . . . 32
2.5.5 Surface Roughness . . . 33
2.6 Ice Crystal Icing Accretion . . . 34
2.6.1 Ice Accretion . . . 35
2.6.2 Water Runback . . . 36
2.7 Ice Crystal Icing Modelling . . . 37
2.7.1 Trajectory Modelling . . . 37
2.7.2 Topography Redefinition . . . 38
2.8 Numerical Ice Accretion Models . . . 39
2.8.1 Oxford Thermofluids Institute Code . . . 43
2.9 Summary . . . 46

2.1 Background

ICI events within the LP and IP compressor stage of turbofans occurs in convective and primarily oceanic cloud systems. Ingested ice particles are formed within convective cloud systems such as tropical storms. ICI occurs due to fully glaciated or mixed-phase (partially melted) crystals impinging upon internal core surfaces. The total air temperature prior to ice ingestion within the initial compressor stages is commonly above freezing.

In ICI conditions, crystals impinge on a warm surface ($T > 0°C$) forming a water layer increasing the adhesion strength and kinetic energy dissipation at impact. The

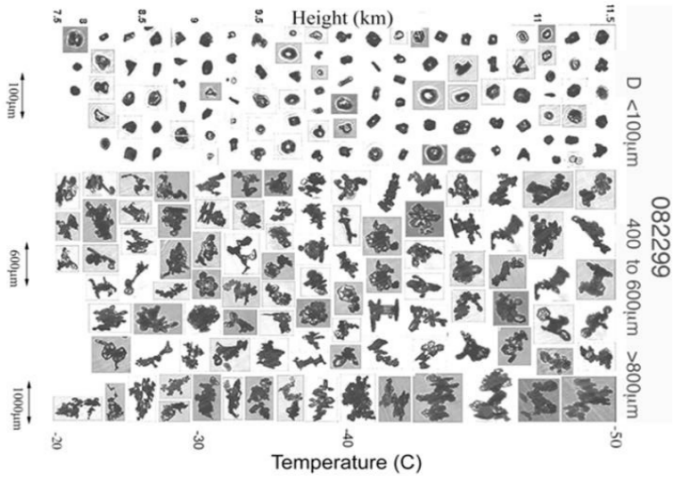

Figure 2.1: Particle shapes measured by Heymsfield et al. in a tropical atmosphere experiment conducted in deep convective clouds [69, 70].

high mass flux of ice particulates within the compressor core will lead to cooling of the accretion surface to a temperature which enables ice growth.

2.2 Ice Crystal Icing Conditions

Ice particles form within convective cloud systems at altitudes where the TAT is below the supercooled pure liquid water limit of -39 $^{\circ}C$ where spontaneous nucleation will occur [47, 64, 89]. The size and shape of crystals have been characterised by flight test campaigns conducted by the HAIC / HIWC field campaign from Darwin, Australia. This work identified the ice concentration or Ice Water Content (IWC) in HIWC conditions ($> 1\mathrm{gm}^{-3}$) [35] which would lead to accretion. ICI conditions are further sub-classified into glaciated (fully frozen) ice crystal cloud conditions and mixed-phase (partially melted) ice crystals. In the latter case, ice content was divided into Liquid Water Content (LWC) and Total Water Content ($TWC = IWC + LWC$) measured in g m^{-3}.

2.2.1 Evaporative Cooling

Vapour concentration and temperature of the of the gas phase are important drivers for evaporative cooling which directly affects particulate melt and accretion rates. Evaporative cooling potential is described by wet bulb temperature. Wet bulb temperature, T_{wb} is theoretically, the adiabatic saturation temperature, this is the temperature at which the air

is saturated due to evaporation and the heat exchange is in equilibrium between the air and water [28]. In practice, the T_{wb} is the limit that water can be cooled by converting sensible heat to latent heat through evaporation and diffusion into an airflow. The evaporative cooling potential is governed by the relative humidity (RH), which describes the ratio of vapour pressure to the saturation vapour pressure (equilibrium). In mixed-phase ice crystal icing and air-compressor fluid flow, total wet bulb (T_{wb0}) measured by stagnation gas properties (T_0,P_0, RH_0), is a reliable property to inform ICI initiation, accretion and stable growth. This describes the local surface temperature impacted by evaporative cooling. The humid airflow leads to evaporative cooling to a point which enables glaciated or mixed-phase accretion at the surface [28, 151].

2.2.2 Altitude

ICI is prevalent at pressure altitudes corresponding to temperatures below $-39°C$, at which spontaneous nucleation of water will occur, meaning water will only exist as ice with no supercooling possible below this temperature [47, 89, 116]. This corresponds to an altitude of $\approx$ 27,000ft which presents a challenge for modelling and test design at sea level. A combination of altitude facilities, directly recreating ICI conditions, and non-pressurised facilities exist to investigate fundamental ICI physics. The fundamental drivers for ICI accretion are T_{wb}, RH and MR. Currie et al. investigated the effects of static pressure on ice accretion [39, 41] and concluded that the shape and volume of ice was similar at 34.5kPa and 69kPa. These test conditions were reproduced by Bucknell et al. [23] with similar results. A study into the effects of altitude matching MR and T_{wb} for the ALF502 was conducted and identified similar icing severity. The results were mainly qualitative as ICI accretion in the LP compressor was observed by a camera mounted at the inner annulus. A similar comparison of results was observed but lacked any quantitative comparisons that were possible in the previous studies mentioned [145].

The values of T_{wb} and MR dominate ICI magnitude. Tsao et al. found that these are not completely independent of each other, due to effects of changing density and heat transfer characteristics [142]. These studies identified two distinct ICI formation regimes. This is driven by freezing of natural melt IWC/ρ_{air} or melting and accumulation of ice

crystals. The dominant value affecting ICI accretion in these studies were the melting and freezing fraction parameters, m_0 and n_0 respectively [140, 141].

2.2.3 Particle Shape

Disperse particle flows can be defined by a mass or volume approach. In the supercooled liquid water (SLW) and crystal (ICI) regimes, particle shape, size and density can vary over the particle cloud and by conditions. SLW droplets are more likely to be closer to a spherical shape, however, ICI particles are distinctly non-spherical. They may be agglomerates or can be in the form of high aspect ratio shapes such as columns or disks. The volume equivalent diameter V_{eq} describes the particle by a single parameter defining its shape. This is the diameter of an equivalent volume sphere D_{eq}.

$$V_{eq} = \frac{\pi D_{eq}^3}{6} \tag{2.1}$$

In disperse flows, non-spherical particles are common, especially in ice crystal icing. Non-spherical shapes will influence the mass-energy exchange with the gas phase. Further, the particle transport will be influenced by the shape and orientation. A non-dimensional measure of a particles spherical shape equivalence is sphericity, ϕ. This is the ratio of surface area of a volume equivalent sphere, to actual surface area [42], this is detailed in Equations 2.2 to 2.4, where A_s is the particle surface area, $A_{n,proj}$ is the cross sectional area normal to the flow direction [106, 120].

$$\phi = \frac{\pi^{1/3}(6V_{eq})^{2/3}}{A_s} \tag{2.2}$$

$$\phi = \frac{\pi D_{eq}^2}{A_s} \tag{2.3}$$

here, crosswise sphericity $\phi_\perp$ describes sphericity contribution by the frontal area normal to the slip velocity vector.

$$\phi_{\perp} = \frac{\pi}{4} \frac{D_{eq}^2}{A_{n,proj}} \tag{2.4}$$

Spheroids can approximate particle volume defined by the aspect ratio E and eccentricity e. Oblate and prolate spheroid shapes are specifically when the spheroid is axi-symmetric about the minor or major axes respectively. These can approximate shape and orientation by just the aspect ratio parameter. This further simplifies Newtonian dynamics for particles as rigid bodies are rotationally symmetric.

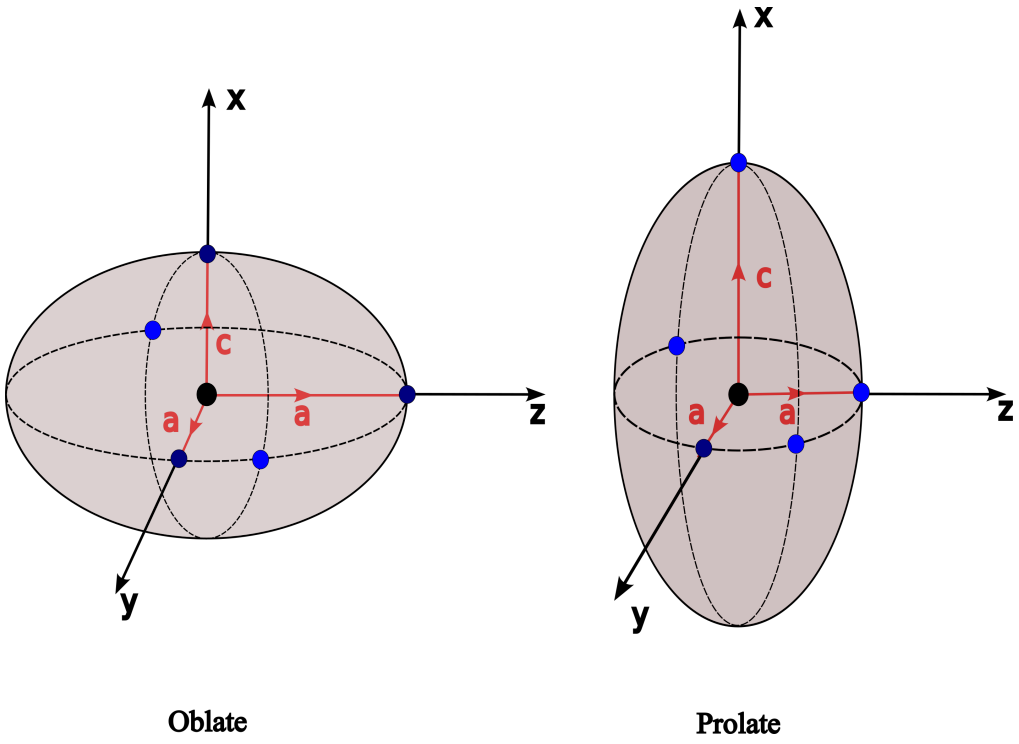

Figure 2.2: Oblate ($E < 1$) and Prolate ($E > 1$) spheroid geometry with respect to principal axes.

The volume of a spheroid with minor and major axes, a and c respectively,

$$V_{spheroid} = \frac{4}{3}\pi a^2 c \tag{2.5}$$

Ratio of spheroid major and minor axes is the aspect ratio, E. An E of unity indicates a sphere, oblate spheroid shapes correspond to $E < 1$ and prolate to $E > 1$. By assuming a spheroid shape, the axisymmetric property enables a simple description of the particle size and shape.

$$E = \frac{c}{a} \tag{2.6}$$

Eccentricity e describes the circularity of the ellipse produced by the major and minor axes,

$$\text{for } E < 1\text{: } e = \sqrt{1 - \left(\frac{c}{a}\right)^2} \quad \Big| \quad \text{for } E > 1\text{: } e = \sqrt{1 - \left(\frac{a}{c}\right)^2} \tag{2.7}$$

$$\phi_{oblate} = \frac{4E^{2/3}}{2 + E^2/e \ln[(1+e)/(1-e)]} \quad \Big| \quad \phi_{prolate} = \frac{2E^{2/3}}{1 + E(\arcsin(e)/e)} \tag{2.8}$$

$$\phi_{\perp,oblate} = E^{2/3} \quad \Big| \quad \phi_{\perp,prolate} = E^{-1/3} \tag{2.9}$$

The particle sphericity term ϕ can be defined by particle D_{eq}, E, respectively.

2.2.4 Particle Size Distribution

Upon ingestion, particles are milled due to impact and fragmentation against the fan and rotor stages. Centrifuging effects will separate smaller mass particles, with lower Stokes number (S_t) into the bypass gas stream as they are more streamline following [5]. Particles which move into the LP compressor can partially melt due to elevated air temperature ($T_a > 0°C$). Studies by Leroy et al. [86, 87] and Coutris et al. [35] investigated the shape and size of HAIC. Here, they summarised the mass-diameter relationship necessary to quantify ice crystal size distribution. Particulate size distribution is defined by its D_{max}, the maximum dimension and D_{eq}, the equivalent diameter relative to the projected area of the particle for a spherical particle, this value can be compared to a mass weighted distribution using the Median Mass Diameter (MMD) [87]. Equation 2.10 shows the general form of the mass size relationship relating particle mass and diameter.

$$m = \alpha D^{\beta} \tag{2.10}$$

In 2019, Coutris et al. found a strong temperature dependence within the m(D) relationship [35], resulting in an MMD - temperature dependence in ICI conditions.

Larger and external surfaces experience icing conditions at altitudes in the ICI or SLD regimes. In external cases, particle $D_{v50} >> 100\mu m$ and modelling focuses on rime and glaze ice build up where surfaces are below freezing. Internal mixed-phase ICI where $T_{wb0} > 0$, particle diameter is commonly $10\mu m < D_{v50} < 200\mu m$, conditions likely found in the engine core, within the LP and IP compressor.

The MMD_{eq}, the 50th percentile of mass-diameter of ice crystals within clouds was found to be between 265μm - 765μm, with smallest MMD_{eq} observed in the ICI TAT ranges. At the lowest temperatures and therefore highest altitudes, smaller ice particulates are most prevalent, since at higher temperatures and higher kinetic energies, impact and aggregation will increase the overall cloud MMD_{eq} [35]. The effects of PSD and particle melt were investigated at RATFac by Knezevici et al. [79, 80]. These studies investigated wet bulb temperature and PSD impact on ice accretion results. It was found that in mixed-phase conditions, particle size was strongly coupled to accretion magnitude. Additionally, the MMD_{eq} was not adequate in describing the particle size distribution as the tail of the distribution at the largest particle diameters had considerable impact on erosion rate and overall MR of the distribution.

Assuming that particle density is constant across the mass-size distribution, PSD in experiments and numerical modelling can be described by the D_{v50}, the median volume diameter which is equal with this constraint and a D_{v90} value is necessary to describe the PSD tail to capture the influence of larger particle sizes upon accretion. Large diameter particles dominate erosion effects, specifically in mixed-phase conditions. Knezevici et al. found that at $T_{wb0} > 0$, the D_{v90} was strongly coupled to the quantity and rate of ice accretion [79, 80].

Particle size distributions can be represented by continuous cumulative volume functions, these can be approximated using size or diameter 'bins' to represent a discrete set of particles. The Rosin-Rammler distribution is suited and widely applicable to describe dispersed particle systems. Equation 2.11 shows the Rosin-Rammler distribution. The exponent term R is the oversize distribution mass fraction, which represents the mass fraction of particles larger than x, relative to a location parameter $\bar{x}$, this equals to the mass fraction when $R = e^{-1}$. Y_d is then the mass fraction undersize. The spread parameter can

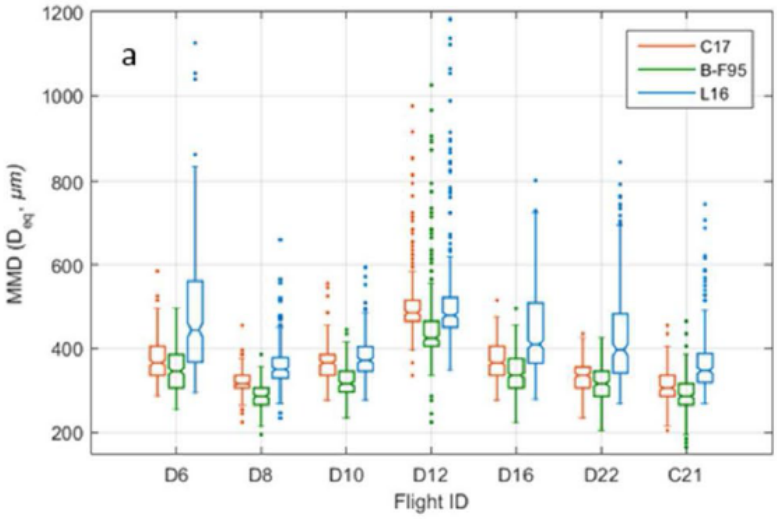

Figure 2.3: Median Mass Diameter distribution relationships from Darwin 2014 (Dxx) and Cayenne 2015 (Cxx) HAIC/HIWC field campaign test flight data [87]

be calculated by taking the natural logarithm twice of the Rosin-Rammler expression. The gradient of the natural log relationship provides the spread parameter term [1].

$$Y_d = 1 - R \tag{2.11}$$

$$Y_d = 1 - e^{-(x/\bar{x})^n} \tag{2.12}$$

$$\ln[-\ln(1 - Y_d)] = n \ln x - n \ln \bar{x} \tag{2.13}$$

$$n = \frac{\ln[-\ln(1 - Y_d)]}{\ln(x/\bar{x})} \tag{2.14}$$

Larger particles dominate erosion effects as observed in the studies conducted at RATFac by Knezevici et al. [79] and Bucknell et al. [23]. Particles that have a higher S_t will have a higher normal velocity component and therefore a higher exchange of kinetic energy at the surface during impact. Bucknell et al. [24] identified a surface angle and kinetic energy semi empirical erosion model driven by local surface angle, particle diameter and velocity from tests conducted at RATFac on an axisymmetric cone test piece.

2.3 Particle Transport

Particle-laden gas flow is a multi-phase flow phenomena with a carrier gas phase in a continuum combined with a dispersed particle phase suspended within it. This leads to a particle-fluid interaction which is driven by mass, momentum and energy exchange between phases. The disperse phase is dominated by forces dependant on the relative mass and volume fractions between the disperse and continuous phases. In the ICI regime, particle sizes range from $50\mu m$ to $200\mu m$ in convective cloud systems [43, 48, 87]. Further, internal mixed-phase ICI particles fall in the $1\mu m$ to $200\mu m$ diameter range. Brownian motion, virtual mass and Saffman lift forces can be neglected as these dominate in sub-micron particle sizes [6]. Particle body forces that dominate are drag, lift, buoyancy, gravitational and turbulent dispersion forces respectively, along with heat transfer and phase change between the dispersed and gas phases respectively [19, 28, 151] .

2.3.1 Flow Conditions

Particle motion suspended in a carrier fluid is described by the slip velocity. This determines the drag on the particle within the fluid and specifies the particle Reynolds number. Particle slip velocity is as follows.

$$u_{slip} = u_p - u_g \tag{2.15}$$

Where u_p is the particle velocity relative to the centre of mass in the global reference frame and u_g is the local fluid velocity at that point in the field. Particle motion within the carrier phase is dependent on the viscosity, relative density and inertia properties of the gas and disperse phases. Stokes number, S_t, is the ratio of particle and gas phase relaxation times. For a flow in steady conditions, the relaxation time describes the time taken for flow velocity at freestream conditions U_∞ to pass the characteristic dimension D_c of the carrier fluid channel [6, 19, 150].

$$\tau_g = \frac{D_c}{U_\infty} \tag{2.16}$$

The particle relaxation time describes the interaction between the particle and carrier fluid phases. A particle in free fall in a carrier fluid, its response to the carrier gas relates to steady conditions. The terminal velocity and acceleration it experiences in free fall are due to gravity , buoyancy and viscous drag forces.

The gravitational force, F_G, on a particle is

$$F_G = \frac{\rho_p \pi D_p^3}{6} g \tag{2.17}$$

The buoyant force, F_B, on a particle is

$$F_B = \frac{\rho_a \pi D_p^3}{6} g \tag{2.18}$$

Viscous drag force, F_D, in the Stokes' drag regime for $Re_p << 1$ is,

$$F_D = 3\pi \mu_a D_p u_{p,slip} \tag{2.19}$$

where μ_a is the gas dynamic viscosity. Shape drag force on a particle is,

$$F_D = \frac{1}{8} \rho_a \pi D_p^2 C_d u_{p,slip}^2 \tag{2.20}$$

where ρ_a is the gas density, C_d is the drag coefficient, determined by the Re_p. Equating shape drag and viscous Stokes drag,

$$\frac{1}{8} \rho_a \pi D_p^2 C_d u_{p,slip}^2 = 3\pi \mu D_p u_{p,slip} \tag{2.21}$$

$$C_d = 24 \frac{\mu}{\rho_a u_p D_p} = \frac{24}{Re_p} \tag{2.22}$$

At terminal velocity, net acceleration of a particle in Stokes drag is 0, therefore,

$$\sum F = 0 \tag{2.23}$$

$$(\rho_p - \rho_a) g \frac{\pi D_p^3}{6} = 3\pi \mu D_p U_t \tag{2.24}$$

$$U_t = (\rho_p - \rho_a) g \frac{D_p^2}{18\mu} \tag{2.25}$$

Terminal velocity of a particle in free fall at higher Re is,

$$\sum F = 0 \tag{2.26}$$

$$(\rho_p - \rho_a) g \frac{\pi D_p^3}{6} = \frac{1}{8} \rho_a \pi D_p^2 C_d U_t^2 \tag{2.27}$$

$$(\rho_p - \rho_a) g \frac{\pi D_p^3}{6} = \frac{1}{8} \pi D_p C_d U_t Re_p \mu \tag{2.28}$$

$$U_t = \frac{4}{3} (\rho_p - \rho_a) g \frac{D_p^2}{C_d Re_p \mu} \tag{2.29}$$

Assuming $\rho_p >> \rho_a$, particle relaxation time is then ratio of the terminal velocity in free fall to acceleration.

$$\tau_p = \frac{U_t}{g} \tag{2.30}$$

$$\text{Stokes' Drag} : \tau_p = \frac{\rho_p D_p^2}{18\mu} \quad \Big| \quad \text{Non Stokes' Drag} : \tau_p = \frac{4}{3} \frac{\rho_p D_p^2}{Re_p C_d \mu} \tag{2.31}$$

Particle dispersion for particle-laden flows can be quantified by the characteristic response times of both the particle and fluid phases. Stokes' number, S_t, is the ratio of particle to carrier fluid relaxation times, τ_p and τ_g respectively,

$$S_t = \frac{\tau_p}{\tau_g} \tag{2.32}$$

Stokes' number quantifies the time needed to respond to a change in local fluid velocity [132]. This may be thought of as the tendency for a particle to follow the potential field of the fluid it is suspended in. This represents the effect of viscous drag on particle inertia between the particle and fluid phases. An S_t close to unity represents streamline following particles and large S_t represents near ballistic particle advection [93, 139].

2.3.2 Particle Forces

In ICI conditions found in the HAIC / HIWC campaigns, the peak concentration of ice (TWC) was between $0.1 \times 10^{-3}\,\mathrm{kg}/m^3$ and $5.0 \times 10^{-3}\,\mathrm{kg}/m^3$ at flight levels corresponding to TAT of $-30°C$ to $-50°C$ [88]. This equates to an air density range of $[0.6, 0.42]$ kg/m^3 according to the U.S Standard Atmosphere [46, 98]. The volume fraction of the ice phase is in the range $[0.0016, 0.012]$ or $< 2\%$. The viscosity gradient, pressure

gradient and buoyancy forces can therefore be neglected. In addition, particle sizes in ICI are in the micron to millimeter range. Therefore, Saffman's lift force, virtual mass force, Brownian motion and the Basset force can be neglected. Lastly, thermophoresis which exerts a force due to kinetic energy of the gas molecules results in a particle force generated by a temperature gradient. Ice crystal icing deals with small temperature gradients ($\pm 10°C$) for the compressor conditions and test campaigns conducted in the ICI regime [21, 54]. Net acceleration of a particle is therefore,

$$\frac{d}{dt}(\mathbf{x_p}) = \mathbf{u_p} \tag{2.33}$$

where $\mathbf{u_p}$ is the particle slip velocity,

$$m_p \frac{d}{dt}(\mathbf{u_p}) = \vec{F} \tag{2.34}$$

$$\sum \vec{F} = \vec{F}_D + \vec{F}_G + \vec{F}_P + \vec{F}_L + \vec{F}_S + \vec{F}_{Tb} + \vec{F}_{Tm} + \vec{F}_B + \vec{F}_{Br} \tag{2.35}$$

$$\sum \vec{F} = \vec{F}_D + \vec{F}_G + \cancelto{0}{\vec{F}_P} + \vec{F}_L + \cancelto{0}{\vec{F}_S} + \vec{F}_{Tb} + \cancelto{0}{\vec{F}_{Tm}} + \cancelto{0}{\vec{F}_B} + \cancelto{0}{\vec{F}_{Br}} \tag{2.36}$$

$$\sum \vec{F} = \vec{F}_D + \vec{F}_G + \vec{F}_L + \vec{F}_{Tb} \tag{2.37}$$

Given the high Stokes number of particles in ICI ($1.05 - 100$), particle relaxation time is far greater than fluid relaxation time, particles primarily behave ballistically [22, 138, 148], however, turbulent dispersion has been noted to have a significant effect on the melting behaviour and mass concentration of particles in previous experiments [38, 80, 129]. Particles can be represented as oblate or prolate spheroids, which represents frontal area, orientation and volume of particles for discrete phase modelling. Particle drag can be approximated for non-spherical particles by accounting for shape, orientation and particle-fluid density ratio. This is best described by crosswise sphericity ($\phi_\perp$) and

Reynolds number. Crosswise sphericity is the ratio of cross-sectional area of equivalent volume to projected cross-sectional area [10].

2.3.3 Gravity and Buoyancy

Particles experience a force relative to its mass due to gravity g, additionally, particles suspended in a fluid experience a buoyancy force opposite to the gravitational force. Archimedes principle states that the buoyancy force is equal to the weight of displaced fluid by the particle.

$$F_{G,B} = \rho_g V_p g - m_p g \tag{2.38}$$

$$\rho_p V_p a_{G,B} = \rho_g V_p g - \rho_p V_p g \tag{2.39}$$

$$a_{G,B} = \frac{(\rho_g - \rho_p)}{\rho_p} g \tag{2.40}$$

Here, V_p is particle volume. As stated previously, relative densities between the gas and ice allows us to neglect buoyancy from calculations. Particle motion is proportional to acceleration due to gravity.

2.3.4 Drag

Particle drag force is described by the shape, discussed in Section 2.2.3, this drag force is described by its volume equivalent spheroid shape.

$$F_D = \frac{1}{2} \rho_g C_d A_{p,eq} U_{slip}^2 \tag{2.41}$$

$$F_D = \frac{1}{2} \rho_g C_d A_{p,eq} \left\| U_p - U_g \right\| (U_p - U_g) \tag{2.42}$$

Stokes' drag law defines particle Reynolds number as.

$$Re_p = \frac{\rho_p \left\| U_g - U_p \right\| D_p}{\mu} \tag{2.43}$$

Where, U_g and U_p are the gas and particle fluid velocities respectively.

Particle drag is the dominant force in ICI multi-phase flows due to the large difference in density between ice and air. Mach number of the gas inside a compressor has a significant effect on accretion and erosion. At higher Mach numbers, evaporative cooling at static conditions is greater than at stagnation conditions. Therefore T_{wb0} is greater leading to less leading edge accretion and higher rates of erosion due to increased kinetic energy [22, 40].

Drag coefficients of non-spherical particles were approximated by a study conducted by Haider and Levenspiel [60], this used the sphericity to account for orientation. For disks and plates, in cases of high lengthwise sphericity, the Haider and Levenspiel model does account for a large range of Re numbers. Hölzer and Sommerfeld [71] updated this study for C_D relating crosswise sphericity and Reynolds number which uses the projected cross sectional area as opposed to the surface area. Hölzer and Sommerfeld's study simplifies the correlation for C_D, however Bagheri [10] found it resulted in a higher uncertainty in results of 14.1% from 5%, this still provides a suitable confidence interval.

2.3.5 Lift

Particle lift force is generated by aerodynamic lift, Saffman's lift and Magnus lift forces. Magnus and aerodynamic lift are generated by particle rotation and orientation respectively. It is assumed in this body of work that particles are oriented at 0° or 90° angle of attack for oblate and prolate spheroids respectively. This assumes a symmetric shape with no lift. Magnus force is generated by rotating bodies creating a pressure differential across the body in its plane of rotation, relative to the fluid parcel [158]. Rotation is neglected in this study. Lastly, Saffman's lift force is dominant for small, submicron particles in a shear flow [56, 122], this may be neglected in the ICI regime.

2.3.6 Turbophoresis

Ice particles ingested by turbomachines are influenced by the local energy dissipation within the flow. Turbophoresis is the force experienced by particles due to velocity fluctuations in the carrier flow. Particles that are small and dense (applicable in ICI) will

disperse from regions of higher turbulence intensity to lower turbulence intensity [27, 56, 117]. Wall deposition and diffusion of particles is governed by the particle density and size relative to the turbulence intensity [75, 97, 122].

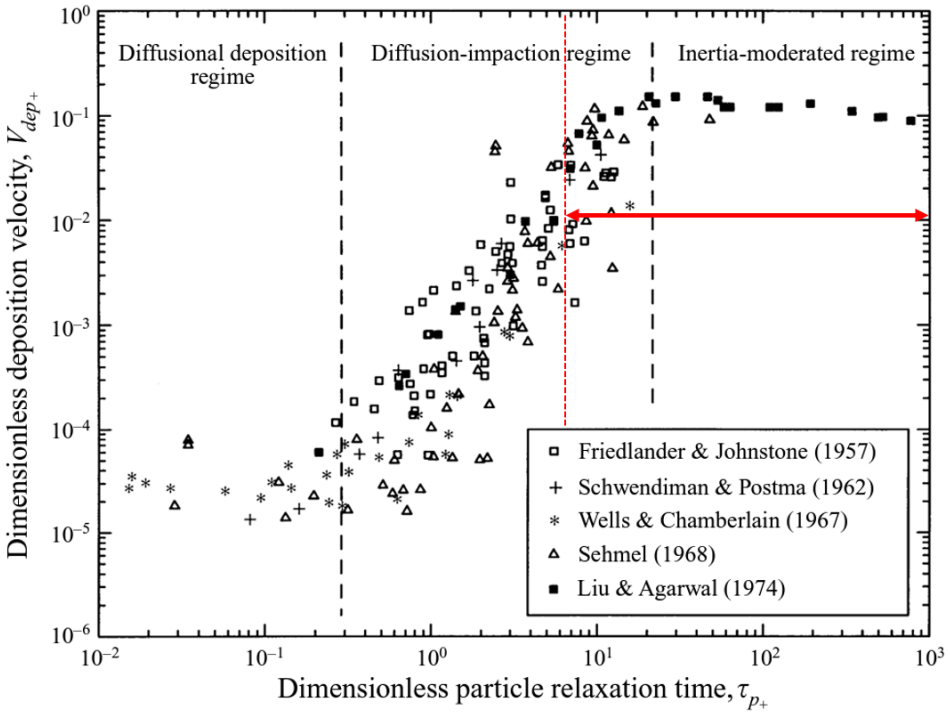

Figure 2.4: Particle deposition for fully developed pipe flow experimental data, taken from [159]. ICI regime particles present in compressor flows have non-dim. particle relaxation times corresponding to the red arrow region.

Here, the dimensionless particle relaxation time τ_{p+} is,

$$\tau_{p+} = \frac{\tau_p v_*^2}{\mu} \tag{2.44}$$

and dimensionless deposition velocity V_+ is defined as,

$$V_+ = \frac{V}{v_*} \tag{2.45}$$

the friction velocity v_* is defined as,

$$v_* = \sqrt{\frac{f}{2}} \bar{U}_g \tag{2.46}$$

lastly, f is the friction factor and $\bar{U}_g$ is the mean channel velocity.

Particles are dispersed through the carrier flow by velocity fluctuations For ICI particle transport, the carrier gas phase properties (P, v_*, U_g, μ) result in dimensionless particle relaxation times predominantly in the inertia-moderated and diffusion-impaction regimes. Smaller particles will disperse and interact with the boundary layer and bounding walls due to this diffusion effect. Forsyth [52] investigated the turbophoresis implication on solid particles in pipe flow from the experiments conducted by Liu & Agarwal [90] and random walk model implementation by Mofakham & Ahmadi [99]. They generated both discrete and continuous random walk models (DRW / CRW) to simulate velocity fluctuation on particles in high temperature gas turbine deposition conditions for small micron particles. DRW models were found to overpredict deposition velocity due to the implications by integration time scales. A continuous random walk model better approximates deposition rates in the diffusion-impaction regime, however underpredicts in the inertia regime, where DRW is more accurate. Currie et al. [38] implemented a DRW turbophoresis model for particle transport in the RATFac icing wind tunnel. These results were compared to experimental measurements for turbulence intensity and mass flux of ice and water through the tunnel test section. This model was found to overpredict particle mass close to the tunnel walls due to a bounce angle limitation of 2° for impacts. Further, it was found that the turbulence intensity was under-predicted by $k-\epsilon$ and $k-\omega$ RANS turbulence models. Reynolds Stress Transport Models can further predict anisotropy within turbulent fluctuations [65, 99].

2.3.7 Inter-Particle Collisions

The interaction between the carrier gas and particle phases is governed by the relative volume fractions of each constituent. In Section 2.3.2, the ice volume fraction for ICI compressor stage icing was found to be between 0.1 and 1.2%. This can be sufficient to neglect pressure gradient and viscous forces between the low density carrier gas and high density ice crystals. However, this describes a more concentrated disperse phase which increases the probability of particle-particle collisions. In ICI particle transport, this may further have implications in agglomerates, phase change due to impact energy

and momentum exchange and mass diffusion. Currently, ICI transport models neglect intra-phase collisions for model and computational complexity reasons.

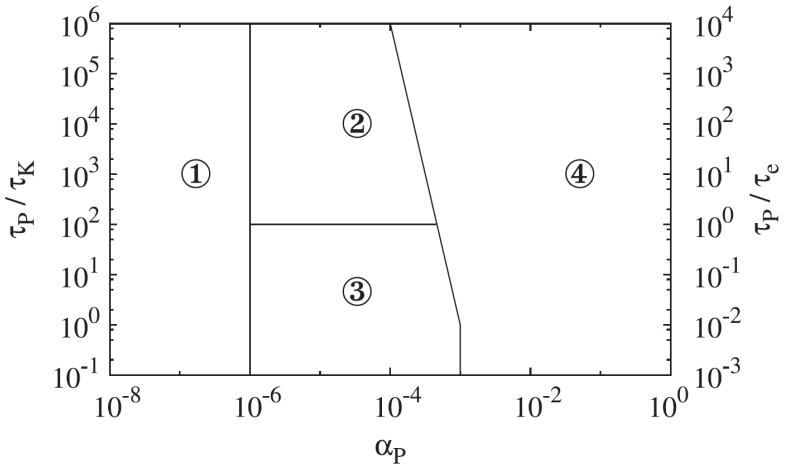

Figure 2.5: Particle coupling regimes depending on the volume fraction α_p in disperse particle flows represented by Lagrange-Euler modelling. Taken from [55] adapted from [45]

Particle interactions become dominant at volume fractions above 10^{-6} , below this one-way coupling is sufficient to describe particle motion. Above this, the particle characteristic time τ_p and Kolmorogov length scale τ_K will specify whether the particles influence the inertia of the carrier fluid or are influenced by intra-phase collisions [45, 149]. Two-way coupling describes the dense, disperse particles which modify the carrier fluid. Three-way coupling is one-way fluid-particle interactions but with particle collisions in more concentrated particle phases. Where $\alpha_p > 1\,0^{-3}$, 4-way coupling is necessary for particle fluid coupling, and intra-phase collisions.

2.4 Particle Heat Transfer and Phase Change

The water content of the air is a driving factor for evaporative cooling capacity and has a significant affect on the particle melting behaviour. Relative humidity (RH) describes the water content in the air as a percentage of saturation at a given pressure and temperature. Villedieu et al. [148] and Wright et al. [154] developed melting models from a hailstone melt model created by Mason [94]. Hauk conducted particle melting experiments by suspending particles in an acoustic levitator to examine convective heat transfer and phase change in ice crystals. Hauk's developed a convective heat transfer model for ice

particles as seen below [67]. Phase change is further included to describe particle melting and sublimation. In mixed-phase ICI conditions, particles entering the compressor are subject to above freezing TAT values. Energy transfer from the gas to particles results in phase change through melting, evaporation and sublimation. Convection, evaporation and sublimation heat transfer drives particle melting through phase change and temperature gradients between the disperse and gas phases.

Particle melting is described by an mass-energy balance between the disperse and gas phases. Mason [94] developed a quasi-steady hailstone melting model with temperature gradients through the ice body, accounting for heat transfer between air and an ice body due to melting, conduction, convection, evaporation and sublimation. Melting commences once the particle temperature reaches freezing, with a water layer encasing an ice core subject to a temperature gradient with the gas phase. Wright et al. [154] implemented this model with respect to icing phenomena in GlennICE using a lumped-system approach, assuming a homogeneous particle temperature. Villedieu et al. [148] adapted the Wright et al. model for non-spherical particles using a sphericity term. Studies conducted by Hauk et al. [67, 68] compared the Villedieu et al. model to an acoustic levitator experiment. Currie et al. [38] developed non-spherical Nusselt number correlations with regards to the ice particle melting model. Yang et al. adapted the models by Hauk and Villedieu et al. [156, 158] to account for combined ice-air porosity enhanced melting and surface convective heat transfer.

Hauk further investigated melting characteristic times relating to particle sphericity (Φ) and gas thermodynamic properties, including temperature, pressure, and RH [67]. Hauk's work drew upon the existing phase change models derived by Villedieu et al. and Wright et al. and derived an equation for particle heat transfer which relates to a Nusselt coefficient for spherical ($\Phi = 1$) and non-spherical particles [67, 148, 154]. This is summarised below in Equation 2.47,

$$Nu_p = 2\phi_p^{\frac{1}{2}} + 0.552 Re_p^{\frac{1}{2}} Pr_p^{\frac{1}{3}} \phi_p^{\frac{1}{4}} \tag{2.47}$$

where ϕ_p is particle sphericity.

Particle aspect ratio, non-spherical particle rotation and particle porosity was further found to influence melting rates in studies by Yang et al. [156, 158]. This concluded a heat transfer enhancement for higher aspect ratio particles and an effect due to surface blowing. Lou et al. conducted a study to determine the melting behaviour of various ice crystal types. The study compared a porous melting particle, a particle with a water skin and a bare ice particle. This study identified a higher melting rate for particles with a water film. This is due to heat transfer from the gas causing evaporation, melting and sublimation compared to only melt and sublimation for the pure ice particle [91].

Particle melting is quantified by the value melt ratio (MR) which is the ratio of liquid water mass or Liquid Water Content (LWC), to liquid water and ice mass, or Total Water Content (TWC), which is used to quantify a bulk cloud melt ratio.

$$MR = \frac{LWC}{LWC + IWC} \tag{2.48}$$

The relationship between MR and accretion has been measured experimentally in IWT facilities to identify critical MR conditions which result in significant ice accretion. Mixed phase ICI studies conducted at the Research Altitude Test Facility (RATFac) of the National Research Council (NRC) in Canada by Currie et al. identified a band of MR values which led to accretion. MR values between 5% and 20% (given appropriate TWC and T_{wb0}), were sufficient for sustained ice accretion to occur. Maximum accretion rates and thicknesses were observed between 10 - 17% [39, 40]. Comparable experimental studies by Bucknell et al. [23, 24] were conducted with good agreement among results for MR and ice accretion response. Bucknell et al. extended this relationship to a sticking probability model, generating a term to quantify the chance of stick given the ice particle melt, size and dynamics. This model indicated that particle sticking or accretion rate is greatest at surface angles closest to perpendicular relative to flow direction.

2.5 Particle Surface Impact

Particle surface interaction within the compressor is a complicated multi-physics problem. This involves impact, energy transfer, water and ice deposit, post impact physics including

bounce, sticking erosion and fragmentation. Models developed by Hauk [67], Trontin et al. [136] and Bucknell et al. focus on a similar energy and mass approach for the surface interaction problem.

Particle impact can be decoupled into fully glaciated - dry wall and mixed-phase-wetted wall impacts. This subdivides impact physics into bounce/fragmentation and stick/erosion. A simple 1D momentum-energy exchange for a non-spherical fully glaciated dry wall impact can be employed. This dictates either bouncing or fragmenting after impact.

Viduarre et al. [146] investigated the breakup behaviour of ice crystals, generating a model bases on number of post impact fragments. This led to the creation of a dimensionless ratio $\mathcal{L}$, the normal kinetic energy to surface energy ratio of the particle which dictates the post impact physics detailed in Equation 2.49 . This ratio was further tuned by Hauk [67] who identified 3 different dry impact regime thresholds.

$$\mathcal{L} = \frac{1}{12}\frac{\rho_p D_p V_{p,normal}^2}{e_\sigma} \tag{2.49}$$

- $\mathcal{L} \leq 0.5$ Quasi-elastic rebound
- $0.5 < \mathcal{L} < 90$ Inelastic rebound with particle cracking (no fragmentation)
- $\mathcal{L} \geq 90$ Inelastic destructive rebound with fragmentation [66, 69].

2.5.1 Stick

In mixed-phase conditions, a water film present on the surface deposited by partially melted crystals can modify the adhesion force and coefficient of restitution of the surface. This can lead to sticking or partial sticking of fragments post impact [23, 40, 76]. A sticking efficiency variable has been used to quantify the likelihood of sticking in multiple studies by NASA, ONERA and Oxford. Trontin et al. [138] employ a model based on MR and TWC. Bucknell et al. produced a similar model experimentally from results obtained at NRC RATFac. Bucknell et al. generated a sticking efficiency term defined by the collection efficiency, impinging mass flux (stick, bounce, erosive) and normalised by the total flux. This was used to generate a sticking probability model P_{stick} as a

polynomial in MR. This model showed a similar peak sticking efficiency band regardless of erosion magnitude, as those observed in NRC RATFac and NASA studies (9% - 13%) [23, 39, 103].

$$P_{stick} = f(MR^5) \tag{2.50}$$

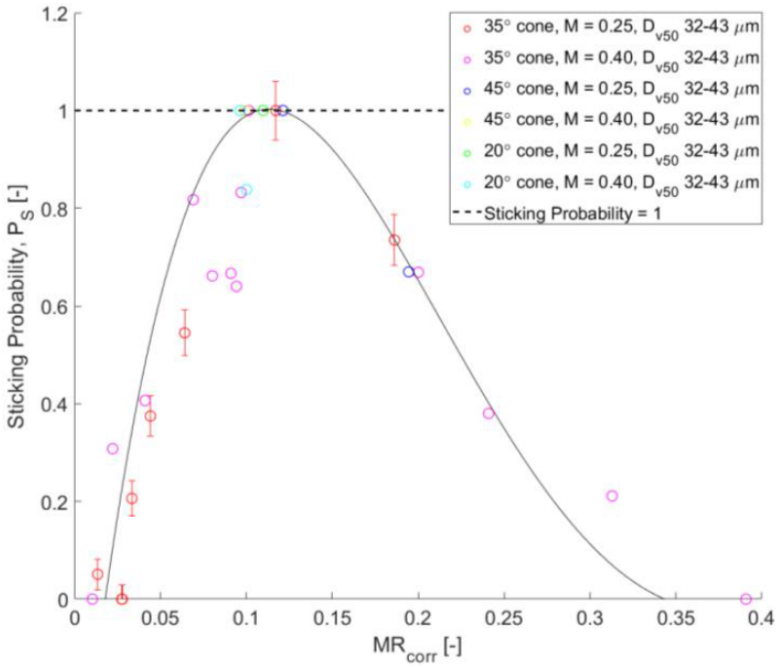

Figure 2.6: Sticking probability for ICI axi-symmetric cone tests conducted at NRC RATFac by Bucknell et al. [23].

2.5.2 Bounce

Particle bounce will depend upon the energy regime that the impact takes place. Bouncing occurs for quasi-elastic and inelastic rebounds where no particle mass loss or destruction takes place [69]. In 3D particle impact can still be resolved at the impact point as a 1D momentum and energy exchange problem as detailed by Villedieu et al. [148] and Bucknell et al. [22]. Between bounces, ice diameter, sphericity and porous ice density is unchanged. Any melt water will deposit on to the surface and the mass will change instantaneously upon impact. Particle rebound velocity $\vec{v_p}'$ is calculated by the tangential ϵ_t and normal ϵ_n coefficients of restitution. This is calculated based on experiments conducted by Hauk [69],

$$\vec{v_p}' = \epsilon_t(\vec{v_p} - (\vec{v_p} \cdot \vec{n})\vec{n}) - \epsilon_n(\vec{v_p} \cdot \vec{n})\vec{n} \tag{2.51}$$

elastic impact is assumed for particles with an energy ratio $\mathcal{L}$ below 0.5,

$$\epsilon_t = 1 \tag{2.52}$$

$$\epsilon_n = 1 \qquad \mathcal{L} < \mathcal{L}_1 \tag{2.53}$$

in-elastic impact is assumed for particles with an energy ratio $\mathcal{L}$ below 90,

$$\epsilon_n = \left(\frac{\mathcal{L}_1}{\mathcal{L}}\right)^{1/3} \qquad \mathcal{L}_1 \geq \mathcal{L} \leq \mathcal{L}_2 \tag{2.54}$$

$$\epsilon_n = \left(\frac{\mathcal{L}_1}{\mathcal{L}}\right)^{1/3} \qquad \mathcal{L} \geq \mathcal{L}_2 \tag{2.55}$$

2.5.3 Fragmentation

Particle breakup following impact was investigated by Hauk et al. [69], crack development and major fragmentation was observed by recording cases where 50% or more of the particle volume is lost to fragments. Modelling of particle breakup and post-impact bouncing of fragmented particles is complex as it requires splitting of the initial spheroid into multiple to represent fragmentation. ONERA employs a single particle fragmentation model with the new particle diameter being selected by a random scaling factor to adjust the D_{eq}. Presently, Trontin et al. quantify the energy exchange at the wall by redistributing kinetic energy tangentially by calculating the tangential coefficient of restitution from fragmentation energy release [137, 138]. In 3D modelling, fragmented particles will spread radially which produces a stochastic post-impact behaviour for fragmentation. Additionally, current models re-inject a single or specified number of particles post-impact to model fragmented particles. Here, particle rebound behaviour is similarly described as in Equations 2.51 to 2.55. In this case, in elastic rebound is generated by modifying the tangential and normal coefficients of restitution based on the energy ratio $\mathcal{L}$, rebound velocity $\vec{v_p}'$

$$\vec{v_p}' = \epsilon_n t(v_p - (\vec{v_p} \cdot \vec{n})\vec{n}) - (\vec{v_p} \cdot \vec{n})(\epsilon_{tt}\vec{t} + \epsilon_{nn}\vec{n}) \tag{2.56}$$

$$\epsilon_{nn} = \Big(\frac{\mathcal{L}_1}{\mathcal{L}}\Big)^{1/3} \qquad \epsilon_{nt} = 0.4\Big(1 - \frac{\mathcal{L}_2}{\mathcal{L}}\Big) \qquad \epsilon_{tt} = 1.0 \qquad \mathcal{L} \geq \mathcal{L}_2 \tag{2.57}$$

2.5.4 Erosion

Erosion processes within literature are modelled in a limited way. Erosion and sticking are highly coupled and depend on MR. The prominent erosion models employing are from ONERA and Oxford both have models developed from previous NRC RATFac experiments where sticking and erosion can be easily controlled. Bucknell et al. developed a semi-empirical erosion model dependent on local surface angle and sticking efficiency. This model is dependent on wall temperature, particle sticking, kinetic energy and surface angle [23]. ONERA's model differs from the Oxford model, with tangential velocity for the kinetic energy term which compares to Bucknell's approach with local geometry angle. Separately, the effects of IWC, T_w and D_P were all tuned using a 2D planar cylindrical nose test campaign [39, 40]. This is different to the model generated by Bucknell et al. where cone angles and local surface angles were tested to enforce a constant surface angle and prevent shed and dropping in the accreted ice [23].

Currie developed a gouge/bounce model (GBM) to model the erosive effects of impact and erosion in ice particles [36]. This study identified the reduction in KE and increase in back scatter of particles by gouging impacts and ejected surface ice mass which causes interference with the impinging mass flux and can augment sticking probability. This study also found particle-particle interactions had a lesser effect in the overall sticking probability.

An improvement to the ONERA erosion and fragmentation models by Charton et al. [29] modified the surface angle - KE model detailed in [138] by including a deformation and cutting term to resolve particle size and momentum with surface erosion and particle fragmentation. This model employs a projected cutting volume on the surface by a particle and an integral method for ice volume removal/ejection. The model was

limited for high melt ratio and high LWC cases as is common in other literature and under-predicted erosion in cases with lower TWC [30].

2.5.5 Surface Roughness

Particle impact at the surface is assumed to be a simple smooth wall impact problem. Particles impacting at the outer ice surface will be interacting with a porous, rough wall in reality. In order to capture ICI impact physics correctly, it would be better to model the wall with a roughness height corresponding to sintered ice accretion. Modelling the rough wall is separate from the EMM and geometry distinction and appears simply in the numerical model to randomise surface angle and roughness height for impinging particles. This would likely improve capture or sticking efficiency within voids as particle re-impingement and sticking would likely be improved by the increased surface area of the rough wall.

Sommerfeld & Huber [128] generated a stochastic particle rough wall collision model in 2D for an isotropic rough wall. This model generated a Gaussian distribution for roughness angle, γ representing a perturbation in the wall normal vector. This introduces a shadow effect dependent on the local surface normal. Particle impact with the rough wall institutes a realisability criteria for particle impact approach velocity $U_p^- \cdot n < 0$. This original approach is problematic as very small impact angles eventually leads to a 0 probability of wall rebound. Konan et al. introduce a multiple collisions probability criterion [82, 83]. This resamples the roughness angle depending on the local approach angle of the successive collisions. It only focuses on 2D impact and does not assess the stochastic effects of multiple rebounds in 3D. Radenkovic & Simonin [113] expanded this method to 3D. This utilised a probabilistic approach by generating a probability density function for a corrected normal vector angle distribution. This imposes an arbitrary correction to the impact normal vector to impose a 'virtual roughness'. Figure 2.7 illustrates the pre and post impact vector transformation for an arbitrary rough wall collision.

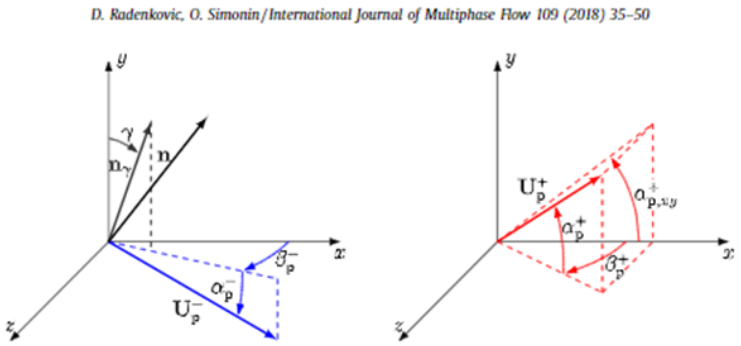

Figure 2.7: Simulated Rough Wall Collision with Correction vector $\mathbf{n}_\gamma$. Taken from [113].

This method provides a stochastic model for Lagrangian particle tracking for particle-rough wall collisions. This method would be a simple implementation to investigate ice deposition in rough wall ice crystal impacts.

2.6 Ice Crystal Icing Accretion

Surface ice accretion is modelled by a combined water–ice boundary value problem with a transient phase change interface. The Stefan condition is a boundary value problem, this described changes in phase at a boundary and the phase boundary velocity due to a combined heat transfer and phase change PDE [16, 96]. The phase transition boundary represents a challenge in directly solving the PDE due to the discrete changes in coefficients representing the medium in each phase. Ice crystal icing accretion state of the art focused on a quasi-steady mass energy-balance with a in built pseudo time step to model the height and velocity of the phase boundary. At the surface, a phase-change conduction energy balance known as the Stefan problem is used to model the temperature profiles, melting, sublimation, conduction and boundary conditions for ice-water accretion from impinging mass flux. The main types of ice accretion models are for SLW and ICI. SLW leads to instant freezing of the supercooled droplets upon impact. The Stefan problem for ice accretion was generated by Messinger [96] for quasi-steady state conditions involving supercooled liquid water droplets (SLW). This modelled glaze and rime ice, with and runback water forming on the surface.

2.6.1 Ice Accretion

Accretion from ICI differs to SLW in that the ice crystals must be mixed-phase in order to generate a water layer to enable sticking and stable accretion growth. Modelling ICI accretion in 3D for compressor stages and rotating reference frames requires the same model formulation and assuming each cell is a flat plate can rely on some simple assumptions [101, 105].

1. Conduction through the ice layer is neglected.

2. Temperature profiles through the ice and water layers are quasi-steady.

3. Runback water flows axially downstream between control volumes.

The limitations of Messinger's model were its steady assumption with no gradient in temperature to model melting and freezing of accreted water and ice. Myers extended the model to include temperature gradients in the ice and water layers which is important to model the transient temperature response. This incorporated layers and time dependence to solve the PDE's within the Stefan problem [101]. The Myers-Messinger modification is referred to in literature as the Extended Messinger Model (EMM) and will be referred to in this way in this body of work.

Ayan and Özgen further expanded the EMM for Turkish Aerospace's TA-ICE to account for mixed-phase ICI conditions. This was validated against the COX and NRC wind tunnel results which were also used for ONERA's EMM implementation. This model employs a similar porous glaze ice model to represent mixed-phase ICI and has good agreement with ONERA's IGLOO2D results [7, 8, 77].

Bucknell et al. adapted the EMM to accommodate a further water layer and temperature gradient at the substrate surface to account for warmed surfaces which are present in ICI conditions. A warm substrate and additional water layer is calculated with $T_s > 0°C$ known as EMM-C (Crystals) [25]. This differs from the method employed by ONERA, TA-ICE and NASA for their EMM implementations. In each case, the ice adheres directly to the surface and water is mixed with the ice layer.

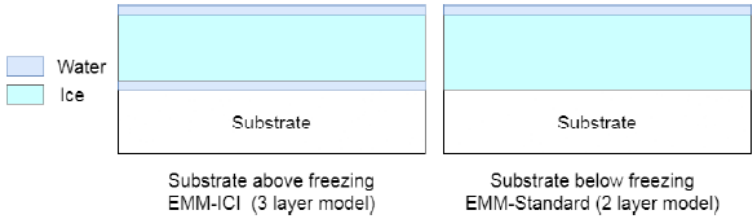

Figure 2.8: EMM-C 3 layer Stefan problem representing ice accretion on warmed surfaces [25].

Baumert et al. conducted an ICI study using IGLOO2D and experimental results from the Braunschweig Icing Wind Tunnel. This study implemented a runback water model which predicts whether water is trapped in the porous ice layer or runs downstream freely on the surface. Additionally they identified a strong temperature dependence on icing severity as liquid water film which freezes on impact reduces the overall surface MR and therefore sticking efficiency [12]. Kim et al. [77] compared the Classic MM and EMM for rotorcraft icing. This study utilised CFD generated skin friction coefficients to generate a local HTC. There was good agreement with results from LEWICE.

Gupta conducted a comprehensive study on the EMM for applications to complex geometries using codes from Georgia Tech, open-access codes such as LEWICE and commercial solvers including STAR-CCM to investigate the numerical implementation of the EMM [58, 59].

2.6.2 Water Runback

Water transported across the surface is a necessary driver for ICI accretion in mixed-phase and warm wall $T_{wb0} > 0°C$ conditions. Evaporation and conduction will increase the icing risk of surfaces and aid in accretion initiation. Existing models by ONERA and Oxford model runback water as a pseudo-steady state water film which is adjusted by flux across each discrete cell boundary. This is set by a water film height [22, 138]. Water runback on surfaces takes place due to drag, friction and adhesion or capillary forces. ONERA's model considers the ice layer in the accretion model to be porous and has a capacity to hold liquid water deposited on the surface. This is coupled with a simple shear driven water transport model [137].

By assessing the literature, it is known that implementation of a 3D ice particle tracking and accretion software has previously been implemented with mixed-phase Myers-Messinger Model approaches. The main challenges in 3D stems from the methods employed to discretise the domain and to account for morphing ice and water boundaries. The availability of test data and reliable PSD and accretion geometry is a further need for validation of ICI accretion modelling. In the EMM-C implementation, ice and runback water must be modelled as a continuous surface accounting for energy exchange between control volumes within the model. This work focused initially on the upgrade of the existing code and the initial work involved in modifying the in-house code ICICLE to a full 3D ICI particle tracking and mixed-phase warm substrate accretion simulation suite.

2.7 Ice Crystal Icing Modelling

Models for ICI are have been developed recently to account for mixed-phase ice particle transport and deposition. Most models within the current literature focus on a modular approach for each separate physical sub model. These commonly comprise of some of the following: continuous phase Navier-Stokes solver, particle transport model, particle - air heat and mass transfer, surface impact and interaction model, ice accretion and erosion model, surface film runback model and substrate heating model.

2.7.1 Trajectory Modelling

Particle transport may be modelled as a continuous Eulerian phase or discrete Lagrangian phase. Lagrangian particle tracking involves the numerical integration of particle body forces for an individual particle or grouped mass of particles represented by one constituent rigid body with mass flux scaling term. This approach is more computationally demanding than an Eulerian approach but enables specific input of melt, orientation, aspect ratio, mass distribution which can be derived from experimental data [20, 58, 158]. Eulerian phase tracking is less computationally expensive and can be effective in bulk particle phase modelling for complex geometries or external aerodynamic icing where particles have a more uniform aspect ratio and are fully glaciated [20, 73].

2.7.2 Topography Redefinition

Within ICI modelling, surface topography height and orientation changes with each accretion simulation step. It is vital to conserve ice and water deposition mass and enable solution stability. Methods to extrude or morph the accreted surface form a part of the accretion solver. Currently the majority of ICI models implement a surface 'panel' or streamwise slice approach to represent accretion control volumes. These can be generated for a structured or unstructured surface mesh.

Moving boundaries in numerical simulations and more importantly multi-phase geometry evolution demands effective mesh adaption and optimisation to preserve geometrical features and conserve mass. Conservation of volume is vital for accurate and stable numerical solutions. Within ICI surface evolution, this is coupled with thermodynamic modelling within the water-ice(-film water) layers. Mesh smoothing and surface motion must preserve volume and local features. Jiao generated a mesh volume and feature conservation paradigm using local surface normal offset to generate an eigenvalue decomposition to preserve feature definition and classify vertices by flatness [74]. Surface mesh evolution in three dimensions for SLW accretion was investigated by Tong et al. utilising Jiao's volume conservation algorithm. This implemented a swept area method to compute local volume flux. Local curvature tended to bunch nodes together in concave sections and the opposite in convex due to nodal normals creating convergence/divergence. This required nodal smoothing to maintain local mesh quality and continuous cell area distribution. The surface evolution method conserves volume and utilises local cell normals to preserve the normal cell face motion [134].

Porter et al. [110] generated a generalised three-dimensional suface extrusion method for unstructured tet surface mesh evolution. This utilised Jiao and Tong's models for unstructured meshes in ICI simulations. This study generated a faceted extrusion method for tet prisms. This applied a volume area integral relation for nodal normals to correct for ice height extrusion to compensate for area change. Porter et al. added in a error correction method using local face normal direction to account for degenerate solutions where the integral would predict a negative extrusion vector. This study found a polynomial to relate nodal unit normal vectors and extrusion height.

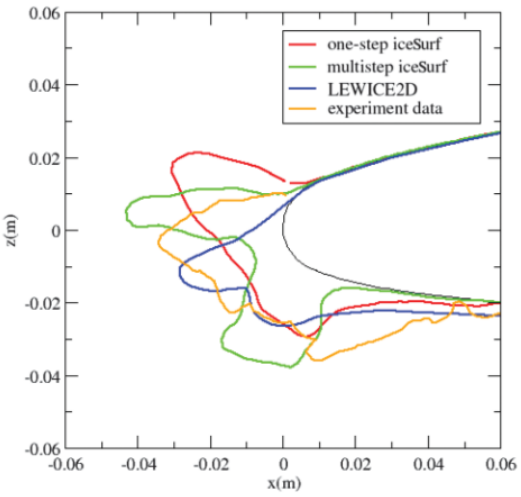

Figure 2.9: Surface mesh evolution with local volume conservation. Tong's model is iceSurf with single layer MM and multi-layer MM implementation. Compared with existing LEWICE model with no volume conservation. Taken from Tong et al. [134].

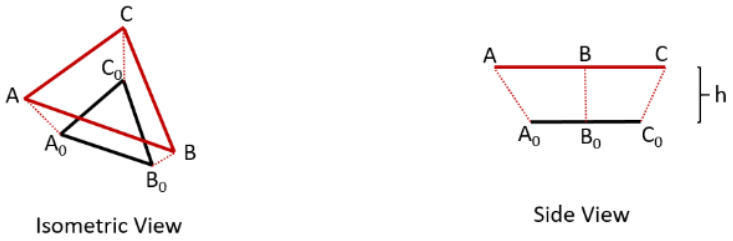

Figure 2.10: Tet Prism Surface Redefinition for ICI Accretion Extrusion taken from Porter et al. [110].

2.8 Numerical Ice Accretion Models

The overall modelling approach is similar across SLD and ICI accretion, with sub-model physics varying slightly across different models and codes. ICI accretion codes exist from Oxford University, MUSIC-HAIC Consortium, NASA, ONERA and ANSYS.

ICICLE is the current in-house ICI accretion code developed at Oxford by Bucknell et al. [22] and later improved by Connolly et al. [34]. ICI codes which are relevant for 2D mixed-phase conditions are ONERA's IGLOO2D, NASA's LEWICE3D, Turkish Aerospace's TA-ICE [15, 105]. LEWICE3D lacks the functionality to include the EMM and therefore neglects temperature gradients within the ice layer [147, 152]. ONERA's model exists with a similar implementation for particle tracking, impact, accretion and erosion.

Simulation of ice accretion is vital in testing and certification of engine compressor stages. Multiple 2D mixed-phase ice crystal icing codes exist currently. Within the past decade other workers have updated the NASA GlennICE icing code to include mixed-phase particle tracking, erosion and particle mass-energy transfer at the surface [154].

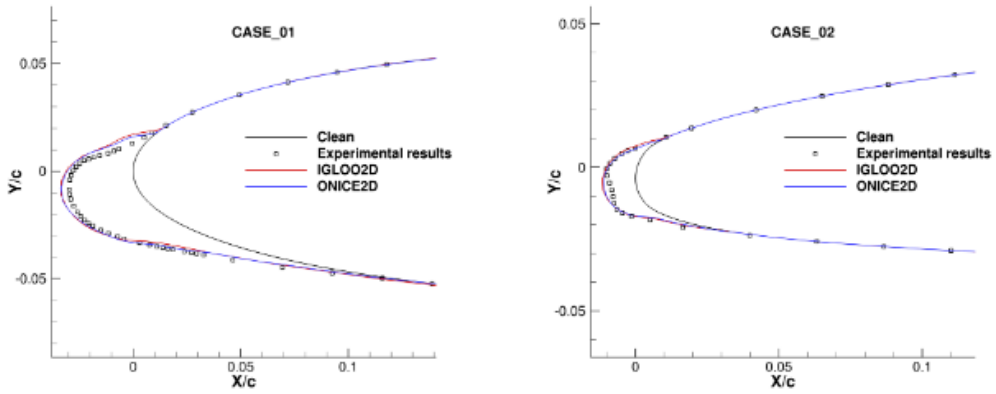

Figure 2.11: Comparison of ONERA's ICI Two-Dimensional Code IGLOO2D and an implementation of LEWICE (ONICE2D) using experimental ice shapes obtained in the Icing Research Tunnel at NASA's Glenn Research Centre taken from [137].

Current state of the art work on three-dimensional ice modelling is reflected in the modification of the IGLOO3D code at ONERA, conducted within the High Altitude Ice Crystals (HAIC) programme [147, 148]. The model captures glaciated and mixed-phase particle behaviour using the EMM, however, it neglects heat exchange between the wall and the particles in impingement processes. This may lead to an inaccurate prediction of the melting of the particles upon impact. Furthermore, an empirical erosion model is incorporated using previous experimental results in [39].

Multiple 3D icing codes exist for supercooled liquid water (SLW) modelling including IGLOO3D at ONERA, FENSAP-ICE developed at McGill University and Newmerical Technologies (now owned by ANSYS Inc.) and a multiphase ice crystal icing (ICI) model in LEWICE3D developed by NASA combined with the updated GlennICE code. A current campaign by ONERA and the HAIC programme is pursuing work involving updating existing ice crystal icing 2D multi-disciplinary models to 3D [147].

ONERA's IGLOO3D code has also been updated to handle mixed-phase ice crystal icing with a mixed-phase implementation of the EMM. The current model has an impact

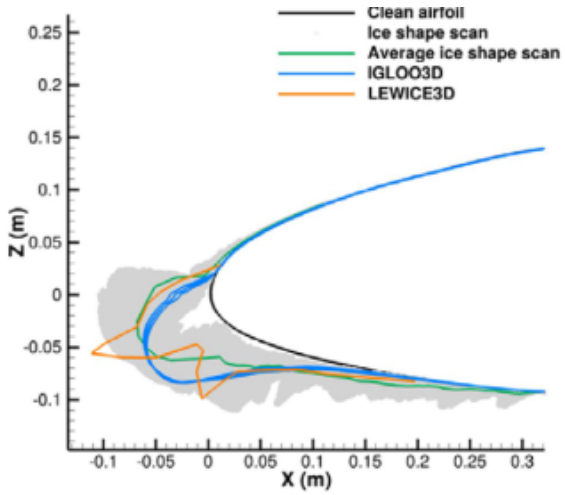

Figure 2.12: Comparison of 3D accretion shapes from SUNSET-2 Program database taken from [111, 112].

angle corrector step to reduce the requirement for repeated particle tracking steps to reduce computational overhead. Tables 2.1 and 2.2 summarise the state of the art for ICI accretion codes and the individual modelling capability.

Table 2.1: Existing Two-Dimensional Numerical Icing Software

Code	Group	Capability	Flowfield	Particle Transport	Accretion	References
LEWICE2D	NASA	SLW	Potential Flow	Eulerian	Classical MM	[153, 155]
IGLOO2D	ONERA	SLW + ICI	Euler + IBM	Lagrangian or Eulerian	Classical MM	[135, 138, 148]
TA-ICE	TAI	SLW + ICI	Potential Flow/Navier-Stokes/IBM	Lagrangian discrete phase.	Extended MM	[9, 105]
ICICLE	OXF/RR	Mixed phase SLW + ICI.	External Solver, Flowfield updating	Lagrangian discrete phase, rotation.	EMM – 3 layer warmed substrate modification	[22, 34, 156, 157]

Table 2.2: Existing Three-Dimensional Numerical Icing Software

Code	Group	Capability	Flowfield	Particle Transport	Accretion	References
LEWICE3D	NASA	SLW + ICI.	External Solver	Lagrangian discrete phase.	Extended MM	[15, 152]
IGLOO3D	ONERA	SLW + ICI	Airflow/Viscous solver, Flowfield updating	Lagrangian or Eulerian discrete phase.	Extended MM	[112, 147]
FENSAP-ICE	ANSYS [1]	SLW + ICI	Viscous Solver, Flowfield updating	Eulerian discrete phase.	Shallow Film Icing Model	[13, 144]

[1] Created by McGill University

2.8.1 Oxford Thermofluids Institute Code

Oxford University has developed a two-dimensional ICI modelling suite known as ICICLE shown in Figure 2.13. Partly developed from the existing particle tracking and accretion codes developed by ONERA, FENSAP-ICE and LEWICE [25, 34, 105, 137, 138, 148, 152]. The inputs comprise a steady state CFD flow solution, clean test geometry, surface discretisation and particle injection parameters (number, size, shape, position and diameter distribution) [22]. This code includes an implementation of the Extended Messinger Model for heat transfer and phase change ice accretion modelling. The EMM in ICICLE is an updated ice crystals form of the EMM for warmed surfaces (EMM-C) [25]. ICICLE combines:

1. A continuous phase viscous flow solution for a specified geometry.

2. Implicit Lagrangian frame particle tracking of non-spherical particles with rotation in 2D.

3. A 3 layer Extended Messinger Model (EMM-C) model for glaciated and mixed-phase conditions on warmed surfaces.

4. Semi-empirical models for sticking and erosion generated from wind tunnel experiments; item Steady state two-way flowfield (momentum) coupling.

The ICICLE suite based in MATLAB, comprises a particle tracking module, a two-way coupled mass and energy transfer calculation for particles and the continuous phase, a surface interaction module which models the behaviour of the particle post impact including dynamics and particle-wall heat transfer. The adapted EMM-C module models accretion and heat transfer in the ice and water layers and models a water film layer between the ice and substrate if the clean substrate is above freezing. Surface runback water flows axially downstream. Erosion of accreted ice is calculated according to the semi-empirical erosion model developed in [23] resulting in a final ice accretion surface profile. Lastly, updated volume parameters for the flowfield are output as a result of mass and energy coupling. Figure 2.14 shows the results for a MR sweep on the stator

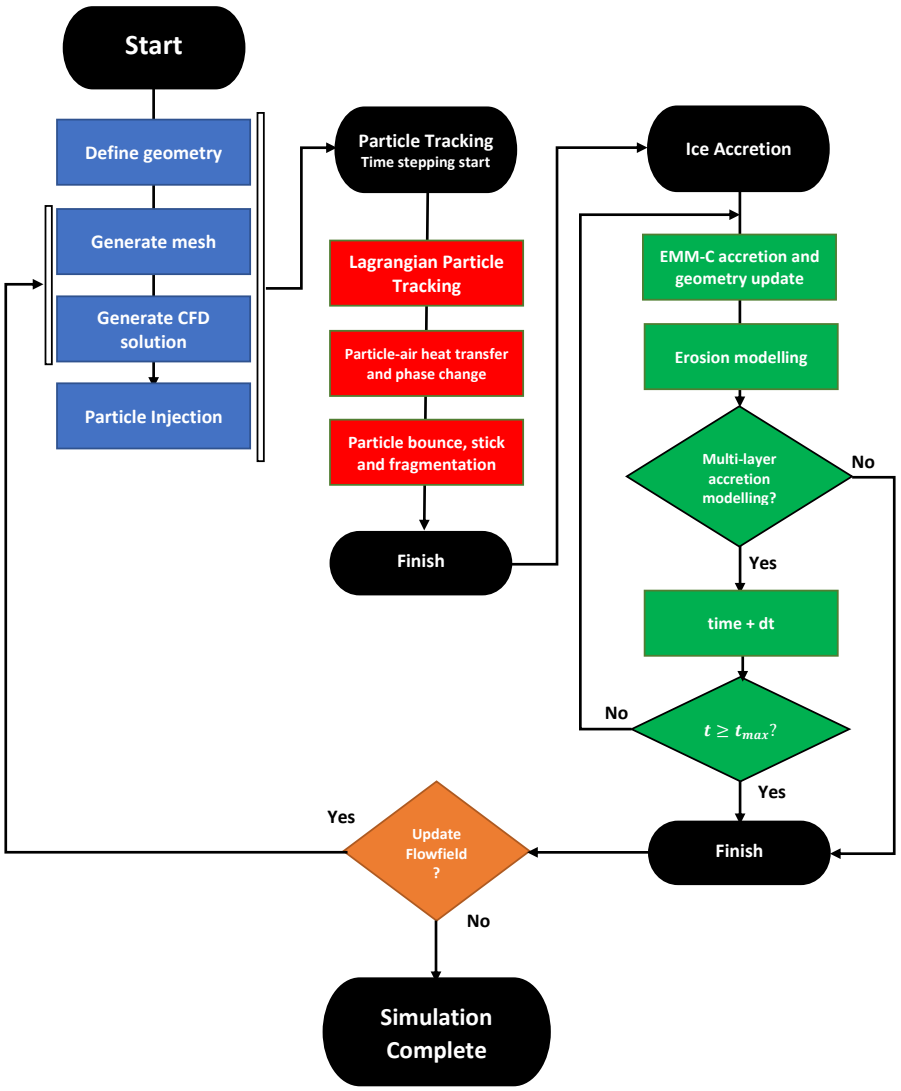

Figure 2.13: Ice Crystal Icing ComputationaL environment developed by Oxford Thermofluids Institute.

conducted at RATFac. ICICLE best predicts accretions outside the high accretion/stick band of MR (9%-13%). These results are performed without flowfield updating and indicate the sensitivity of the results on local flow properties [22].

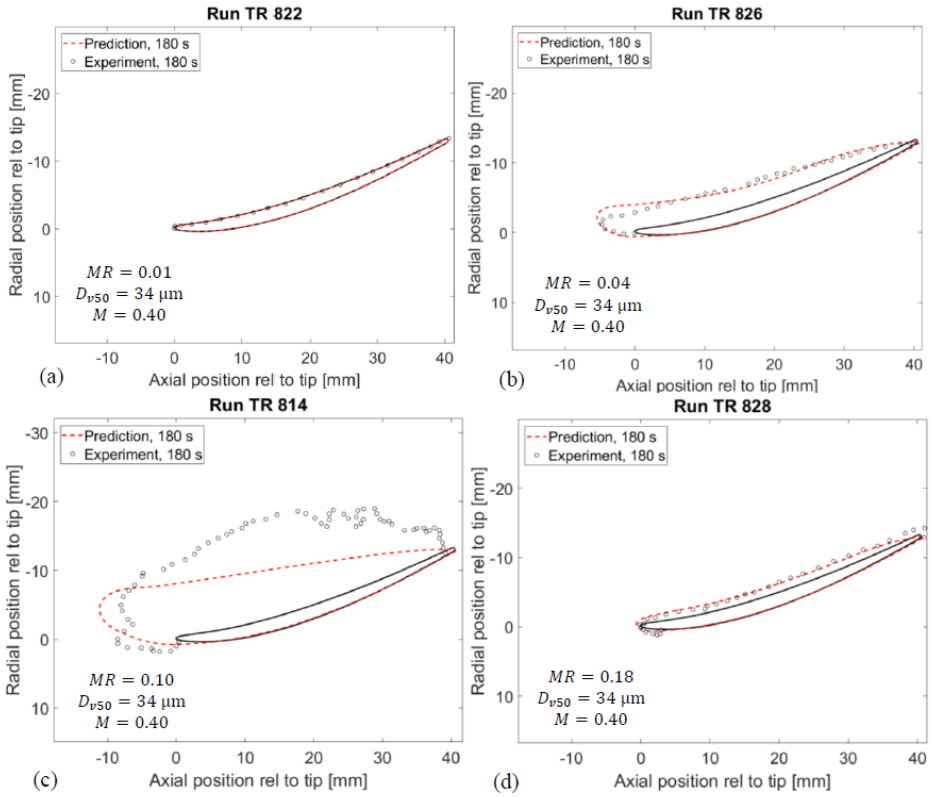

Figure 2.14: Stator RATFac test and simulation results from ICICLE at a range of MR values [22].

ICICLE 2 was further expanded to introduce two way coupling between the ice accretion profile and the flowfield. Connolly et al. [34] summarises how the geometry is updated and exported to a CFD solver to generate a new flowfield solution in an automated process. They note how the potential field and collection efficiency of the geometry are changed as ice grows on the surface [22]. Figure 2.15 shows the results for ICICLE with viscous flowfield coupling within the solution step. Here it shows the updated flowfield aids in the accuracy of the local ice accretion geometry as the pressure field and stagnation point are shifted throughout the solution step.

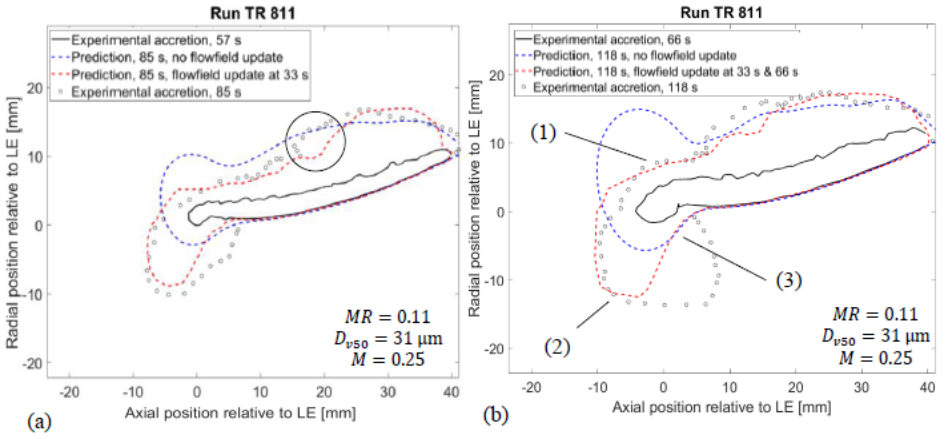

Figure 2.15: Stator experimental test data and simulations from ICICLE incl. flowfield updating.

2.9 Summary

This section details the present state of the art for ICI accretion modelling and simulation. The need for accurate 3D ICI accretion modelling is prescient given the complex ice geometries observed in experiments and the highly coupled flow field effects on ice accretion simulation. Existing ICI accretion software lack the implementation of the EMM necessary for mixed-phase warmed-wall ICI accretion in 3D. The vital parts necessary for accurate ICI modelling include ice volume conservation and accretion spatial discretisation to represent 3D streamwise heat transfer coefficients. Lastly water runback and ice initiation is not directly modelled within ICI accretion codes beyond simple bounded water film representation with uni-direction mass flux.

3
Model Development

This chapter describes the ICI modelling tool ICICLE and its updates within this body of work. The layout of its numerical model specification and components are summarised herein.

3.1 Overview 48
3.1.1 Knowledge Gap 49
3.1.2 ICICLE 3D Design 49
3.1.3 ICICLE Update Summary 51
3.2 Continuous Phase Modelling 53
3.2.1 Flow Solution 53
3.2.2 Data Structures 53
3.3 Discrete Phase Modelling 54
3.3.1 Particle Transport 54
3.3.2 Equations of Motion 54
3.3.3 Random Walk Model 57
3.3.4 Particle Cloud Scaling 58
3.3.5 Particle Size Distribution 59

3.3.6 Particle Phase Change 60
3.3.7 Particle Impact 62
3.3.8 Surface Roughness 66
3.4 Particle - Gas Coupling 69
3.5 Thermodynamic Accretion Models 71
3.5.1 Thermodynamic Ice Crystal Icing Accretion 71
3.5.2 Numerical Solution Steps 74
3.5.3 Water Runback 76
3.5.4 Substrate Heat Transfer 76
3.6 Topography Update 78
3.6.1 Surface Mesh Extrusion 78
3.6.2 Deposition Mass Smoothing 78
3.6.3 Volume Re-scaling 79
3.7 Summary 80

3.1 Overview

This chapter summarises the work undertaken in improving modelling capability to better reproduce the flow conditions and ice accretion phenomena resulting from ICI conditions within the LP and IP compressor.

ICI presents a risk to turbofan engine performance, maintenance scheduling and compressor stage longevity. Furthermore, certification and validation of performance of turbofan designs requires engine and stage testing to demonstrate compliance with safety regulations as discussed in Chapter 1. Modelling and simulation of ICI accretion provides a validation or design tool and complement to testing which remains an expensive and specialised process yielding little knowledge of physical phenomena.

3.1.1 Knowledge Gap

Existing ICI accretion tools have been summarised in Section 2.8, from each subsection, a gap in knowledge was identified specifically relating to turbomachinery and altitude ICI. The requirements for applying the existing physical models to turbomachinery cases are as follows:

- planar and axisymmetric 3D geometry/flowfields for turbomachinery;
- generalised 3D transport and melting;
- its effects on mass dispersion and phase exchang;
- two-way mass, energy and momentum coupling;
- heat and mass transfer modelling for turbomachinery;
- unsteady water runback and ice accretion.

In this work, the aim has been to develop a generalised 3D particle transport, two-way-coupled, warmed substrate mixed-phase accretion model. A 3D framework is a prerequisite necessary to fully validate particle tracking, melting, impact, accretion and erosion physics models. Tests conducted previously by the University of Oxford on an axisymmetric cone and prismatic compressor stator vane are the primary experimental data used to validate these models.

3.1.2 ICICLE 3D Design

Developing ICICLE from a 2D into a 3D modelling suite required modification to the existing physical models, mesh discretisation and morphing methods used within the code. A summary of its current capability is displayed in Figure 3.1.

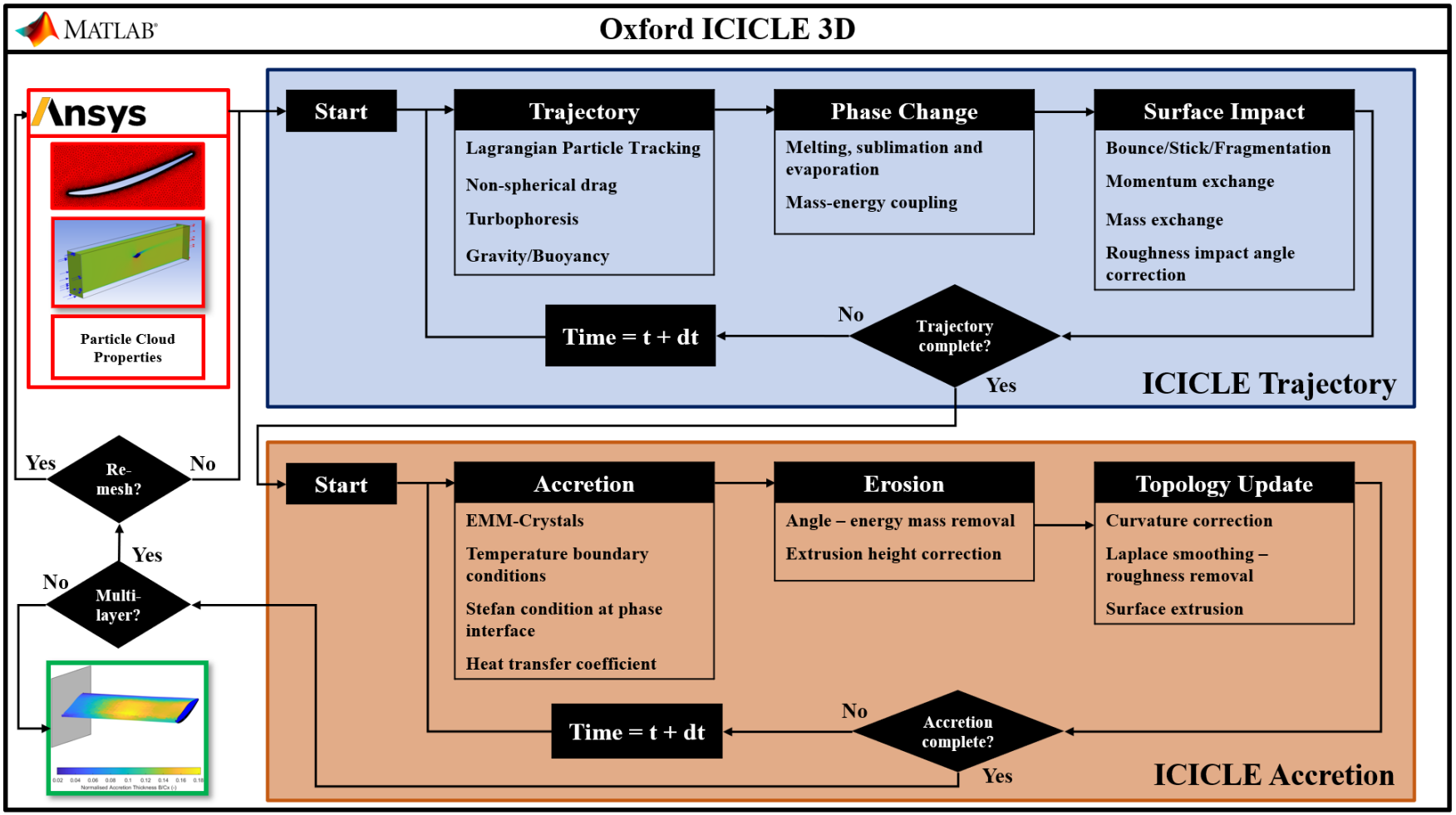

Figure 3.1: ICICLE 3D Software Environment Flow Diagram showing key physics modules

In the existing design, a flow solution produced within the commercial software ANSYS FLUENT is exported to MATLAB and overlayed onto an isotropic grid representing the flow domain. This provides a basis for probing flow properties for relevant particle tracking and melting models. To achieve this functionality the following physics models were implemented:

1. 3D Lagrangian particle tracking.
2. 3D Surface impact and interaction.
3. 3D non-spherical particle and roughness distribution wall impact treatment.
4. Modification to time-stepping scheme and discretisation method.
5. 3D formulation of accretion and surface water transport model.
6. 3D topography update using extrusion applying mass conservation.

3.1.3 ICICLE Update Summary

Capabilities within ICICLE were updated by multiple colleagues within the University of Oxford's Particle Deposition Group. Table 3.1 is a summary detailing the adjustments performed within this thesis and concurrent work by colleagues on the 2D version of ICICLE.

Table 3.1: Ice Crystal Icing ComputationaL Environment Model Updates

Model Aspect	Original ICICLE 2D	Updated in thesis (3D)	Updated by colleagues[1] (2D)
Gas Property Search	Scattered Interpolation	kd-tree algorithm, IDW	kd-tree algorithm, IDW
Surface Proximity Search	$\vec{\mathbf{n}} < D_p$	kd-tree, vector - cell intersection, realisability condition $V_n < 0$	kd-tree, point-in-polygon, realisability condition $V_n < 0$
Particle motion	Drag, Gravity	Lift, Turbophoresis	Lift, Magnus Lift, Rotation [158], Turbophoresis
Particle melting	Villedieu et al. [148] and Wright et al. [154] melting model	n/a	Rotation and porosity dependent melting, Yang et al. [156, 158]
Particle-gas coupling	Steady enthalpy-mass balance	Unsteady enthalpy-mass transport model	n/a
Surface impact	Semi-empirical bounce-stick-shatter-erosion model	Stochastic rough wall 'Sommerfeld-shadow-model' [127]	Updated sticking-erosion particle size model, Yang et al. [157]
Wall heat transfer	Adiabatic-wall	Quasi-steady conduction	Semi-infinite 1D conduction
Accretion	EMM-C, Bucknell et al. [25]	Generalised to 3D, quasi-steady water film transport	Steady water film, Connolly [31]
Topographical Update	Surface normal projected extrusion	Volume extrusion predictor-corrector method	Curvature correction Connolly [31]

[1]Many updates by this thesis and other colleagues were shared between 2D and 3D ICICLE versions. Specific descriptions of this thesis contribution are detailed in the column 'Updated within thesis'. Duplications suggest the update to ICICLE 2D was implemented by another person.

3.2 Continuous Phase Modelling

3.2.1 Flow Solution

ICICLE 3D employs an external solver from which a flow solution is imported. The commercial CFD software ANSYS Fluent was used to model the continuous phase. A steady state RANS solution was generated in each case using the coupled pressure based solver. The Realisable $k-\epsilon$, $k-\omega$ (SST) and Reynolds Stress Model (RSM) are employed. Further details regarding continuous phase modelling are summarised in Chapter 4.

To reduce the computational expense and overall solution time, the continuous phase solution was imported directly into MATLAB for ICICLE, specifying the flow variables at nodal and cell centre positions and providing a fast and simple method to probe the flow solution and to employ a simpler basis for two-way heat and energy coupling for the discrete and continuous phases.

3.2.2 Data Structures

The continuous phase solution variables are formed into a k-dimensional tree. This was employed to partition flow variables at each node and cell centre for fast multi-dimensional searches [133]. Within MATLAB, the kD neighbourhood tree can generate a binary substructure to recursively partition data within each dimension. The implementation within MATLAB can be used in a vectorised form and provided a complexity order of O(k-log(n)), improving on the existing interpolation method with a complexity of $O(k^n)$ where for each particle, the location within the volume required a search and interpolation function using the existing flowfield data. This enables a fast and vectorised form look-up method for particle transport equations and particle surface collisions. The kD-tree then enables a nearest-neighbour look up method which was applied in 3 different modes. Table 3.2 details the node numbering basis for the algorithm. This is required to generate a cell based interpolation depending on the bounding cell type.

These depend on the local cell type, which selects the nodal interpolation method as described above. The kNN Fluid Variable Look-up Algorithm uses the MATLAB *knnsearch* function, which outputs the node index N_K for nearest neighbour $K = 1$,

Table 3.2: K-D Tree Fluid Cell Search Algorithm

Type	k
Nearest Neighbour	1
Tetradehral Cell	6
Hexahedral Cell	8

or up to K nodes. It also outputs the Euclidean distance D_k to the look up location D. An inverse distance weighted (IDW) sum was then calculated. The weighted sum was calculated from the node positions and then the variable f, which represented the flowfield property at the node location. This is an efficient flowfield look-up approach commonly used in CFD codes. Calculation of property $\bar{f}$ at a particle location was performed as follows,

$$\bar{f} = \frac{\sum_1^k f(N_k)(D_k - D)^2}{\sum_1^k f(N_k)} \tag{3.1}$$

3.3 Discrete Phase Modelling

3.3.1 Particle Transport

Particle transport may be modelled as a continuous Eulerian phase or discrete Lagrangian phase. Lagrangian particle tracking involves the numerical integration of particle body forces for an individual particle or grouped mass of particles represented by one constituent rigid body with mass flux scaling term. This approach is more computationally demanding than an Eulerian approach but enables specific input of melt, orientation, aspect ratio, mass distribution which can be derived from experimental data [20, 58, 158].

3.3.2 Equations of Motion

Particle body forces that dominate are drag, lift, gravitational and turbulent dispersion forces respectively, along with heat transfer and phase change between the dispersed and gas phases respectively,

$$\frac{d}{dt}(\mathbf{x_p}) = \mathbf{u_p} \tag{3.2}$$

$$m_p \frac{d}{dt}(\mathbf{u_p}) = \vec{F} \tag{3.3}$$

where m_p, u_p and x_p are the particle mass, velocity and position respectively. The resulting forces are

$$\sum \vec{F} = \vec{F}_D + \vec{F}_G + \vec{F}_L + \vec{F}_{Tb} \tag{3.4}$$

where, $\vec{F}_D$ $\vec{F}_G$, $\vec{F}_L$, $\vec{F}_{Tb}$ are the drag, gravitational, lift and turbophoretic forces respectively. Given the generally high Stokes number of particles in ICI ($1.05 - 100$), where the particle relaxation time is far greater than fluid relaxation time, particles primarily behave ballistically [80, 138, 148]. However, turbulent dispersion has been noted to have a significant effect on the melting behaviour and mass concentration of particles in previous experiments [129]. Currie et al. [38] implemented a DRW turbophoresis model for particle transport in the RATFac icing wind tunnel. These results were compared to experimental measurements for turbulence intensity and mass flux of ice and water through the tunnel test section. This model was found to overpredict particle mass close to the tunnel walls due to a bounce angle limitation of 2° for impacts. Particles are represented as oblate or prolate spheroids, which allow the frontal area, orientation and volume of particles to be set for discrete phase modelling. Particle drag can be approximated for non-spherical particles by accounting for shape, orientation and particle-fluid density ratio. These are concisely described by lengthwise and crosswise sphericity ($\phi_\perp$, $\phi_{||}$) and Reynolds number [10, 60].

$$V_{eq} = \frac{\pi D_{eq}^3}{6} \tag{3.5}$$

$$\phi = \frac{\pi^{1/3}(6V_{eq})^{2/3}}{A_{surf}} \tag{3.6}$$

$$\phi_\perp = \frac{\pi}{4}\frac{D_{eq}^2}{A_{n,proj}} \tag{3.7}$$

$$\phi_{||} = \frac{\pi}{4} \frac{D_{eq}^2}{0.5A_{surf} - A_{len,proj}} \tag{3.8}$$

Particle drag coefficients were generated according to orientation to the global axes, lengthwise and crosswise sphericity was determined as detailed in Figure 3.2.

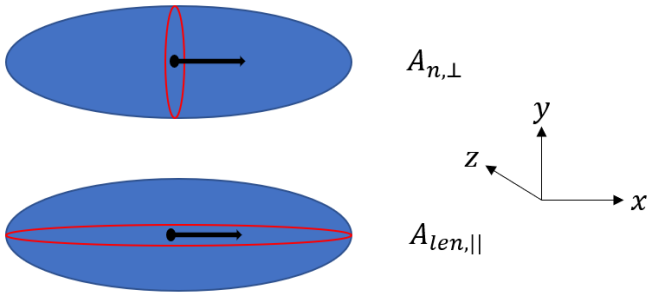

Figure 3.2: Particle sphericity and orientation, specified relative to axial flow direction.

3.3.2.1 Drag

Particle drag force was calculated for the volume equivalent spheroid shape $V_{p,eq}$. Particle drag F_D was defined by its frontal area A_p, for each particle subject to a slip velocity U_{slip} with the carrier gas,

$$F_D = \frac{1}{2}\rho_g C_d A_{p,eq} U_{slip}^2 \tag{3.9}$$

$$F_D = \frac{1}{2}\rho_g C_d A_{p,eq} \left\|U_p - U_g\right\| \left(U_p - U_g\right) \tag{3.10}$$

Stokes' drag law defines particle Reynolds number Re_p as,

$$Re_p = \frac{\rho_p \left\|U_g - U_p\right\| D_p}{\mu} \tag{3.11}$$

where, U_g and U_p are the gas and particle fluid velocities respectively.

Drag coefficients for spheroids, and high aspect ratio non-spherical solid particles were generated from from existing numerical studies by Haider and Levenspiel, along with Holzer and Sommerfelds update to account for orientation addressing lengthwise and crosswise drag corrections [60, 71]. The drag correlation for columns and plate

shapes considering sphericity, along with orientation-specific lengthwise and crosswise sphericity was as follows,

$$C_d = \frac{8}{Re_p}\frac{1}{\sqrt{\phi_{||}}} + \frac{16}{Re_p}\frac{1}{\sqrt{\phi}} + \frac{3}{\sqrt{Re_p}}\frac{1}{\sqrt{\phi^{0.75}}} + 0.421^{0.4(-\log\phi)^{0.2}}\frac{1}{\phi_{\perp}} \tag{3.12}$$

3.3.3 Random Walk Model

Turbomachinery flows have narrow compressor gas paths where the boundary layer and pressure driven secondary flows dominate, turbophoresis is known to redistribute concentrated dispersed phase flows. This flow information is absent from a RANS CFD solution and a model of the turbulent flow fluctuations is required to assess the effects on particle mass and melt distributions. The well known Discrete Random Walk model (DRW) was implemented to model these predominantly wall normal velocity fluctuations.

The instantaneous flow velocity u may be described by bulk mean flow velocity $\bar{u}$ and velocity fluctuation u' respectively,

$$u = \bar{u} + u' \tag{3.13}$$

Using a $k-\epsilon$ model the RMS unsteady velocity vector

$$\mathbf{U} = \sqrt{\overline{u'^2}} = \sqrt{2k/3} \tag{3.14}$$

To obtain a stochastic instantaneous unsteady velocity term a random number, γ, was sampled from a Gaussian distribution with zero mean and unit variance. This was applied to the components of the RMS velocity. Isotropic turbulence stipulates these are all equivalent.

$$u' = \gamma\mathbf{U} \tag{3.15}$$

Therefore the DRW model applies a fluctuation in x,y and z components at the given k value for the a duration specified by the minimum of the eddy transit time $t_{transit}$, specified by an eddy length scale L_e, or an integral timescale, τ_{int}.

$$t_{interaction} = min(\tau_{int}, t_{transit}) \tag{3.16}$$

where

$$t_{transit} = \tau_p \ln\left(1 - \frac{L_e}{\tau_p |u_{slip}|}\right) \tag{3.17}$$

and the integral timescale $\tau_{int} = 2T_L$ is determined from the Lagrangian integral time scale T_L, specified by the turbulence model. For the k_ϵ model:

$$T_L \approx 0.15\frac{k}{\epsilon} \tag{3.18}$$

and for the Reynolds Stress Model:

$$T_L \approx 0.3\frac{k}{\epsilon} \tag{3.19}$$

Considering the gas path dimensions and Mach numbers for the flows relating to compressor ICI, it is necessary to resolve the turbulence within the flow due to secondary flows and any separations across compressor stages. Instantaneous field velocity within the gas path affects the drag forces of suspended particles. This will affect the melting response times of particles. It is therefore important to accurately represent the velocity field and select a turbulence model approach which is sufficiently representative of these fluctuations affecting mass diffusion and melting.

Lagrangian modelling involves a point mass approach with each particle experiencing a mean fluid velocity and turbulent fluctuations. This requires a large number of particles to be seeded to accurately model the interaction between the disperse and carrier gas phases.

3.3.4 Particle Cloud Scaling

Within Lagrangian frame trajectory integration, each particle represents a particle size, orientation, melt and shape. In order to reduce computational complexity, particle injections were represented by distributions in each parameter and scaled by a mass flux scalar to represent the freestream ice and water mass flux. These ‘super particles’ represented a particle cloud stream-tube of mass flux. This reduced the computational demand for the simulation and was used to further match experimentally measured TWC and MR values from icing wind tunnel experiments. It should be noted that each ‘super particle’ was divided by N_{DRW} streams to allow turbophoretic force effects to be

calculated. Each particle sampled a scaling parameter from a unit Gaussian probability distribution. This represented a distribution in velocity fluctuations experienced by each mass/shape setting. This approach was implemented as increasing the number of injected streams by a factor of N_{DRW} would not be possible given computational resource limitations. Ice cloud mass flux $\dot{m}_{i,w}$ was defined in terms of concentration or TWC_{in} and flow velocity U_{in},

$$\dot{m}_{i,w} = TWC_{in}U_{in} \tag{3.20}$$

the local mass scaling term applied to each particle is defined by the total injection mass flux and area A_{in}, this is divided by the number of particles N_{inj} at each particle mass m_p,

$$\lambda_{mass} = \frac{\dot{m}_{i,w}A_{in}}{m_p N_{inj}} \tag{3.21}$$

this results in a scaling term based on particle size, enabling each injected 'super particle' to adopt a mass fraction of both the size distribution and the freestream mass flux.

$$\lambda_{mass} = \frac{6}{\pi}\frac{\dot{m}_{i,w}A_{in}}{\rho_p D_{eq}^3 N_{inj}} \tag{3.22}$$

Non-uniform and anisotropic distributions of particle mass, size and shape require a scaling parameter in a vector quantity.

$$\vec{\lambda}_{mass} = \lambda_{mass,x}\mathrm{i} + \lambda_{mass,y}\mathrm{j} \tag{3.23}$$

This functionality is needed, for example, to generate radial distributed ice particle mass and melt over compressor annular stages.

3.3.5 Particle Size Distribution

Within ICICLE 3D, particle size distributions were represented by Rosin-Rammler functions. The particle scaling parameter was adjusted for each particle size bin within the distribution, such that N_{bins} were injected at each injection position and scaled according to the mass fraction Y_d within the distribution,

$$Y_d = 1 - e^{-(x/\bar{x})^n} \tag{3.24}$$

the mass fraction of each bin size was represented by the number of bins, within this work this was usually set by the limitations of the experimental measurement system,

$$M_{bin} = \frac{Y_d^i - Y_d^{i-1}}{\sum_{n=1}^{n_{bins}}(Y_d)} \tag{3.25}$$

therefore, a 'super particle' holds a size distribution mass fraction M_{bin} and a freestream mass flux fraction λ_{mass},

$$\lambda_{mass} = \frac{6}{\pi}\frac{\dot{m}_{i,w}A_{in}M_{bin}}{\rho_p D_{eq}^3 N_{inj}} \tag{3.26}$$

This is important to correctly describe the local particle size to accurately model phase change behaviour, while preserving the system mass flux to accurately conserve mass when modelling impingement or deposit mass transfer.

3.3.6 Particle Phase Change

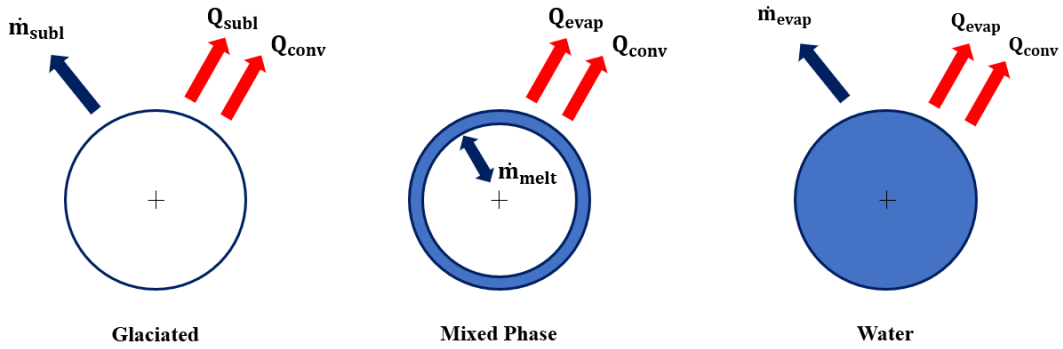

Figure 3.3: Lumped System Analysis for Melting Ice Crystals

The particle temperature can be assumed spatially constant for particles with Biot numbers, $Bi = h_p L_p/k_p << 1$. This means employing a lumped-system analysis. Particle-air heat transfer is described as follows:

$$m_p c_p \frac{dT_{p,m}}{dt} = \sum \frac{dQ_p}{dt} \tag{3.27}$$

$$m_p c_p \frac{dT_{p,m}}{dt} = q_{conv} + q_{melt} + q_{subl} + q_{evap} \tag{3.28}$$

Modelling ice crystal three phase particle melting is separated into three distinct regimes.

1. The below freezing, sensible heating phase ($T_p < T_f$):

$$\sum q = q_{conv} - \cancelto{0}{q_{melt}} q_{subl} - \cancelto{0}{q_{evap}} \tag{3.29}$$

$$m_p c_{p,i} \frac{dT_{p,m}}{dt} = \pi d_p k_a \frac{Nu_p}{\phi}(T_a - T_{p,s}) - \dot{m}_{sub}\Big[L_f(T_p) + L_v(T_p)\Big] \tag{3.30}$$

Where, L_f and L_v are the latent heat of fusion and vaporisation respectively.

$$\dot{m}_{sub} = \frac{\pi d_p}{\phi} \rho_a D_{v,a} \text{Sh}(\gamma_{v,p} - \gamma_{v,a}) \tag{3.31}$$

2. At freezing, melting phase ($T_p = T_f$):

$$\sum q = q_{conv} - q_{melt} - \cancelto{0}{q_{subl}} q_{evap} \tag{3.32}$$

$$q_{conv} = \dot{m}_{melt} L_f + \dot{m}_{evap} L_v \tag{3.33}$$

$$\frac{dm_{p,i}}{dt} = -\dot{m}_{melt} L_f \tag{3.34}$$

$$\dot{m}_{melt} L_f = \frac{\pi d_p}{\phi} k_a Nu_p (T_a - T_{p,s}) - \frac{\pi d_p}{\phi} \rho_a D_{v,a} \text{Sh}(\gamma_{v,p} - \gamma_{v,a}) L_v \tag{3.35}$$

$$m_{p,w} = m_p - m_{p,i} \tag{3.36}$$

$$\frac{dm_p}{dt} = -\dot{m}_{evap} \tag{3.37}$$

3. Above freezing, water only, evaporation phase ($T_p > T_f$):

$$\sum q = q_{conv} - \cancelto{0}{q_{melt}} \cancelto{0}{q_{subl}} q_{evap} \tag{3.38}$$

$$m_p c_{p,w} \frac{dT_p}{dt} = \frac{dQ_p}{dt} \tag{3.39}$$

$$= q_{conv} - \dot{m}_{evap} L_v \tag{3.40}$$

$$= \pi d_p k_a \frac{Nu_p}{\phi}(T_a - T_{p,s}) - \frac{\pi d_p}{\phi} \rho_a D_{v,a} \mathrm{Sh} (\gamma_{v,p} - \gamma_{v,a}) L_v \tag{3.41}$$

$$m_{p,w} = m_p - m_{p,i} \tag{3.42}$$

$$\frac{dm_p}{dt} = -\dot{m}_{p,evap} \tag{3.43}$$

Villedieu et al. [148] generated a sphericity - Melt Ratio linear distribution such that a pure water droplet can be assumed to be spherical from an initial sphericity ϕ_{in}. This is necessary to account for the approach to a spherical water droplet $\phi_p = 1$ at fully liquid conditions $MR = 1$.

$$\phi = \mathrm{MR}(1 - \phi_{in}) + \phi_{in} \tag{3.44}$$

3.3.7 Particle Impact

In the original ICICLE code, the particle impact was calculated based on the local x and y velocity components and the surface angle. This was changed to a spherical co-ordinate method with generalised vector component projection along the line between the point of impact and the particle centroid. Particle wall impact is described in Figure 3.4. Particle initial velocity v_p was distributed along the normal and tangential directions by experimentally defined restitution coefficients ϵ_t and ϵ_n,

$$v_{p,2} = \epsilon_t [v_p - (v_p \cdot n)n] - \epsilon_n (v_p \cdot n)(\epsilon_{nt} t + \epsilon_{nn} n) \tag{3.45}$$

Impact was modified by assuming a particle impinges upon the surface when it is 1 radius away from the wall (projected along the local unit normal). This avoids particles of the smallest diameter potentially passing through the mesh spacing and provides a more accurate slip velocity at impact. Projecting the impact position at the wall at 1

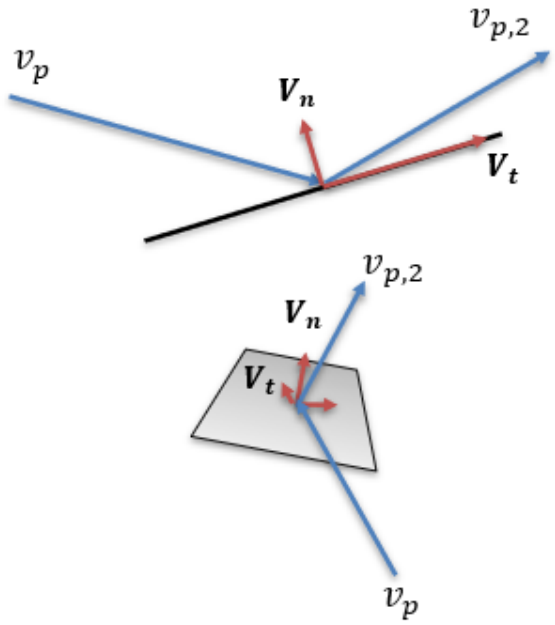

Figure 3.4: Particle Bounce Stick Momentum Exchange Model in Generalised 3D.

radius also ensures that, when probing the flow solution, the local gas velocity is non-zero during impact at the particle centroid. Figure 3.5 illustrates this modification. Adaptive time-stepping was introduced to account for the lower particle velocities and improve the accuracy of particle dynamics close to the wall and in the boundary layer.

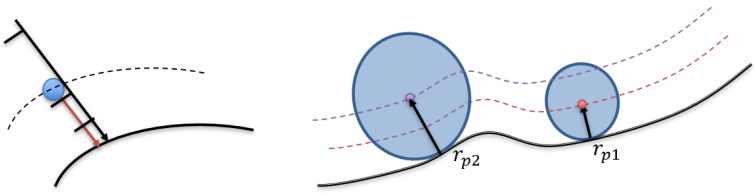

Figure 3.5: Particle impact visualised: (1) adaptive near-wall timestepping to improve slip velocity gradient at wall. (2) Projected particle offset along normal vector for accurate gas property calculation.

3.3.7.1 Droplet Break-up

Particle transport relating to turbomachinery involves rigid body impact physics and inertia moderated water droplet breakup. Below is the summary of 'modes' of water and ice disintegration phenomena due to impact, shearing and drag and slip dominated breakup.

Droplet primary / secondary break-up was not considered in the model. The Weber number relates droplet inertia to surface energy. This can identify whether a droplet is

surface energy dominant or inertia dominant and whether inertia will overcome surface tension leading to break-up. Critical Weber number We_{cr} dictates the threshold for break-up [44]. For ICI compressor conditions in this study, $We_{cr} \sim 12.57$.

$$We_{cr} = 4\pi\Big(1 + \frac{\rho_g}{\rho_p}\Big) \tag{3.46}$$

King et al. [78] found that Weber number must be held between 12 and 15 for the NASA Icing Wind Tunnel (SLW facility) to avoid excess droplet deformation during the contraction/acceleration of flow. Droplets equivalent in size in typical ice crystal ice clouds entering engines have Weber numbers in a range from 0.1 and 1. This was sufficient to assume through transport break-up can be neglected.

3.3.7.2 Particle Sticking

Currie et al. [39] conducted experiments identifying mass deposition and accretion growth rates coupled to particle Melt Ratio (MR). Particle sticking is moderated by the adhesion, water surface tension and inertia properties of the impinging droplets. Trontin et al. [138] examined particle sticking with regards to the SLW regime. An empirical scaling parameter, K_c, and an overall sticking efficiency P_{stick}, generated from experiments is presented as follows,

$$K_c = 2.5 \tag{3.47}$$

$$P_{stick} = (K_c - 2)\mathrm{MR}_p^3 - \frac{1}{2}\mathrm{MR}_p^2 + K_c\mathrm{MR} \tag{3.48}$$

Bucknell et al. [23] examined the distribution of deposition / accretion growth from further experiments to produce a polynomial relating stick probability to *Melt Ratio* $P_{stick}(MR)$.

$$P_{stick} = x_1\mathrm{MR}^5 + x_2\mathrm{MR}^4 + x_3\mathrm{MR}^3 + x_4\mathrm{MR}^2 + x_5\mathrm{MR} + x_6 \tag{3.49}$$

Where x_1 to x_6 are [182.9, -494.0, 477.7, -196.1, 30.19, -0.526] respectively.

Yang et al. [157] expanded on the ONERA model implementation above by generating a linear combination of surface and constituent particle sticking probability.

$$P_{stick,total} = P_{stick,p} + (1 - P_{stick,p})P_{stick,surf} \tag{3.50}$$

Figure 3.6 illustrates the ONERA, Bucknell and Yang sticking efficiency models. The main thing to note is Currie et al.'s sticking model which informed Bucknell et al.'s sticking model is distinctly controlled by the ICI threat band of *Melt Ratio*, as investigated in Section 2. This opposes ONERA's and Yang et al.'s methodology which normalised sticking efficiency, with purely liquid water set to $P_{stick} = 1$.

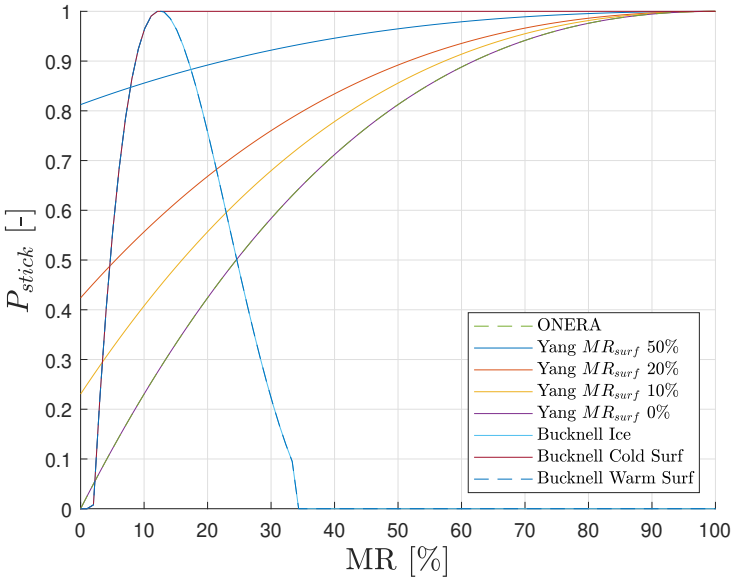

Figure 3.6: Examination of Stick Probability Models from literature.

This assumption may be overly simplistic in capturing the physical interactions during a 'stick' event. An ice crystal of mixed-phase constitution, may move in the presence of a running water film. This is not addressed in any sticking studies to date. Sticking efficiency is a phenomena associated with SLW icing which is moderated by Weber number. ICI involves water film transport and impinging mixed-phase particulates. It was instructive to adopt the Yang et al. [157] model as the particle and surface melt ratio is accounted for when calculating the overall sticking efficiency.

3.3.8 Surface Roughness

Iced surfaces have roughness and heat transfer properties specific to flow conditions and geometry. Previous workers have attempted to classify experimentally measured roughness and its impact on heat transfer augmentation. Shin [125] performed studies on a NACA 0012 airfoil investigating the roughness distribution during SLW icing events. This highlights the development of an initial transient roughness which grows but becomes a stable distribution later in the accretion / erosion process. A series of follow-up validation studies by Anderson et al. [2, 3] identified the accumulation and freezing fraction parameters relating roughness distribution and height over the airfoil. While these studies were for SLW icing however, the deposition and freezing fraction may be used analogously for ICI impingement. This produces a roughness height R between 0.371 mm and 1.373 mm. Han and Palacios [62, 63] used LEWICE 3D to simulate heat transfer experiments on an iced NACA 0012 airfoil of chord length 0.35 m [61]. The peak experimental roughness height was found to be 0.7 mm. This was used to inform an initial specification for roughness height in CFD and heat transfer modelling in this body of work. Additionally, the mean roughness height normalised by the leading edge diameter (R/D_{LE}) was found to be between 0.06 and 0.07 [2].

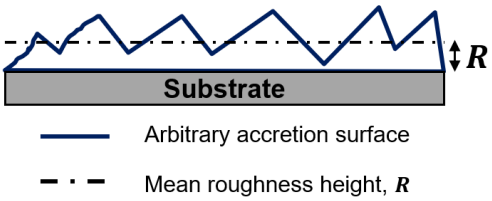

Figure 3.7: Iced Roughness Height Schematic with Mean Roughness R illustrated

3.3.8.1 Rough Wall Impact

Roughness further impacts the trajectory and impingement conditions of ice and water. Rough surfaces increase the surface area and modify impact momentum exchange and coefficients of restitution (CoR). Well established models generated by extensive work in solid particulate multi-phase flow by Tsuiji et al. [143] established a ‘virtual wall’

angle correction. Sommerfeld further expanded to deal with random bounce models for two-phase flows [127], this was to examine probabilistic 'virtual wall' inclination angles and impinging particle sizes. These are generated by a Gaussian distribution for 'virtual wall' angles. Sommerfeld and Huber [128] compared these findings to experiments stochastic wall normal correction to particle impact. Sommerfeld identified a 'shadow effect' where particle impingement vectors are coincident with the leeward wall, and must return to the flow after bouncing. Here, they introduce a truncated normal distribution to remove angle inclination corrections which will produce no impact. Konan et al. [82] expanded this algorithm to deal with realisability accounting for 'shadow effect' impingement and multiple impacts.

Radenkovic & Simonin [114, 115] introduced this correction model to a 3D isotropic and further anisotropic virtual wall surface. This is distinctly applicable to turbomachinery due to anistropy in pressure and shear stresses over a compressor stage. This will generate a variation in roughness height over an impact surface. Due to the lack of post bounce concentration data in ICI experiments, it is not possible to assess this model beyond a simple evaluation. The model was implemented and tested against a RATFac cone case.

The virtual wall perturbation angle γ is illustrated in Figure 3.8(i). The wall impact angle β is defined below in Figure 3.8(ii).

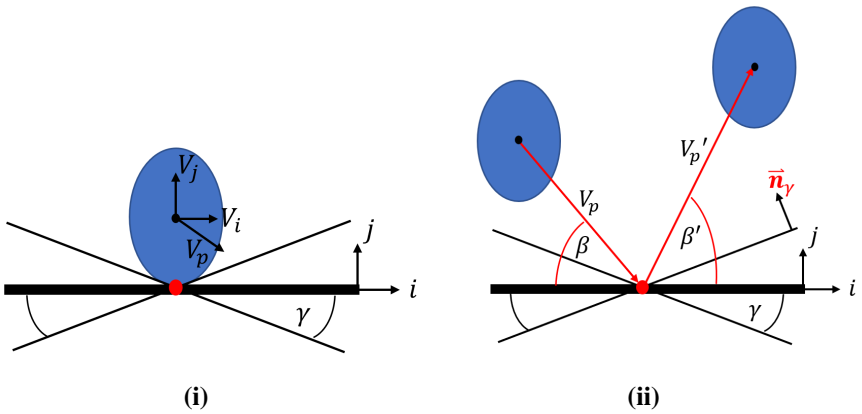

Figure 3.8: (i)Virtual Wall Projection with Angle Correction Representing Isotropic Rough Wall in 2D (ii) Rough Wall Impact Considering Sommerfeld Distribution defined by β, γ

The virtual wall inclination angle, γ, was sampled from the Sommerfeld Distribution

[113, 128]. This accounts for a shadow effect which imposes a zero probability for inclination angles which are co-incident with incoming particle vectors.

$$P(\gamma|\beta) = \frac{1}{\sqrt{2\pi{\sigma_\gamma}^2}} \frac{\sin(\beta-\gamma)}{\sin\beta} \exp\Big(-\frac{\gamma^2}{2{\sigma_\gamma}^2}\Big) f(\beta,\gamma) \tag{3.51}$$

where the function $f(\beta,\gamma)$ is a normalisation factor for the probability distribution, generated by integrating the PDF with respect to γ.

$$f(\beta,\gamma) = 1/\int_{\beta}^{\pi/2} \frac{1}{\sqrt{2\pi{\sigma_\gamma}^2}} \frac{\sin(\beta-\gamma)}{\sin\beta} \exp\Big(-\frac{\gamma^2}{2{\sigma_\gamma}^2}\Big) d\gamma \tag{3.52}$$

With a smooth wall, the exit angle β' was generated on the basis of the CoR described in the one dimensional momentum balance and surface bounce-stick-fragmentation energy model (see Section 3.3.7). With a rough-wall, a value for γ generated by the Sommerfeld distribution on the interval $[-\frac{\pi}{2}, \frac{\pi}{2}]$ was added to β'. Additionally, β' must be > 0 such that the particle will re-enter the flow. If not, the sampling procedure was simply repeated. It is necessary to note that unlike the Sommerfeld and Radenkovic & Simonin studies, the RMS roughness height and CoR values are not investigated. This is simply a robust and effective model for dealing with stochastic collisions validated against experiments for solid particulates.

3.3.8.2 Surface Angle Impact Distribution

Using the Sommerfeld distribution to generate a stochastic impact angle modification, it was necessary to discretise the distribution and sample a value for γ at each impact. From this, the incoming angle β and corrected outgoing angle β' (Note in 3D this would be specified by 2 incoming angles about the impact plane (α, β).

The standard deviation in perturbation angle σ_γ was specified by the roughness distribution. The mean roughness height to correlation length scale $(\frac{d}{c_L})$ for iced roughness was calculated to be on this interval [0.06,0.07]. From Radenkovic & Simonin's [113] statistical evaluations of rough wall impact, they evaluated the standard deviation for local surface incoming angle distribution. Their study focused on smaller roughness heights and so the maximum ratio they evaluate is 0.063. This equates to the following standard

deviation for γ by assuming the rough wall is isotropic. This is important as different particle sizes will therefore have a range of impact angles and velocities.

$$\frac{d}{c_L} = 0.063 \qquad \sigma_\gamma = 5.10^\circ \tag{3.53}$$

Figure 3.9 shows the Sommerfeld distribution for different impact angles β. From this the corrected probability density function was sampled for virtual wall angle γ. Bin size was not preserved as the truncated distribution was normalised by integrating the inverse continuous distribution function (CDF), this produced bins of 0 height which affect the bin width when summing the probability for angle samples.

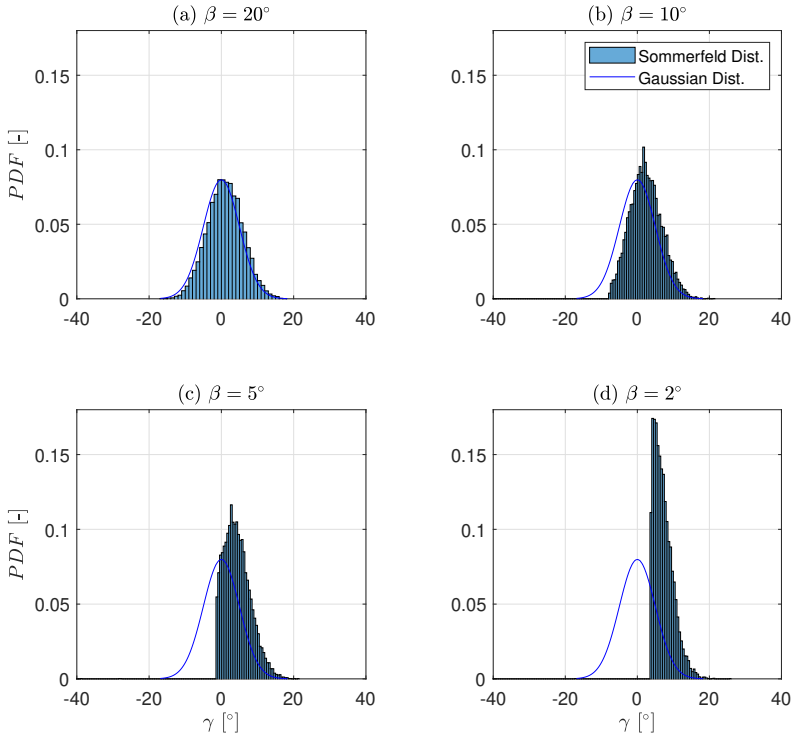

Figure 3.9: Sommerfeld and Normal Gaussian PDF of γ for $\sigma_\gamma = 5^\circ$. Using $\frac{d}{c_L} = 0.063$

3.4 Particle - Gas Coupling

Interaction between the particle and continuous phases is important given the relative volume fractions of ice to humid air. Modelling mass, momentum and energy exchange is generated by a source term approach modifying the local gas properties due to particle

phase change and sensible heating. Within this body of work, momentum exchange was neglected due to the density of air relative to ice. Mass and energy source terms were summed over each particle time-step. Each source term was summed spatially over a 100×100 element coarse grid at 10% axial increments over the domain, this generated a two-way coupling source mesh of 100,000 elements. This was to improve stability and reduce computational overhead as opposed to a direct source in cell approach. The heat transfer between the fluid and the discrete phase is described as follows,

$$q_g = \dot{m}_g C_{p,g} dT_g = -q_p \tag{3.54}$$

with the heat transfer to particles segregated into:

$$q_p = q_{sens} + q_{melt} + q_{latent}. \tag{3.55}$$

Fully glaciated particles may only exchange energy through sublimation or sensible heating.

$$q_{p,i} = \dot{m}_{p,i} C_{p,i} dT + \dot{m}_{evap}(L_v + L_f) \tag{3.56}$$

Mixed phase particles may only exchange energy through evaporation or melting.

$$q_{p,mp} = \dot{m}_{freeze} L_f + \dot{m}_{evap} L_v \tag{3.57}$$

Fully molten particles may only exchange energy through evaporation or sensible heating.

$$q_{p,w} = \dot{m}_{p,w} C_{p,w} dT + \dot{m}_{evap} L_v \tag{3.58}$$

Enthalpy exchanged with the gas phase over one timestep is therefore

$$\dot{m}_g \Delta h_g = \sum_{1}^{N_p} (q_{p,i} + q_{p,w} + q_{p,mp}) \Delta t \tag{3.59}$$

The only mechanism of mass exchange between particle and carrier gas is evaporation/sublimation. This in turn modifies the vapour mass fraction which increases the relative humidity and decreases evaporative cooling potential. Further, ice particles cool the carrier gas significantly which is a phenomenon used to effectively measure

icing conditions in experimental facilities and within turbofan compressors. As the gas temperature drops, this lowers the saturation pressure which further limits evaporative cooling capacity of the gas on the ice crystals. This will generate a higher melting rate for particles. Mass exchange between ice particles and the gas over one time-step is as follows.

$$\Delta\omega_g = \frac{1}{\dot{m}_g}\sum_{1}^{N_p}(\dot{m}_{evap})\Delta t \tag{3.60}$$

3.5 Thermodynamic Accretion Models

3.5.1 Thermodynamic Ice Crystal Icing Accretion

This work draws on the existing development of an ice accretion model by Bucknell et al. [25] [20], Trontin et al. [138] and Villedieu et al. [148]. The EMM-C model implemented in ICICLE introduced an additional water layer component within the 2D EMM model for warmed substrates. The temperature gradient and boundary conditions in the surface water film was modelled in the same manner as the original EMM with a mirror image of this reflected in the ice-substrate interface. The modes of ice accretion within the EMM and EMM-C models are as follows.

3.5.1.1 Running Wet

In this condition a liquid water film is present on the surface only. The only unknown is the water film height h_{film}, specified by impingement flux, $\dot{m}_{stick,w}$, water run back flux, $\dot{m}_{run}$ and evaporation flux $\dot{m}_{e,s}$,

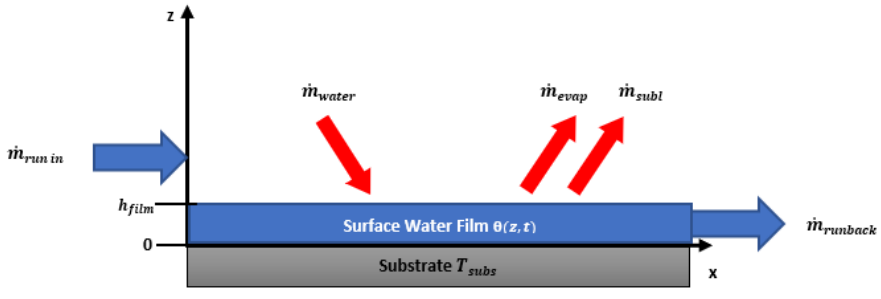

Figure 3.10: Accretion Model for Purely Liquid Runback Water

$$\rho_w \frac{\partial h}{\partial t} = (\dot{m}_{stick,w} + \dot{m}_{run} - \dot{m}_{e,s}) \tag{3.61}$$

3.5.1.2 Mixed Phase Ice Accretion - $T_f \leq 0°C$

This condition consists of a cool substrate, with an ice layer present onthe surface and a water layer formed at the outer surface.

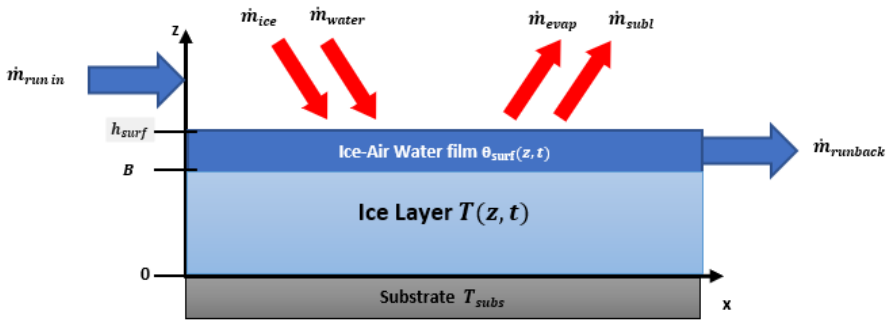

Figure 3.11: Ice Crystal Icing Accretion Model for a Cold Substrate

The one dimensional heat equations for the ice and water layers are as follows,

$$\frac{\partial^2 T}{\partial z^2} = \frac{\rho_i C_{p,i}}{k_i} \frac{\partial T}{\partial t} \tag{3.62}$$

$$\frac{\partial^2 \theta}{\partial z^2} = \frac{\rho_w C_{p,w}}{k_w} \frac{\partial \theta}{\partial t} \tag{3.63}$$

The continuity balance for ice and water layers is as follows,

$$\rho_i \frac{\partial B}{\partial t} + \rho_w \frac{\partial h}{\partial t} = (\dot{m}_{acc} + \dot{m}_{run} - \dot{m}_{e,s}) \tag{3.64}$$

The energy balance between the ice and water generates the LHS Stefan condition,

$$\rho_i L_f \frac{\partial B}{\partial t} = k_i \frac{\partial T}{\partial z} - k_w \frac{\partial \theta}{\partial z} \tag{3.65}$$

3.5.1.3 Mixed Phase Ice Accretion - $T_f > 0°C$

Finally in this condition a warm substrate leads to a liquid water film at the substrate surface. An ice layer forms at the point at which the water film reaches freezing point. A water layer also forms at the outer surface of the ice.

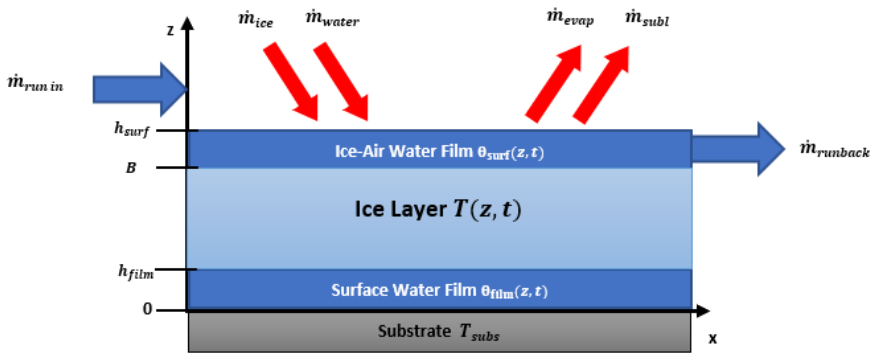

Figure 3.12: Ice Crystal Icing Accretion Model for a Warmed Substrate

The one dimensional heat equations for the ice and water layers are as follows,

$$\frac{\partial^2 T}{\partial z^2} = \frac{\rho_i C_{p,i}}{k_i}\frac{\partial T}{\partial t} \tag{3.66}$$

$$\frac{\partial^2 \theta}{\partial z^2} = \frac{\rho_w C_{p,w}}{k_w}\frac{\partial \theta}{\partial t} \tag{3.67}$$

The continuity balances for ice, surface and ice-air water layers is as follows,

$$\rho_i \frac{\partial B}{\partial t} + \rho_w \frac{\partial h}{\partial t} = (\dot{m}_{stick,i} + \dot{m}_{stick,w} + \dot{m}_{run} - \dot{m}_{e,s}) \tag{3.68}$$

$$\rho_w \frac{\partial h_{surf}}{\partial t} = (\dot{m}_{stick,w} + \dot{m}_{run} - \dot{m}_{e,s} - \dot{m}_f) \tag{3.69}$$

The energy balance between the ice and water generates the LHS Stefan condition,

$$\rho_i L_f \frac{\partial h}{\partial t} = k_i \frac{\partial T}{\partial z} - k_w \frac{\partial \theta}{\partial z} \tag{3.70}$$

Ice layer growth contributions are from freezing or melting of both the substrate film and outer surface water layers.

$$\frac{dB}{dt} = \frac{dB_{film}}{dt} + \frac{dB_{surf}}{dt} \tag{3.71}$$

$$\frac{dB_{film}}{dt} = -\frac{\rho_w}{\rho_i}\frac{dh}{dt} \tag{3.72}$$

The mass balance to describe the ice growth at the outer surface is as follows,

$$\rho_i \frac{dB_{surf}}{dt} = \dot{m}_{stick,i} + \dot{m}_f \tag{3.73}$$

where freezing rate $\dot{m}_f$ is defined in terms of the freezing heat rate,

$$\dot{m}_f = \frac{1}{L_f} q_f \tag{3.74}$$

The energy balance at the air-water interface is as follows.

$$-k_w \frac{\partial \theta}{\partial z}_{z=B+h} = (q_{in}) - (q_{out}) \tag{3.75}$$

$$-k_w \frac{\partial \theta}{\partial z}_{z=B+h} = (q_{con} + q_{sub} + q_{cool,w} + q_{cool,i}) - (q_{aero} + q_f + q_{ke,w} + q_{ke,i} + q_{run,w}) \tag{3.76}$$

The energy flux for ice growth was calculated by the difference in energy transferred to the ice layer from the water at each interface. The ice - water interface in each case was assumed to be 273.15 K. Energy changes in each layer of ice and water occurs due to convection, sensible cooling of ice and water, aerodynamic cooling of the substrate due to freestream, freezing and melting of ice and water, kinetic heating due to particle impact and aero conditions.

3.5.2 Numerical Solution Steps

The EMM calculation procedure is selected depending on the ICI conditions. If the substrate is warm and the $T_{subs} > 0°C$ the EMM-C mode is selected.

Model assumptions for the EMM-C are as follows:

- If $T_s > 0$ assume a water film layer at the surface.
- Conduction through the ice layer in the normal direction is neglected and therefore temperature is constant.
- $T(0,t) = T_s$. Ice or water is in perfect thermal contact.
- $T(B,t) = \theta(B,t) = T_f$. The interfaces between the ice and water are at freezing temperature.
- $\frac{\partial^2 T}{\partial z^2} = \frac{\partial^2 \theta}{\partial z^2} = 0$. Temperature profiles through the ice and water layers are quasi-steady.

- The runback water flows axially downstream between the control volumes.

The mixed-phase ICI EMM solution procedure is separated into 2 steps. First, if liquid water is deposited on the surface, then the mass balance in Equation 3.61 is solved for a set time step given the mass flux of the deposited water.

$$h = \frac{1}{\rho_w}(\dot{m}_{stick,w} + \dot{m}_{run} - \dot{m}_{e,s})dt \tag{3.77}$$

Following the solution of the water film, the film height was then fixed for the rest of the solution step. Step 2 calculates the growth of the ice and outer water layers extruded from the surface film. Equations 3.68 and 3.69 are the mass balance of the system. The energy balance is stated in Equation 3.76 assuming that there is no temperature profile in the ice and that the ice is homogeneous and the temperature is quasi-steady. Substituting into the energy and mass balances for the growth rate equations. The Stefan condition that specifies the phase boundary velocity is given by Equation 3.70. The water growth rate is summarised in Equation 3.83. This ODE was numerically integrated and solved in ICICLE using the Runge-Kutta-Fehlberg method, as it is effective in modelling stiff ODE problems. B_i and h_i represent the initial values for B and h in this calculation.

$$\frac{d\theta}{dz} = \frac{\theta - T_{subs}}{h} \tag{3.78}$$

Integrating with respect to height z,

$$\theta = \frac{\theta - T_{subs}}{h} z + T_{subs} \tag{3.79}$$

$$h = \frac{1}{\rho_w}(\dot{m}_{in} - \dot{m}_{out})dt \tag{3.80}$$

$$\rho_i \frac{\partial B}{\partial t} + \rho_w \frac{\partial h}{\partial t} = (\dot{m}_{in} - \dot{m}_{out}) \tag{3.81}$$

Integrating both sides with respect to time:

$$B = \frac{1}{\rho_i}(\dot{m}_{in} - \dot{m}_{out})dt + \frac{\rho_w}{\rho_i}(h_0 - h_1) + B_0 \tag{3.82}$$

Substituting Equations 3.78 and 3.82 into the Stefan condition in Equation 3.70.

$$\frac{dh}{dt} = \frac{1}{\rho_w L_f}\left(- \frac{k_w(\theta_h - T_{subs})}{h} + \frac{k_i(q_{in} - q_{out}\theta_h)}{k_i + q_{out}(B_i + \frac{1}{\rho_i}(\dot{m}_{in} - \dot{m}_{out})dt + \frac{\rho_w}{\rho_i}(h_0 - h_1))}\right) \tag{3.83}$$

Solving the Stefan problem in the previous EMM-C implementation within ICICLE involved discretising the domain into panels representing a unit width and varying axial distance representing a cell of the geometry. The EMM-C in 2D allowed enthalpy to transfer between cells through water runback and the remainder of the problem is a phase-change energy transfer problem in 1D. The expansion to 3D assumed no lateral conduction in the ice layer and simply changes the degrees of freedom available for the ice layer expansion.

3.5.3 Water Runback

The water flowing downstream has a significant effect on the enthalpy exchange at the surface. This is also a primary driver for ice crystal icing sticking and ice accretion initiation. Within ICICLE, a steady water runback mass balance was calculated using the wall shear stress τ_w and assuming a linear velocity and temperature profile. This method was initially implemented by Currie et al. [37], which is summarised in Equation 3.84 and in ICICLE by Connolly [31]. For three dimensions, this calculation was generated as a finite-difference approximation between the 2 neighbouring nodes in the stream and span directions for the exposure time.

$$\frac{dh_{film}}{ds} = \sqrt{\frac{\mu_f}{2\dot{m}_{net}\tau_w\rho_w}}\frac{\Delta\dot{m}_{net}}{\Delta s} \tag{3.84}$$

3.5.4 Substrate Heat Transfer

Heat transfer between the accreting ice and water and the substrate can be modelled as a conjugate heat transfer coupled system. Assuming either a lumped capacitance model for substrate temperature response or a 1D conduction model would be appropriate to

model the initial thermally soaked body and its response to latent heat exchange with the water and ice, respectively. Connolly performed an initial assessment of wall heat transfer compared to steady-state FEA [31]. The current literature suggests that it is reasonable to assume that iced substrates will adopt the free-stream recovery wet bulb temperature under steady conditions. Instead, an improved model using a lumped capacitance approach was used for simplicity. Fourier's law was applied, where

- the water layer and substrate are in perfect thermal contact;
- conduction is one-dimensional between water and substrate;
- conduction is quasi-steady for water-film thickness and exposure time;
- substrate temperature is held fixed once it reaches the $0.5°C$. This is to eliminate the simulation unsteadiness after the ice accretion layer forms.
- the temperature gradient is linear through the water layer $\frac{d^2T}{dx^2} = 0$
- the substrate is isothermal over each EMM time step.

For a substrate cell number j, conduction is as follows,

$$q = \rho_{subs} c_{p,subs} \frac{dT}{dt} = \frac{1}{A_{subs}} \frac{dQ}{dt} = k_w \frac{d^2T}{dx^2} \tag{3.85}$$

discretising this with respect to substrate cell properties, EMM time step extent and the enclosing water film properties assuming steady conduction,

$$\frac{dT}{dx} = \frac{T_{film} - T_{subs}}{h_{film}} \tag{3.86}$$

$$\Delta q_{cond,film} = k_w \frac{T_{film,j} - T_{subs,j}}{\Delta h_{film,j}} \Delta t_{EMM} \tag{3.87}$$

where q is the heat flux rate $\mathrm{Wm^{-2}s^{-1}}$ The thickness of the substrate Δx_{subs} was calculated for each case, for the stator case it is the distance between the film-substrate interface and the camber line. The lumped capacitance approach was used for the substrate which marches in time by step i,

$$\Delta q_{cond,subs} = \rho_{subs} c_{p,subs} (T_{subs,i+1} - T_{subs,i}) \Delta x_{subs} \tag{3.88}$$

$$\Delta q_{cond,film} = \Delta q_{cond,subs} \tag{3.89}$$

$$\Delta T_{subs} = k_w \frac{T_{film,j} - T_{subs,j}}{\Delta h_{film,j}} \Delta t_{EMM} \frac{1}{\rho_{subs} c_{p,subs} \Delta x_{subs}} \tag{3.90}$$

$$T_{subs,i+1} = T_{subs,i} + \Delta T_{subs} \tag{3.91}$$

3.6 Topography Update

3.6.1 Surface Mesh Extrusion

The surface mesh extrusion was generated in three dimensions along the surface normal for each surface cell. Following this, a series of smoothing and volume correction steps were performed to account for surface curvature and discontinuous surface extrusion heights.

$$z_{1D} = \tilde{\mathbf{n}} \cdot z_{EMM} \tag{3.92}$$

Cell extrusion representing ice growth is discontinuous and will result in stepped cells. Each panel can represent a curved surface with a convex or concave ice layer. Therefore, the ice height and final surface positions must be calculated with a height weighted sum of unit normals. Integration of the EMM equations requires a simple trapezoidal prism volume ratio scaling approach to calculated equivalent height of ice from convex or concave panel faces. Figure 3.13 shows the extrusion of a quad cell surface corresponding to a calculated ice height B generated by the EMM equations, this then enables a calculation of a corrected height due to local curvature.

3.6.2 Deposition Mass Smoothing

Ice and water deposition is driven by individual particle impact, a sticking probability and erosion efficiency generating a net impinging flux. This was generated by the ‘super-particle’ mentioned above in Section 3.3.4 which means a streamtube of mass flux on

a surface cell collects all deposited mass over the exposure time. In order to represent deposition physically, it was useful to implement a radial basis function approach to generate a Gaussian distribution for each local cell mass flux. This is generated by convolving a 0 mean Gaussian kernel over the surface mass flux distribution. This can be implemented using an image processing approach, similar to Gaussian smoothing for image intensity. The size of the smoothing radius is determined by the extrusion height/cell streamwise distance ratio.

3.6.3 Volume Re-scaling

When extruding an arbitrary mesh, concave and convex shapes require correction to the extrusion for ice accretion or implementing the model in a curvilinear method. In order for curvilinear approaches to work, the surface must be discretised sufficiently to capture changes in the surface angle. A volume correction is more appropriate, specifically for unstructured meshes for example. The surface curvature and inter-facial gaps will dictate the cross-section of the trapezoid. The unit normals of each bounding side $\hat{n}_C A$ and $\hat{n}_D B$ can be used to calculate the volume of each trapezoidal prism when extruded.

$$dB = \tilde{\mathbf{n}} B \tag{3.93}$$

$$dB_{corner} = \frac{\sum_{i=1}^{N} \tilde{\mathbf{n}}_i B_i}{N} \tag{3.94}$$

$$V_{ice,3D} = \int_0^B (0.5|a \times b| + 0.5|c \times d|) dB \tag{3.95}$$

$$dB_{corrected} = f(dB^3) \tag{3.96}$$

A local ice height for each cell extrusion is then extracted from the corrected ice height $dB_{corrected}$, Newton Raphson numerical approach is used to solve the ice height for the curvature corrected volume.

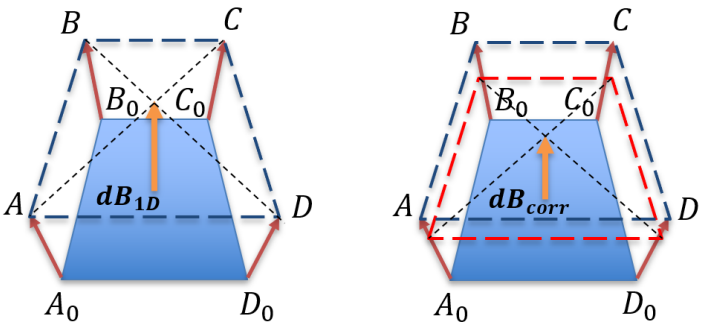

Figure 3.13: Quad cell face extrusion using trapezoidal volume correction method along cell node normals.

3.7 Summary

The chapter comprised individual numerical models implemented within this thesis in ICICLE 3D for the continuous phase, ice particle transport and melting, and accretion. It was pertinent to use an Euler-Lagrangian framework for the multi-phase transport modelling. This enables more control over the particle cloud parameters such as size, aspect ratio and Melt Ratio. This forms the framework for the combined particle transport and accretion model which will be discussed in more detail in Chapters 6 - 8.

4
Computational Methodology

Ice Crystal Icing (ICI) simulations require a multi-physics model which combines CFD, particle tracking, accretion, and mesh adaption. These individual simulations have further sub-models which require specification. This chapter describes the computational steps required to perform the baseline and coupled cases concerning ICI experiments.

4.1 Continuous Phase Modelling 82
4.1.1 Meshing 82
4.1.2 Flowfield 83
4.1.3 Gas Property Convergence Assessment 84
4.1.4 Parallel Computing 84
4.1.5 Case Setup - Multizone Approaches 85
4.1.6 Multi-Zone Flowfield Solver: Implementation in RATFac Validation Tests 86
4.2 Particle Cloud Seeding 89
4.3 Vapour Mixture Specification 90
4.3.1 Vapour Pressure 91
4.3.2 Vapour Mass Fraction 92

4.4 Particle Transport 92
4.4.1 Numerical Advection Discretisation 93
4.4.2 Numerical Integration Algorithm 94
4.5 Accretion 94
4.6 Summary 96

4.1 Continuous Phase Modelling

The specification of the continuous phase simulation are described below. Requirements relating to computer resources, numerical schemes and flow properties are presented.

4.1.1 Meshing

ICICLE 3D requires a mesh and flow solution to couple particle tracking, melting and accretion models to. Meshing was controlled within the ICICLE environment by driving the STL files, mesh generation and CFD methods programmatically. Meshing was generated by importing a CAD file or point cloud into ICICLE 3D and generating a *.lua* script for BoxerMesh (or, in some cases, ICEM), a meshing tool appropriate for complex and changing geometry, in turbomachinery applications. The steps used in the meshing pre-processor for ICICLE are illustrated below in 4.1. Meshes were generated

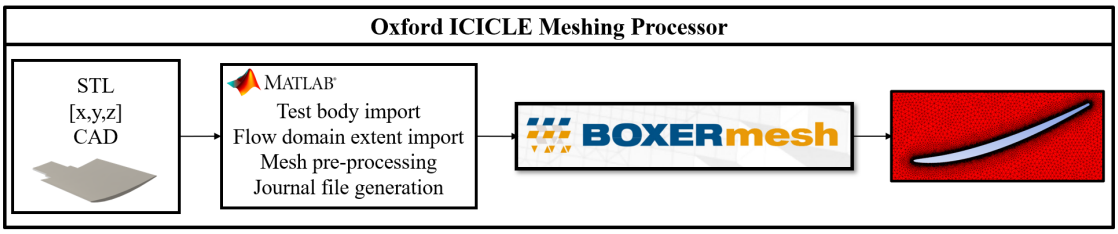

Figure 4.1: Meshing Processor Flow Diagram for ICICLE, BOXERMesh logo taken from [26].

using ICEM 2021 R2 or BoxerMesh 3.3.3. A structured mesh multi-block approach was used for the RATFac tunnel specification and cone cases. Unstructured meshes were used for the stator enabling flowfield updates programmatically and without manual user intervention. The boundary layer is defined with a maximum wall cell $y+ < 5$. In cases

where scalable wall functions were used, $y \geq 30$ is adopted. A region of more densely packed cells around the test article was generated with a radius of 4 characteristic lengths (chord lengths in the case of the stator). Unstructured meshes generated in ICEM and BoxerMesh were produced programmatically using *.rpl* or *.lua* scripting. This enabled automation of geometry read-in, specification of mesh domain extents, and mesh sizing. Octree meshing was used in both ICEM and BoxerMesh, BoxerMesh was specifically designed for application in the turbomachinery environment.

4.1.1.1 Inflation Layers - resolving boundary layers and near wall flow

Hexahedral cells were extruded from each wetted wall to resolve the boundary layer and steep velocity gradient close to the wall. In cases where the $k-\omega$ SST model was implemented, 10 inflation layers with an extrusion ratio of 1.2 were used. This was specifically for the stator vane analysis, where strong separations, tip leakage and a sharp leading edge were present. For cases using the Realizable $k-\epsilon$ model with scalable wall functions inflation layers were initiated on the basis of the value of wall cell y^+ as specified above. For the Reynolds Stress Model, the inflation layers were generated with the same near wall description as the Realizable $k-\epsilon$ model implementation.

4.1.2 Flowfield

The flowfield solution was generated using ANSYS FLUENT 2021 R2. In each case, a steady-state RANS solution was generated. The pressure-based Second Order Upwind discretisation scheme was used for advection. The Green-Gauss node gradient method was used to discretise convective and diffusive fluxes. This is more accurate than cell centre or least squares methods. Structured and unstructured cases are possible, but higher-order discretisation schemes require structured meshes (e.g., QUICK) [4]. Turbulence closure was employed using eddy-viscosity and Reynolds stress models (RSM). The Realisable $k-\epsilon$ (RKE) model was used in most studies as it effectively predicts turbulence intensity compared to experiments; this is detailed in Chapter 6. Fluid viscosity was specified by Sutherland's law, and air was modelled as an ideal gas. Inlet boundaries were specified using a *velocity-inlet* profile. This enabled specification of the total

temperature and velocity profile, which corresponds to experimental measurements, and allowed the extent of the computational domain to be suitably truncated. The fluid exits the domain via a *pressure-outlet* boundary which had a specified static pressure (based on the measurement).

4.1.3 Gas Property Convergence Assessment

In validation experiments, flow properties are evaluated under dry (no-ice) and wet (iced) operating conditions. A Kiel head probe measurement was used to measure both total pressure and temperature in dry conditions. This enables Mach number to be calculated as a useful compressible flow solution convergence estimation. The Mach number at the Kiel head probe plane was then calculated as a mass-averaged quantity. Figure 4.2 illustrates a simulation run using boundary conditions from the TR495 test case at the NRC RATFac facility where the steady Mach number was measured as 0.391. The static pressure at the pressure outlet was iteratively updated until the required measured Mach number, total pressure, and temperature were achieved. In blind simulations, the static pressure at the exit is imposed without requiring this step.

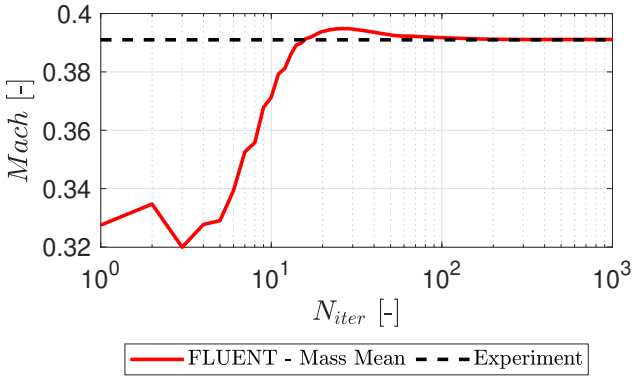

Figure 4.2: Mass averaged Mach number at Kiel probe position. This example is for Test Case TR495 with steady state $Mach$ number of 0.391.

4.1.4 Parallel Computing

Use of the University of Oxford Advanced Research Computing (ARC) facility enabled the execution of much of the work presented in this thesis [118]. Flowfield solutions

were generated using ANSYS FLUENT 2021 R2 in MPI and batch mode. This enabled recursive and high mesh count RANS RSM simulations. In each case, the simulations were performed using 48 nodes, and required <4hrs compute time. FLUENT journal files and boundary conditions were generated programmatically using MATLAB 2022b. The main function loop enables recursive flowfield solutions, and this functionality has been developed, but was not employed in this thesis. The computational flow is shown diagrammatically in Figure 4.3.

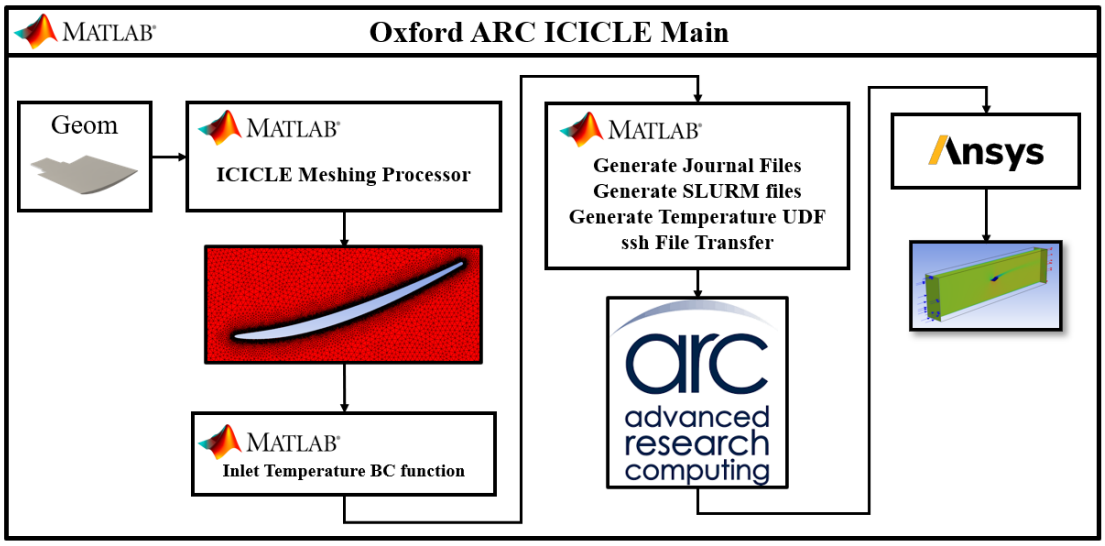

Figure 4.3: Flow Chart describing data exchange and running files for Oxford ARC HPC deployment.

4.1.5 Case Setup - Multizone Approaches

The purpose of developing the ICICLE code was to allow accretion and shedding to be determined on individual engine components and subsystems in the context of other engine components where accretion does not occur. Similarly in validation tests there are elements of the test rig whose operation is stable and unchanging with the test article employed downstream. Thus a multi-zone approach to modelling where the stable region upstream is modelled and used to provide boundary conditions for a truncated downstream domain has been developed. This allows the investigation of large complex geometries at high resolution while minimising the computational resource required (although this remains extensive). The primary focus of the first zone, is to model particle

transport, melting and break-up. Further downstream, surface accretion is important, specifically on vanes, and across the casing and hub. The likelihood of accretion narrows the location at which high fidelity simulations are necessary. This has general application in turbomachinery but is illustrated below using the validation tests conducted in the NRC RATFac facility in this thesis.

4.1.6 Multi-Zone Flowfield Solver: Implementation in RATFac Validation Tests

For the RATFac tunnel, ICICLE was used to model, discretely, the initial ice melting and transport from the tunnel ice injection pipe through to the measurement plane. To match tunnel conditions TWC measurements made using the the CIKP provided at the tunnel centreline are targeted. Furthermore, additional 'Ice-On' gas-vapour relative humidity measurements made by the TAT-RH probe are available for comparison. Data from both 'dry' (ice off) and 'wet' (ice on) operating conditions allow mass flow rate, pressure and temperature boundary conditions within the model to be determined.

4.1.6.1 Inlet Domain

The inlet section comprising the ice injection pipe, warm and humid plenum air, contraction and start of the working section, as detailed in Figure 4.4 is shown below in Figure 4.6. Here the injection pipe and plenum conditions were taken from RATFac operating conditions. The measured properties for 'wet' T_0 by the TAT-RH and 'dry' P_0 by the Kiel probe form the boundary conditions in this case.

A plane intersecting the CIKP probe was generated to extract total and static temperature and pressure. A surface was then fitted to this data, to generate a polynomial functions for each boundary condition which are used within an ANSYS FLUENT UDF. This provides a location to generate a particle cloud matching step against experimental measurements.

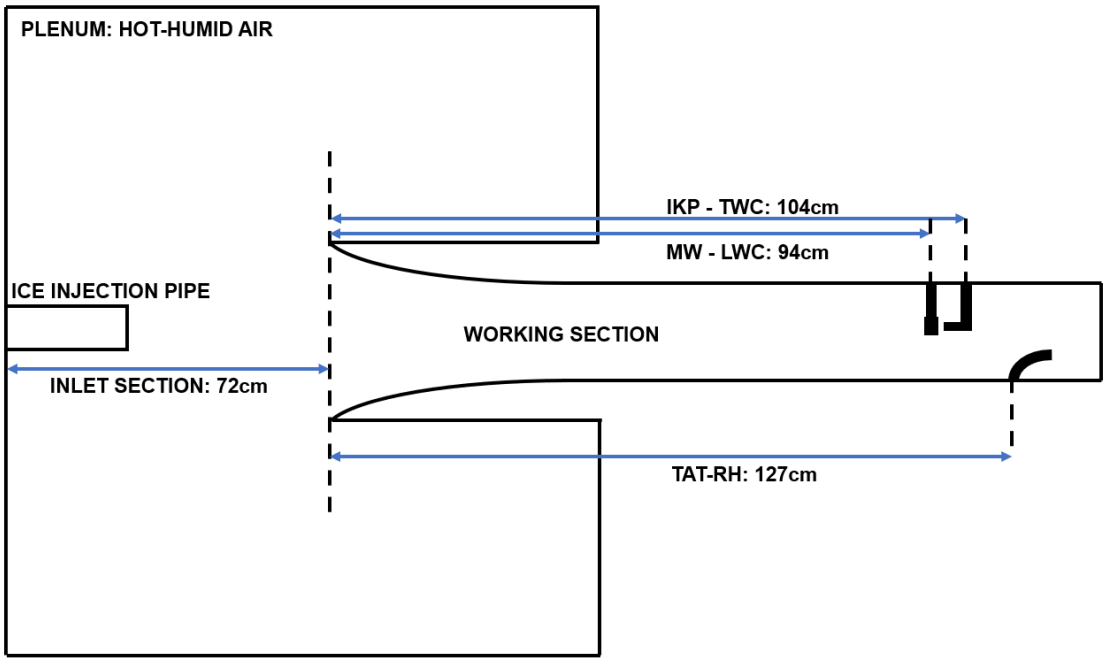

Figure 4.4: RATFac Altitude Icing Wind Tunnel Inlet Section Schematic for CFD Domain Initialisation

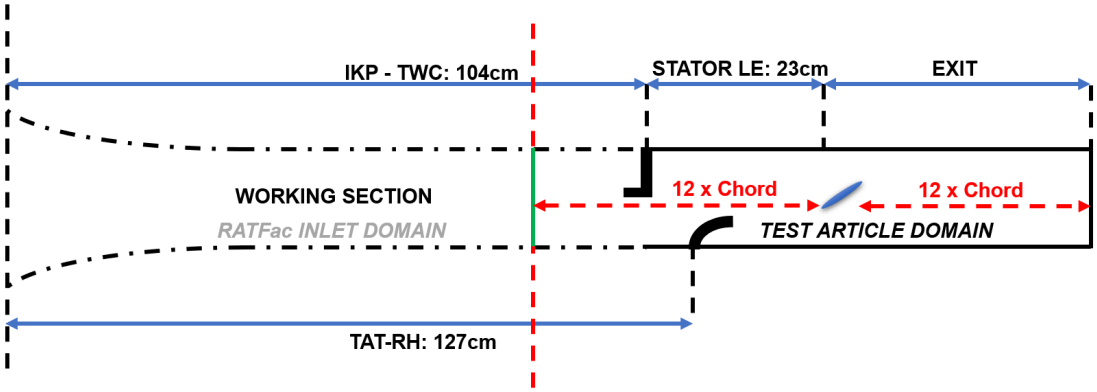

Figure 4.5: RATFac Altitude Icing Wind Tunnel Working Section Schematic for CFD Domain Initialisation

4.1.6.2 Test Article Domain

The experimental working section, i.e. the test article where impact with accretion is expected and its bounding walls constitutes the **Test Article Domain**, as illustrated in Figure 4.6. As mentioned above a UDF was used to specify the inlet gas properties from the **Inlet Domain** simulation. The test article walls are typically adiabatic to model approximate steady 'clean' conditions where the stator will adopt the recovery temperature or an imposed 'wet' operating close to freezing. The dotted line in Figure

4.7 indicates the total temperature measurement position. This is the exit plane for the RATFac Inlet Domain. The gas property profile for the UDF was constructed from the domain inlet position, this enabled an iterative approach by adjusting the test domain exit (out) properties in order to match the measured properties.

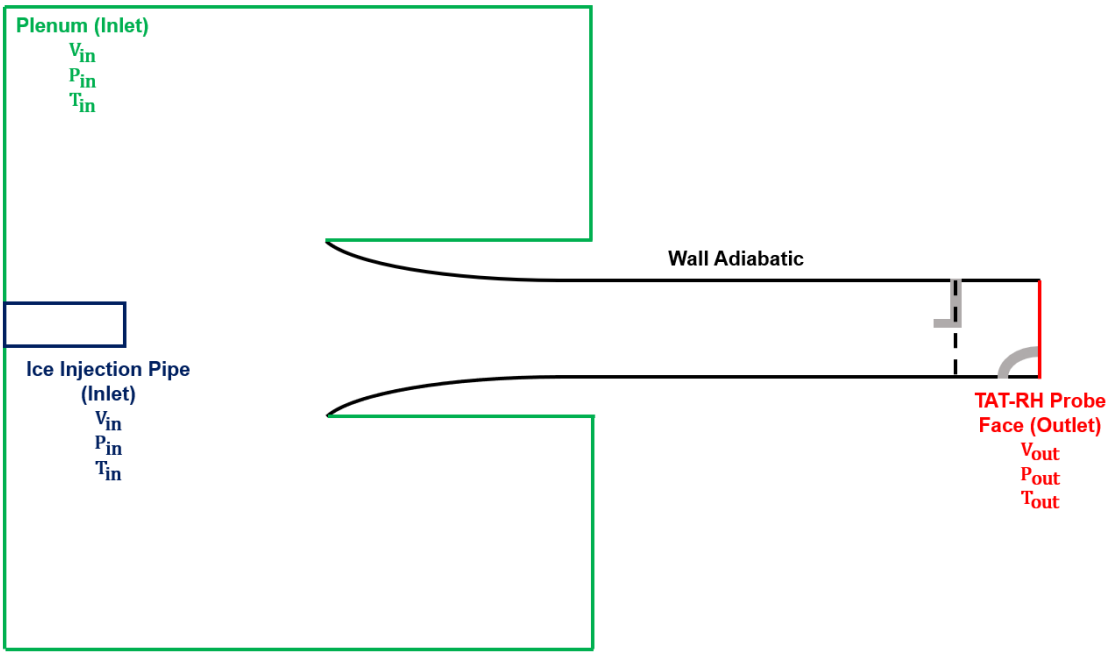

Figure 4.6: RATFac Altitude Icing Wind Tunnel Boundary Conditions Schematic for CFD Domain Initialisation

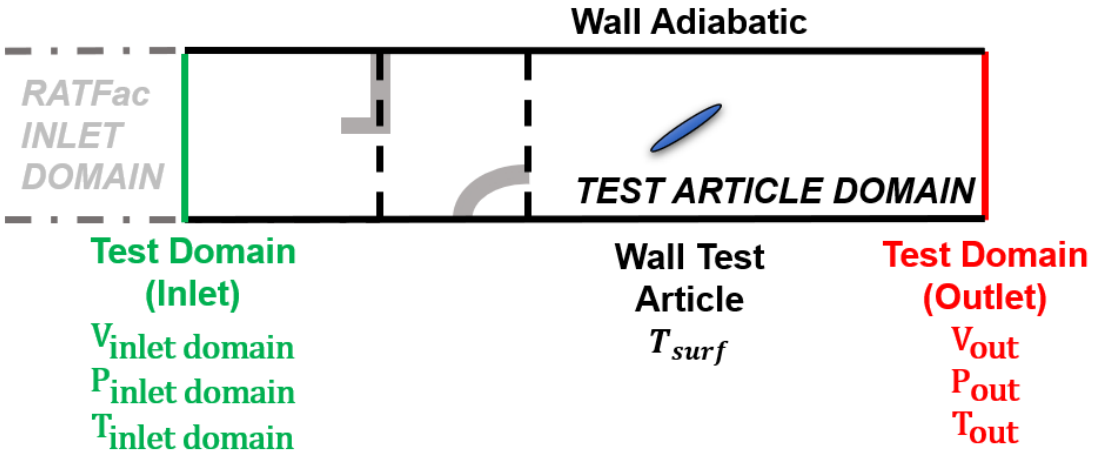

Figure 4.7: Test article domain schematic detailing boundary conditions for multi-zone flowfield solver

4.1.6.3 UDF Gas Boundary Conditions

Passing of the boundary conditions between the upstream and downstream computational domains (at the measurement plane) is achieved through the interpolation of the temperature, velocity and pressure boundary conditions using a surface fit and specification in a ANSYS FLUENT UDF. First, in ICICLE, a 5$^{\text{th}}$ order multivariate polynomial surface was fitted to the gas properties using MATLAB 2022b *fit* function. This enabled the original exit mesh cell node values to be used and can be modified to account for wall temperature effects. For a general function:

$$\begin{aligned} f(\xi,\eta) = p_{00} + p_{10}\xi + p_{01}\eta + p_{20}\xi^2 + p_{11}\xi\eta + p_{02}\eta^2 + p_{30}\xi^3 + p_{21}\xi^2\eta \\ + p_{12}\xi\eta^2 + p_{03}\eta^3 + p_{40}\xi^4 + p_{31}\xi^3\eta + p_{22}\xi^2\eta^2 + p_{13}\xi\eta^3 + p_{04}\eta^4 \\ + p_{50}\xi^5 + p_{41}\xi^4\eta + p_{32}\xi^3\eta^2 + p_{23}\xi^2\eta^3 + p_{14}\xi\eta^4 + p_{05}\eta^5, \end{aligned} \tag{4.1}$$

where p_{00} to p_{ij} are generated outputs by the Matlab *fit* function. These were produced for gas velocity, total temperature and static pressure. This method was employed to enable parameterisation of test article boundary conditions. Furthermore, in cases where the downstream article has any planar or axisymmetry, the inlet profile can still be used. This was more effective than a UDF importing an inlet face boundary profile from a previous solution, as it requires the mesh discretisation to be conformal. A 5$^{\text{th}}$ order polynomial was seen to capture surface variation without overfitting the data on the highly defined surfaces used. Figure 4.8 details the simulated total temperature distribution and surface fit at the TAT-RH measurement plane position.

4.2 Particle Cloud Seeding

Particles were seeded in a uniformly spaced rake or 2D rectangular distribution. Lagrangian particle tracking and Rosin-Rammler particle size distributions require specification of diameter and mass fraction. In ICICLE, at each seed location, a size distribution was injected with an equal number of bins at each physical seed location. This further extends to particle aspect ratio (E), orientation and turbophoresis. As a result, each distribution was discretised by a user defined value (nominally drawn from experimental

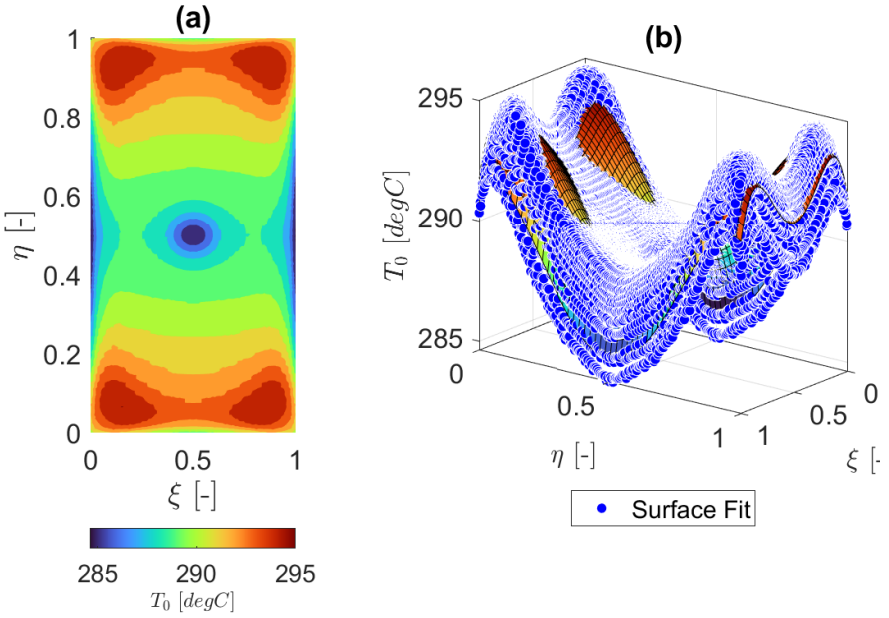

Figure 4.8: (i) Simulated Total Temperature Distribution at TAT-RH Probe Measurement Plane for Example Case, (ii) 5th Order Polynomial Surface Fit for Temperature Distribution, Contour plot from (i) is plotted.

results or literature). Then a spatial distribution over the injection area was specified to generate a variation in mass flux (TWC), *Melt Ratio*, diameter or other properties mentioned above. This was to ensure a fixed injection count at each position, with the variation in each parameter changing but not the particle or bin granularity. The particle size distribution measurements, taken downstream of the ice injection pipe, allow this model of the upstream section of the RATFac of the test rig to be used as the primary tool for the validation of particle tracking, break-up and phase change models.

4.3 Vapour Mixture Specification

The vapour phase was overlaid onto the 'dry' CFD flow solution within the ICICLE environment. Here as a specification for specific humidity (SH) or relative humidity (RH). This is dependent on your inlet boundary conditions or measurements. This was then used to generate a vapour mass fraction based on the local psychrometric properties.

4.3.1 Vapour Pressure

Vapour pressure is necessary to identify the vapour mass fraction. We can specify the partial pressure according to Dalton's Law of partial pressures. Within ICICLE, saturation vapour pressures of ice ($< 0^\circ$ C) and water ($> 0^\circ$ C) are calculated using the Hyland & Wexler polynomials [72]. Saturation vapour pressure of ice is as follows;

$$P_{vap,sat} = \exp A_1 T^{-1} + A_2 + A_3 T + A_4 T^2 + A_5 T^3 + A_6 T^4 A_7 \log T \tag{4.2}$$

Table 4.1 summarised the polynomial coefficients, A_{1-7} , for this expression.

Table 4.1: Saturation Vapour Pressure for Ice, Polynomial coefficients

A	Value
1	-5674.5359
2	6.3925247
3	-0.009677843
4	6.2215701×10^{-7}
5	2.0747825×10^{-9}
6	$-9.484021 \times 10^{-13}$
7	4.1630159

Saturation vapour pressure of water is as follows;

$$P_{vap,sat} = \exp \left(B_1 T^{-1} + B_2 + B_3 T + B_4 T^2 + B_5 T^3 + B_6 \log T \right) \tag{4.3}$$

Table 4.2 summarised the polynomial coefficients for this expression.

Table 4.2: Saturation Vapour Pressure for Water, Polynomial coefficients

A	Value
1	-5800.2206
2	1.3914993
3	-0.048640239
4	0.000041764768
5	$-1.4452093 \times 10^{-8}$
6	6.5459673

4.3.2 Vapour Mass Fraction

Assuming an imposed freestream Relative humidity (RH), the vapour mass fraction was calculated from the 'dry' flowfield properties. The Hyland & Wexler formulae are used to generate a saturation vapour pressure at each control volume.

$$P_{vap,sat} = P_{H\&W} \tag{4.4}$$

$$P_{vap,g} = RH \cdot P_{H\&W} \tag{4.5}$$

$$\omega_g = \frac{M_w}{M_a}\left(\frac{P_{vap,g}}{P - P_{vap,g}}\right) \tag{4.6}$$

Here the mass flux of vapour, $\dot{m}_v$, within the flowfield was propagated as a ratio of 'dry' air mass flux, $\dot{m}_a$, at each control volume. This is necessary to resolve the distribution in specific humidity (SH) within the flowfield. The local control volume mass flux can be directly calculated from a CFD solution.

$$\dot{m}_v = \omega_g \dot{m}_a = \omega_g \rho_g U_g \tag{4.7}$$

$$SH = \frac{\dot{m}_v}{\dot{m}_a + \dot{m}_v} \tag{4.8}$$

These calculations can be performed with respect to static or stagnation conditions depending on experimental/freestream properties. Within turbomachinery modelling, it is not possible to assume a fixed 'freestream' value for vapour fraction or RH, therefore a known upstream value must be distributed with respect to gas properties and vapour mixture.

4.4 Particle Transport

Particle transport calculations were performed using a Lagrangian transport model. This provides for a higher resolution approach to control particle size, shape, orientation and

Melt Ratio. Additionally, the stochastic nature of the impact and turbophoresis (DRW) models are better resolved with this approach. The drawback to Lagrangian reference frame modelling is the 'curse of dimensions' or the multiplier effect as you vary each property. This may be moderated by advances in computational resources and inherent parallelism in model implementation.

4.4.1 Numerical Advection Discretisation

Particle trajectory modelling is discretised using an adaptive time-step approach defined by CFL number,

$$\Delta t_{CFL} = \left(\alpha \left(\frac{U_x}{\Delta x} + \frac{U_y}{\Delta y} + \frac{U_z}{\Delta z} \right) \right)^{-1} \tag{4.9}$$

where α is the under-relaxation coefficient for particle trajectory calculations. An $alpha$ value imposed an adaptive time-step which is useful in reducing computation steps for unconditionally stable systems. The time step is blended to a minimum value calculated from the wall-normal distance as particles may 'pass' through the wall mesh if the wall cell sizing is sufficiently large, this will also traverse the boundary. Particles are limited by a near wall CFL number controlled by particle diameter D_p.

$$\Delta t_{wall} = \left(\alpha \left(\frac{U_{x,wall}}{D_{p,x}} + \frac{U_{y,wall}}{D_{p,y}} + \frac{U_{z,wall}}{D_{p,z}} \right) \right)^{-1} \tag{4.10}$$

Assessments by Bucknell et al. [22] identified an insensitivity to CFL number, however for stability CFL is restricted to 1 due to the integration methods holding particle forces constant. Trajectory and melting equations are integrated using a first order Analytical discretisation scheme from ANSYS - FLUENT DPM [4]. The particle velocity is discretised as follows, by assuming fixed particle forces over the integration timestep (Δt).

$$U_p^{k+1} = U_n + \exp^{-\Delta t/\tau_p}(U_p^n - U_g^n) - a\tau_p(\exp^{-\Delta t/\tau_p} - 1) \tag{4.11}$$

4.4.2 Numerical Integration Algorithm

Particle tracking was conducted using Dual Time-Stepping (DTS) which employed a pseudo-time derivative to solve for mass and energy exchange for two-way coupled flows. Here an 'exposure' time produced a mass flux of ice and air. The flowfield is 'frozen' or in steady state. Particle tracking is performed on the flowfield and source terms are collected at each mesh volume cell for evaporation and sensible heating / cooling. Then the flowfield is updated by interpolating between each axial source term plane section. Figure 4.9 details this algorithm. It is different to a classic source-in-cell approach [4] as source terms are interpolated over a coarse over-set grid as opposed to individual cell volumes. This is to aid solution convergence and reduce computational cost. This approach effectively smoothed source terms spatially.

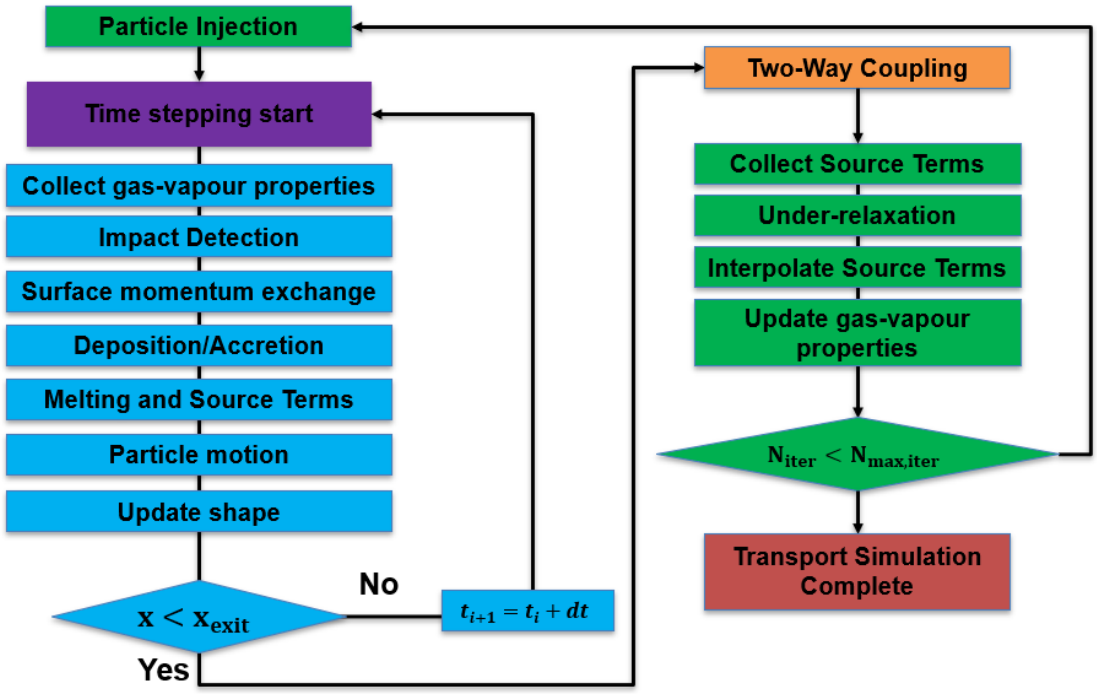

Figure 4.9: Flow chart for ICICLE 3D Particle Tracking module. Dual time stepping steady outer temporal loop and inner unsteady particle transport loop described.

4.5 Accretion

In solving for the accretion, a similar Dual Time-Stepping method was employed, this time due to the non-linear unsteady PDE formulation of the Bucknell-Myers-Messinger

model, see Chapter 3 for further details. Source terms for energy and mass exchange between the gas, ice / water layers and the substrate were generated. These were held fixed over the 'accretion' time. This is equivalent to the 'exposure' time for particle tracking and must be equivalent to conserve mass and energy. By discretising the PDE formulation to generate a quasi-steady 1 layer finite volume formulation of the EMM-C model, a non-linear ODE for the phase boundary extrusion height can be obtained reducing the complexity of the solution step.

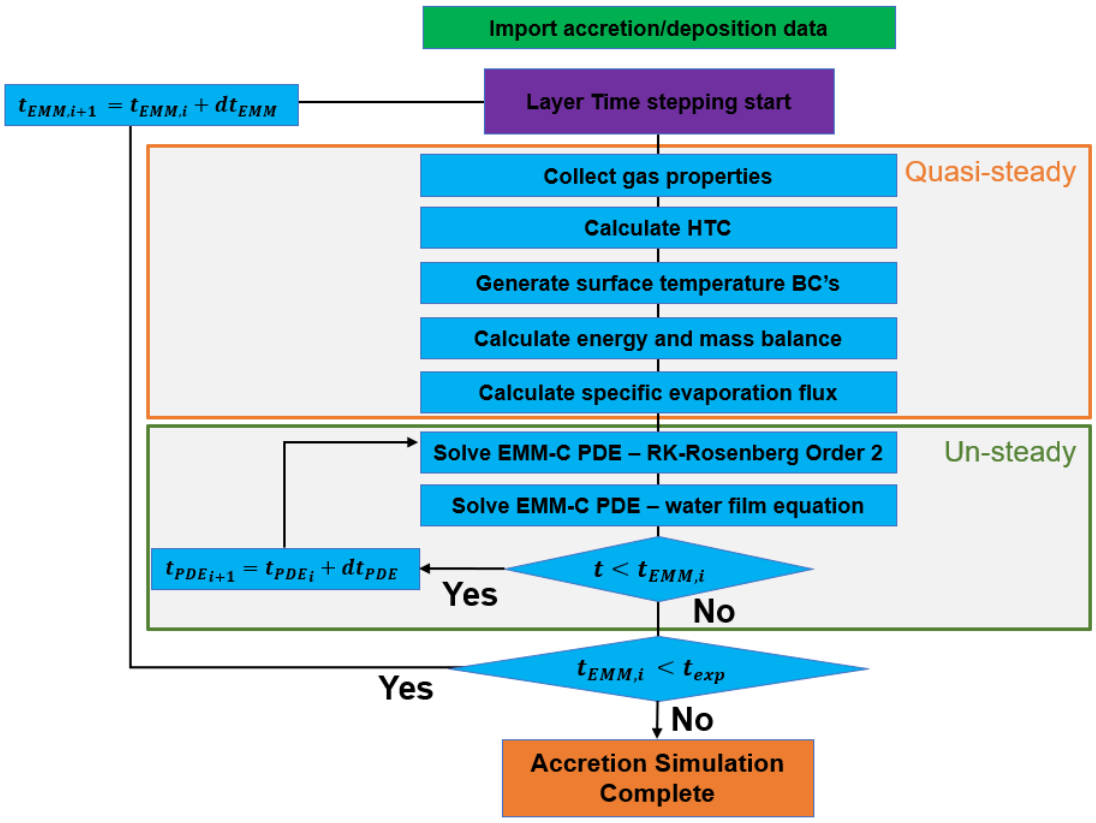

Figure 4.10: Flow chart for ICICLE 3D Accretion module. Quasi steady outer temporal loop and inner unsteady temporal loop described.

The accretion differential equations were solved using the Runge-Kutta-Rosenberg method [133]. This is useful for stiff ODE's. The MATLAB *ode23s* solver was used to solve for the velocity of the film in Equation 3.83. The solution process is schematically shown in Figure 4.10.

4.6 Summary

This chapter details the specification of the numerical solution approach within ICICLE and the related meshing and flowfield specifications. The complexity and boundary condition requirements to simulate the gas, vapour and particle phases demand a coupled multi-step CFD and multi-zone domain approach to converge known gas and vapour properties. This is also necessary due to the computational complexity of the problem. Part of the solution step is conducted using a high performance computer (HPC) to take advantage of the parallelism within the ICICLE and CFD simulation steps.

5

Previous Ice Crystal Icing Experiments

Ice Crystal Icing (ICI) experiments conducted by the Particle Deposition Group, University of Oxford form the basis of the numerical modelling challenge and validation data within this thesis. These experiments are detailed below to give the reader a full description of the conditions, measurements, and test article geometries used within this thesis.

5.1 Ice Crystal Icing Experiments 98
5.2 Working Section Measurements 99
5.2.1 Gas-Vapour Mixture Properties 99
5.2.2 Particle Size Distribution Measurements 100
5.2.3 Bulk Particle Cloud Measurements 101
5.3 Test Articles 104
5.3.1 35° Cone 104
5.3.2 Compressor Stator Vane 104
5.4 Ice Accretion 105
5.4.1 2D Accretion Data 105
5.4.2 3D Accretion Data 106

5.5 Test Matrices 107

5.1 Ice Crystal Icing Experiments

Tests conducted by the Particulate Deposition Group, Oxford Thermofluids Institute at RATFac investigated ICI accretion on an axisymmetric cone body, a prismatic engine representative stator blade and a linear vane segment/swan neck duct. These studies investigated the impact of aerodynamic conditions, PSD, geometry and surface heating [21, 23, 24, 33]. The experimental campaigns provide a basis for model development and validation.

The studies tested a range of conditions for PSD, Mach, P, T, TWC, MR and surface angle (vane A.o.A and cone half angle). A semi-empirical erosion and sticking model was developed to quantify the sticking and erosion efficiency of particle impact on an axi-symmetric cone test body [23]. Transient data extraction techniques were examined in both the stator and cone studies, investigating shadowgraphy, depth of field and laser grid projection methods to extract ICI accretion geometries experimentally [21, 33] . ICI accretion magnitude and growth histories were calculated to quantify the change in potential field around the clean test geometry and ice shape. The tests conducted by the University of Oxford relating to ICI experiments are summarised in Table 5.1.

The National Research Council in Canada houses the RATFac altitude wind tunnel for engine sub-stages and components, as shown in Figure 5.1. RATFac is an open loop altitude icing wind tunnel, preventing any ice crystals or humidified air from recirculating [81]. This means a jet of cold air and glaciated ice, which is important for producing a fixed inlet RH and P, T, Mach condition for the ice cloud and warmed air. By design, this makes RATFac tunnel experiments appropriate for numerical model validation due to well defined boundary conditions.

It operates at Mach ≤ 0.5 and total pressure $\leq 15\,\text{kPa}$. This facility, introduces ice to the flow using a grinder and steam system to create ice crystals and a mixed jet of warmer air, simulating both relative humidity and liquid water content. This, therefore, can operate in set mixed-phase and glaciated conditions, matching those found in the

Table 5.1: Oxford Icing Experiments [21, 23, 24, 31–33]

Campaign	Year	Facility	Mach	Accretion Measurements
Cone	2017	RATFac	0.25 to 0.4	2D shadowgraph ice thickness, PIV
Compressor Stator	2017	RATFac	0.25 to 0.4	2D shadowgraph ice thickness, surface temp., TWC, MR, PIV
Compressor Stator	2019	RATFac	0.25 to 0.4	2D shadowgraph ice thickness, DIC 3D ice thickness, TWC, MR PIV
Swan Neck Duct	2019	RATFac	0.25 to 0.4	2D shadowgraph ice thickness, DIC 3D ice thickness, surface temp., TWC, MR, PIV
Triple NACA Airfoil	2021	AIWT	0.25 to 0.4	2D shadowgraph ice thickness, surface temp., TWC, MR, PIV

warmer compressor sections. A measurement plane within the working section of the tunnel is used to characterise the tunnel operating conditions. Probes measuring LWC, TWC, IWC, humidity and total temperature enable specific mixed-phase ICI conditions to be generated, reproducing conditions within the LP and IP compressor [40, 41]. Furthermore, hot wire anemometer has been used to quantify turbulence intensity within the tunnel working section in 'dry' conditions by Knezevici et al. [81].

5.2 Working Section Measurements

5.2.1 Gas-Vapour Mixture Properties

Measurements of the carrier gas-vapour mixture were calculated at steady 'dry' conditions with no ice injected, and then during the ice on test time. Measurements include total pressure, P_0, total temperature, T_0 and relative humidity, RH. These were measured in dry conditions using a Kiel head probe while wet 'icing' conditions are made using the TAT-RH probe [81, 131].

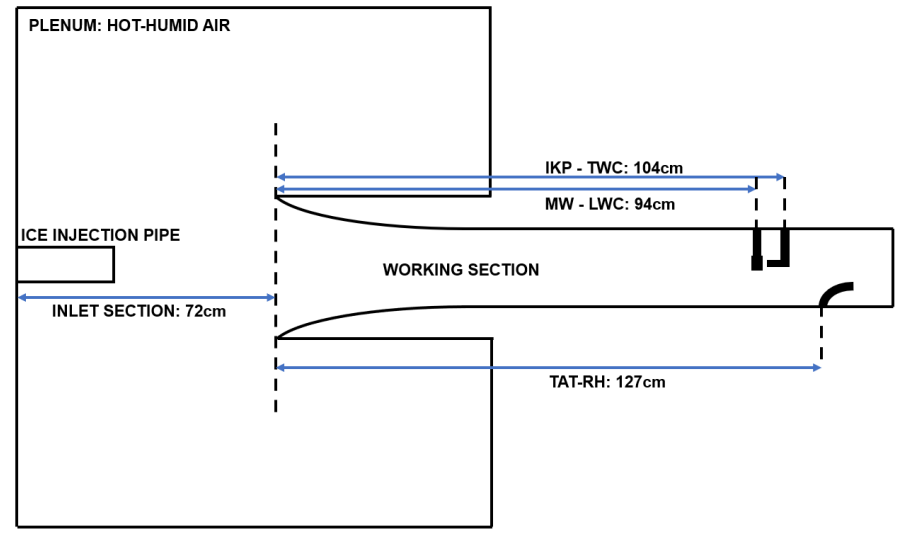

(i)

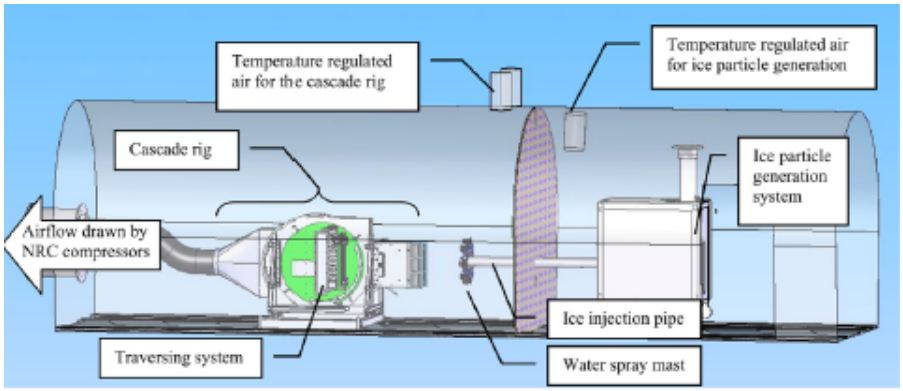

(ii)

Figure 5.1: (i) RATFac tunnel cross section with sensor axial positions displayed. (flow L-R) (ii) National Research Council of Canada - Research Altitude Test Facility [130].

5.2.2 Particle Size Distribution Measurements

Particle size distribution was measured upstream of the bellmouth of the working section at the NRC RATFac tunnel using particle imaging velocimetry (PIV) which is detailed in [53]. This provides a 26 bin resolution for particle size distribution at different grinder settings. In each study within this chapter, experimental diameter mass fractions were used as an input for ICICLE.

5.2.3 Bulk Particle Cloud Measurements

Spatial measurements of particle bulk cloud properties were made using a Compact Iso-Kinetic Probe (CIKP) for total water content, TWC, and a Science Engineering Associates (SEA) Multi-Wire Probe (MWP) for liquid water content, LWC.

5.2.3.1 Total Water Content

The probe axial positions are detailed in Figure 5.2i. Calibration tests were also performed to obtain an area resolved measurement for TWC over the measurement plane. This involved a clockwise traverse through five passage locations at a range of nominal TWC settings to assess the TWC distribution over the working section measurement plane. Figure 5.2i illustrates the CIKP traverse path, where η and ξ represent the tunnel height and width extents respectively. The measurements commenced at the centreline and traverse clockwise (looking downstream). The overall transient measurement was conducted over 270 seconds. The initial and final centreline measurements, at position 0, were $\sim$55 seconds in length. This can be seen in Figure 5.2ii, The remaining ice cloud measurements at positions 1-4 take $\sim$30 seconds. The transit time between positions was $\sim$12 seconds. Between these measurements, the CIKP probe moves either across the flowfield or inline with the tunnel walls.

Uncertainty quantification yielded precision and bias errors. From the raw data, outliers, greater than 3 standard deviations from the raw mean, were rejected. This eliminated erroneous readings and initial transient relaxation measurements as the probe halted following transit. The mean and sample standard deviation at each location were then calculated. Figure 5.2ii shows a typical result: the Test Run 651 traverse measurement. The mean and 95% confidence intervals are shown. A bias error is evident at positions 2 and 4 following the traverse of the probe through the core flow where the TWC is highest. This suggests that the settling time or phase lag between temperature and humidity sensors of the probe is inadequate in these locations.

Figure 5.3i illustrates the CIKP traverse path from a stowed position (5), buried in the tunnel wall. The probe enterd the gas path and measured ice and water content over an exposure time of approximately 270 seconds.

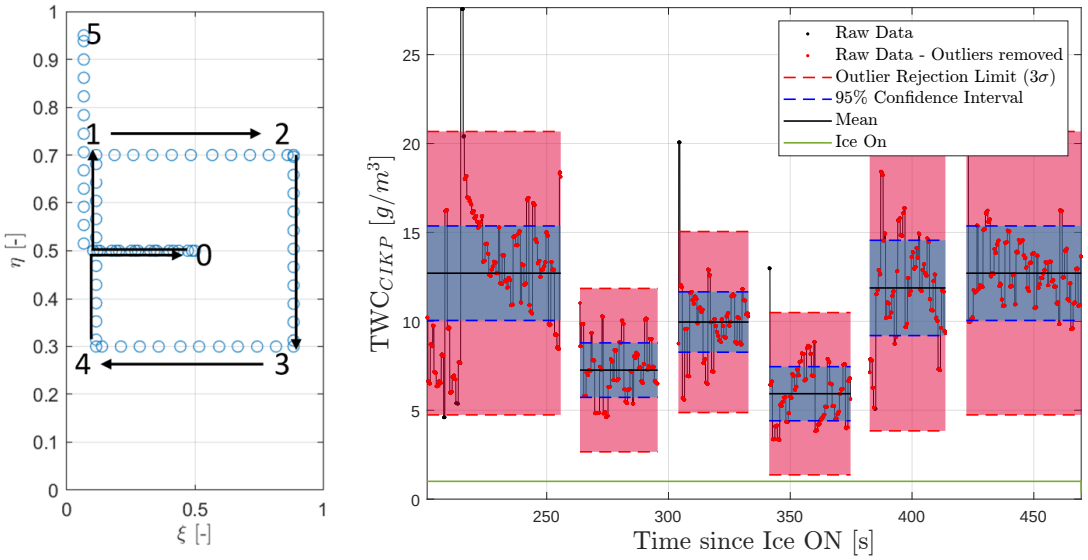

(i) (ii)

Figure 5.2: (i) Traverse path for CIKP TWC probe across the RATFac Tunnel inlet plane. Traverse path moves over the following positions: 0 -> 1 -> 2 -> 3 -> 4 -> 0. (ii) Total Water Content Traverse CIKP Probe Trace for Calibration Test Run TR644.

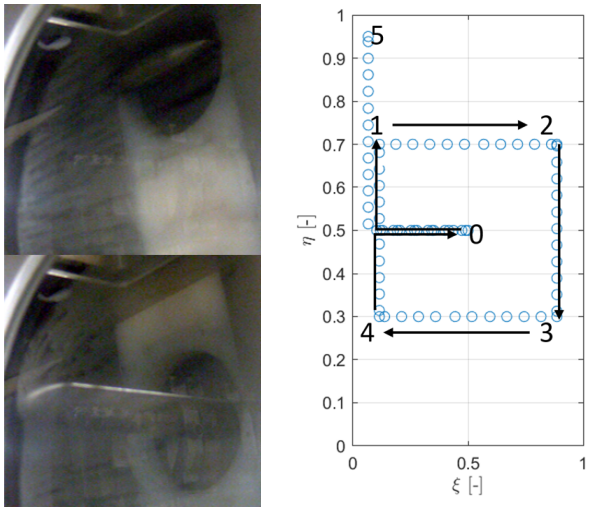

(i) (ii)

Figure 5.3: (i) CIKP in (top image) stowed/position 5 and (bottom image) position 2. (ii) TWC probe traverse measurement positions looking in the flow direction of the tunnel.

5.2.3.2 Liquid Water Content

Liquid water content was measured using the SEA Multi-Wire Probe. This is a heated probe with 3 different wire diameters. The probe surface was heated to $140°C$. The difference between 'dry' or no-ice, and 'wet' or iced conditions is evaluated to generate

a calibration response between 'dry' and 'wet' conditions. There are 2 sensing wires used within this experimental campaign, of diameter 0.21 inch and 0.83 inch respectively. These are combined to produce an average LWC reading. LWC surveys were conducted over the tunnel face at the mid-height ($\eta = 0.5$) position. An example raw and processed reading is displayed below. Figure 5.4 shows the Ice on period, and the alignment of the probe at the centreline (when Multi-wire X and Y positions are both 0). It is evident from 320 seconds onwards the probe is in the core flow. Figure 5.5 shows the steady ice core survey period and here we can assume the LWC reading corresponds to the steady state response from 350 seconds onwards for this example.

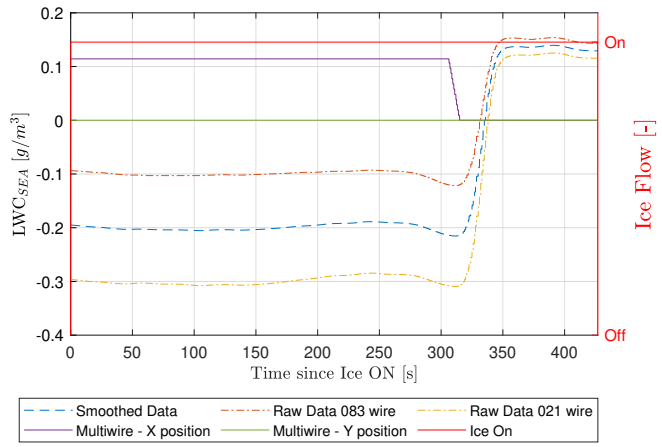

Figure 5.4: Raw experimental measurements from SEA Multi-Wire Probe.

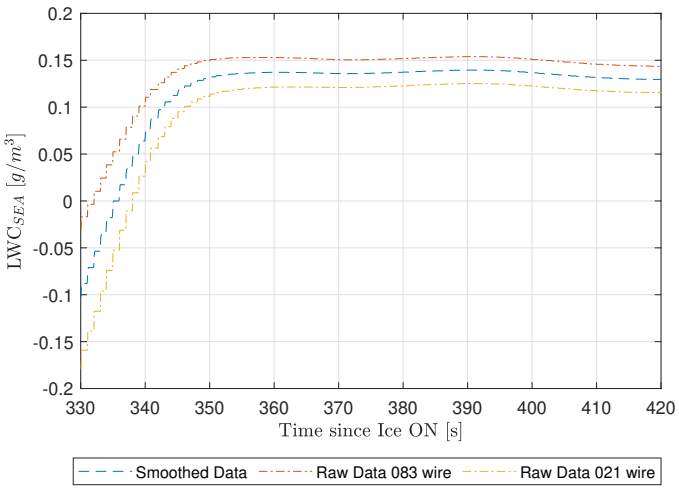

Figure 5.5: Experimental measurements from SEA Multi-Wire Probe during core flow measurement survey. Here the steady conditions achieved after 350 seconds are used to describe the experimental LWC.

5.3 Test Articles

The test geometry used within ICICLE for validation and comparison to experimental data are the stator, and cone cases from test campaigns conducted at RATFac [21, 23, 33].

5.3.1 35° Cone

A simple two-dimensional test case was used to examine the effects of surface roughness on the impact model. A 35° cone test case from the RATFac experiments was used to assess the model. Figure 5.6 shows the cone test article during ice-on conditions throughout the experimental exposure.

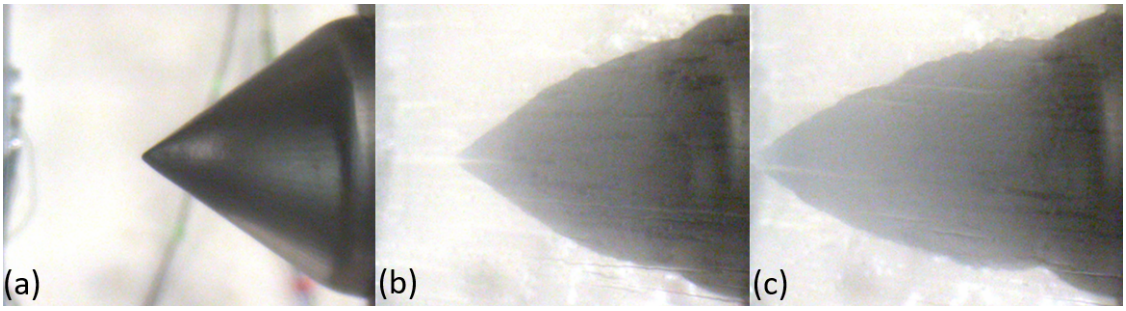

Figure 5.6: Experimental measurements for (a) 0%, (b) 50% and (c) 100% test times for 35° Cone Test Case 737.

5.3.2 Compressor Stator Vane

A prismatic compressor stator vane was used to represent geometry that is at-risk for engine icing. The vane aspect ratio was 2.1. It is built in at one end and has a significant tip gap (equivalent to 23% of the tunnel span). This was in part to aid in shadowgraph measurements since icing at the root/tip would obscure side-on imagery.

The vane was made from a Ti-alloy representative of gas turbine compressor vane materials. Further information on the test campaign is summarised in [21].

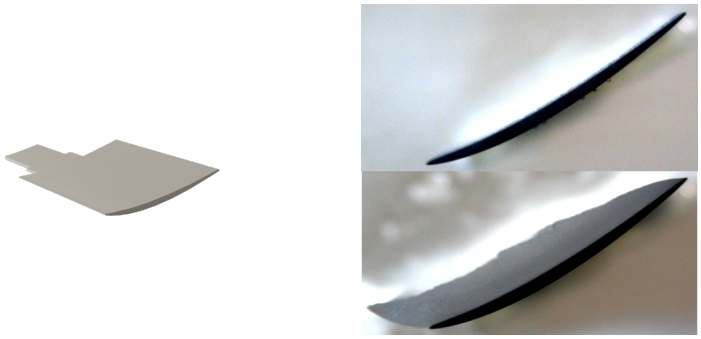

(i) (ii)

Figure 5.7: (i) Representative prismatic compressor stator vane. (ii) Spanwise view of stator tip mounted in RATFac wind tunnel at 0% and 100% icing time for Test Case 854 [21].

5.4 Ice Accretion

5.4.1 2D Accretion Data

Ice accretion thickness data from altitude icing wind tunnel tests present a challenge to data collection. Ice shape and thickness data in two-dimensions is limited by optical access and the shape and symmetrical features of the test body. Axisymmetric, prismatic and 2D symmetric shapes such as cylinders, airfoils and wedges are suited for this method. The shadow graph method is employed by most icing research to extract a temporally resolved ice accretion shape. Figure 5.8 illustrates the shadowgraph extraction technique applied to the stator experiment. This method can be limited where the tunnel has variable melt and mass flux over the test article and may tend to overpredict ice thickness in this case as the shadowgraph will generally capture the largest shape overall and not a mean thickness over the span of the body.

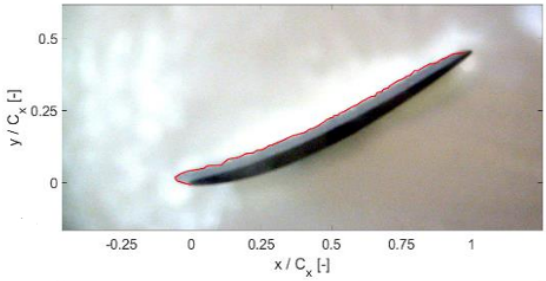

Figure 5.8: Ice Accretion Thickness Shadowgraph Measurement, taken from [21].

5.4.2 3D Accretion Data

The Oxford Thermofluids Institute conducted a series of ICI tests and employed a novel optical measurement technique known as digital image projection (DIP). 3D spatial and temporal data was collected for spanwise distributions of ice accretion by Connolly et al. [33] which provides a basis for validation and identified a bias of ice accretion growth at the root of the blade (including the test window mount). These results are the primary justification for expanding the modelling capability. This will identify the impact of ice growth on the local pressure field and the secondary flows present with the LP compressor resulting from such accretions.

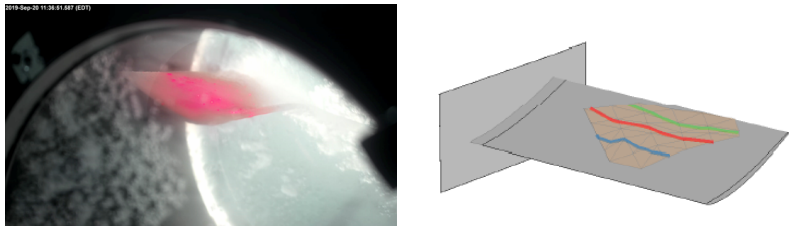

(i) **(ii)**

Figure 5.9: (i)Prismatic stator test piece used for ICI accretion test campaigns and 3D ICI accretion modelling [21]. (ii) Spanwise distribution of ice thickness from DIP imaging [33].

5.5 Test Matrices

The experimental data comprised 3 different specific modes of operation. Sensor calibration summarised in Table 5.2. Here, the conditions relate to the probe survey results for TWC which are used to generate 3D spatial data to validate the particle transport, melting and turbophoresis models. This is evaluated in Chapter 6.

Table 5.2: Calibration Tests: RATFac Test Campaign Data

Run	T_0	T_r	P_0	M_{inf}	RH_0	V_{inf}	P_s	T_s	$D_{v,10}$	$D_{v,50}$	$D_{v,90}$	MR	T_{wb0}	T_{wb}	TWC_{cl}
	$(°C)$	$(°C)$	(kPa)	(-)	$(\%)$	(m/s)	(kPa)	$(°C)$	(μm)	(μm)	(μm)	$(\%)$	$(\%)$	$(°C)$	(g m^{-3})
644	10.0	9.03	34.50	0.40	45	132.8	30.9	1.22	23	43	81	8.26	2.18	-1.38	3.51
647	10.0	9.03	34.50	0.40	45	132.8	30.9	1.22	16	33	58	10.23	2.68	-0.73	3.72
649	10.0	9.03	34.50	0.40	45	132.8	30.9	1.22	22	42	80	9.02	2.54	-0.95	6.21
651	10.0	9.03	34.50	0.40	45	132.8	30.9	1.22	29	52	99	9.84	2.91	-0.60	10.46
653	10.0	9.03	34.50	0.40	45	132.8	30.9	1.22	14	30	53	9.42	2.30	-1.43	7.98
655	10.0	9.03	34.50	0.40	40	132.8	30.9	1.22	15	29	52	8.02	1.58	-2.34	7.88

The cone test matrix is summarised in Table 5.3. The cone test article provides the source of experimental data to evaluate the heat transfer and impingement characteristics of rough wall modelling addressed in Chapter 7.

A representative LP compressor stator geometry was the basis for evaluating complex 3D accretion and substrate heat transfer modelling. The test matrix for this is summarised in Table 5.4. The data was used to evaluate the accretion and substrate conduction models, this is addressed in Chapter 8.

Table 5.3: Cone Test Article: RATFac Test Campaign Data

Run	T_0	T_r	P_0	M_{inf}	RH_0	V_{inf}	P_s	T_s	$D_{v,10}$	$D_{v,50}$	$D_{v,90}$	MR	T_{wb0}	T_{wb0}	TWC_{cl}
	$(°C)$	$(°C)$	(kPa)	(-)	$(\%)$	(m/s)	(kPa)	$(°C)$	(μm)	(μm)	(μm)	$(\%)$	$(°C)$	$(°C)$	(g m^{-3})
667	10	9.03	34.5	0.4	45	132.8	30.9	1.22	23	43	81	9.14	2.61	-0.97	8.13
677	10	9.62	34.5	0.25	45	83.8	30.9	6.50	23	43	81	12.13	2.78	1.41	7.57
737	10	9.03	34.5	0.4	45	132.8	30.9	1.22	16	34	52	10.14	2.64	-0.78	7.65
739	10	9.03	34.5	0.4	65	132.8	30.9	1.22	16	34	52	16.77	5.16	1.61	7.54

Table 5.4: Stator Test Article: RATFac Test Campaign

Run	T_0	T_r	P_0	M_{inf}	RH_0	V_{inf}	P_s	T_s	$D_{v,10}$	$D_{v,50}$	$D_{v,90}$	MR	T_{wb0}	T_{wb}	TWC_{cl}
	$(°C)$	$(°C)$	(kPa)	(-)	$(\%)$	(m/s)	(kPa)	$(°C)$	(μm)	(μm)	(μm)	$(\%)$	$(°C)$	$(°C)$	(g m^{-3})
842	10.1	9.03	35.6	0.4	35	132.8	30.9	1.22	16	34	52	9.14	2.61	-2.66	8.79
854	10.6	9.03	36.3	0.4	36	132.8	30.9	1.22	16	34	52	9.25	2.65	-2.78	3.89
485	10.3	9.12	38.3	0.4	35.8	132.8	30.9	1.22	16	34	52	12.13	1.34	-2.50	7.45
495	11.2	9.03	29.0	0.41	35.8	132.8	30.9	1.22	16	34	52	4.11	1.11	-3.01	4.28

6

Validation of Particle Transport Model Enhancements Against Previous RATFac Experiments

This chapter summarises work relating to modelling ice crystal transport in three-dimensions. The ICICLE code was updated and is then validated within this chapter against experimental measurements. The novel aspects of this chapter include implementation of a turbophoresis and two-way coupling model in three-dimensions for ice crystal icing with a spatial convergence assessment to provide a minimum particle count density to resolve mass and melt transport in three-dimensions. An investigation into the choice of turbulence model was also carried out to inform its impacts on dispersion and melting.

6.1 Overview 110

6.2 Validation Test Case 111

6.3 Numerical Arrangement 111

6.3.1 Continuous Phase Model 111

6.3.2 Mesh Dependency Study 111

6.3.3 Turbulence Modelling 113
6.4 Particle Stream Spatial Convergence 114
6.4.1 Particle Stream Specification 114
6.4.2 Turbophoresis and Stream Convergence 115
6.4.3 Results 116
6.5 Model Assessment 118
6.5.1 Effect of Mach Number 118
6.5.2 Effect of Turbulence Model 120
6.5.3 Effect of Turbophoresis 121
6.5.4 Effect of Particle Shape and Orientation 124
6.6 Combined Transport Model 129
6.6.1 One-Way Coupling 129
6.6.2 Experimental Temperature and Humidity Measurement 132
6.6.3 Two-Way Coupling 133
6.6.4 Validation of Particle Phase Change Simulations 136
6.7 Summary 140

6.1 Overview

The purpose of this chapter is to describe the functionality, implementation and validation of the particle transport features of the ICICLE code. This is most easily achieved with reference to the validation case used, as each element can only be demonstrated in relation a specific geometry and its related boundary conditions. Thus the validation test case and quality of the measured data are first considered. Secondly, the individual gas and particle cloud parameters are assessed with respect to turbulence, Mach number, turbophoresis and particle shape and orientation.

6.2 Validation Test Case

For validation purposes, experiments previously conducted by the University of Oxford in the RATFac altitude icing wind tunnel, defined in Chapter 5, are used to validate the ICICLE 3D particle transport model. These provide measurements for water, ice and gas properties within the working section. The RATFac inlet and mixing section, bellmouth and working section are simulated using a structured mesh CFD case to inform each aspect of the particle transport validation.

6.3 Numerical Arrangement

6.3.1 Continuous Phase Model

Simulations of the continuous phase were generated for ICICLE 3D using ANSYS FLUENT 2021 R2 and ICEM CFD 2021 R2. A structured mesh was employed to improve solution convergence. The symmetric geometry of the wind tunnel facility facilitates this meshing strategy. Turbulence models were assessed in comparison to tunnel turbulence intensity measurements. The Realisable $k-\epsilon$ turbulence model was applied throughout the remainder of the chapter due to its stability and relatively low reduced computational overhead.

The COUPLED pressure velocity scheme was implemented due to the low compressible flow present ($0.25 < Mach < 0.4$). A Second-Order Upwind scheme was employed for discretisation of momentum and energy equations. Solution convergence levels were set to $\leq 10^{-4}$ for both Continuity and Energy equations and $< 10^{-6}$ for all other velocity and turbulence terms. Figure 6.1 illustrates the CFD flow domain used to describe the RATFac inlet.

6.3.2 Mesh Dependency Study

The flowfield solution used as an input to the ICI transport model requires a grid independent solution. The wall cell y^+ value was set to 50, to fall within the log-linear wall region [123]. This is necessary for Realisable $k-\epsilon$ with scalable wall functions. The mesh was refined to assess the solution sensitivity. Mass averaged total properties

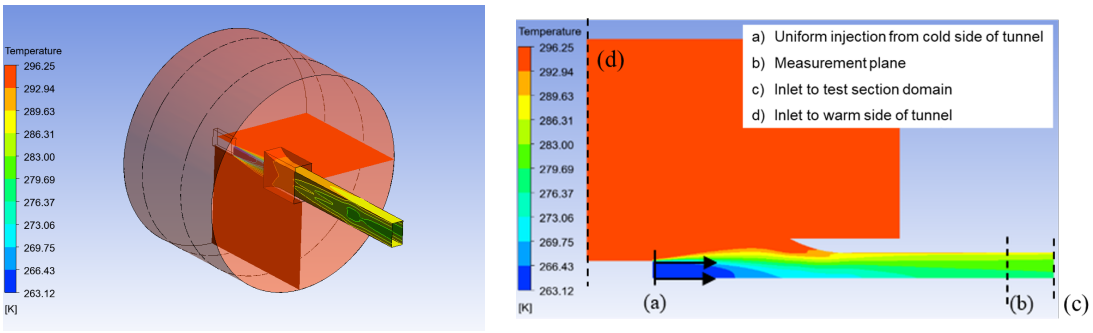

Figure 6.1: (i) Cylindrical section is the plenum with warm humid air, the smaller rectangle is the ice injection pipe. Warm humid air mixes with the cold free jet and contracts into the working section. (ii) RATFac tunnel 1/2 cross-section slice showing tunnel inlet, ice injection pipe and measurement plane locations.

are used which can account for variation in density over the measurement plane. These are the primary properties used to calculate particle slip and melting. A mesh > 4 million cells was fine enough to achieve solution convergence for this case. Figure 6.2 details the results of this study. This is applicable to the RATFac inlet test case but is not sufficient if different Mach number or geometry were used. It is useful to benchmark and assess the validity of the CFD solution from successive mesh refinements.

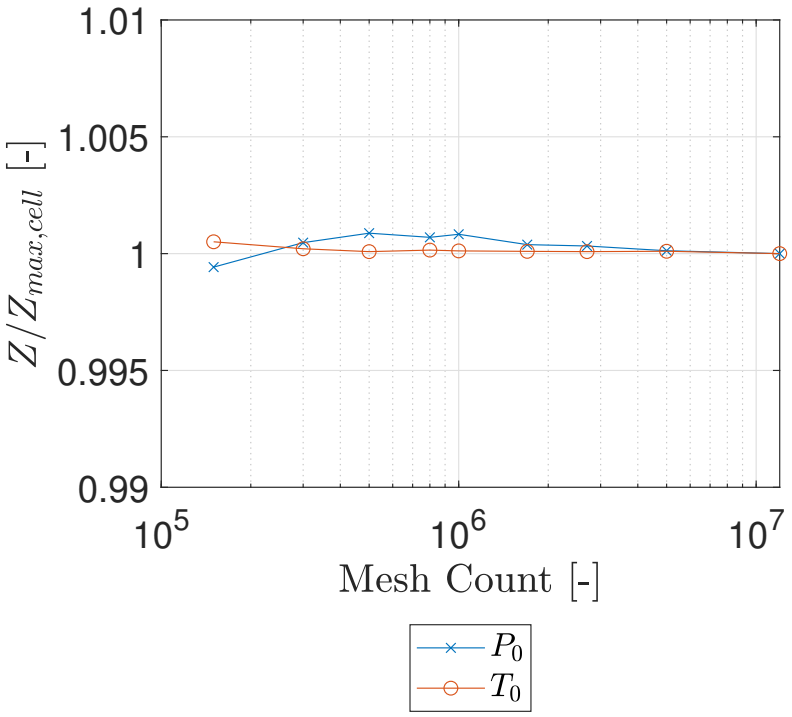

Figure 6.2: Normalised Gas Property vs. Mesh Count, Test Case: Full 3D RATFac Inlet Case.

6.3.3 Turbulence Modelling

Ice particles ingested by turbomachines are influenced by the local energy dissipation and transfer processes within the flow. Turbophoresis describes the force experienced by particles due to velocity fluctuations in the carrier flow. Particles that are small and dense (applicable in ICI) will disperse from regions of higher turbulence intensity to lower turbulence intensity [27, 56, 117]. Turbulent dispersion is a significant driver of melting during ice crystal icing particle transport. Within ICI modelling, RANS modelling can capture steady flow fields, when appropriate turbulence models are applied. Typical of these are eddy-viscosity or Reynolds Stress approaches. The eddy-viscosity approach employs an eddy current analogy to relate velocity gradient and normal Reynolds stresses. The Reynolds stress model directly calculates components of the Reynolds stress tensor. To then model turbophoresis, instantaneous velocity fluctuations must be approximated from RMS velocity fields and the turbulent kinetic energy within an eddy. The Reynolds Stress Model solves turbulent fluctuations in each principal direction and generates an anisotropic turbulent dissipation flux, this accounts for Reynolds shearing stresses.

Measurements of turbulence intensity with respect to the mean velocity were performed at inlet planes of the NRC's RATFac wind tunnel, see [81]. Turbulent kinetic energy production within the wind tunnel is strongly driven by the shear layer which exists between the cold free jet exiting the ice grinder and warmer air in the plenum which becomes entrained in this jet to form the inlet flow. Instantaneous flow velocity measurements of a dry flow using a hot wire anemometer were used to calculate turbulent intensity at different tunnel operating conditions summarised in Table 6.1.

Table 6.1: RATFac Turbulence Intensity Measurements from [81]

Mach	$\mathbf{I_{turb}}$	$\mathbf{L_{turb}}$
(-)	(%)	(m)
0.25	7.75	0.08
0.4	10.40	0.07

6.4 Particle Stream Spatial Convergence

Particle modelling is computationally expensive and requires distributions for particle size, shape, and injection distribution. Furthermore, when flow turbulence is included the carrier gas properties along with two-way mass energy coupling, inherent unsteadiness exists within the flow solution. An efficient assessment of particle stream convergence is therefore required as the number of particle injections required to provide a representative discrete phase is likely to be high. This is achieved by successive refinement of the injections and determination of a convergence parameter. Each control volume contains mass, energy and turbulence statistics governing particle transport. Convergence of results is particularly important in model validation and reporting resulting accretion and erosion results.

This approach to convergence neglects the deposition regime of multi-phase flow. This is important as deposition is further driven by the melting of the particles and the sizing of the surface mesh. This study aims to investigate the sensitivity and accuracy of particle transport models relevant to ice crystal icing. There were two aspects to this approach. First, a particle stream convergence study was conducted for the validation test case. Second, particle mass flux was integrated over the measurement plane position. This generated an area averaged mass flow rate for each cell. This was the method for evaluating the convergence of the model. The simulated TWC is then compared to the experimental measurements at the probe survey locations.

6.4.1 Particle Stream Specification

The injected particle size distributions follow a Rosin-Rammler distribution. The distribution for Test Run 649 is summarised in Table 6.2, used for this convergence study. The distribution is sampled into 26 bins and the mass fraction of particles of each size determined. This is set by the bin sizes within the post processing of particle size distributions at NRC RATFac. The particle size distribution for different grinder settings were generated in prescribed 26 bin distributions with refinement at the smaller diameters ($< 20\mu m$) [53]. The injection positions were uniformly spaced across the inlet for all runs. An injection refinement results in additional injection sites. At each injection site a ‘super

particle' was injected the set of size and shape dependent injections at that point. These were scaled to generate the mass flux of ice at the inlet. The scaling was applied such that the transport model for each particle is not affected. The injection then consisted of:

1. a 26 bin Rosin Rammler size distribution.

2. a 100 stream sampling of the DRW velocity fluctuation magnitude.

Therefore, 2600 injections at each seed location were needed to fully represent the size distribution and stochastic velocity fluctuations within the DRW model. Figure 6.3 shows the injection count and particle total water content for the convergence study case. These results represent the RATFac shadowgraph measurements for the smallest grinder setting. These were used to evaluate the particle cloud representation and discretisation. Specifically, the experimental bin count N_{bins} and the discretisation of the DRW velocity fluctuations, N_{DRW}, was held fixed and run for successive injections to evaluate the model stochastic properties. N_{DRW} was set to 100 at all turbophoretic runs to discretise the turbulent velocity fluctuations.

Table 6.2: Particle Size Distribution Statistics for Convergence Study

Mach	$\mathbf{P_0}$	$\mathbf{T_0}$	$\mathbf{RH_0}$	$\mathbf{D_{min}}$	$\mathbf{D_{max}}$	$\mathbf{D_m}$	**n**	$\mathbf{N_{bins}}$	$\mathbf{N_{DRW}}$	$\mathbf{TWC_{cl}}$
(-)	(kPa)	(K)	(%)	(μm)	(μm)	(μm)	(-)	(-)	(-)	(gm^{-3})
0.4	34.5	283	0.45	2	162	53.1	2.09	26	100	6.21

6.4.2 Turbophoresis and Stream Convergence

The turbophoresis model generates a stochastic particle velocity fluctuation. 50 simulations at each chosen spatial injection density were performed to assess the variation associated with the random choice of instantaneous fluctuating velocity, which is approximately Gaussianly distributed. To assess convergence the total water content was integrated across the plane where TWC is measured. TWC within each control volume was calculated by summing particle mass and scaling it by the cell normal area $A_{n,k}$ and gas velocity $U_{g,k}$. This then provided a pointwise TWC value. Here the TWC was

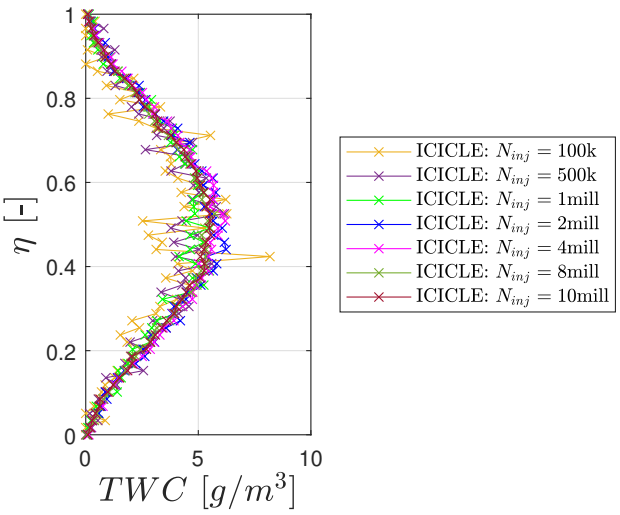

Figure 6.3: Predicted Total Water Content distribution at tunnel CIKP measurement plane with changing particle injection counts. Experimental reading for TWC at Test 649 is 6.21gm^{-}3.

mass averaged over the tunnel measurement plane by dividing it by the cell density and summing over the tunnel face to generate an overall concentration χ.

$$TWC_k = \frac{\sum_1^{N_p}(m_p \lambda_{p,mass})}{U_{g,k} A_{n,k}} \tag{6.1}$$

$$\chi = \sum_1^k \frac{TWC_k}{\rho_{g,k}} \tag{6.2}$$

In Figure 6.4, the concentration normalised by the concentration at the highest spatial injection density is shown. The error bars on the distribution show the standard deviation between individual injection events at each injection spatial density. Where $N_i > 6 \times 10^6$ the change in variance appears insignificant.

6.4.3 Results

Figure 6.5 shows the mean absolute difference for each particle concentration, where a MAD of $< 1\%$ is proposed as a convergence criterion. This useful metric can be applied while conducting simulations to avoid unnecessary calculations. The MAD limit may appear high compared to typical convergence criteria, but floor in the value is determined partially by the stochastic RMS velocity fluctuations in the DRW model, the number of samples chosen to discretise these fluctuations and computational resources.

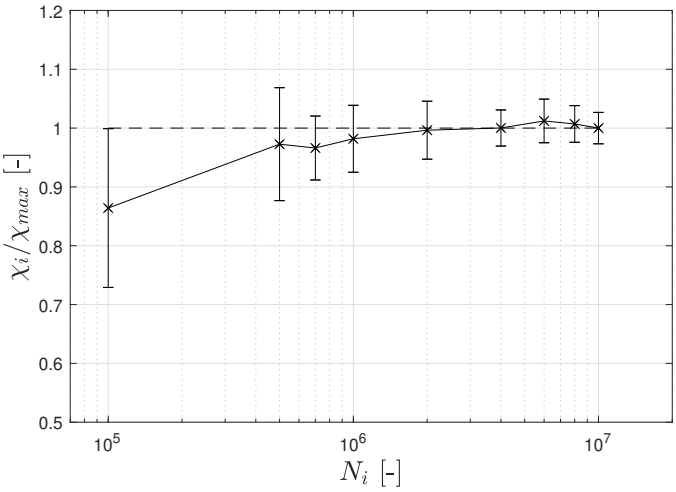

Figure 6.4: Particle Concentration χ_i per Injection Count N_i normalised by maximum (χ_i)for Convergence study with Turbophoresis and Rosin Rammler Size Distribution. Test Case: Full 3D RATFac Inlet Case.

Clearly a large number of injections are required, highlighting the well known drawback of deterministic Lagrangian particle tracking approaches, where computational resources must be balanced against the modelling uncertainty achieved. Further sensitivity analysis can be used to further balance the number of injection locations vs the number of samples of the instantaneous velocity field. This is likely to be strongly tunnel and test article geometry dependent. For the RATFac tunnel system, an injection density of $N_i = 2 \times 10^6$ was chosen for remaining numerical experiments within this thesis. This balanced the computational resources available with the time to conduct each test run.

It should be noted that there is further room for investigation of the sensitivity of convergence to the turbophoretic DRW model, with a similar number of successive refinements in particle number. For example, turbophoresis generates a higher melting in particles due to additional energy from velocity fluctuations. Within the convergence study, fully evaporated particles are not calculated in the concentration term. This leaves a discrepancy which may only be quantified by adding a corrective integral term for evaporated mass.

The simulated result was generated by integrating particle mass over the tunnel height at the centreline position. These were normalised by the finest injection count result. This corresponded to a particle injection density of 1.12×10^9 injections $/\,\mathrm{m}^2$. Figure 6.5 shows the successive particle injection densities. It was appropriate to assume that

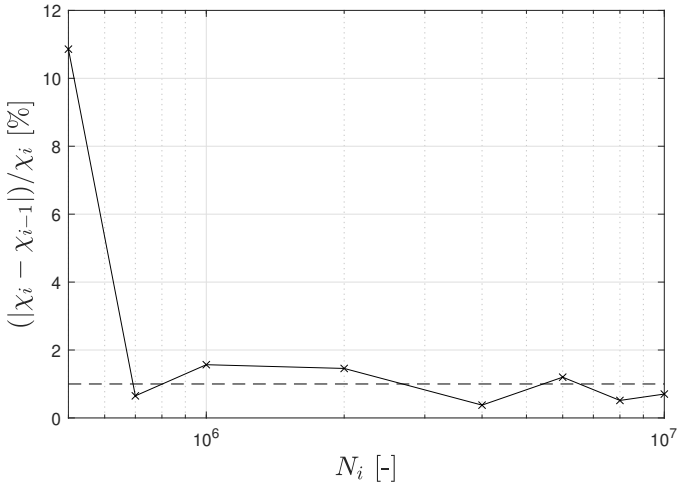

Figure 6.5: Mean Absolute Difference in Particle Concentration χ_i per Injection Count N_i for Convergence study, normalised by maximum injection count. Test Case: Full 3D RATFac Inlet Case.

above 2 million injections in this case sufficiently describes particle cloud characteristics relative to experimental conditions. This must be repeated for each geometry and mass flow setting but is a benchmark of the number of particles required to model particle mass distribution sufficiently.

6.5 Model Assessment

The model specified above and in Chapter 3 was employed to simulate experimental ICI conditions from the NRC RATFac test campaigns conducted by the University of Oxford. Additional experimental results and particle cloud conditions are summarised in App A. Changing inlet boundary conditions highlights their effect on the particle transport and melting.

6.5.1 Effect of Mach Number

The carrier gas Mach number at a fixed inlet ice mass flow rate was investigated. The results from this study are shown in Figure 6.6. The conditions chosen were those of Test Run 677 (Mach 0.25) and Test Run 667 (Mach 0.4) see Table 6.3. In both test runs, the PSD was the baseline condition as specified in Table 6.2. This was to match the PSD

and TWC nominal set points, and allowed the difference in mass diffusion and melting response due to variation in carrier gas Mach number to be assessed.

Table 6.3: Mach Number Study: Gas Properties

Run	**Mach**	$\mathbf{P_0}$	$\mathbf{T_0}$	$\mathbf{T_s}$	$\mathbf{T_{wb0}}$	$\mathbf{RH_0}$	$\mathbf{U_\infty}$	**TWC**
	(-)	(kPa)	(K)	(K)	(K)	(%)	(m/s)	(g/m^3)
677	0.25	34.5	283	279.2	275.93	0.45	83	7.57
667	0.4	34.5	283	274.5	275.75	0.45	132	8.13

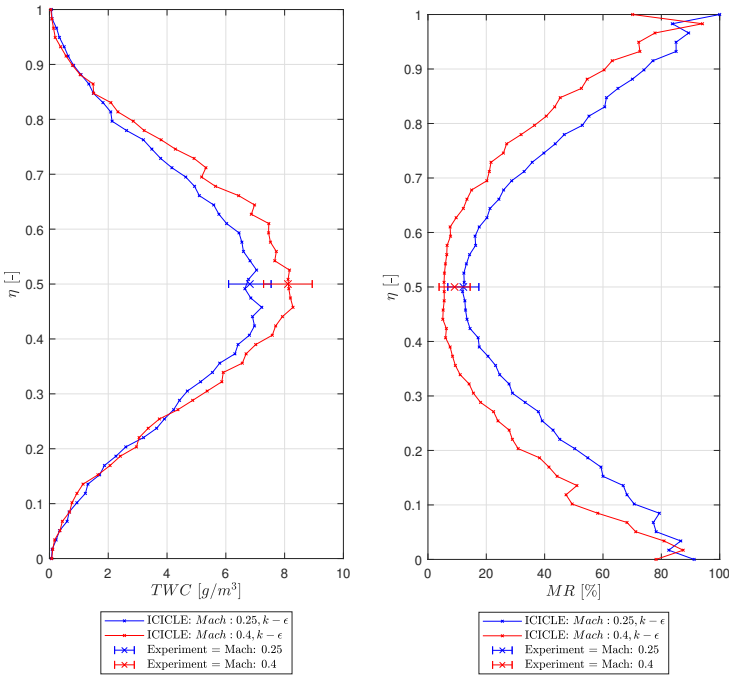

Figure 6.6: Mach Number study: (i) Total Water Content and (ii) Melt Ratio simulation results at probe measurement position.

It is evident that a lower Mach number produces a higher rate of melting for the same total pressure and temperature conditions. This is due to the reduced evaporative cooling energy recovery at lower Mach number. As a result, the static temperature is higher to achieve the same total temperature. This generates a higher rate of melting. This is important in considerations for turbofan compressor stage icing where static gas temperatures can vary over stages and across thrust settings. It is important to note that the stagnation wet bulb temperatures are equivalent at each Mach number, which is

used to approximate accretion onset and severity within literature. However, the static temperature of the flow at Mach 0.25 is higher which results in a higher Melt Ratio of the particle cloud. This is important as stagnation wet bulb temperature does not explicitly define accretion magnitude (although it is closely analogous to Melt Ratio). This is important as turbomachinery sensors within the compressor are limited and a wall temperature measurement which will be moderated by the stagnation / recovery wet bulb temperature may be insufficient to identify icing conditions.

6.5.2 Effect of Turbulence Model

An assessment was carried out between the Realisable $k-\epsilon$, $k-\omega$ and Reynolds Stress turbulence models for Test Run 667 conditions. Figures 6.7, 6.8 and 6.9 show the turbulence intensity through the contraction and bell-mouth into the working section of the RATFac tunnel. The Reynolds Stress model appears to represent the shearing and mixing between the hot and cold gases more effectively. This may be due to the strongly anisotropic nature of the turbulent structures shown in the contour plots which cannot be captured by the eddy-viscosity models. The lensing effect caused by the flow acceleration and contraction creates a turbulence intensity peak at the centre-line. The Realisable $k-\epsilon$ and $k-\omega$ models show 2 nodal peaks offset from the centre which seem non-physical. While this is particularly pronounced for this experimental test case, anisotropic Reynolds stresses are always present close to passage walls. From the simulations The Reynolds Stress Model predicts 15% greater I_{turb} at the tunnel centre-line, than the Realisable $k-\epsilon$ model. At $I_{turb} = 5.8\%$ is still considerably less than that measured in the experiment, $I_{turb,exp} = 10.4\%$.

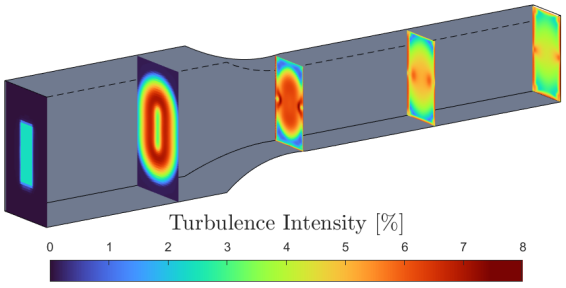

Figure 6.7: Turbulence Intensity RATFac Realisable $k-\epsilon$ Model

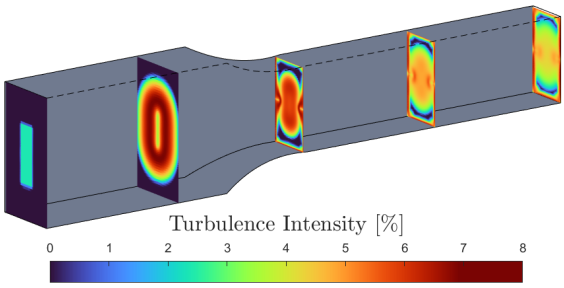

Figure 6.8: Turbulence Intensity RATFac $k-\omega$ SST model

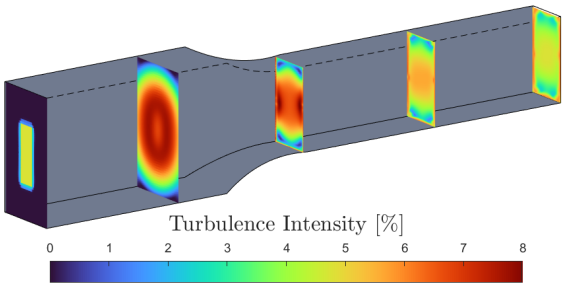

Figure 6.9: Turbulence Intensity RATFac Reynolds Stress Model

The effect of the chosen turbulence model on particle transport was also investigated. The results, shown in Fig. 6.10, show differing best agreement depending on whether TWC or MR is considered. The peak value of TWC is well predicted by the Realisable $k-\epsilon$ model, however, the Reynolds Stress turbulence model captures the melting behaviour better (accepting that there is only a single measurement position available for comparison for each point). The $k-\omega$ SST appears to predict a similar melting response to the Realisable $k-\epsilon$, but performs the poorest for predicting TWC. The Reynolds stress model appears to capture turbulent dispersion better and later plots show better agreement with measured data close to the tunnel walls. As melt ratio is a key driver of sticking probability and thus accretion, this suggests that the RSM approach is needed for accurate ICI transport modelling.

6.5.3 Effect of Turbophoresis

The inclusion of the turbophoresis model was necessary due to the volume fraction of ice and water within the flow. Additionally, in highly turbulent conditions, where $I_{turb} > 5\%$, it is important to capture the energy exchange between the gas and particles correctly. One case is presented with and without turbophoretic effects included, this is for the one-way

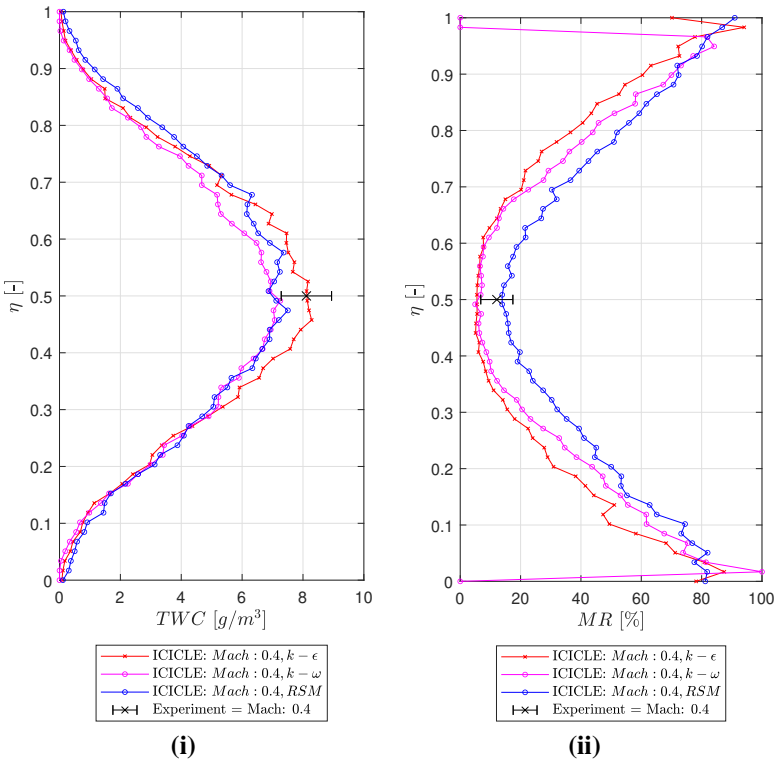

Figure 6.10: Turbulence model comparison: (i) Total Water Content and (ii) Melt Ratio simulation results at probe measurement position, Test Run 667.

coupled particle transport model. Test Case 649 is used to generate the conditions for this study. Figure 6.11 shows the total water content and Melt Ratio responses when considering turbophoresis. It is clear that the centreline value for TWC is poorly matched for the No turbophoresis simulation, the excess concentration at the centreline suggests the current state of the art approach to modelling ice crystal icing transport is insufficient. The TWC curves should match or sum to the equivalent volume, however, experimental TWC measurements describe liquid and solid water phases. Background vapour content is subtracted from the measurement. Consideration of the change in vapour fraction due to turbophoresis has not been evaluated. Additionally, since the only forces present on the particles are lift and drag, non-turbophoretic particle transport appears to produce poor matching with experimental measurements. No ice mass is present at the wall, despite ice and water being observed running along the tunnel walls. Additionally, Figure 6.11(ii) shows a lack of melting near the centreline ($0.4 < \eta < 0.6$), due to the lower gas temperature at this location. Therefore, most melting appears to occur at the inlet

mixing and contraction sections of the wind tunnel for simple drag driven ice crystal transport. Turbophoresis generates on overall melting increase due to additional kinetic energy imparted on the particles.

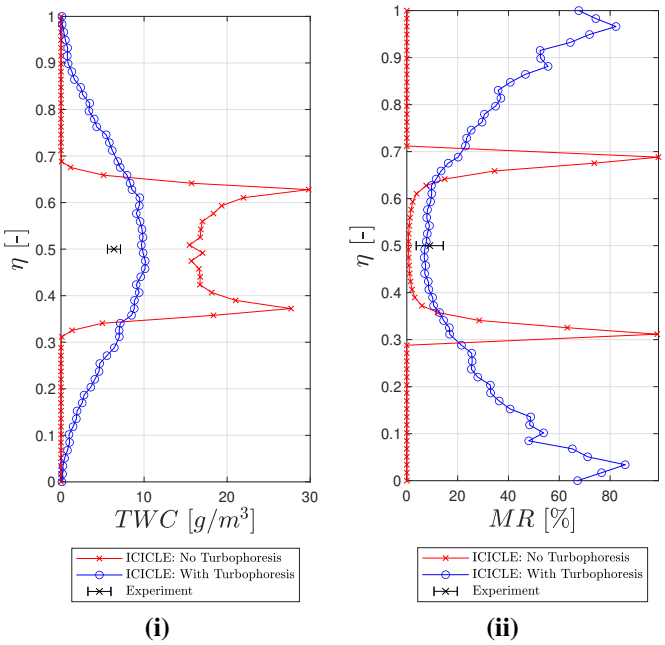

Figure 6.11: Turbophoresis model comparison: (i) Total Water Content and (ii) Melt Ratio simulation results at probe measurement position, Test Run 649. One-way coupling.

Figure 6.12 shows the test data by connecting the traverse measurement locations through the centreline to visualise a slice through the centre-line diagonally. Here the inclusion of the turbophoretic force is most noticeable compared to experimental measurements for TWC. There is no mass close to the wall in the 'No turbophoresis' simulations since the particles are transported as ballistic spheroids. This highlights the need to model turbophoretic effects even in larger mass particles, due to the turbulent kinetic energy in the flow being significant in mass dispersion. Further, this has a significant effect on the melting response of the particles, the centre-line Melt Ratio is close to 0%. This is because particles are not mixed or excited sufficiently by the energetic flow. In turbomachinery, the gas path is highly turbulent with flow turning, wake interaction and flow acceleration / deceleration. These results highlight the importance of considering the entire system and the complexity when modelling Euler-Lagrangian particle tracking and phase change for ice crystal icing.

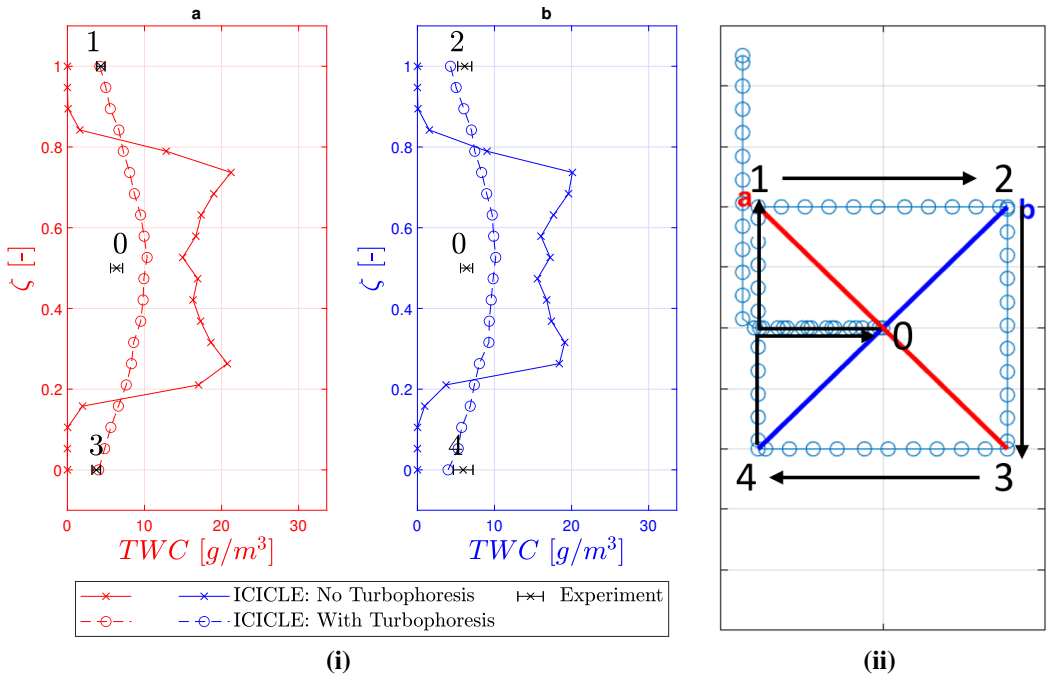

Figure 6.12: (i) Comparison of No Turbophoresis and With Turbophoresis simulation results for Test 649. (ii) TWC probe traverse measurement positions. Blue and red lines in (i) represent a slice through measurement positions.

6.5.4 Effect of Particle Shape and Orientation

This study investigated melting and dispersion effects from particle shape (aspect ratio) and orientation. It can be shown that drag forces quickly diminish particle rotation in real flows and rotation is only significant immediately after impact: thus it is neglected here. Particle shape influences the Stokes number and sphericity or surface area to volume ratio. Particle aspect ratio for spheroid shapes with respect to the principal axes is described in Section 2.2.3 Equations 2.6 - 2.9. Oblate or prolate spheroid shapes can be simply described by a diameter D_p and aspect ratio E due to their axisymmetry.

Investigation of particle shape and orientation was conducted within this study. Oblate and Prolate spheroids were injected with an Aspect Ratio (E) which was varied from 0.1 to 10 to represent disk, spheres and columnar shapes. Broad-wise and end-on orientations were also assessed to evaluate the melting and transport implications due to particle orientation. This corresponds to an A.o.A of $0°$ and $90°$ with respect to the principal axis.

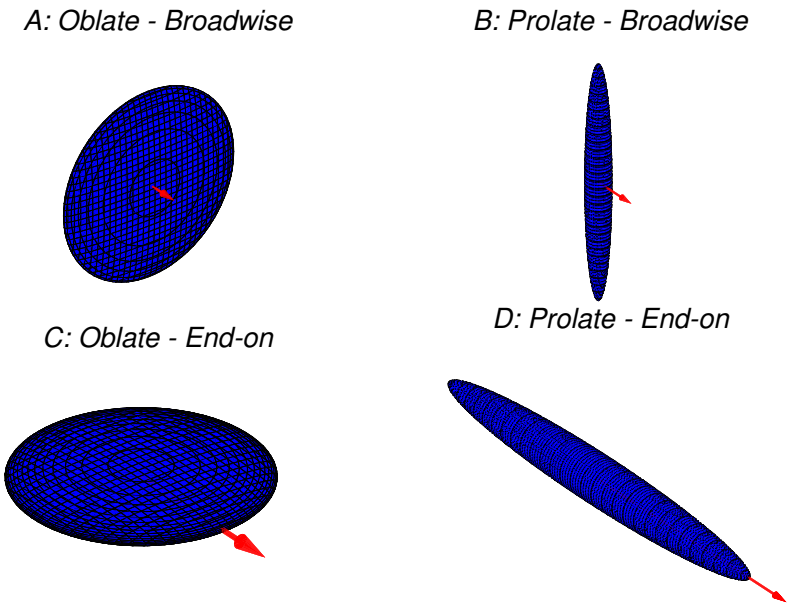

Figure 6.13: Particle Shapes approximated as Oblate and Prolate spheroid shapes. Particle orientation within the study is specified by broad-wise and end-on configurations.

The particle Nusselt number is moderated by sphericity (ϕ) this is calculated using the non-spherical Nusselt relation from Villedieu et al. [148].

6.5.4.1 Effect of Shape

Figure 6.14(i) shows the inverse of particle sphericity $1/\phi$ plotted versus Aspect Ratio E. For the same change in aspect ratio prolate spheroids have higher sphericity compared to oblate spheroids ($\phi \to 0$ at $E = 0, \infty$). Prolate spheroids tend to a line, while oblate spheroids approach a circle of infinite radius: both of infinite surface area. Figure 6.14(ii) shows the melting augmentation due to particle sphericity, where higher E values produce more melting. Oblate or disk-shaped particles have a higher surface area at equivalent conjugate aspect ratio values. This is important in the initial melting response time as particles melt and approach a spherical (fully melted) shape. This response is more significant at inlet or real particle cloud conditions before significant milling, centrifuging,, and break-up when encountering turbomachinery.

Figure 6.15 shows the effects of the Nusselt number due to sphericity. Higher Aspect Ratio particles have a lower Nusselt number compared to spherical particles. This is due to the formulation of the lumped capacitance melting regime, detailed in Section 3.3.6 Equation 3.32, where:

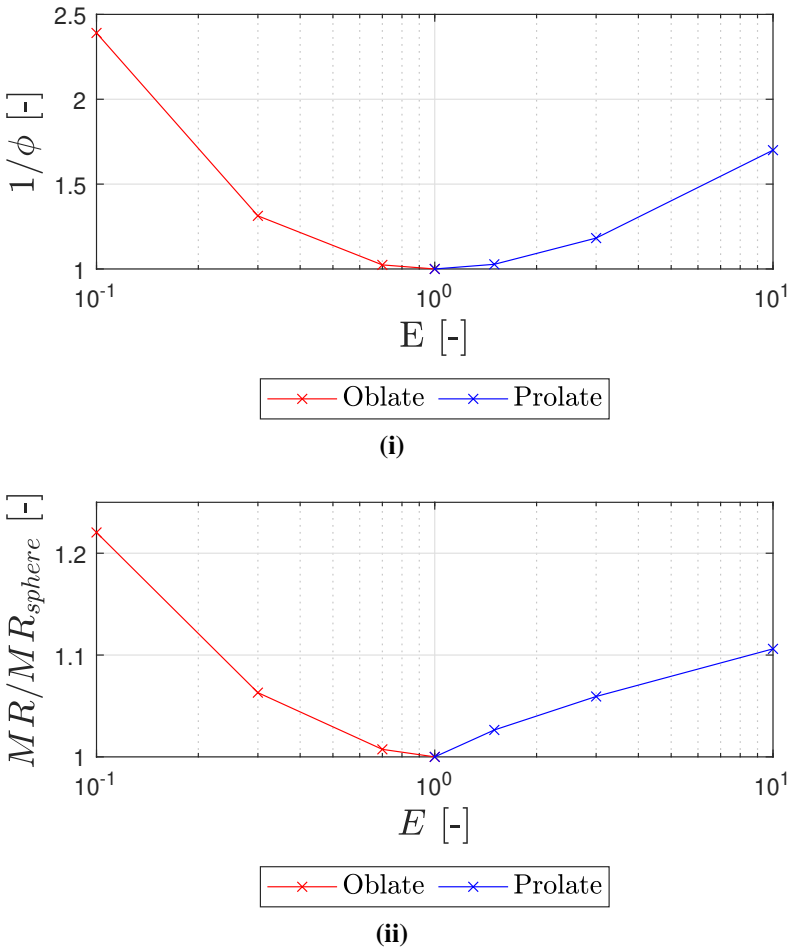

Figure 6.14: (i) Particle aspect ratio E vs 1/Particle Sphericity (ii) Particle Melting Ratio normalised by spherical particle Melt Ratio vs aspect ratio E. Oblate particles ($E << 1$) produces a higher melting augmentation driven primarily by higher surface area.

$$\dot{m}_{melt} \propto \frac{1}{\phi} Nu(\phi) \tag{6.3}$$

6.5.4.2 Effect of Orientation

Figure 6.16 details the aspect ratio and orientation study results. Broadwise orientation produces up to a 5% melting augmentation compared to end-on. Broadwise particles have a longer residence time due to the elevated drag coefficient. This means that although particle drag is effectively modelled according to orientation, melting is only addressed as a bulk sphericity. This highlights a future need to correct melting models to account for orientation as heat transfer is modelled by overall sphericity. Lumped

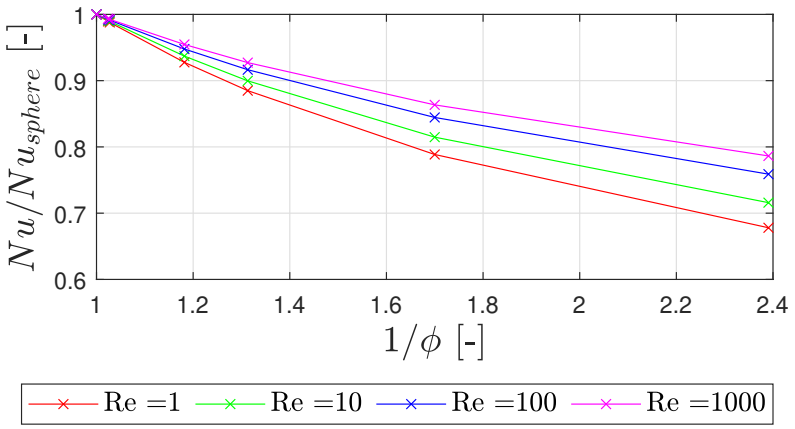

Figure 6.15: Particle Nusselt number vs 1 / particle sphericity, normalised by the Nusselt number of a spherical particle. Plotted for a range of Re values.

capacitance approaches also neglect windward-dominated heat transfer at the particle leading edge (rear side).

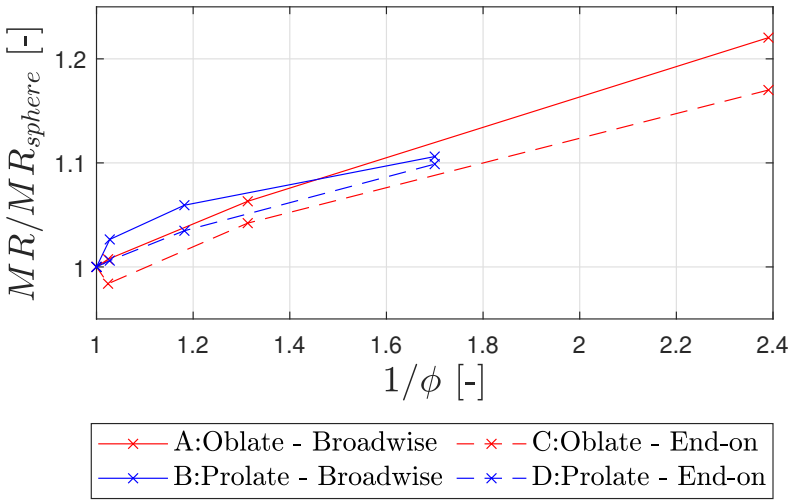

Figure 6.16: Bulk mean Melt Ratio normalised by spherical particle Melt Ratio vs 1/ particle sphericity

Particle rotation is fairly insensitive to gas conditions and only dominates at impact. Particles become increasingly spherical with increasing particle melt, and are spherical when fully molten. Particle heat transfer is modelled using a lumped capacitance approach. This assumed that particle Biot number or the ratio of convection to conduction is low. Effectively, conduction dominates heat transfer and there is little transient response. Biot number is defined in terms of convective heat transfer coefficient H, characteristic dimension L_p and thermal conductivity of the particle k_p,

$$Bi = \frac{HL_p}{k_p} \tag{6.4}$$

where heat transfer coefficient H is defined by Nusselt number Nu_p, thermal conductivity of the gas k_g, and L_p,

$$H = \frac{Nu_p k_g}{L_p} \tag{6.5}$$

substituting Equation 6.5 in to 6.4,

$$Bi = Nu_p \frac{k_g}{k_p} \tag{6.6}$$

The particle Nusselt number is calculated as follows, assuming a value of Re between [1,1000], and a sphericity, ϕ between [0.1, 1]. The conductivity of air, water and ice are 0.026 and 0.54 and 2.2 W m^{-1} K^{-1} respectively. Therefore, Nusselt number for these values, varies between [9.43, 17.6]. Ice particle Nusselt number from Villedieu et al. [148] is defined in terms of Reynolds number, Prandtl number and particle sphericity ϕ.

$$Nu_p = 2\sqrt{\phi} + 0.552 Re_p^{\frac{1}{2}} Pr_p^{\frac{1}{3}} \phi_p^{\frac{1}{4}} \tag{6.7}$$

It is reasonable to assume that the Nusselt number is between 9.43 and 17.6 for the following calculations; therefore, a mean value of 13.52 is adopted. Assuming there is no porosity in the ice particle, the Biot number is as follows.

For solid ice:

$$Bi_{ice} = 13.52 \frac{0.026}{2.2} = 0.159 \tag{6.8}$$

Assuming 50% Melt Ratio for water and ice:

$$Bi_{water+ice} = 13.52 \frac{0.026}{0.5 \cdot (0.54 + 2.2)} = 0.257 \tag{6.9}$$

Assuming fully glaciated 20% porosity for ice and air:

$$Bi_{water+ice+air} = 13.52 \frac{0.026}{(0.2 \cdot 0.026 + 0.8 \cdot 0.54)} = 0.804 \tag{6.10}$$

The lumped capacitance assumption may not appropriate for mixed-phase and porous ice particles as the Bi number approaches 1 for mixed-phase, porous ice particles. The distribution in temperature and the effects on convective heat transfer are not addressed in this model. Assuming the ice particle body is isothermal will mean that melting rates will not vary with particle size; this is incorrect, since larger particles are more porous and agglomerated. This suggests the need to correct for larger particles spatial melting behaviour. The findings within this chapter will be offset due to larger particles inaccurate melting description.

6.6 Combined Transport Model

Using the model specifications addressed previously within this chapter, it was necessary to assess the particle transport model and investigate the necessity of two-way coupling when representing ice crystal icing conditions. Below, an assessment of one-way and two-way coupling with respect to ice particle cloud properties is summarised.

6.6.1 One-Way Coupling

Simulations of particle melting and mass diffusion were performed under the convergent injection conditions discussed above. Calibration test cases 644, 649 and 651 from University of Oxford's 2017 RATFac test campaign were used to compare area resolved TWC results against ICICLE 3D simulations. Figure 6.18 shows the TWC results from the TR649 test case with overlaid traverse TWC probe measurement data. As mentioned above, the probe measurements taken after traversing the passage (as opposed to traversing along the wall) appear to be unreliable. These are included in the comparison plots, but have been enclosed by a grey box in each case. Here, the most notable feature of the data is that the TWC is strongly biased towards the passage centreline and under-predicted at the passage walls. The physical drivers are discussed in the two-way coupling discussion. The different differences in the tunnel measurement values are highlighted in Figure 6.17, where the diagonal edges connecting each traverse position have been imposed. The red data set provides more reliable data, again suggesting a long thermal transient affecting the measurement probes.

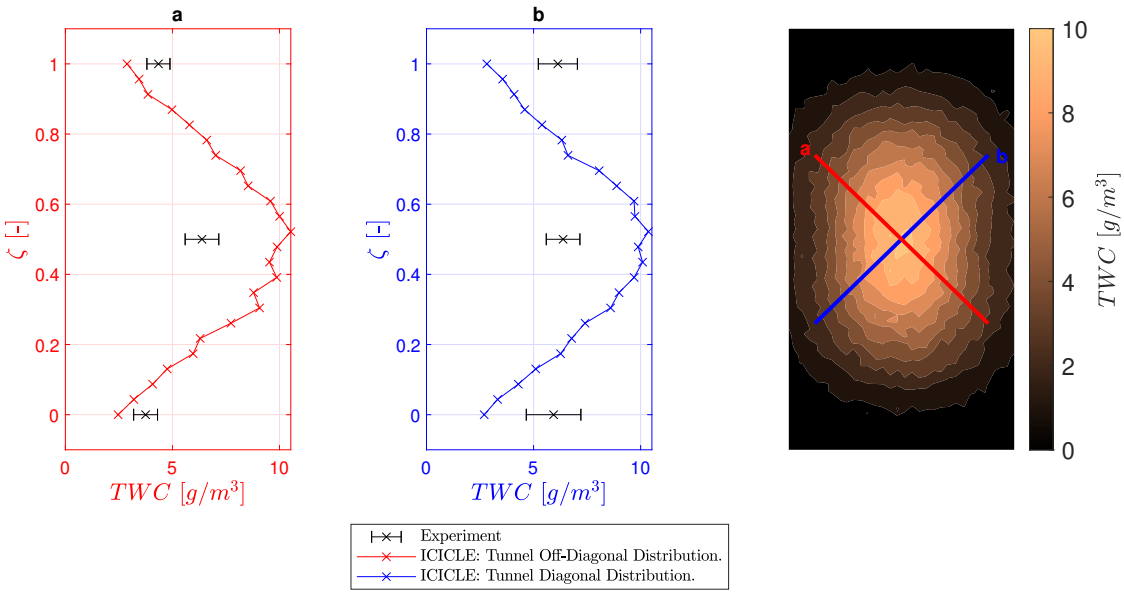

Figure 6.17: Comparison of diagonal extent simulation results against experiment for Test 649. The TWC contour plot in Fig. 6.24 shows the diagonal extents connecting traverse measurement positions.

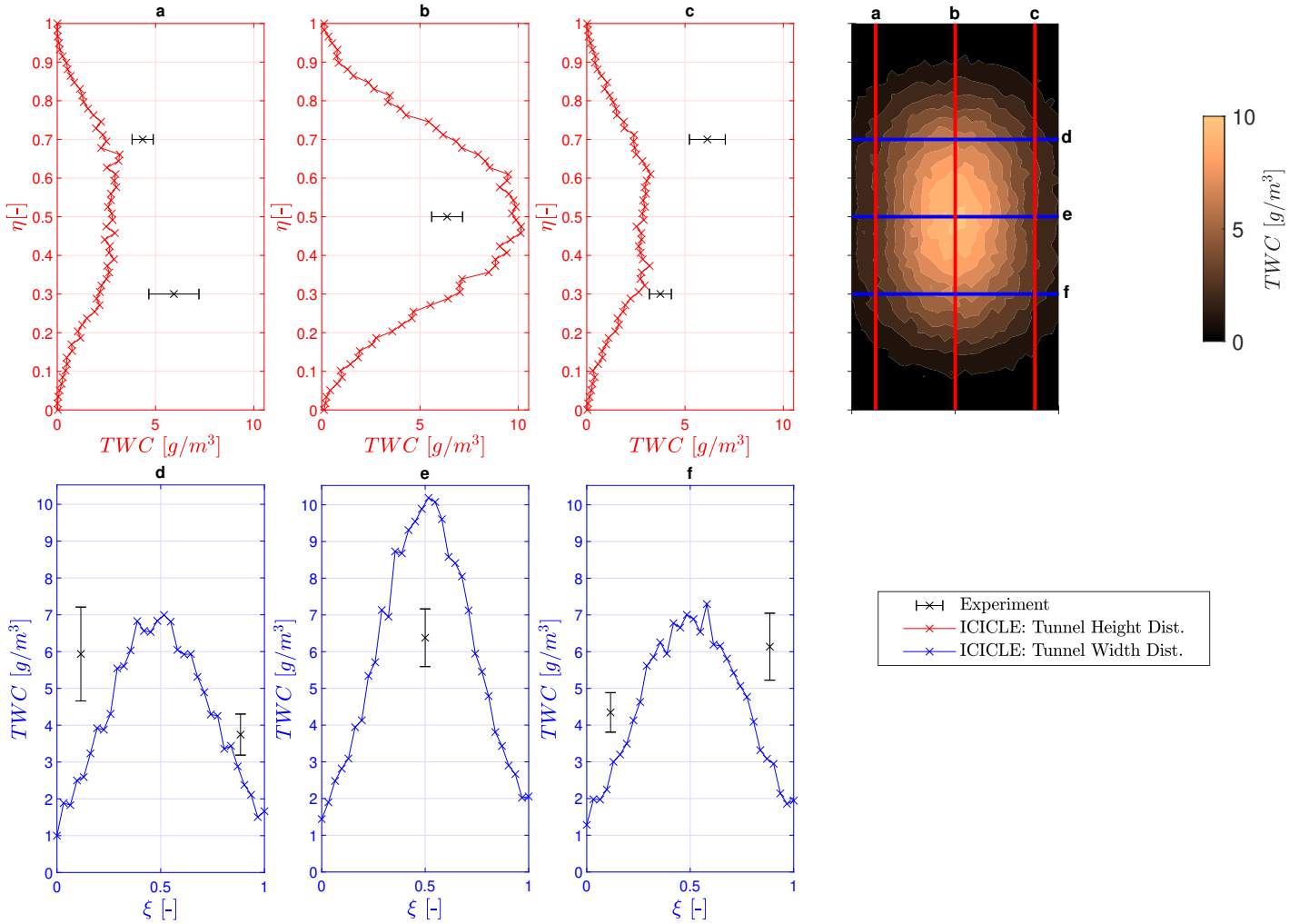

Figure 6.18: One-Way Coupling Simulation results for Test Run 649, for TWC, including vertical and horizontal slices at CIKP probe traverse measurement positions.

6.6.2 Experimental Temperature and Humidity Measurement

Interaction between the particle and continuous phases is important given the relative volume fractions of ice to humid air. Modelling mass, momentum, and energy exchange is generated by a source term approach modifying the local gas properties due to particle phase change and sensible heating. Within this body of work, momentum exchange is neglected due to the density of air relative to ice.

The only mechanism of mass exchange between particle and carrier gas is evaporation/sublimation. This in turn modifies the vapour mass fraction, which increases the relative humidity and decreases the evaporative cooling potential. In addition, ice particles significantly cool the carrier gas, a phenomenon that is used to effectively measure icing conditions in experimental facilities and within turbofan compressors. As the gas temperature drops, this lowers the saturation pressure which further limits evaporative cooling capacity of the gas on the ice crystals. This will generate a higher melting rate for particles.

Within the experimental campaign, total temperature and RH was measured with the TAT-RH probe designed by Gas Turbine Laboratory at the National Research Council (NRC) in Canada. This is a rearward facing probe which measures T_0 and RH during ice on conditions.

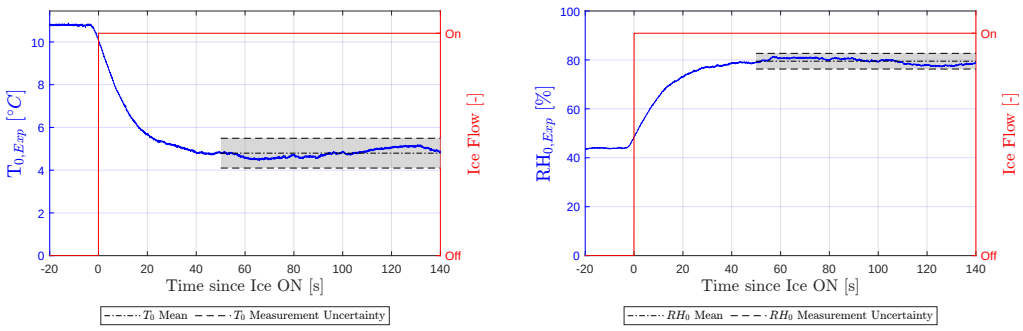

(i) **(ii)**

Figure 6.19: Experimental readings for (i) Total Air Temperature and (ii) Recovery Relative Humidity measured by TAT-RH probe during Ice-on conditions. Test Run 651.

Uncertainty quantification was performed for the TAT and RH_0 readings. There is a bias uncertainty within the energy balance comparison conducted by NRCC which

assessed that there is a measurement bias of $\pm 0.5°C$ and $\pm 2\% SH$. Further the tunnel reaches steady state conditions following ice-on after 50-60seconds [81]. The steady state response to ice on conditions is fixed at 50 seconds ice on time. The population mean and standard deviation for the probe measurements were calculated in each case at a 95% confidence interval. These uncertainties were propagated to generate a combined measurement and temporal uncertainty magnitude. These are shown in Figure 6.19.

6.6.3 Two-Way Coupling

Source terms are linearly distributed through the domain extent and scaled by an under-relaxation factor α for each term. To assess solution stability and convergence. α values of 1.0 and 0.7 were set for each simulation run. It is evident that while the temperature is more quickly matched with $\alpha = 1$ the relative humidity converges after 20 iterations for both values considered. Enthalpy exchanged with the gas phase is as follows.

$$\dot{m}_g \Delta h_g = \sum_{1}^{N_p} (q_{p,i} + q_{p,w} + q_{p,mp}) \Delta t \tag{6.11}$$

Mass exchange between ice particles and the gas is modelled as follows.

$$\Delta \omega_g = \frac{1}{\dot{m}_g} \sum_{1}^{N_p} (\dot{m}_{evap}) \Delta t \tag{6.12}$$

Figure 6.20 shows the effect of implementing two way mass-energy coupling between the continuous and distributed phases on total temperature T_0 and total relative humidity RH_0. The conditions are nominally the same as in Figure 6.19. The two-way coupling approach employs a quasi-steady, domain source term interpolation from the measurement plane position. Here it can be seen that the steady temperature response curve from the two-way coupling study converges to $\sim 6°C$ in each case above 20 iterations. (Each iteration represents $\sim 1s$.) The faster response of the simulation compared to the experimental results is expected as the thermal mass of the probe is not considered, nor any transient in other flow conditions. There is a clear bias error when the mean total temperature is compared to the experiment of $\sim 1.1°C$ above the mean total temperature steady response region. The origin of this error is unknown. Calculation of the mass and enthalpy source terms was conducted as described below.

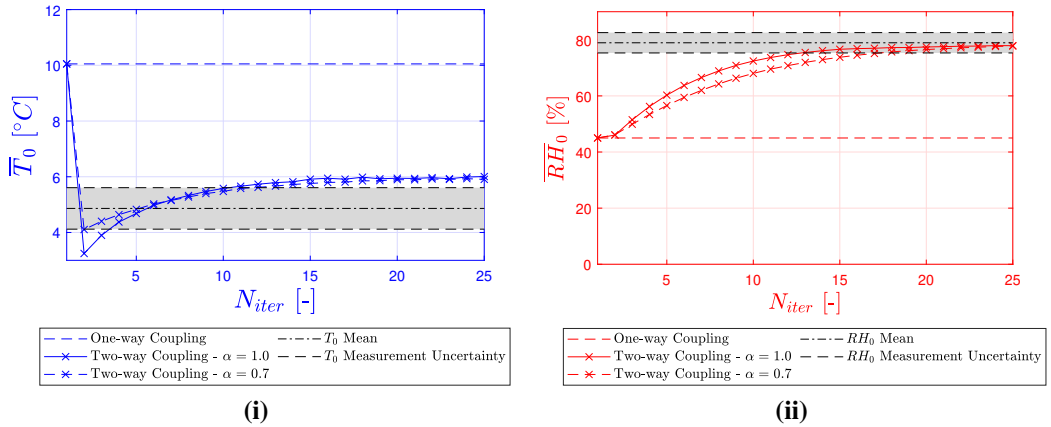

(i) **(ii)**

Figure 6.20: (i) Mean total temperature and (ii) Mean total relative humidity, at TAT-RH Probe plane compared to experimental results. Test Case 651.

Figure 6.20(ii) details the RH_0 results from the same probe and test run. Here the same RATFac uncertainty quantification from [81] is used along with assessing the mean and standard deviation over the test time.

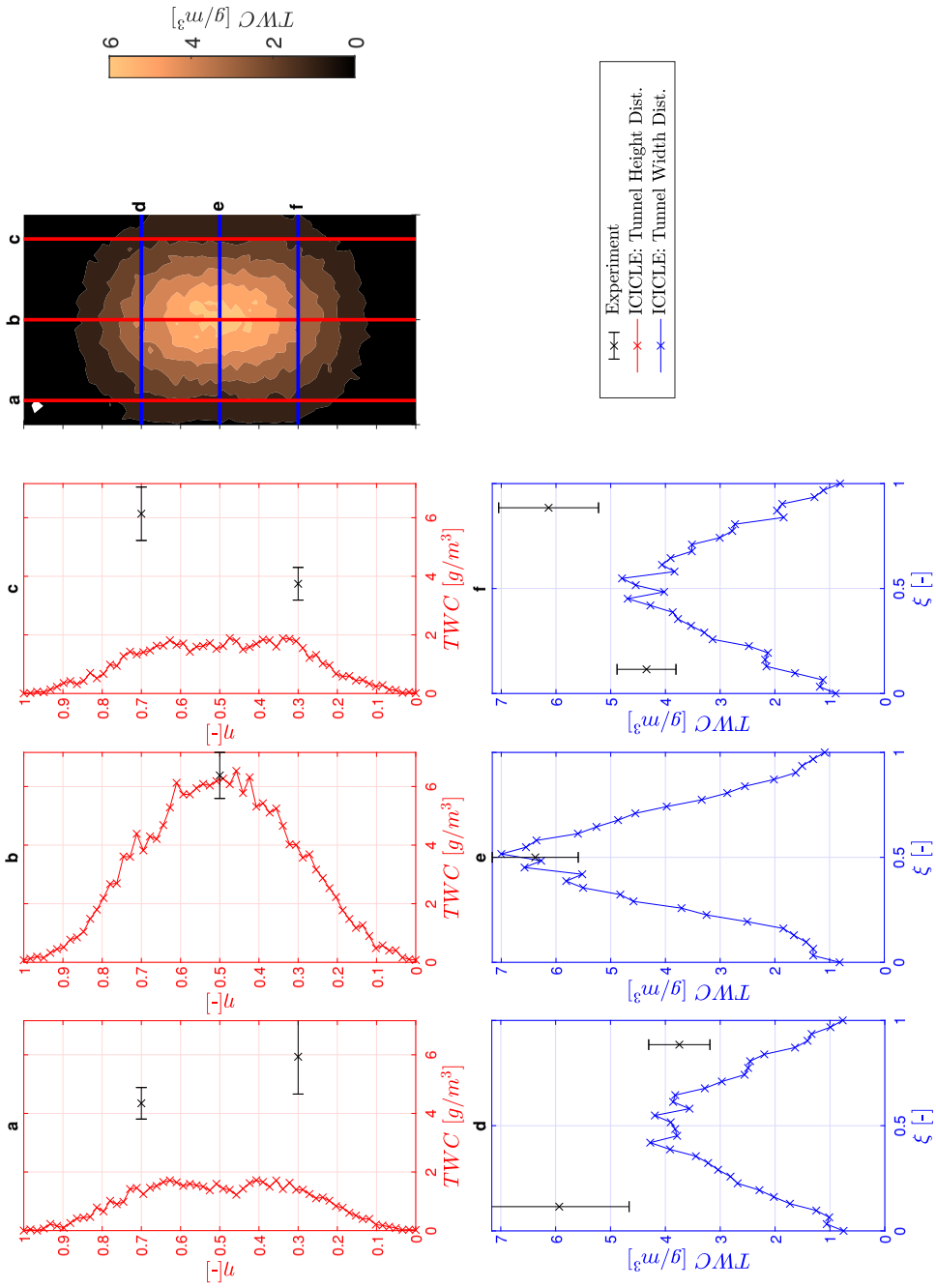

Figure 6.21: Two-Way Coupling Simulation results for Test Run 649, for TWC, including vertical and horizontal slices at CIKP probe traverse measurement positions.

6.6.4 Validation of Particle Phase Change Simulations

Validation of the phase change model has been performed against a set of calibration measurements. The particle cloud statistics and TWC_{cl} measurements are shown in Table 6.4. The gas properties are the same as Test Case 667 in 6.3. A single case (Test Case 651) will be presented in full to demonstrate the model output.

Table 6.4: Particle Injection Statistics for Validation Study

Run	**PSD**	$\mathbf{D_{min}}$	$\mathbf{D_{max}}$	$\mathbf{D_m}$	**n**	$\mathbf{N_{bins}}$	$\mathbf{TWC_{cl}}$	$\mathbf{MR_{cl}}$
(-)	(-)	(μm)	(μm)	(μm)	(-)	(-)	(g/m^3)	$(\%)$
644	Baseline	2	162	53.1	2.09	26	3.51	8.06
649	Baseline	2	162	53.1	2.09	26	6.21	9.02
651	Large	2	202	63.3	1.98	26	12.46	9.84

Using two-way mass-energy coupling full 2-D distributions of total water content and melt ratio were obtained as shown in Figure 6.22.

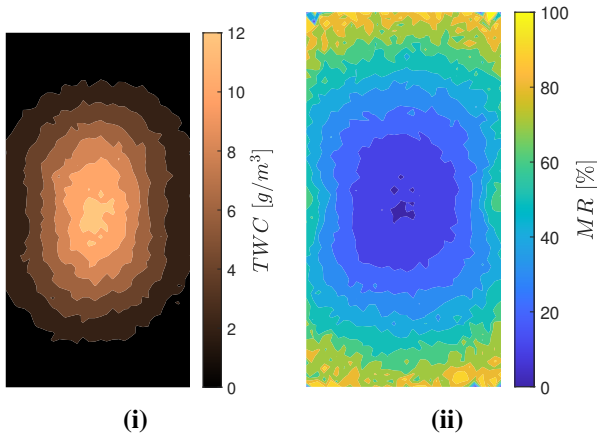

Figure 6.22: Two-Way Coupling Simulation results for (i) TWC and (ii) MR at probe measurement positions. Test Case 651.

There is clearly a strong spatial variation seen in both quantities and this strongly affects the distribution of accretion on the walls and/or a test article installed downstream. More subtle features, such as a vertical 'droop' in the TWC and MR distributions caused by gravitational effects, are also captured, as well as near wall variation in the melt ratio along the vertical walls caused by the tunnel secondary flows. This is important for turbomachinery ICI physics and work going forward. Sticking efficiency and erosion

models are generated from centreline values, however particle Melt Ratio and TWC spatially varies generating high Melt Ratio and low TWC values near the wall. This is a property of the local flow velocity, however from experiments, high accretion rates have been observed experimentally for equivalent conditions [21, 32].

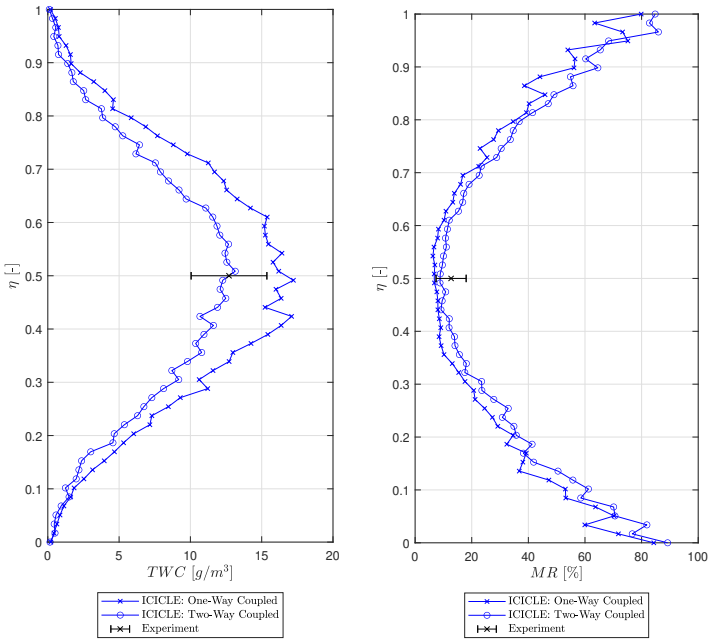

Figure 6.23: Test Run 651: Two-Way Coupling Simulation results for (i) TWC and (ii) MR at probe measurement positions. Experimental readings have been overlaid.

Looking in more detail at results on the vertical centreline, Figure 6.23, the average Melt Ratio with two-way coupling is seen to be $\sim 110\%$ of that predicted by the one-way coupled simulation. This is driven by the combined effect of higher humidity in the flow which reduces evaporative cooling and raises the wet bulb temperature experienced by particles. Additionally, the higher RH caused by mass transfer results in a 25% reduction in TWC at the measurement plane position, this is due to the higher wet bulb temperature causing particles to melt and evaporate faster over the residence time. The measurable effects demonstrate the value and necessity of employing two-way coupling even for a simulation neglecting deposition which would exacerbate evaporative heat and mass transfer. where centreline Melt Ratio is fairly constant, but nearer the walls ($\eta = 0$ and $\eta = 1$) Melt Ratio is more inconsistent. Largest particles will have similar melt

times in each case, whereas $D_p << D_{v50}$ will experienced higher melting. This is significant as smaller particles have lower wall normal velocities and are more sensitive to turbophoresis. This will drive up high Melt Ratio and liquid water particles impacting at the wall, therefore exacerbating accretion. It is reasonable to conclude that two-way coupling and turbophoresis is necessary in turbofan compressors where tightly wall bounded flows, pressure gradients/accelerations and highly turbulent flow is present. To validate the approach the experimental measurements of TWC for each of the 3 test cases (644, 649, 651) and are compared to the predicted results. Figure 6.24(i) shows a spatial distribution of TWC with two diagonal slices overlaid: the blue and red diagonal lines shown connect up the probe traverse measurement positions, Figure 6.24 (ii) details the probe traverse path with the same diagonal extents pictured.

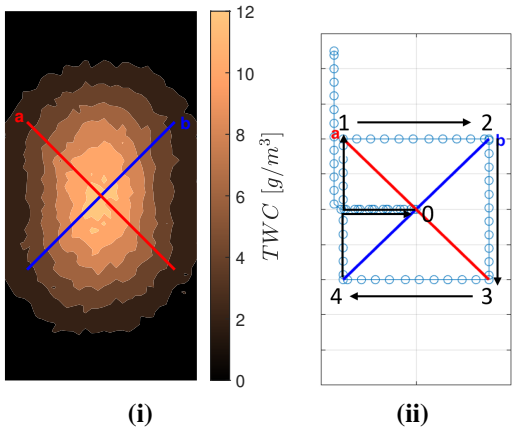

Figure 6.24: Test Run 651: Two-Way Coupling Simulation results for (i) TWC and (ii) TWC probe traverse measurement positions. Blue and red lines in (i) represent a slice through measurement positions.

Figures 6.25a, 6.26a and 6.27a show good agreement using two-way mass-energy coupling with the tunnel TWC experimental measurements, with large over-prediction in TWC using one-way coupling. The reduction in TWC due to two-way coupling is likely due to the higher RH in the domain, which will reduce evaporative cooling and exacerbate melting rates in the smaller particles. Larger particles are less affected as observed in Figure 6.23.

Figures 6.25b, 6.26b and 6.27b show a discrepancy in TWC at position 2 and 4. There is no physical driver for a change in flow composition between points 1 and 2

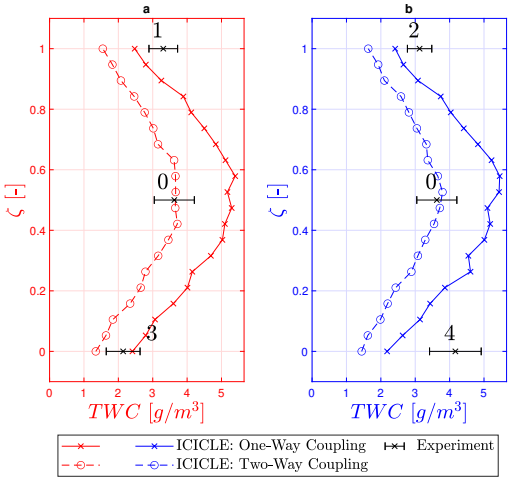

Figure 6.25: Comparison of One-way and Two-way coupled simulation results for Test 644. The TWC contour plot in Fig. 6.24 shows the diagonal extents connecting traverse measurement positions.

or between points 3 and 4. This is likely due to the change in the thermal condition of the probe resulting from a transient traverse across the flowfield prior to measurements 2 and 4 in comparison to the traverse through relatively isotropic flow conditions near the wall prior to measurements 1 and 3. The latter conditions seem better conditioned to achieve a reliable steady-state response from the probe.

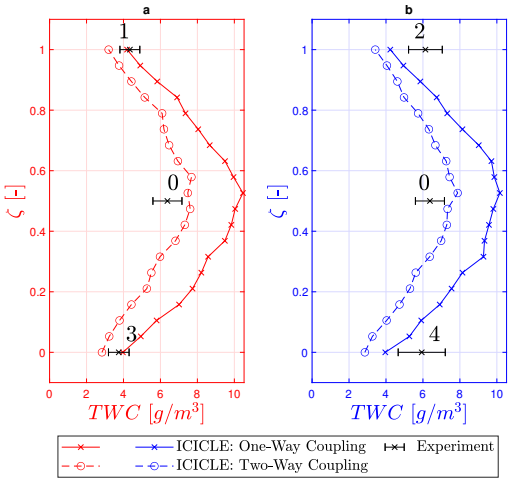

Figure 6.26: Comparison of One-way and Two-way coupled simulation results for Test 649. The TWC contour plot in Fig. 6.24 shows the diagonal extents connecting traverse measurement positions.

Figure 6.27 appears to carry the largest uncertainty in TWC measurements compared to the previous test cases. Test case 644 and 649 were both at the *Baseline* particle

size distribution, Test Case 651, was conducted at the *Large* particle size distribution. Therefore, it is reasonable to assume that the probe measurement uncertainty scales with particle size or D_{v90} specifically. This can be important especially when conducting probe design for tunnel and external ice crystal icing detection. The uncertainty is likely due to larger particles being more porous or possibly agglomerated and having non-spherical melting responses which may affect the probe energy balance uncertainty quantification.

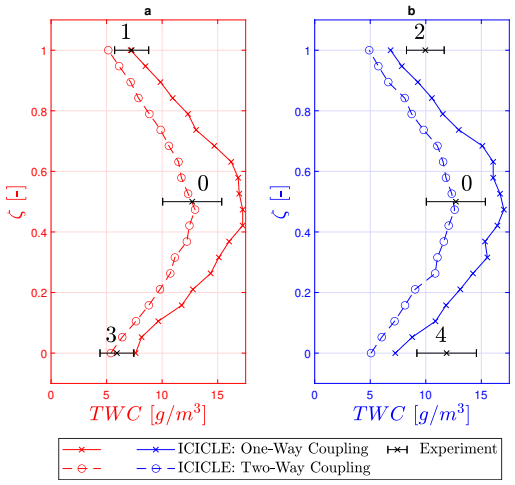

Figure 6.27: Comparison of One-way and Two-way coupled simulation results for Test 651. The TWC contour plot in Fig. 6.24 shows the diagonal extents connecting traverse measurement positions. **Note: Largest PSD** is equivalent to **Largest Uncertainty Bounds**

Figures 6.25, 6.26 and 6.27 demonstrate the validation of this combined ice crystal icing transport, melting, turbophoresis and two-way coupling for a range of ice mass flow rates and particle size distributions. Good agreement with experiments utilising literature drag, phase change and turbophoresis models shows this combined model is applicable for turbomachinery flows in ice crystal icing. Furthermore, the bias in results in Figures 6.25b, 6.26b and 6.27b highlight the need to improve ice crystal icing altitude facility instrumentation and spatial measurements of ice cloud properties.

6.7 Summary

In this chapter, literature and in-house models are implemented in a 3-D code environment to model glaciated and mixed-phase ice particle transport. The code is validated using experiments conducted by the Oxford Thermofluids Institute's Particle Deposition Group

at conditions typical of turbofan compressor ice crystal icing events. Uniquely, the model combines a DRW turbulent transport model with two-way mass-energy coupling in a 3-D environment with convergence assessment of particle phase modelling. Validation is performed against spatial distributions of ice concentration (TWC).

Turbophoresis is seen to be have significant influence on melting and mass dispersion in ICI transport. Better modelling of mass diffusion along with elevated kinetic energy exchange produces a significant variation in melting and mass concentration over the duct face. This is important in compressor ICI modelling where the flow is strongly wall bounded, and experiences significant turning and strong turbulence from repeated stages. Furthermore, the eddy-viscosity turbulence model employed under-predicted the turbulence present within the flow compared to experimental results. Along with neglecting of anisotropy present near the wall (and at high Re) this resulted in Melt Ratio 60 - 90% using the Realisable $k - \epsilon$ model in comparison to a Reynolds Stress Model.

The combination of two-way coupling, non-spherical particle drag coefficient and the use of a turbophoresis model, produced reliable approximation of experimental conditions. Comparison of simulations to gas-vapour measurements suggest the model generates an offset to the predicted total temperature measurement but still within 10% of the total temperature experimental measurement 95% confidence interval, the relative humidity, however, closely matched the experimental measurements.

Comparative studies conducted without two-way coupling showed much poorer agreement with experiments. The chapter has formalised the methodology and fidelity required to model ICI phenomena found to occur in the LP compressor and booster. It shows the sensitivity of melting response is driven by mass exchange between phases and highlights the need to model channel turbulence effectively. The methodology may be applied to an engine compressor geometry study requiring only known external flight cycle boundary conditions as encountered during icing events.

7

Evaluation of Surface Response Model Against Previous Fundamental Conical Experiments at RATFac

This chapter focuses on the surface impact and heat transfer models for Ice Crystal Icing relating to turbomachinery. A literature-based solid particle roughness model is implemented, and demonstrated. The effects on rough wall impact scattering and accretion are investigated. Importantly, a novel topography smoothing, volume correction, and extrusion algorithm is presented to deal with accretion topography changes within the simulation, reducing the number of CFD re-initialisation steps required for stable solution of the model in the 3D environment.

7.1 Overview 143
7.2 Numerical Arrangement 143
7.3 Model Assessment 144
7.3.1 Effect on Particle Trajectory 144
7.3.2 Effect on Surface Impact 145
7.3.3 Effect on Accretion and Heat Transfer 145

7.4 Summary 148

7.1 Overview

In order to assess the stochastic rough wall model within ICICLE, it was necessary to examine the trajectory of the particles and the impact effects on a simple geometry. The test case and information are summarised in the following.

7.2 Numerical Arrangement

The test case used to examine the surface response, was the 35° cone, described in Chapter 5. This provides a simple geometry and test matrix to investigate the effects of the modelling aspects relating to surface roughness, which affects impingement and heat transfer. The flowfield was produced in ANSYS FLUENT 2021 R2, an example Mach number contour is shown in Figure 7.1. Here, the working section, test article and gas properties are described. Test case 737 as described in Table 5.3 was used as a baseline case to examine the effect of roughness on impingement, accretion and heat transfer at the surface.

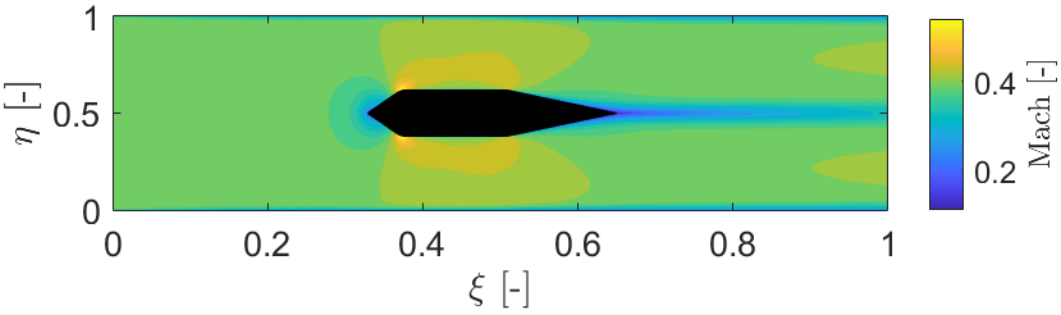

Figure 7.1: Mach number contour plot for 35° Cone Test Case 737.

7.3 Model Assessment

7.3.1 Effect on Particle Trajectory

The sensitivity of the wall roughness to impact was examined. A representative injection with a 'Rosin-Rammler' 26 bin particle size distribution was seeded. This reflects the measurement granularity of the particle size distribution within RATFac [79, 80]. 26,000 particle injection sites were used and the particle Melt Ratio distributions were generated with the same methodology as used in Chapter 6. Figure 7.2(i) shows the particle trajectories for the smooth-walled model and Figure 7.2 (ii) the stochastic rough-walled model, respectively. It is clear there is a more random distribution in bounce angle and exit trajectory in (ii). In the smooth-wall case, the majority of trajectories are symmetric about the centreline. This figure demonstrates the physical effects of rough wall impact modelling.

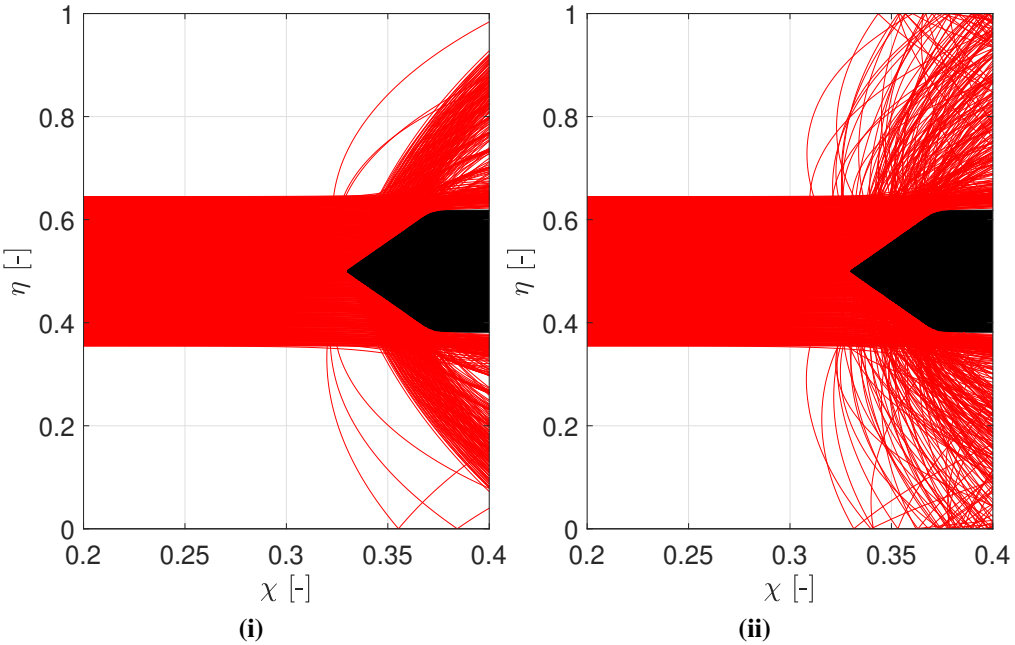

Figure 7.2: Particle trajectory plot for TR737 35° cone case to demonstrate (i) Smooth Wall b) Rough Wall Impact Considering Sommerfeld Distribution defined by β, γ. Note: Injection is 26 bin Rosin Rammler with 520,000 particles (26,000 injection sites).

The total water content and Melt Ratio were plotted at the cone trailing edge, corresponding to $\chi = 0.375$, over the height of the tunnel face from the centreline over the interval η = [0.5, 1.0] as shown in Figure 7.3.

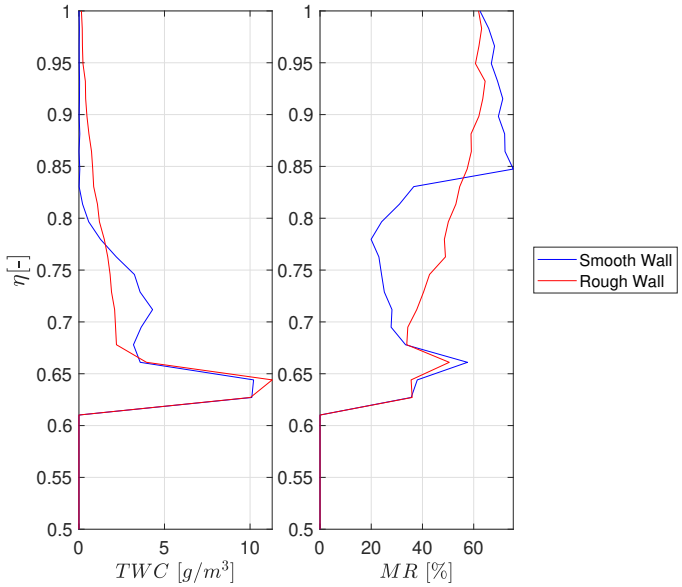

Figure 7.3: Particle TWC and MR distribution at $\chi = 0.375$ axial position for Smooth and Rough wall impact models. Assumes $\sigma_\gamma = 5°$

7.3.2 Effect on Surface Impact

Higher surface roughness will increase local surface convective heat transfer. With respect to ice crystal icing, this will increase the capture surface area. Stochastic rough-wall modelling is summarised above, where particles interact with a rough wall. This imposes a 'virtual-wall' correction angle during impact calculations. Experimental ice accretion measurements were conducted using 2D backlit shadowgraphy by Bucknell et al. [21]. A comparison is made to one such experiment and subsequent ice accretion thickness measurement on the $35°$ Cone Test Case (Cone Test 737). The results of current modelling of the particle trajectories, TWC, MR and accretion profiles along with images of the accretion taken from the experimental campaign are shown in 7.2 (a) to (c).

7.3.3 Effect on Accretion and Heat Transfer

The surface roughness of ice accretions and clean substrates have significant effects on heat transfer augmentation. This affects convective heating and evaporative cooling, requiring the determination of suitable boundary conditions within the accretion thermodynamic model and sufficient spatial and temporal resolution to capture the changing physical drivers. In turbomachinery, adverse pressure gradients, stream-wise and radial

velocity distributions, generate a three-dimensional variation in the thickness, temperature, and roughness distribution on surfaces. The transient roughness behaviour means heat transfer cannot be calculated by local impingement flow and freestream conditions, and is unsteady throughout an icing event.

Typically in SLW icing a mean roughness height has been imposed to generate boundary layer properties for the Thermodynamic Accretion model. These roughness properties are tuned to allow a 'single shot', or, 1 particle cloud deposit-accretion-growth cycle to be applied in modelling. This assumes the flowfield mass, momentum and energy are unchanged. This may be unrealistic if compared to the real roughness developing on the surface. In ICI there are likely to be development of accretions followed by shedding of ice, requiring a temporally changing roughness to be applied at each surface location.

Mass and energy exchange between the gas and iced surface was modelled within ICICLE assuming quasi-steady energy and mass fluxes over the 'exposure' time. For sensible, kinetic, aerodynamic and melting energy exchange, the particle impingement properties were used. However, for convection, evaporation, and sublimation, gas properties are needed relative to the surface. This is challenging as in turbomachinery flows there is no 'freestream' value, gas properties governing saturation vapour pressure, and adiabatic wall temperatures vary in the stream and radial directions.

It is instructive to use properties at the edge of boundary layer for freestream properties then, $P_{0,e}$, $T_{0,e}$, where the edge of the boundary layer can be approximated using CFD or assumed to adopt a fixed value (generating a control volume bounding region around the body).

$$q_{evap} = L_v \dot{m} = \frac{L_v H_{conv}}{C_p L e^{1-a}} \frac{M_w}{M_a} \left(\frac{P_{vap,surf}}{\mathbf{P_{0,surf}} - P_{vap,surf}} - \frac{P_{vap,e}}{\mathbf{P_{0,e}} - P_{vap,e}} \right) \tag{7.1}$$

$$q_{conv} = H_{conv}(T_{surf} - T_{recovery}) \tag{7.2}$$

where recovery temperature is as follows,

$$T_{recovery} = T_s \left(1 + Pr^{1/3} \frac{\gamma_a - 1}{2} M^2\right) \tag{7.3}$$

In ICICLE this value is fixed at the empirical roughness height 0.7mm, producing a stand-off height for evaporative and convective models. To understand the solution sensitivity to this property, a solution was run with this stand-off height doubled. Figure 7.4 shows results for Test Case 737 for the 35° cone. Here, the accretion thickness is seen to be insensitive to doubling this height. This is due to kinetic energy recovery, which is likely to conserve total properties. It is therefore more appropriate to infer accretion heat and mass flux properties at the fluid-solid boundary. Here, mass and energy transfer coefficients can be derived experimentally or from CFD.

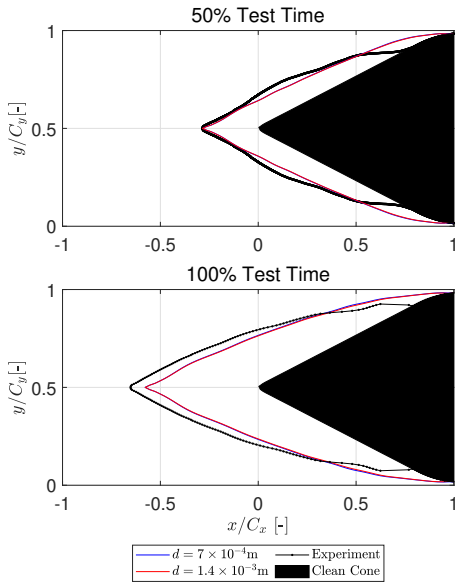

Figure 7.4: Comparison of roughness diameter d informed boundary layer thickness term. Test Case 737, 35° cone. Top plot is 50% test time, Bottom plot 100%.

The use of freestream properties may not be sufficient for some turbomachinery applications where more rapid pressure and temperature rises may affect the boundary layer thickness. Additionally, local to tip gaps and vane roots where secondary flows are present, the boundary layer properties will be vary significantly, and large-scale flow mixing and work on the flow may drive the total temperature. This result demonstrated in Figure 7.4, suggests that the energy balance assumptions within the accretion EMM model are robust, and that convection and evaporation, which are scaled by the heat and mass transfer coefficients may be insignificant to the accretion net mass flux. This is important for modelling, as the convection and evaporation heat and mass transfer are therefore more sensitive to initial conditions than boundary layer diffusion effects.

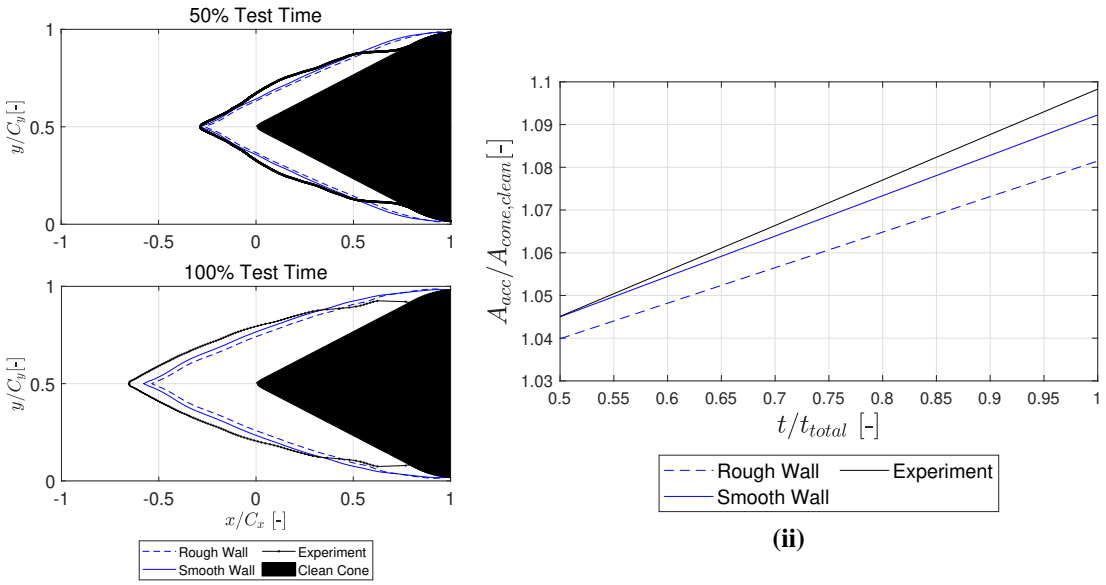

Figure 7.5: (i) Comparison of Smooth Wall and Stochastic Rough Wall models against ice accretion. Test Case 737, 35° cone. Top plot is 50% test time, Bottom plot 100%. (ii) Comparison between Smooth and Rough wall boundary conditions against accretion area ratio, normalised by clean cone cross sectional area.

Figure 7.5(i) shows the ICICLE simulation result for smooth and rough wall test cases. In both cases, water runback is inhibited (steady film). This is to evaluate the effect on accretion purely due to geometric rough wall impact properties. Figure 7.5(ii) shows the accretion area from 7.5(i) normalised by the clean cone cross sectional area against time normalised by total experimental time. Here it is evident the rough wall model reduces the overall accretion by approximately 1%. This is not overly significant but will be mostly due to its simple geometry and it will only experience single particle impacts. The effects on a secondary impact assuming a rough wall may be significant due to the adjustment in TWC and Melt Ratio distribution shown in Figure 7.3.

7.4 Summary

This chapter has focused on the representation of the accretion surface numerically. The interaction between a simulated particle and a wall is a complex process involving momentum-energy exchange and sticking probability for ice crystal icing. In order to better capture the physics during impact, it was necessary to implement a stochastic

rough bouncing model for calculation of exit trajectory angles. This is necessary due to the macroscopic and microscopic roughness scales associated with ice accretions. When evaluating the roughness model against particle trajectory and melting response, the model appeared to smooth the mass and melting distribution of particles following impact. Interestingly, the rough wall model under-predicted accretion slightly. This may be due to the distribution of bounce angles producing a variation in the erosion model specifically. Demonstration of this rough wall impact model was important to highlight the need to capture surface topography effectively for ice crystal icing. THe next step would be to perform a parametric study on roughness height values R to assess the sensitivity to melting and accretion rates.

8

Evaluation of Transport and Accretion Models against previous LP Compressor Stator Vane Experiments at RATFac

This chapter presents the combination of literature assessment, experimental data analysis and methodology presented above to validate the combined Ice Crystal Icing Transport and Accretion model. The novelty here is in applying to a representative LP compressor stator vane with an assessment against three-dimensional ice accretion measurement from previous colleagues.

8.1 Overview 151

8.2 Numerical Arrangement 151

8.2.1 Working Section Inlet 154

8.3 Particle Cloud Properties 154

8.3.1 Particle Cloud Properties - Working Section Inlet 155

8.4 Volume Extrusion 157

8.5 Heat Transfer 157

8.5.1 Substrate Response 159

8.6 Accretion Adhesion Conditions 163
8.6.1 Surface Pressure Coefficient 163
8.6.2 Tip Leakage 164
8.7 Comparison to Ice Thickness Data 164
8.7.1 Two-Dimensional shadowgraph results 165
8.7.2 Three-dimensional DIC Data 169
8.8 Summary 172

8.1 Overview

In this chapter the stator will be used for full three-dimensional validation. The cone case has been utilised in Chapter 7. The prismatic stator test piece and the resulting ice accretion post test are shown in summarised in Chapter 5. This case demonstrates a complex three-dimensional flowfield. Here, it is this chapter demonstrates to evaluation of the particle transport models, multi-zone CFD arrangement and unsteady accretion model.

8.2 Numerical Arrangement

The main metric for validation was to compare experimental results from previous ice accretion tests performed at RATFac with model results generated in ICICLE. The test piece used was a simplified compressor stator vane. To fully represent the previous experiment, the stator was modelled as a cantilever beam built in at one end with a tip gap to the opposing tunnel wall. For comparative purposes a simplification to the CFD to model the blade with periodic end faces, effectively generating a 2-D oncoming flow over an infinitely wide 3-D profile, which provides a means of comparison to the previous 2-D ICICLE results.

The schematic in Figure 8.1 details the arrangement of the fluid volume of interest. Here, the working section of the tunnel is modelled. Condition (a) has periodic or repeating boundaries. This produces an infinite span description of the stator. This is

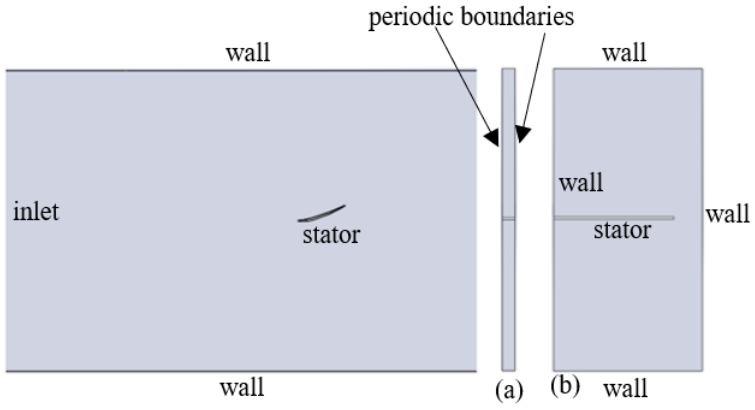

Figure 8.1: Validation test cases for ICICLE. Representative engine stator vane (a) periodic endwall condition. (b) Full 3D RATFac tunnel simulation with tip-gap.

important for demonstrating the differences between 2D and 3D flowfields. Second, condition (b), is the description of the full 3D experimental working section and model.

Table 8.1: Summary of mesh characteristics for prismatic stator test cases.

Test Case	Description	Cell Count	Y+
1	Periodic	7450397	1.5
2	Cantilevered	98645735	1.5

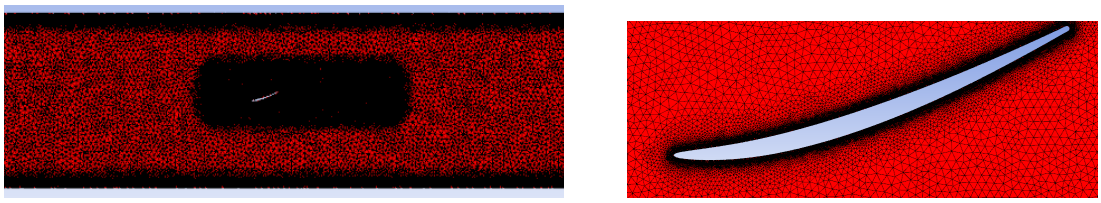

(i) **(ii)**

Figure 8.2: (i) ICEM Mesh of 'clean' stator geometry and tunnel working section. (ii) Mesh clustering at the stator wall to resolve the boundary layer to a Y+ < 5.

A series of RANS simulations were performed to model the flow conditions within the RATFac icing wind tunnel. Turbulent dissipation was calculated using the $k-\omega$ SST model. The low compressible flow at Mach 0.25 and 0.4 required a compressible solver. Given the low Mach number the pressure-based COUPLED numerical scheme was employed to solve the NS equations [57] [51]. These conditions are informed by the tests conducted by Connolly et al. [32] and Bucknell et al. [21]. The computational domain begins at the position of the iso-kinetic probe at the tunnel entrance in order to match static

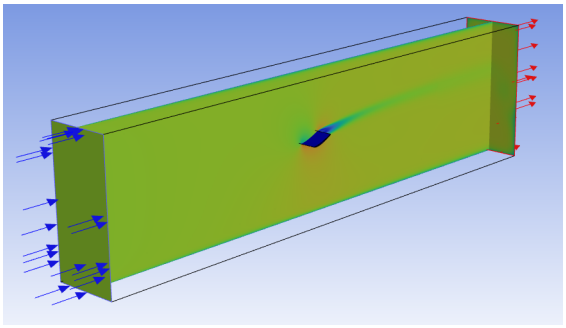

Figure 8.3: Mid-span slice of stator flow domain.

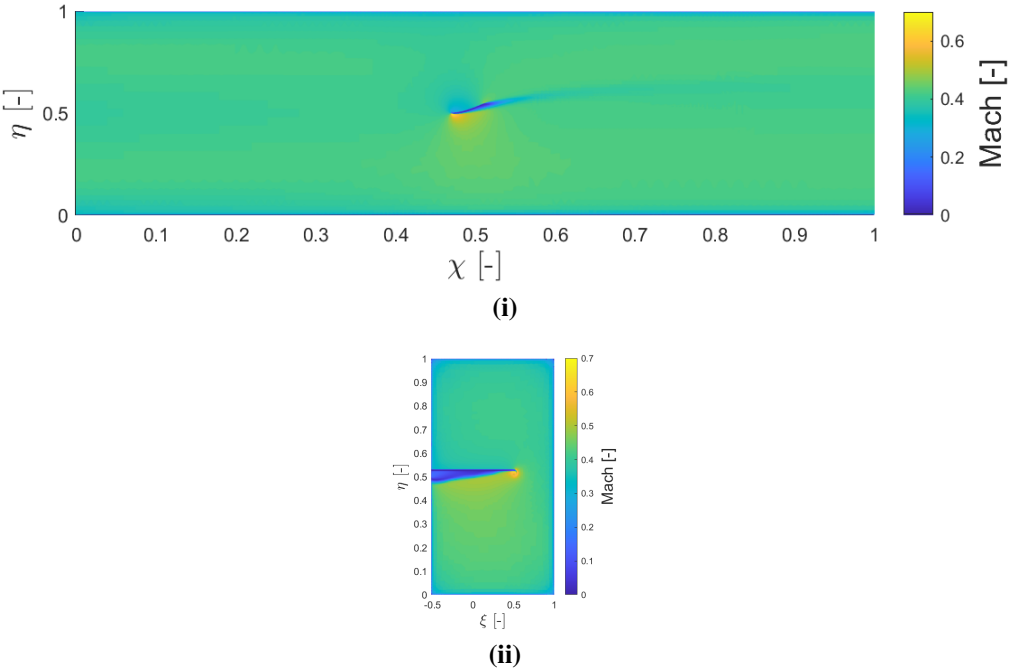

Figure 8.4: (i) FLUENT viscous flow simulation of prismatic stator test in RATFac icing wind tunnel. Cantilevered flow solution, taken at mid-span. (ii) Mach number distribution for cantilevered stator case taken at stator mid-chord.

pressure in RATFac and represents the 1m of working section length from the TWC probe position. The continuous phase solution was iteratively solved to match a Mach number of 0.4 at the Kiel probe positioned at 1.741m downstream from the ice injection pipe.

From the RANS simulation it is clear there is little flow turning at the stator due to the lack of multiple blades and large tip gap losses in the full 3D simulation which would not be representative of compressor gas path flows. This serves as a simple example of 3D coupled flows and a well documented test case for validation of simulated conditions.

8.2.1 Working Section Inlet

Downstream of the bell mouth at the CIKP measurement position, total temperature and pressure T_0 and P_0 distributions were used to initiate the simulation of the working section and test body. This enabled a simplification of the working section by deleting 1.763 m of flow domain. The icing solution similarly used the predetermined MR and TWC profiles calculated from the full domain for a given PSD. The distribution of total temperature at the RATFac working section inlet, for the baseline PSD and MR is shown in Figure 8.5. The variation of total temperature is seen to be 108-116% of the inlet total temperature for this case.

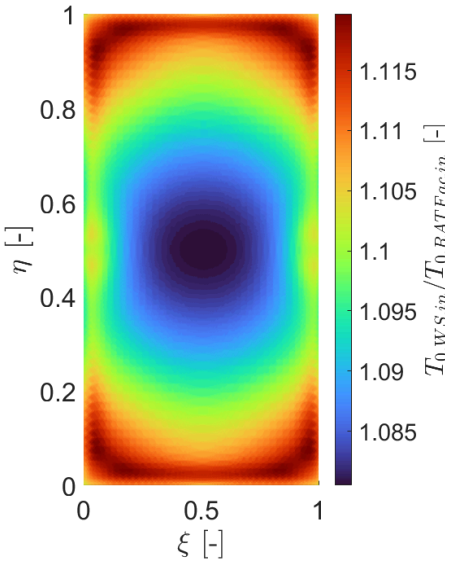

Figure 8.5: Normalised distribution of total temperature at RATFac working section inlet relative to total temperature at full RATFac inlet centreline position, for ice injection temperature at 263K and RATFac inlet total temperature 265K.

8.3 Particle Cloud Properties

Particle cloud properties are specified by experimental measurements of the particle size distribution, TWC and Melt Ratio. Table 8.2 summarised the particle size distribution statistics for each of the validation cases concerned.

Table 8.2: Particle Injection Statistics for Stator Test Cases

Run	$\mathbf{D_{min}}$	$\mathbf{D_{max}}$	$\mathbf{D_m}$	**n**	$\mathbf{N_{bins}}$	$\mathbf{D_{v10}}$	$\mathbf{D_{v50}}$	$\mathbf{D_{v90}}$
(-)	(μm)	(μm)	(μm)	(-)	(-)	(μm)	(μm)	(μm)
Small	2	104	38.3	2.09	26	16	34	54

8.3.1 Particle Cloud Properties - Working Section Inlet

Figures 8.6 and 8.7 are for the initial conditions for Test Run 485 and 495 respectively. They correspond to the inlet of the *Test Article* domain as discussed in Chapter 4 which corresponds to the CIKP (TWC) measurement plane.

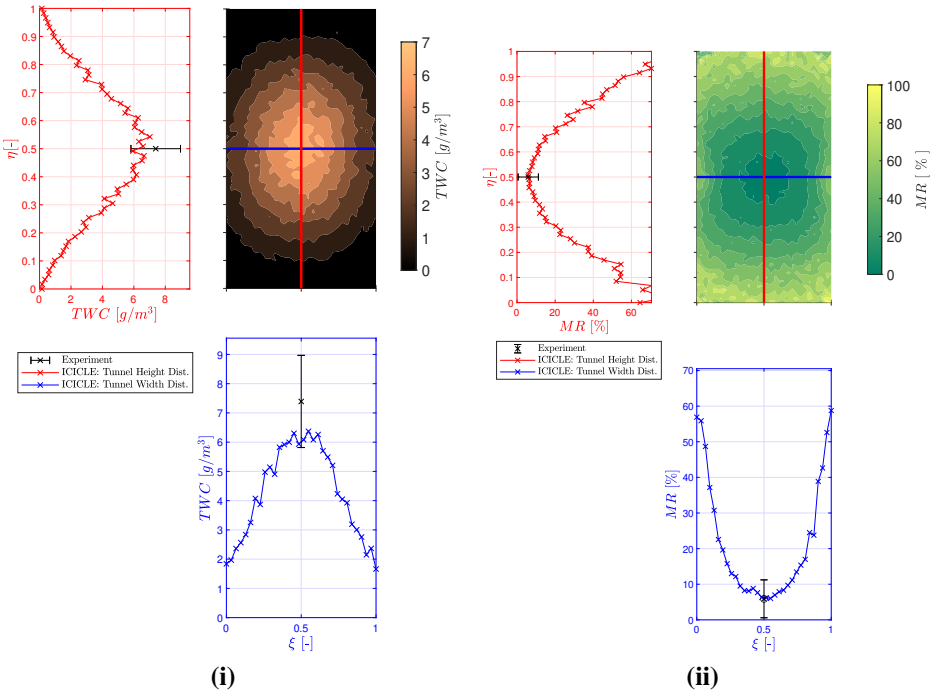

Figure 8.6: (i) TWC Distribution at CIKP Measurement Plane (ii) Melt Ratio Distribution at MW Probe Measurement Plane. Test Run 485

Here the same methodology as detailed in Chapter 6 relating to stream convergence, DRW model and particle size distribution granularity is applied in each case below. Figure 8.6 shows a good agreement between ICICLE 3D and experimental results for TWC and Melt Ratio. Figure 8.7 (i) shows that there is slight under prediction in TWC values at the centreline compared to experiment. It is clear from Figure 8.6(ii) and 8.7(ii) that Melt Ratio is between 80-100% at the tunnel walls, compared to the 6-8% at the centreline. This suggests that the MR interval for maximum ice accretion growth may be wider

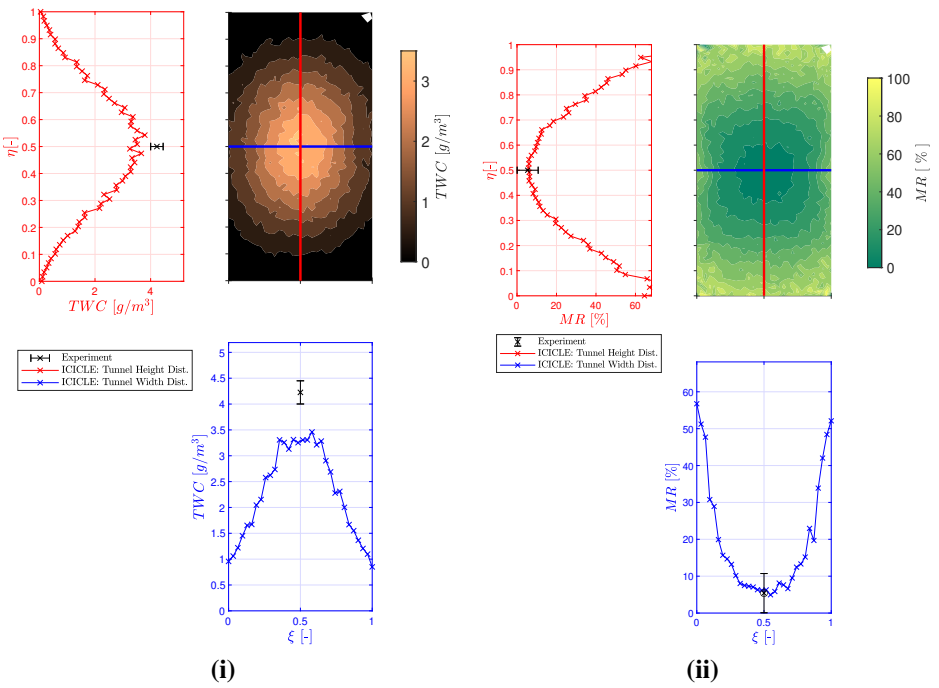

Figure 8.7: (i) TWC Distribution at CIKP Measurement Plane (ii) Melt Ratio Distribution at MW Probe Measurement Plane. Test Run 495

given the higher particle melt at the walls where accretion is present. The particle melt and concentration across the tunnel span illustrates the need for accurate modelling and measurement of turbulent dispersion in 3D ice crystal icing simulations.

This will likely have an effect on the overall accretion model, as TWC and Melt Ratio are inversely proportional over the tunnel domain. This is a property of the turbulent dissipation flux creating slower warmer gas in flow near and within the boundary layer. Smaller, more melted particles will be more numerous near the walls and will enable greater accretion rates. This opposes current symmetric formulations of sticking and erosion model formulations which are tuned to centreline properties. The Melt Ratio plateau region observed in literature across which mixed-phase ice accretion is maximized is $\sim$ 5% to 30%. This indicates that particle MR may be higher in places with similar accretion thickness, suggesting a wider range of melt ratios contributing to ice accretion severity.

8.4 Volume Extrusion

Following the extrusion step within the EMM, the discontinuous surface must be adjusted to produce a water-tight surface. Analytically this could be complex and for the whole domain an exact solution would be very difficult to implement within each EMM timestep. Figure 8.8 shows the original and curvature correction accretion volume for the Test Case 495 stator case, normalised by the maximum 1D volume. This is for 1s exposure time, meaning the overall accretion thickness is proportional to the cell width ($\sim 1mm$). The stator is used due to its camber and high surface curvature at the leading edge. It is important to note, this is to conserve accretion mass, it is clear close to the leading edge, on the R-H plot, volume correction is necessary, a reduction in the volume of up to 3% is important in capturing the shape and total accretion volume. Near the mid-chord on the pressure surface ($c/S = 0.5$), there is a slight increase in volume due to the concavity of the cambered vane.

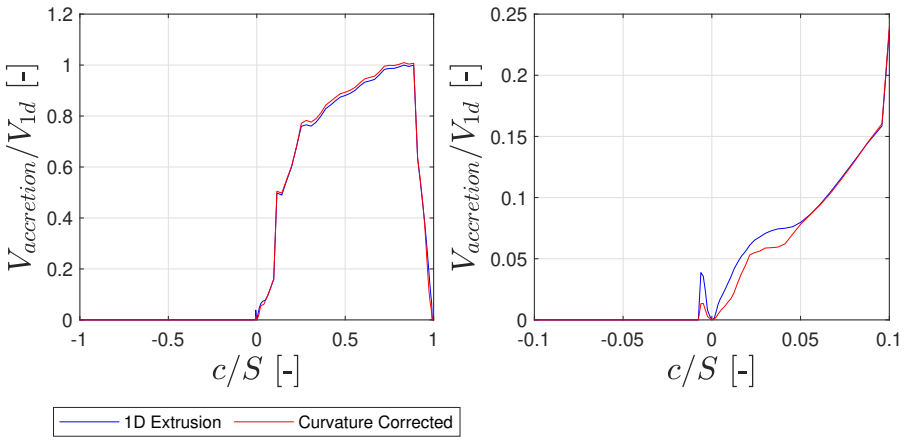

Figure 8.8: Quad cell face extrusion using trapezoidal volume correction method along cell node normals.

8.5 Heat Transfer

Heat transfer between the gas, ice and surface is governed by the relative resistance to heat transfer in each medium. Convective heat transfer in the gas and conduction in the ice and substrate will moderate the overall energy exchange between the 3 media (gas, ice, metal). The surface heat transfer coefficient (H) is calculated in each CFD

case against an adiabatic wall BC simulation, detailed in Equation 8.1. This requires 2 simulations for each gas condition and stator incidence angle. One simulation assuming an adiabatic wall. The second, at a fixed wall temperature T_{surf}. The heat transfer coefficient over the surface can then be determined numerically due to the differences between the adiabatic and isothermal simulations.

$$H = \frac{q_{surf} - q_{ad,w}}{T_{surf} - T_{ad,w}} = \frac{q_{surf} - 0}{T_{surf} - T_{ad,w}} \tag{8.1}$$

Experiments examining forced convection heat transfer on flat and inclined plates were conducted by Motwani et al. [100] and El-Shamy et al. [124]. These experiments generated Reynolds-Prandtl number relations for flat-plate turbulent heat transfer. Mahgoub et al. [92] examined these with respect to porous media. Table 8.3 summarises each empirical forced convection heat transfer correlation.

Table 8.3: Heat Transfer Correlations

Model	Equation	Reference
Motwani [0°, 15°]	$Nu = 0.056\mathrm{Re}.^{0.77}$	[100]
Motwani [30°, 45°]	$Nu = 0.084\mathrm{Re}.^{0.68}$	[100]
El-Shamy Flat	$Nu = 0.21\mathrm{Re}.^{0.66}$	[92, 124]
El-Shamy Inclined	$Nu = (1 + \sin\alpha)^{0.38} + 0.13\mathrm{Re}.^{0.703}$	[92, 124]
Chilton-Colburn Re Analogy	Nu = Re $\mathrm{Pr}^{1/3} \frac{C_f}{2}$	[123]

Figure 8.9(i) and 8.10(i) detail the Nu distribution over the stator vane test article. CFD derived heat transfer coefficient distributions (H) calculated using Equation 8.1 are compared to the empirical Nusselt number correlations listed in Table 8.3.

The pressure surface ($s/c \geq 0$) distribution is best matched by the Motwani [30°, 45°] empirical formula and the Chilton-Colburn-Re Analogy. Due to the compressible, turbulent flow around the stator, and the separation bubble formed within the wake, the modified Re-Analogy will not be accurate in capturing the heat transfer in the boundary layer on the suction surface ($s/c \leq 0$). The suction surface ($s/c \leq 0$) does not experience accretion at these incidence angles and therefore is not a vital part of the modelling capability. Additionally, the flat plate boundary layer analogies break down near the leading edge, where stagnation point heat transfer will dominate. They are not applicable

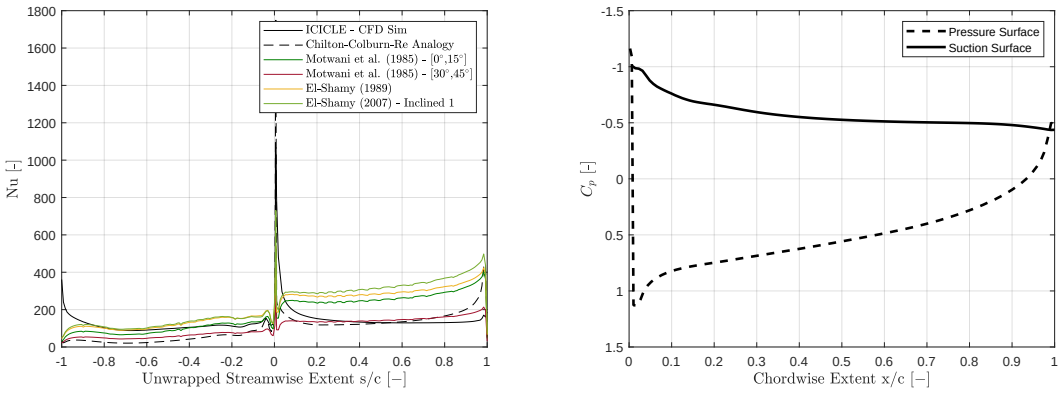

(i) **(ii)**

Figure 8.9: (i) Nusselt number vs Normalised streamwise extent (-ve is suction surface) (ii) coefficient of pressure plot vs chordwise extent over stator surface for Test Run 485.

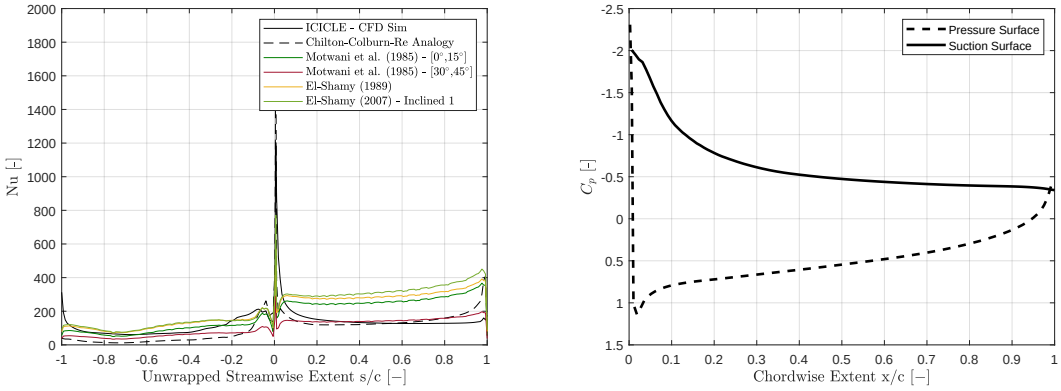

(i) **(ii)**

Figure 8.10: (i) Nusselt number vs Normalised streamwise extent (-ve is suction surface) (ii) coefficient of pressure plot vs chordwise extent over stator surface for Test Run 495.

for separating, recirculating flows, which were present for the stator cases as it acts similar to a bluff body and is not part of a vane cascade. It may be more useful to employ a correlation for heat transfer coefficient as opposed to a CFD approach, since this will enable calculations that do not require two CFD flow solutions to be produced. This has a direct benefit to the speed of solution.

8.5.1 Substrate Response

Figure 8.11 shows accretion water and ice film heights and surface temperature for Test Run 495 over 15 seconds exposure time for 2 different substrate thermal models. Figure

8.11(i) shows the infinite heat capacity model, where the substrate adopts the recovery wet bulb temperature. The inset plot shows the 'Stefan' or phase boundary temperature, where above freezing it merely shows the water film exposed temperature.

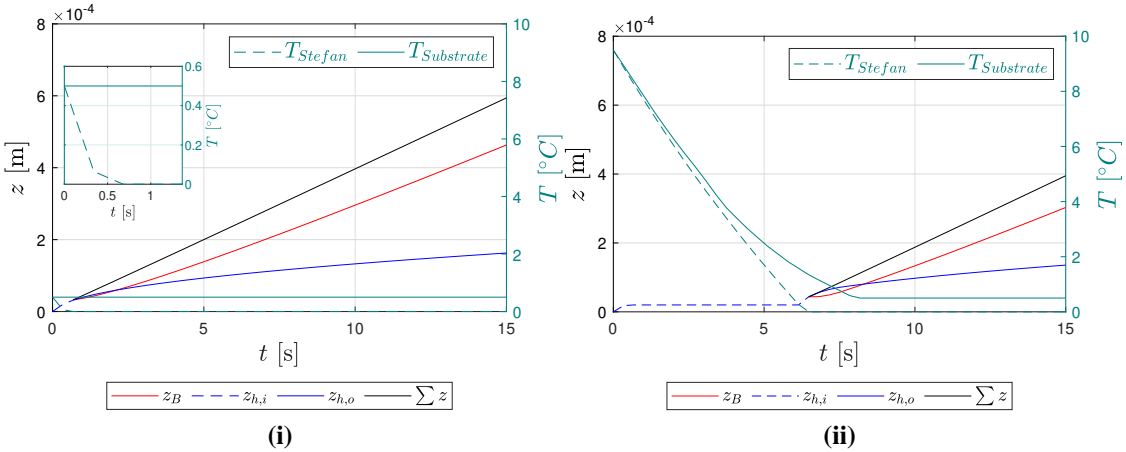

Figure 8.11: Ice and Water thickness on left y axis, Stefan and Substrate temperature on right y axisvs exposure time for (i) Adiabatic Wall - Recovery Wet Bulb (ii) Thin Film Equation with Wall Conduction. B is ice thickness, h,i is inner water film thickness and h,o is outer water film thickness.

Figure 8.11(ii) shows the response to the one-dimensional surface conduction model, this illustrates the $\sim$ 5 second delay to the onset of ice accretion in order to enable the water layer to generate a great enough thickness such that the Stefan condition temperature can approach freezing. Here the onset of accretion is delayed by the heat transfer from the substrate to the water film and the enthalpy/mass removal due to runback water. After 15 seconds, the accretion height in the fixed substrate temperature case is approximately 1.5x higher than that of the running water/conduction case.

Figure 8.12 shows thermocouple readings taken from the stator mid-chord corresponding to the centreline. Note, the thermocouple traces are for a separate test run, where shedding was being investigated, but they are instructive for the purposes of model assessment. The T_{subs} EMM value is actually representing the surface temperature, which is different to the thermocouple measurement, since they are embedded in the body. There will be an additional temperature differential due to the space between the stator surface and the sensor location. This explains why the curve is steeper in the EMM simulation initially, as the conduction model considers heat flux between the water

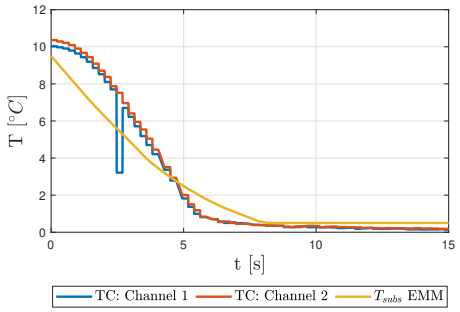

Figure 8.12: Thermocouple (TC) response from experiments channel 1 and 2, are embedded at the mid-chord at the centreline location, these are compared to predicted substrate temperature in EMM simulation for Test Run 495. (Thermocouple data is from a different test run as 495 was not available, gas conditions are matched however TWC is $3.79g/m^3$ compared to $4.28g/m^3$ for TR495.)

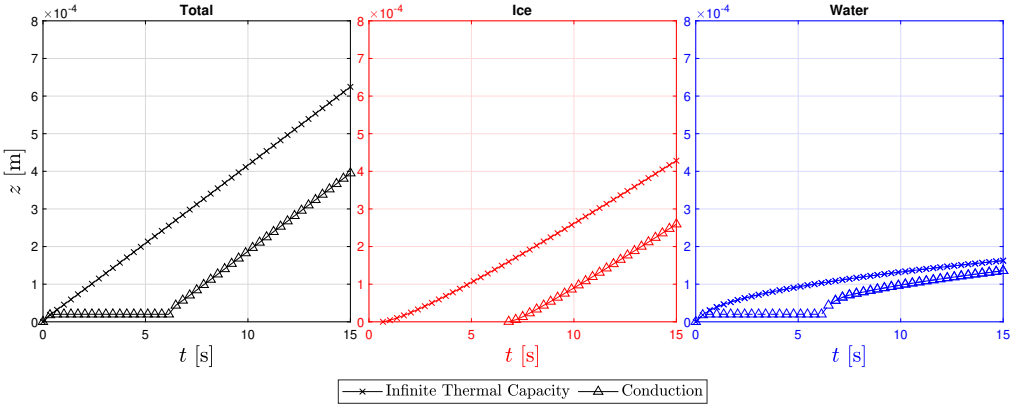

Figure 8.13: Total, Ice and Water thicknesses vs exposure time for infinite thermal capacity and 1D steady conduction.

film and substrate. There is an initial slow response, then a steeper gradient and faster settling time for the experimental measurements, this will be due to the 'spin-up' time of the grinder ice generation system when it is activated, so icing conditions will not step change compared to in the EMM simulations.

Accretion onset is either moderated by a growing water film present or the water runback removing enthalpy from the substrate. Although they give similar results, it is worth mentioning they model different phenomena entirely. In Figure 8.15(i), assuming the surface adopts the total wet bulb temperature $T_{wb,0}$, it is interesting to note the evaporative cooling heat flux has a much smaller contribution than the conduction and freezing (or melting when negative) fluxes. Figure 8.14 shows the full three-dimensional results for ice and water thickness normalised by chord length. The conduction model

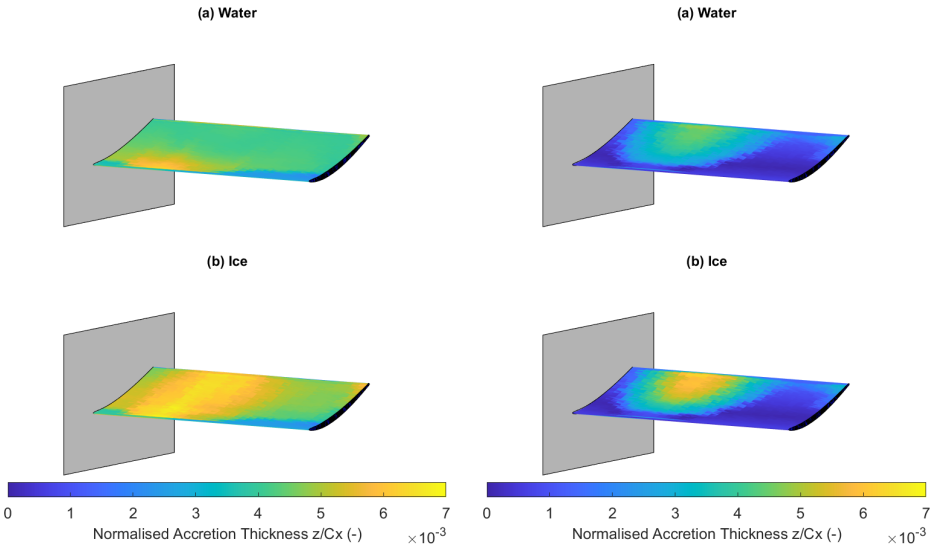

(i) Infinite Thermal Capacity **(ii)** Conduction

Figure 8.14: Normalised Accretion Thickness results for Stator Vane test case with (i) T_{wall} fixed to recovery temperature T_r and (ii) T_{wall} determined by conduction and experimental initial conditions.

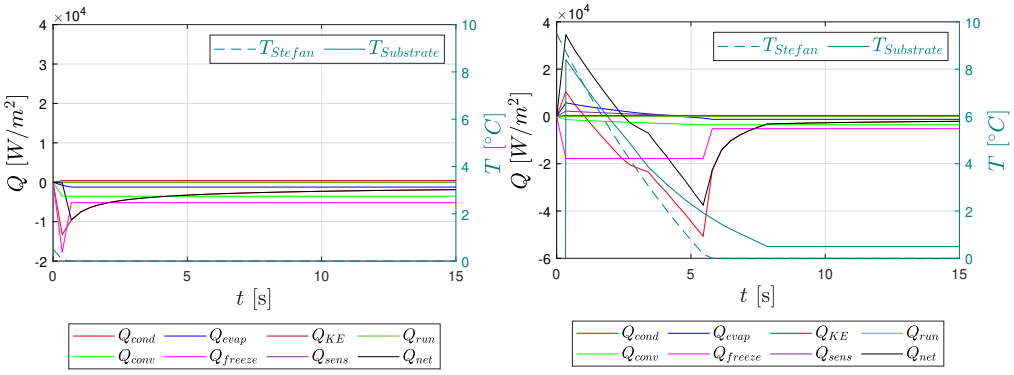

(i) **(ii)**

Figure 8.15: Heat flux components at surface for (i) Adiabatic Wall and (ii)Thin Film Equation with Wall Conduction

results in the same maximum ice thickness located approximately one-third of the way up the span, however there is a distinct difference and the rest of the stator has very little accretion elsewhere. The conduction model is necessary to capture the transient substrate temperature response to model the 'initiation' time for accretion, however as seen in Figure 8.15 the heat flux after approximately 10 seconds is equivalent. So it is appropriate to use low order modelling for conduction.

8.6 Accretion Adhesion Conditions

With respect to accretion initiation and adhesion, it is interesting to note the shape of ice around the leading edge. The accretion generates a 'horn' shape similar to the leading edge shape. This is certainly due to the flow turning and stagnation point heating compacting, smoothing and melting the ice into a specific shape. This will partly be due to the local static pressure at the surface, relative to the freestream. It was instructive to assess the surface pressure coefficient to identify local pressure distribution compared to experimental accretion shapes.

8.6.1 Surface Pressure Coefficient

The stagnation region and flow turning around the suction surface from the stagnation point has little to no accretion as seen in Figure 8.16(i). This will be due to the local surface pressure. It is therefore possible to generate a risk region based upon pressure coefficient C_p. This was not investigated in-depth within this thesis but Figure 8.16(ii) shows the C_p value which is calculated from the location of the ice accretion compared to the stator leading edge position. This can help to truncate the area required in a simulation.

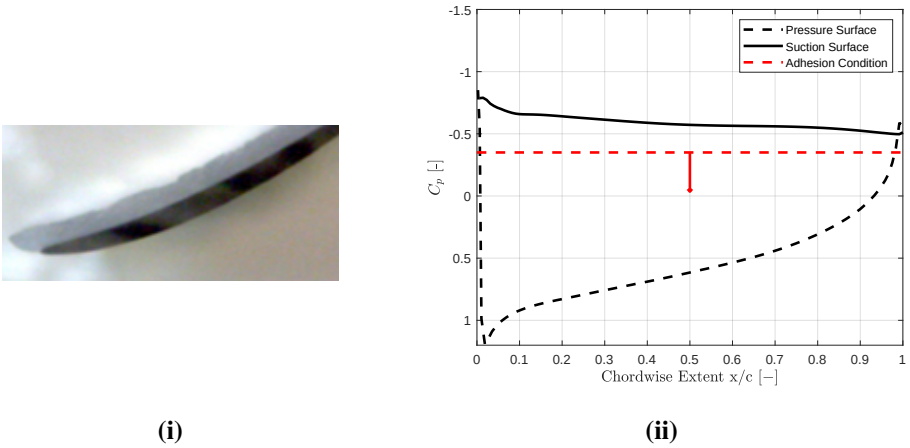

(i) **(ii)**

Figure 8.16: (i) TR854 leading edge accretion (ii) coefficient of pressure plot vs chordwise extent over stator surface for Test Run 854 with accretion minimum adhesion pressure coefficient shown(Bottom image in (i)).

8.6.2 Tip Leakage

It is additionally noted that the stator geometry was built-in at one end and with a tip gap of 22% of the tunnel width. Therefore extremely significant tip leakage flows are present, affecting the spanwise flow distribution over the stator vane. Figure 8.17(i) details the z or spanwise velocity component over the stator vane at the boundary layer edge / roughness height stand-off distance. 8.17(ii) shows the stator mounting in the experiment to understand the physical setup.

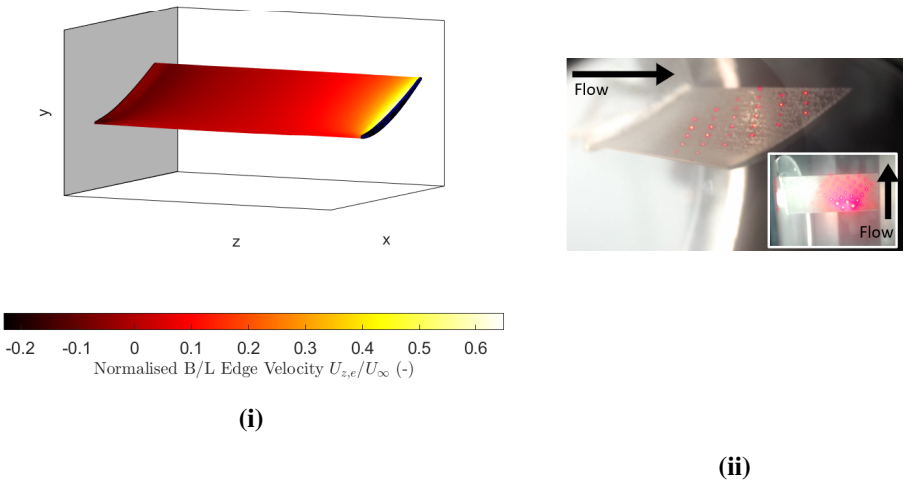

(i) **(ii)**

Figure 8.17: (i) Tangential Velocity component at the edge of boundary layer for TR495 stator test case. +ve U_z will concentrate accretion towards the centreline due to tip leakage effects. (ii) Stator test article looking towards the pressure surface from slightly upstream. (Equivalent to plot) Inset image: Top down view.

8.7 Comparison to Ice Thickness Data

Four different angle of attack conditions were simulated in ICICLE 3D to validate it against two-dimensional ice accretion shadow graph data, additionally, two cases were examined against three dimensional DIC ice accretion thickness data from an imaging system and experiments conducted by Connolly et al. [31, 33].

8.7.1 Two-Dimensional shadowgraph results

Two A.o.A cases comparing against 2D shadowgraph measurements are presented below. Simulations used a frozen flowfield with no updating across EMM-C timesteps. Table 8.4 lists the tunnel conditions for both.

Table 8.4: Two Dimensional Comparison: Gas Properties

Run	**Mach**	$\mathbf{P_0}$	$\mathbf{T_0}$	$\mathbf{T_s}$	$\mathbf{T_{wb0}}$	$\mathbf{RH_0}$	**TWC**	**MR**	**AoA**
	(-)	(kPa)	(K)	(K)	(K)	(g/m^3)	(%)	(%)	(°)
842	0.4	34.5	283	274.5	275.75	36.9	8.79	6.87	0
854	0.4	34.5	283	274.5	275.75	35.9	3.89	6.53	+10

Particle injections consisted of 2.6 million particles uniformly spaced across the injection area. The injection area was calculated using a recursive method from a coarser injection to calculate a minimum area which will capture injected particles at the stator surface. This was to increase the particle concentration at the surface and reduce the computation overhead to minimise simulated particles that did not impact the stator vane. Particles were injected at the measurement plane to correspond with MR distributions given above. In each case, mass and energy is one way coupled between the continuous and disperse phases. Specific humidity is conserved across the working section and defined by the inlet RH_0, T_0 and P_0.

8.7.1.1 Periodic/Infinite Span Domain

The periodic end-walled, infinite span 2D case was generated at the tunnel centreline using experimental Melt Ratio and TWC values given above. This provides for a basis of comparison to experimental measurements and full 3D simulations. It is effectively a two-dimensional simulation with 0 swirl (z velocity). The tunnel centreline corresponds approximately with the 2/3 span position of the stator vane. A case was run in full 3D to compare the results at the tunnel centreline position.

Figure 8.18 compares the full 3D and periodic (2D) conditions at the 2/3 span position. In the periodic case, the leading-edge accretion shape is predicted better than the full 3D case. Both show good agreement, however the angle of the ice accretion horn in the periodic case is better aligned with the experiment. Across the chord of the

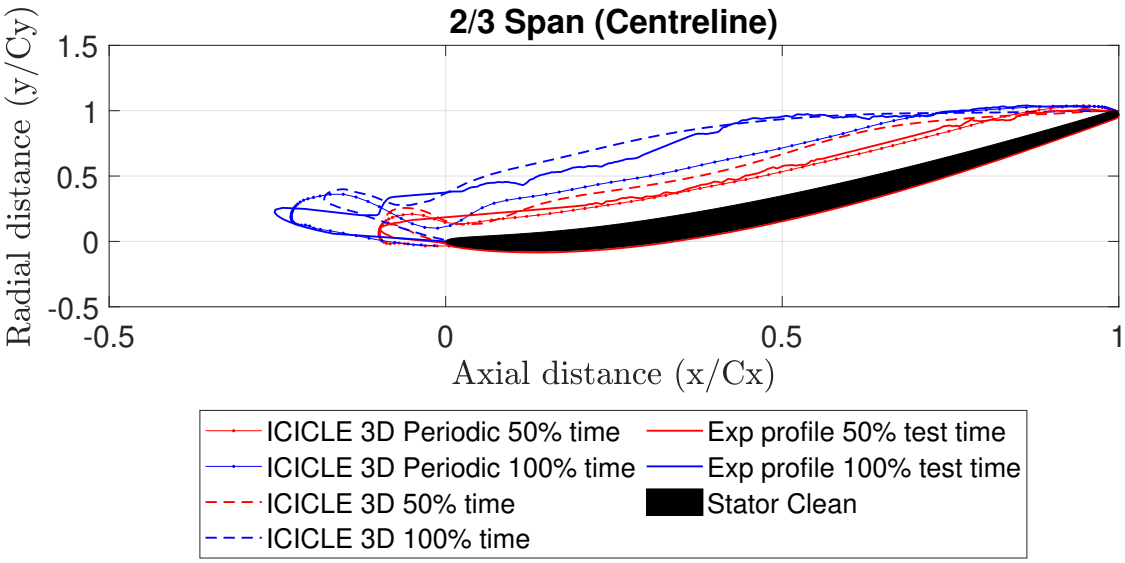

Figure 8.18: Comparison of simulated ice accretion in ICICLE 3D for periodic (infinite-span, 2D flowfield representation) and full 3D numerical flowfield. This is plotted against experimental shadow-graph data from TR 842 0° AoA Small PSD.

vane however, it is clear the periodic case is less accurate and generates a shallower accretion shape. There is good agreement at the 50% test time between the shadowgraph, and both simulations. However, at the 100% test time, the periodic case significantly under predicts the accretion shape. This suggests the 2D assumption is not sufficient to model the stator accretion, the under-prediction is more apparent at the 100% test time, here the particles will be experiencing freestream conditions at impact which may exacerbate erosion and fragmentation.

8.7.1.2 Full Three-Dimensional Domain

Figure 8.19 shows TR842 the 0° A.o.A case. The plot displays the full three-dimensional domain results at the 1/4, 1/2 and 3/4 span positions of the stator respectively. The experimental profile at the 1/4 span position (measured from the fixed end) appears to show the least accurate ice profile compared to the other span locations.

Full 3D simulations appear to better predict leading edge growth and overall accretion shape at the 1/2 and 3/4 span positions, particularly the sharp leading-edge ice shape which appears to move upwards as the ice accretion thickness increases. This would likely be due to drift in stagnation point caused by accreted ice. The highest simulated values for TWC occur at the tunnel centre-line which as we can see demonstrated in

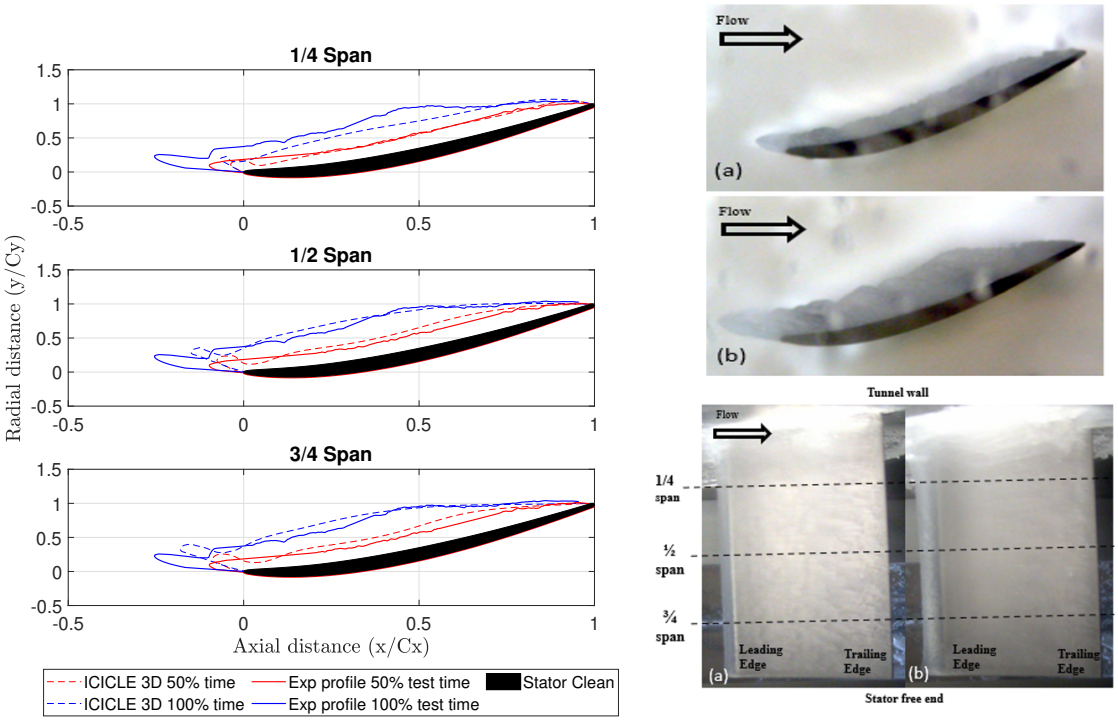

(i) **(ii)**

Figure 8.19: (i) Comparison of simulated ice accretion in ICICLE 3D and experimental shadowgraph data from TR 842 0° AoA Small PSD. (ii) Experimental test images at 50% and 100% test times. Top 2 images are side on - shadowgraph plane, Bottom 2 images are top down view. Note these images are not to scale.

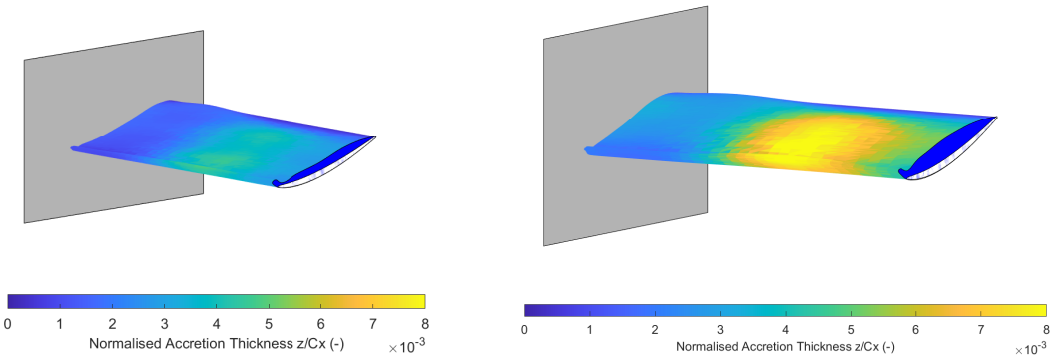

(i) **(ii)**

Figure 8.20: Accretion Thickness normalised by axial chord length (i) 50% Test Time (ii) 100% Test Time Test Run 842

Figures 8.6(i) and 8.7(ii). Due to the inverse relationship between TWC and Melt Ratio, the highest Melt Ratio is found at the tunnel wall (0 span) which corresponds with the lowest TWC value. This generates a different response to the experimental result, for

example in Figure 8.19(ii) in the bottom images, you can observe a larger accretion at the tunnel wall. This is likely due to runback water traversing the tunnel wall and increasing the accretion mass flux at the vane built-in end.

Figure 8.20 shows the ICICLE 3D outputs for the accretion surface, coloured by its thickness, normalised by the axial chord length (C_x). It is clear the accretion 'horn' shape is well captured and overall the maximum accretion is centred around the right half of the stator span. This corresponds to the centre 'core' region of highest TWC.

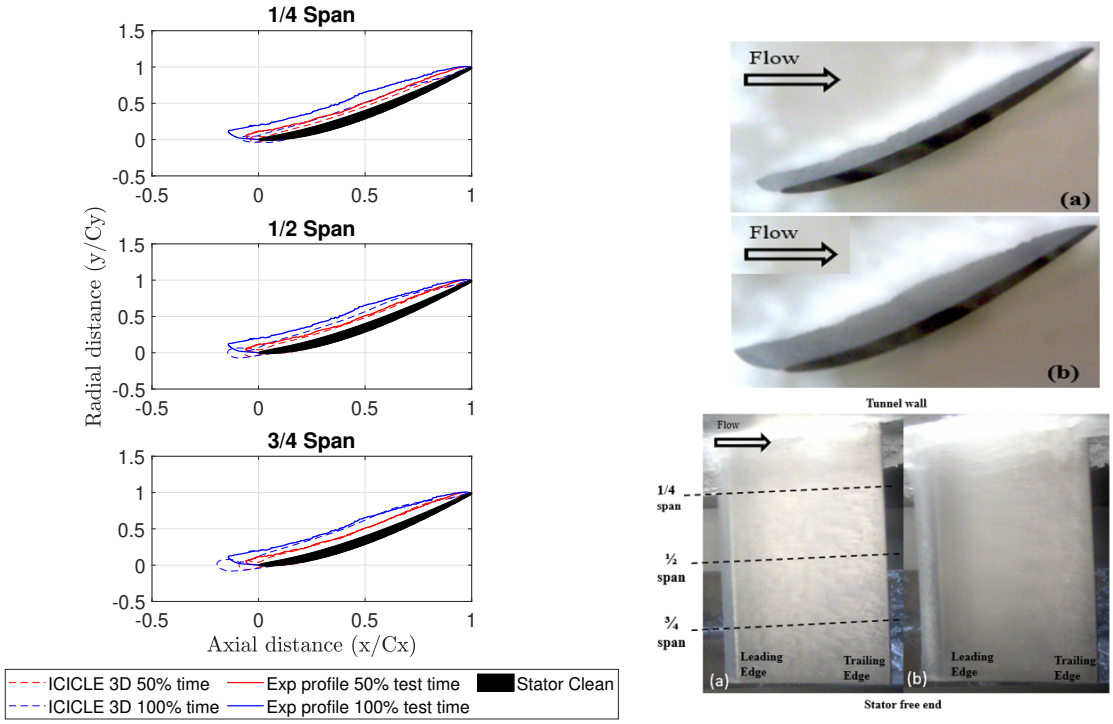

(i) (ii)

Figure 8.21: (i) Comparison of simulated ice accretion in ICICLE 3D and experimental shadowgraph data from TR 854 $+10°$ AoA Small PSD. (ii) Experimental test images at 50% and 100% test times. Top 2 images are side on - shadowgraph plane, Bottom 2 images are top down view. Note these images are not to scale.

Figures 8.21 and 8.22 detail the same simulation results arrangement for Test Case 854 at +10° angle of attack. In this orientation, the stator is certainly stalled, as there is no cascade to turn the flow, this is insignificant to the capture of ice at the surface, but will not be representative of local flow disturbances near the leading edge. The stator experience a significant sharp ice 'horn' illustrated in Figure 8.21(ii). This is captured effectively by the simulation result in 8.21(i), with a bias towards the 1/2 and 3/4 span

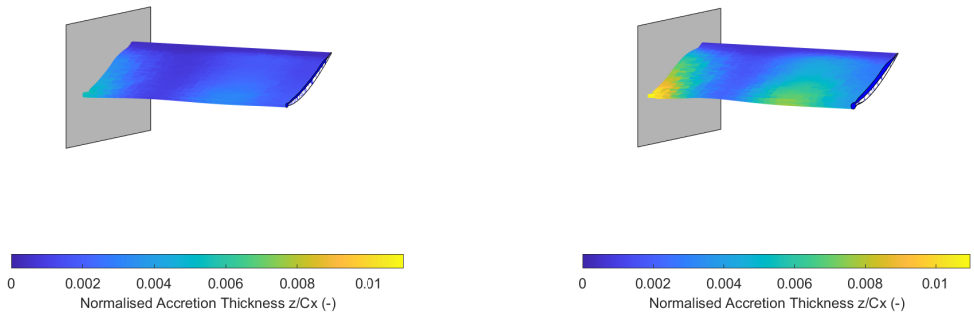

(i) **(ii)**

Figure 8.22: Accretion Thickness normalised by axial chord length (i) 50% Test Time (ii) 100% Test Time Test Run 854

positions where TWC is highest. This complements the results seen for TR842 and suggests ICICLE is effective in predicting the total accretion volume and sharp leading edge protuberances observed in compressor stator icing.

8.7.2 Three-dimensional DIC Data

Two cases at different $A.o.A$ were evaluated and simulated in ICICLE 3D to compare against three-dimensional ice accretion measurements using the DIC system discussed earlier. This generates a point cloud of ice heights over the stator surface which could be compared against three-dimensional simulations. Simulations used a frozen flowfield with no updating across EMM-C timesteps, this is due to the challenges relating to mesh quality and computational cost. Connolly et al. [34] demonstrated the importance in the effect on collection efficiency. Connolly et al. found that the shape effect is insensitive until the accretion thickness has exceeded 10% of chord length. The initial substrate cooling occurs over 5-10 seconds and it the most important feature to capture accretion onset. There will be an overprediction due to this approach within each test case. Table 8.5 summarises the tunnel working section measured conditions for each case.

Figure 8.23 shows the DIC measurement along with ICICLE 3D results, overlaid on the stator body. The spanwise ice thickness distributions are shown to illustrate each position. Figure 8.23 illustrates the DIC measurement area, localized to the ½

Table 8.5: Three-Dimensional Validation Study: Gas Properties

Run	**Mach**	$\mathbf{P_0}$	$\mathbf{T_0}$	$\mathbf{T_s}$	$\mathbf{T_{wb0}}$	$\mathbf{RH_0}$	**TWC**	**MR**	**AoA**
	(-)	(kPa)	(K)	(K)	(K)	(%)	(g/m^3)	(%)	(°)
485	0.4	34.5	283.3	274.5	274.25	38.3	7.45	5.19	+1.5
495	0.4	34.5	284.2	274.5	274.45	33.5	4.28	5.48	-1.5

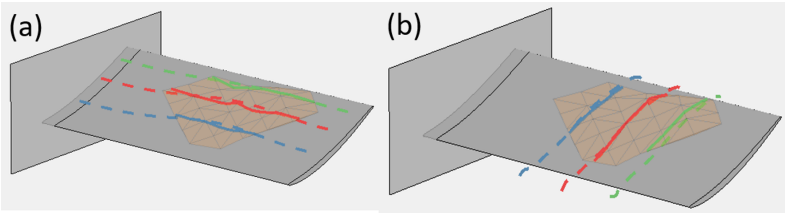

Figure 8.23: DIC measurement area overlaid with ice thickness (i) spanwise distribution and (ii) chordwise distribution for TR 485 at 100% test time.

span to free-end portion of the stator vane. DIC measurements were time-averaged over 10-20 seconds and are displayed in a chordwise and spanwise distributions shown in Figures 8.24 and Figure 8.27.

The three-dimensional ice accretion thickness measurements from the DIC system are calculated as a surface generated through Delaunay-triangulation within MATLAB. This surface is then averaged in the chordwise and spanwise directions respectively by generating an interpolation spline at fixed chord and span locations. Figure 8.24 illustrates the results of this for Test Run 485. In Figure 8.24(i) the accretion shape matches effectively over the mid-chord for the each of the span locations (measured from the built-in end). At the 50% and 75% span locations, the line intersects with the edge portion of the DIC measurement area, as shown in Figure 8.23, which produces a thickness measurement only at the rear portion of the stator surface. In 8.24(ii), there is good agreement at the 25% and 75% chord positions between ICICLE and the DIC measurements. The mid-chord, 50% position in ICICLE has a slight deviation from the DIC measurement. This may be an effect of the erosion model tuning.

Looking at the experimental ice accretion thicknesses in Figure 8.25, there is a larger accretion thickness observed at the tip and root locations in the top down R-H images. The tunnel wall end has higher accretion compared to the mid-span due to the water and ice running along the wall and combining with the vane. This is not considered

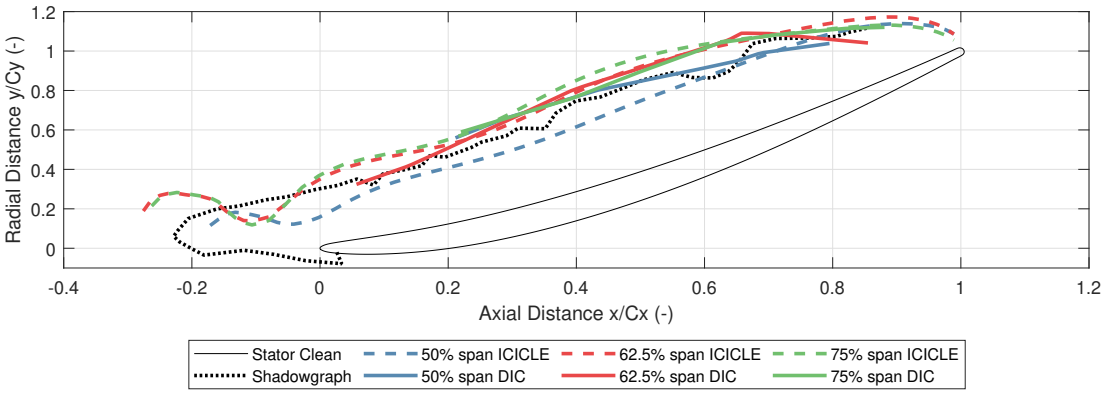

(i)

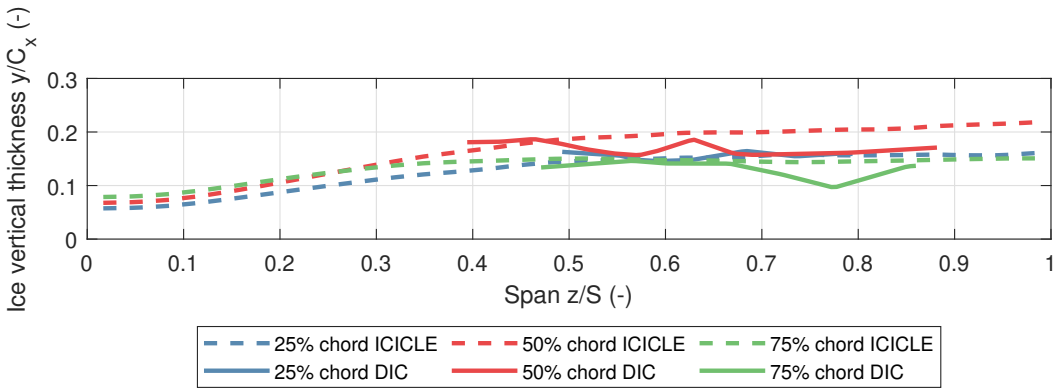

(ii)

Figure 8.24: Comparison of simulated ice accretion in ICICLE 3D and experimental shadowgraph data from TR 485 $-1.5°$ AoA Small PSD. ICICLE Simulation results for TR485 overlaid with shadowgraph and spatially averaged DIC measurements in (i) Chordwise distribution and (ii) Spanwise distribution

where accretion at two surfaces combine together. Additionally, the free-end near to the centreline corresponds with the highest TWC which will result in a peak in accretion.

Figure 8.27(i) and Figure 8.27(ii) show the same plot arrangement as above for Test Run 495 which is at $-1.5°$ angle of attack. This will have a lower frontal area and less separation around the pressure surface. It is clear in Figure 8.27(ii) the vertical thickness is more constant between span of 0.4 to 1. There a slight inflection between 0.7 and 0.8. This will correspond with the lowest Melt Ratio at the centre line position.

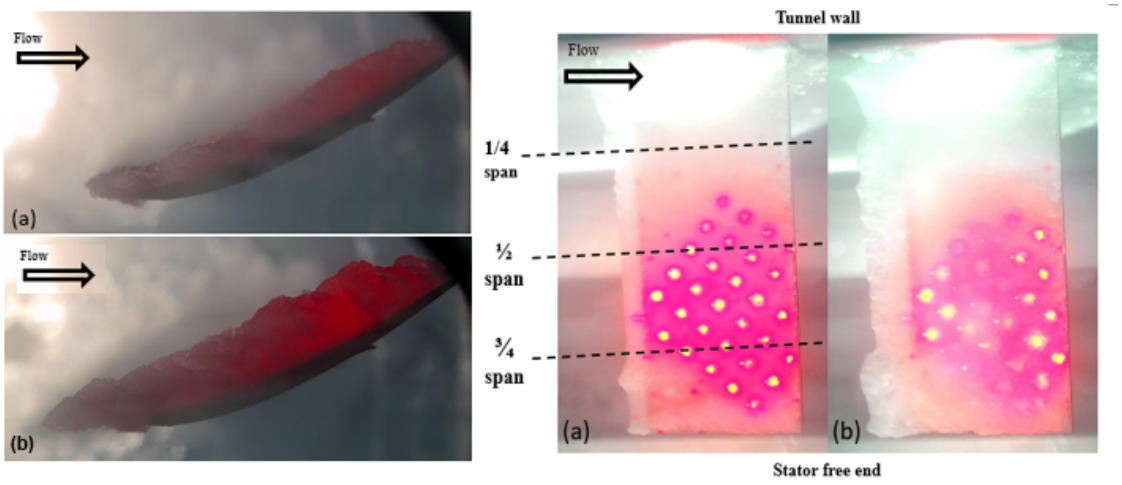

Figure 8.25: Test Case 485 $-1.5°$ AoA Small PSD. Experimental test images at (a) 50% and (b) 100% test times. Left 2 images are side on - shadowgraph plane, Right 2 images are top down view. Note these images are not to scale.

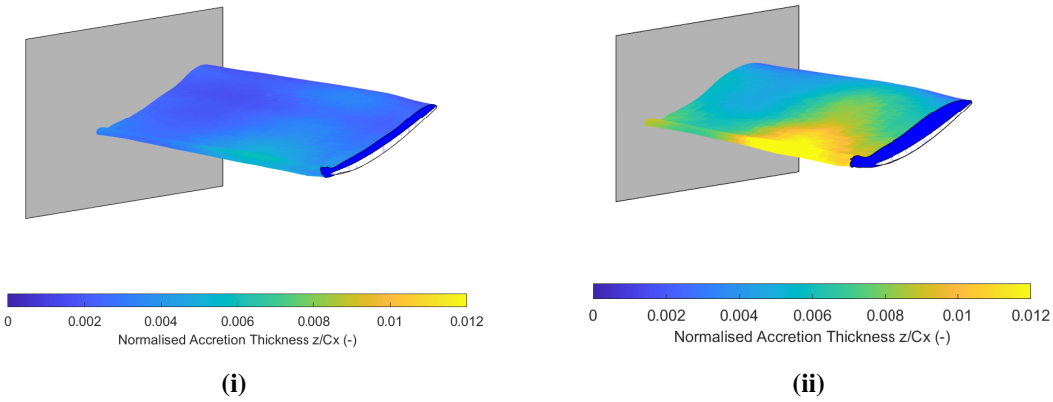

Figure 8.26: Accretion Thickness normalised by axial chord length (i) 50% Test Time (ii) 100% Test Time Test Run 495

8.8 Summary

Ice crystal icing modelling in three-dimensions is limited by the availability of experimental data and the effective modelling of icing wind tunnel conditions. This chapter involved validation of the complete ICICLE simulation environment to model warmed surface ICI accretion in three-dimensions and validate with experimental data at engine realistic conditions. This model expanded an existing icing physics and CFD modelling suite to three-dimensions with a new experimentally derived three-dimensional inlet particle melt and concentration to examine ice accretion experimental results from the

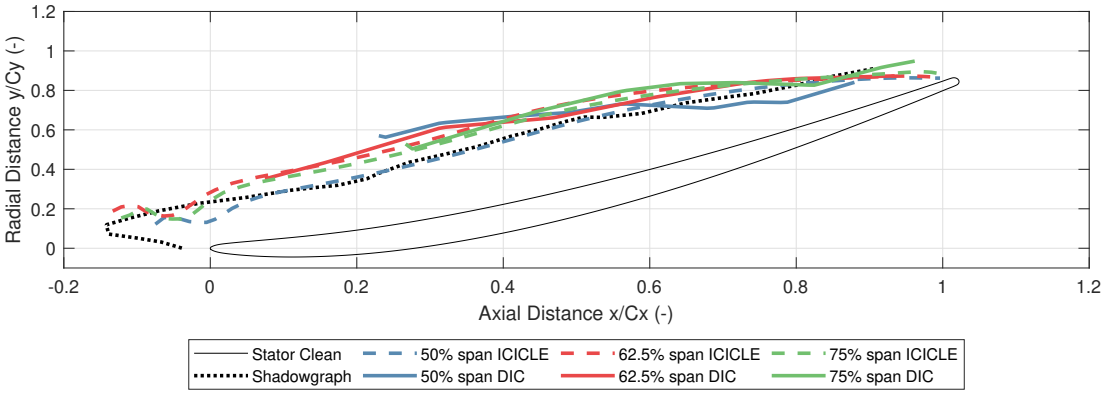

(i)

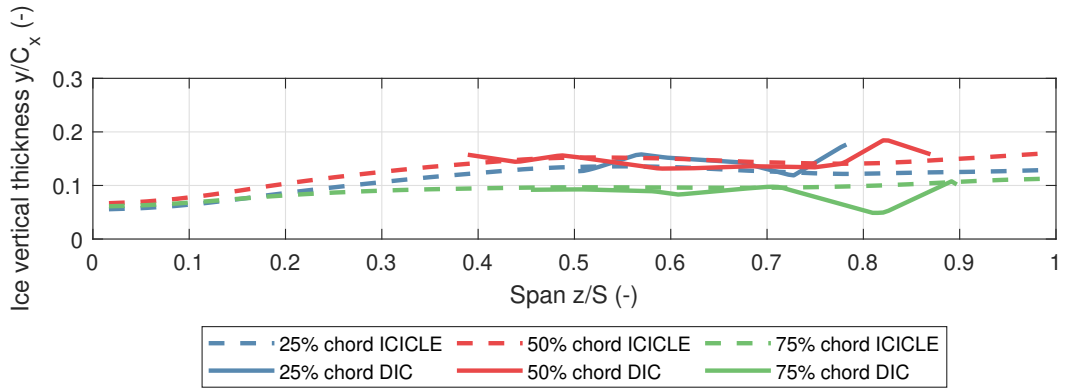

(ii)

Figure 8.27: Comparison of simulated ice accretion in ICICLE 3D and experimental shadowgraph data from TR 495 $+1.5°$ AoA Small PSD. ICICLE Simulation results for TR495 overlaid with shadowgraph and spatially averaged DIC measurements in (i) Chordwise distribution and (ii) Spanwise distribution

RATFac icing wind tunnel.

1. In simulating stator vane experimental conditions, the ICICLE 3D model generates good agreement at the 1/2 and 3/4 span positions and along the mid-chord for ice thickness results. The leading-edge ice accretion shapes are well predicted, specifically the sharp leading-edge growth shape and the appearance of an upwards growing ice horn shape. A combination of a lack of flowfield update and the sharp geometry will result in discrepancy in the ice accretion height prediction, due to particle impingement efficiency variation as ice thickness increases throughout the simulation, this effect was demonstrated by Connolly et al. [34].

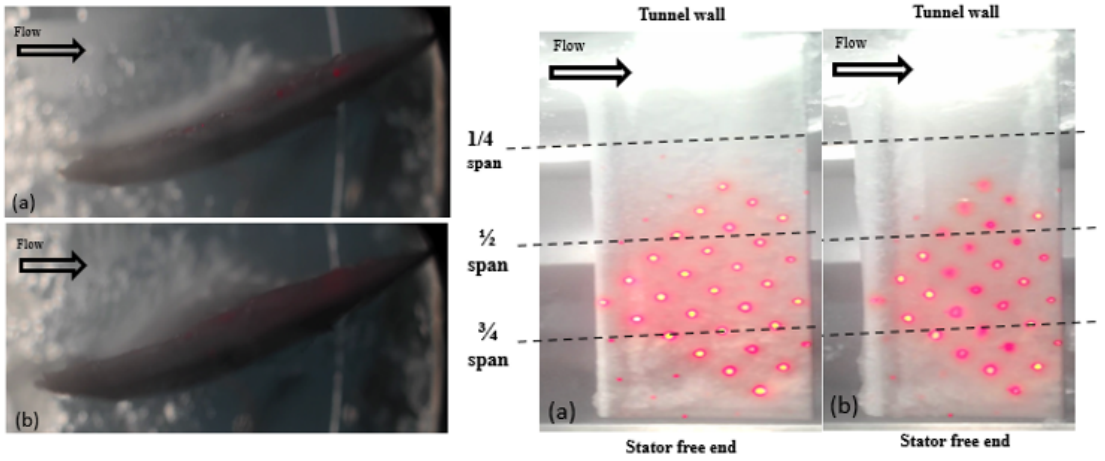

Figure 8.28: Test Case 495 $+1.5°$ AoA Small PSD. Experimental test images at (a) 50% and (b) 100% test times. Left 2 images are side on - shadowgraph plane, Right 2 images are top down view. Note these images are not to scale.

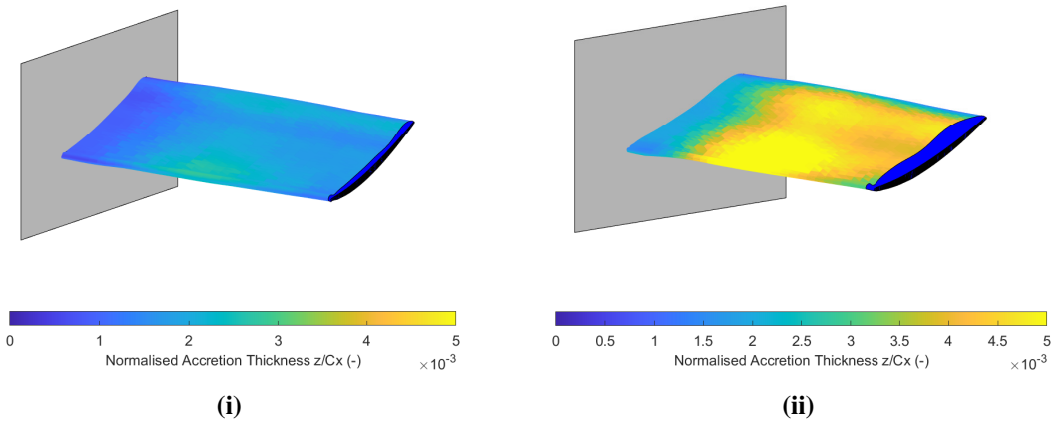

Figure 8.29: Accretion Thickness normalised by axial chord length (i) 50% Test Time (ii) 100% Test Time Test Run 495

2. Comparison to three-dimensional ice accretion DIC results shows that ICICLE 3D predicts the mid chord and leading-edge ice accretion thickness effectively which compares well to two-dimensional shadowgraph data. Across the span of the DIC measurement area, ICICLE 3D matches well and produces a similar accretion leading edge 'horn' shape as observed in experiments. Additionally, 3D spatial measurements of ice accretion thickness are necessary to validate and improve the accuracy of ICI accretion models given the sensitivity to local flow conditions and its application to flows within compressors and rotating stages.

3. Within most literature simulations, TWC is assumed to be a bulk property based on experimental conditions, this is clearly not the case and an inappropriate assumption for flowfields with significant variations in temperature and velocity, this is very important for accurately predicting the mass flux and melting over an accretion surface.

4. It is evident from top down views and three-dimensional simulations and DIC measurements that ICICLE 3D may underpredict close to the tunnel wall. This is due to the lower TWC values associated with this location, this model does not consider accretion and water runback at intersecting surfaces, therefore ice accretion mass will be underpredicted at the stator root.

5. This model provides a basis for validation of three-dimensional ice accretion simulation in compressor-accretion conditions. An expansion to rotating reference frames and an application to a turbomachinery flowfield would be necessary to generate accurate compressor accretion predictions.

9 Thesis Summary

9.1 Conclusions

This project involved a closer look at the numerical and overall system approach to ice crystal icing transport and accretion. Until recently, the common approach to modelling accretion involved simplified two-dimensional cases compared to experiments or complex three-dimensional case studies with no appreciable validation or accuracy assessments. This work aimed to advance the accuracy and individual models pertaining to icing and examine three dimensional transport and accretion data. The increase in accuracy when compared to existing approaches, has been demonstrated by the influence of turbophoresis and two-way coupling on the concentration (TWC) and melt ratio.

1. This work specifically focused on warmed substrate accretion relating to compressor ice crystal icing. Part of the work involved expansion of an existing code to three-dimensions in each aspect. A particle transport model was established with additional turbophoresis and two-way mass energy coupling introduced. This is very important for applying to real turbomachinery cases with wall bounded, highly turbulent, accelerating flows. It was found that turbophoresis and two-way coupling bridged the gap between the existing state of the art transport model results. An

increased melting rate for smaller particulates of up to when considering two-way coupling is important in turbomachinery as these particles will interact with walls, vanes and encourage accretion initiation.

2. A numerical scheme was introduced to account for the complex experimental setup we see in altitude icing facilities. Probes cannot measure properties all at once in the same position. Ice crystal icing is an inherent transient problem, this means it is necessary to produce a multi-step simulation, validation methodology. This is directly applicable to testing in icing facilities. Assessment of test conditions and dimensionality reduction of test matrices is possible with a robust simulation tool generating comparable conditions.

3. Inclusion of turbophoresis produces a more realistic description of TWC and enhances the bulk melt ratio by up to 10% for a turbulence intensity of 4% to 6%. Two-way coupling generates a correction to the evaporation rate and reduces the overall TWC compared to one-way coupling. The accuracy of these models were evaluated using a convergence metric, determining an injection density of $N > 6 \times 10^6$ to describe the RATFac ice cloud size distribution and turbulent dispersion conditions numerically. Accretion modelling was applied to simplified cone and engine representative stator cases from the RATFac campaigns conducted by previous colleagues. These enabled the demonstration of the improvements in model fidelity.

4. There was a significant contribution to improvements in numerical integration and modelling for ice crystal icing particles interacting with the gas-phase and surfaces respectively. Particle tracking was performed using a dual time stepping (DTS) method for two-way coupling to enable unsteadiness in the gas-phase along the particle residence time. Impact at the surface is a well studied phenomena in solid and mixed phase particles. However, ice crystal icing lacks accurate representation of roughened surfaces with respect to impact and surface-gas heat transfer. A literature stochastic bounce model representing a isotropic rough

wall was introduced and generated an appreciable change in mass and melting distribution after a single impact event.

5. Simulation of mixed phase warmed substrate accretion was conducted against a series of representative compressor stator vane icing experiments. Previous experimental data for the particle cloud, gas, vane temperature and ice accretion thickness distributions were compared against an updated three-dimensional ice crystal icing accretion model. A peak mass concentration of ice and water, or total water content, was observed at the tunnel centreline, corresponding to the lowest particle cloud Melt Ratio. The total water content near the walls was lowest, but Melt Ratio highest. The at wall conditions corresponded to excess accretion on the representative stator vane root. This suggests the current sticking models may be insufficient or the water and ice sliding downstream along the walls is not captured.

6. Ice accretion is a by product of a sufficient impinging mass flux combined with a net negative energy balance from sensible, evaporative and convective cooling. The influence of runback water energy recovery was investigated to assess the impact of unsteady mass exchange. Lastly, conduction through the substrate was investigated as it is applicable in compressor icing cases where gas and metal temperatures are transient and ice or water ingested can have a wet compression effect changing the compressor performance.

7. This model did not consider any rotating components or mixing planes, however it is important to understand the capability and complexity of each sub model and its effects on the melting response and accretion magnitude. This provides a basis for further test condition identification which can significantly reduce the test matrix scope for an engine manufacturer for example. Identifying specific gas-vapour and particle cloud conditions within ICICLE initially would reduce the need for exhaustive calibration, shakedown studies.

The work has advanced the understanding of the individual physical processes involved in ice crystal icing. Expanding the modelling fidelity and capability to include unsteady

two-way coupling and turbophoresis has further identified which models have the greatest effect on ice crystal icing transport and accretion. Accurately defining the particle melt ratio and concentration (TWC) is important when describing glaciated, naturally melting ice crystal events such as those experienced by turbofan engines. This is of profound importance for identifying specific turbofan compressor icing threat conditions which can result in excess maintenance costs, vibration, engine damage and overly conservative, inefficient designs.

9.2 Further Work

The next steps and wider area in this body of research are driven by the different application areas for the work.

First, a primary aim of the work is to apply it to model turbomachinery. To do so the code needs to be extended to account for rotating frames of reference and mixing plane considerations. This will have implications for two-way coupling and particle phase change modelling. Second, the computational resource requirements for these models are very high. It would be pertinent to perform model order or dimensionality reduction given the vast problem space. This will make the models less generalised, but could stitch the gap between full fidelity models and a reduced order model representing the most sensitive variables. Beyond this the following requires onwards work.

1. Model validation: a wider validation data set needs to be examined for transport and accretion simulations. This would come from literature/NACA cases. Generating an ‘open-source’ icing repository for representative compressor geometries would be useful for cross comparison between existing literature models.

2. Ice accretion at intersections: considering the ice accretion shapes which developed at the stator tip and root, it is important to focus on expanding the fidelity of the accretion model to deal with ice growing at corners or joins. This is particularly relevant to turbomachinery icing at the outer annulus.

3. Momentum coupling in three-dimensions: Considering the volume fraction of ice crystals and accretion growths, it is vital to model two-way coupling (or effectively 4-way coupling) between the gas and particle phases. This further requires impact and agglomeration modelling between particles and the effects on mass dispersion and melting response.

4. Experiments: The use of this model to predict and scope experimental conditions should be exploited. This has a significant impact on the overall cost and the design of ice crystal icing experiments.

Appendices

List of Figures

1.1 Engine powerloss events from Boeing database as of Jan 2019 [17]. . . 2

1.2 Ultrafan turbofan schematic, red box shows the likely ICI sites adapted from [119]. 3

1.3 Ice crystal icing FAR14 Part 33 Appendix D certification envelope. . . . 4

2.1 Particle shapes measured by Heymsfield et al. in a tropical atmosphere experiment conducted in deep convective clouds [69, 70]. 11

2.2 Oblate ($E < 1$) and Prolate ($E > 1$) spheroid geometry with respect to principal axes. 14

2.3 Median Mass Diameter distribution relationships from Darwin 2014 (Dxx) and Cayenne 2015 (Cxx) HAIC/HIWC field campaign test flight data [87] 17

2.4 Particle deposition for fully developed pipe flow experimental data, taken from [159]. ICI regime particles present in compressor flows have non-dim. particle relaxation times corresponding to the red arrow region. . . 24

2.5 Particle coupling regimes depending on the volume fraction α_p in disperse particle flows represented by Lagrange-Euler modelling. Taken from [55] adapted from [45] 26

2.6 Sticking probability for ICI axi-symmetric cone tests conducted at NRC RATFac by Bucknell et al. [23]. 30

2.7 Simulated Rough Wall Collision with Correction vector $\mathbf{n}_\gamma$. Taken from [113]. 34

2.8 EMM-C 3 layer Stefan problem representing ice accretion on warmed surfaces [25]. 36
2.9 Surface mesh evolution with local volume conservation. Tong's model is iceSurf with single layer MM and multi-layer MM implementation. Compared with existing LEWICE model with no volume conservation. Taken from Tong et al. [134]. 39
2.10 Tet Prism Surface Redefinition for ICI Accretion Extrusion taken from Porter et al. [110]. 39
2.11 Comparison of ONERA's ICI Two-Dimensional Code IGLOO2D and an implementation of LEWICE (ONICE2D) using experimental ice shapes obtained in the Icing Research Tunnel at NASA's Glenn Research Centre taken from [137]. 40
2.12 Comparison of 3D accretion shapes from SUNSET-2 Program database taken from [111, 112]. 41
2.13 Ice Crystal Icing ComputationaL environment developed by Oxford Thermofluids Institute. 44
2.14 Stator RATFac test and simulation results from ICICLE at a range of MR values [22]. 45
2.15 Stator experimental test data and simulations from ICICLE incl. flowfield updating. 46

3.1 ICICLE 3D Software Environment Flow Diagram showing key physics modules 50
3.2 Particle sphericity and orientation, specified relative to axial flow direction. 56
3.3 Lumped System Analysis for Melting Ice Crystals 60
3.4 Particle Bounce Stick Momentum Exchange Model in Generalised 3D. . 63
3.5 Particle impact visualised: (1) adaptive near-wall timestepping to improve slip velocity gradient at wall. (2) Projected particle offset along normal vector for accurate gas property calculation. 63
3.6 Examination of Stick Probability Models from literature. 65
3.7 Iced Roughness Height Schematic with Mean Roughness R illustrated . 66

3.8 (i)Virtual Wall Projection with Angle Correction Representing Isotropic Rough Wall in 2D (ii) Rough Wall Impact Considering Sommerfeld Distribution defined by β, γ 67
3.9 Sommerfeld and Normal Gaussian PDF of γ for $\sigma_\gamma = 5°$. Using $\frac{d}{c_L} = 0.063$ 69
3.10 Accretion Model for Purely Liquid Runback Water 71
3.11 Ice Crystal Icing Accretion Model for a Cold Substrate 72
3.12 Ice Crystal Icing Accretion Model for a Warmed Substrate 73
3.13 Quad cell face extrusion using trapezoidal volume correction method along cell node normals. 80

4.1 Meshing Processor Flow Diagram for ICICLE, BOXERMesh logo taken from [26]. 82
4.2 Mass averaged Mach number at Kiel probe position. This example is for Test Case TR495 with steady state $Mach$ number of 0.391. 84
4.3 Flow Chart describing data exchange and running files for Oxford ARC HPC deployment. 85
4.4 RATFac Altitude Icing Wind Tunnel Inlet Section Schematic for CFD Domain Initialisation 87
4.5 RATFac Altitude Icing Wind Tunnel Working Section Schematic for CFD Domain Initialisation 87
4.6 RATFac Altitude Icing Wind Tunnel Boundary Conditions Schematic for CFD Domain Initialisation 88
4.7 Test article domain schematic detailing boundary conditions for multi-zone flowfield solver 88
4.8 (i) Simulated Total Temperature Distribution at TAT-RH Probe Measurement Plane for Example Case, (ii) 5$^{\text{th}}$ Order Polynomial Surface Fit for Temperature Distribution, Contour plot from (i) is plotted. 90
4.9 Flow chart for ICICLE 3D Particle Tracking module. Dual time stepping steady outer temporal loop and inner unsteady particle transport loop described. 94

4.10 Flow chart for ICICLE 3D Accretion module. Quasi steady outer temporal loop and inner unsteady temporal loop described. 95

5.1 (i) RATFac tunnel cross section with sensor axial positions displayed. (flow L-R) (ii) National Research Council of Canada - Research Altitude Test Facility [130]. 100

5.2 (i) Traverse path for CIKP TWC probe across the RATFac Tunnel inlet plane. Traverse path moves over the following positions: 0 -> 1 -> 2 -> 3 -> 4 -> 0. (ii) Total Water Content Traverse CIKP Probe Trace for Calibration Test Run TR644. 102

5.3 (i) CIKP in (top image) stowed/position 5 and (bottom image) position 2. (ii) TWC probe traverse measurement positions looking in the flow direction of the tunnel. 102

5.4 Raw experimental measurements from SEA Multi-Wire Probe. 103

5.5 Experimental measurements from SEA Multi-Wire Probe during core flow measurement survey. Here the steady conditions achieved after 350 seconds are used to describe the experimental LWC. 103

5.6 Experimental measurements for (a) 0%, (b) 50% and (c) 100% test times for 35° Cone Test Case 737. 104

5.7 (i) Representative prismatic compressor stator vane. (ii) Spanwise view of stator tip mounted in RATFac wind tunnel at 0% and 100% icing time for Test Case 854 [21]. 105

5.8 Ice Accretion Thickness Shadowgraph Measurement, taken from [21]. . 105

5.9 (i)Prismatic stator test piece used for ICI accretion test campaigns and 3D ICI accretion modelling [21]. (ii) Spanwise distribution of ice thickness from DIP imaging [33]. 106

6.1 (i) Cylindrical section is the plenum with warm humid air, the smaller rectangle is the ice injection pipe. Warm humid air mixes with the cold free jet and contracts into the working section. (ii) RATFac tunnel 1/2 cross-section slice showing tunnel inlet, ice injection pipe and measurement plane locations. 112

6.2 Normalised Gas Property vs. Mesh Count, Test Case: Full 3D RATFac Inlet Case. 112

6.3 Predicted Total Water Content distribution at tunnel CIKP measurement plane with changing particle injection counts. Experimental reading for TWC at Test 649 is 6.21gm$^{-}3$. 116

6.4 Particle Concentration χ_i per Injection Count N_i normalised by maximum (χ_i)for Convergence study with Turbophoresis and Rosin Rammler Size Distribution. Test Case: Full 3D RATFac Inlet Case. 117

6.5 Mean Absolute Difference in Particle Concentration χ_i per Injection Count N_i for Convergence study, normalised by maximum injection count. Test Case: Full 3D RATFac Inlet Case. 118

6.6 Mach Number study: (i) Total Water Content and (ii) Melt Ratio simulation results at probe measurement position. 119

6.7 Turbulence Intensity RATFac Realisable $k - \epsilon$ Model 120

6.8 Turbulence Intensity RATFac $k - \omega$ SST model 121

6.9 Turbulence Intensity RATFac Reynolds Stress Model 121

6.10 Turbulence model comparison: (i) Total Water Content and (ii) Melt Ratio simulation results at probe measurement position, Test Run 667. . 122

6.11 Turbophoresis model comparison: (i) Total Water Content and (ii) Melt Ratio simulation results at probe measurement position, Test Run 649. One-way coupling. 123

6.12 (i) Comparison of No Turbophoresis and With Turbophoresis simulation results for Test 649. (ii) TWC probe traverse measurement positions. Blue and red lines in (i) represent a slice through measurement positions. 124

6.13 Particle Shapes approximated as Oblate and Prolate spheroid shapes. Particle orientation within the study is specified by broad-wise and end-on configurations. 125

6.14 (i) Particle aspect ratio E vs 1/Particle Sphericity (ii) Particle Melting Ratio normalised by spherical particle Melt Ratio vs aspect ratio E. Oblate particles ($E << 1$) produces a higher melting augmentation driven primarily by higher surface area. 126

6.15 Particle Nusselt number vs 1 / particle sphericity, normalised by the Nusselt number of a spherical particle. Plotted for a range of Re values. 127

6.16 Bulk mean Melt Ratio normalised by spherical particle Melt Ratio vs 1/ particle sphericity 127

6.17 Comparison of diagonal extent simulation results against experiment for Test 649. The TWC contour plot in Fig. 6.24 shows the diagonal extents connecting traverse measurement positions. 130

6.18 One-Way Coupling Simulation results for Test Run 649, for TWC, including vertical and horizontal slices at CIKP probe traverse measurement positions. 131

6.19 Experimental readings for (i) Total Air Temperature and (ii) Recovery Relative Humidity measured by TAT-RH probe during Ice-on conditions. Test Run 651. 132

6.20 (i) Mean total temperature and (ii) Mean total relative humidity, at TAT-RH Probe plane compared to experimental results. Test Case 651. . . . 134

6.21 Two-Way Coupling Simulation results for Test Run 649, for TWC, including vertical and horizontal slices at CIKP probe traverse measurement positions. 135

6.22 Two-Way Coupling Simulation results for (i) TWC and (ii) MR at probe measurement positions. Test Case 651. 136

6.23 Test Run 651: Two-Way Coupling Simulation results for (i) TWC and (ii) MR at probe measurement positions. Experimental readings have been overlaid. 137

6.24 Test Run 651: Two-Way Coupling Simulation results for (i) TWC and (ii) TWC probe traverse measurement positions. Blue and red lines in (i) represent a slice through measurement positions. 138

6.25 Comparison of One-way and Two-way coupled simulation results for Test 644. The TWC contour plot in Fig. 6.24 shows the diagonal extents connecting traverse measurement positions. 139

6.26 Comparison of One-way and Two-way coupled simulation results for Test 649. The TWC contour plot in Fig. 6.24 shows the diagonal extents connecting traverse measurement positions. 139

6.27 Comparison of One-way and Two-way coupled simulation results for Test 651. The TWC contour plot in Fig. 6.24 shows the diagonal extents connecting traverse measurement positions. **Note: Largest PSD** is equivalent to **Largest Uncertainty Bounds** 140

7.1 Mach number contour plot for 35° Cone Test Case 737. 143

7.2 Particle trajectory plot for TR737 35° cone case to demonstrate (i) Smooth Wall b) Rough Wall Impact Considering Sommerfeld Distribution defined by β, γ. Note: Injection is 26 bin Rosin Rammler with 520,000 particles (26,000 injection sites). 144

7.3 Particle TWC and MR distribution at $\chi = 0.375$ axial position for Smooth and Rough wall impact models. Assumes $\sigma_{\gamma} = 5^{\circ}$ 145

7.4 Comparison of roughness diameter d informed boundary layer thickness term. Test Case 737, 35° cone. Top plot is 50% test time, Bottom plot 100%. 147

7.5 (i) Comparison of Smooth Wall and Stochastic Rough Wall models against ice accretion. Test Case 737, 35° cone. Top plot is 50% test time, Bottom plot 100%. (ii) Comparison between Smooth and Rough wall boundary conditions against accretion area ratio, normalised by clean cone cross sectional area. 148

8.1 Validation test cases for ICICLE. Representative engine stator vane (a) periodic endwall condition. (b) Full 3D RATFac tunnel simulation with tip-gap. 152

8.2 (i) ICEM Mesh of 'clean' stator geometry and tunnel working section. (ii) Mesh clustering at the stator wall to resolve the boundary layer to a Y+ < 5. 152

8.3 Mid-span slice of stator flow domain. 153

8.4 (i) FLUENT viscous flow simulation of prismatic stator test in RATFac icing wind tunnel. Cantilevered flow solution, taken at mid-span. (ii) Mach number distribution for cantilevered stator case taken at stator mid-chord. 153

8.5 Normalised distribution of total temperature at RATFac working section inlet relative to total temperature at full RATFac inlet centreline position, for ice injection temperature at 263K and RATFac inlet total temperature 265K. 154

8.6 (i) TWC Distribution at CIKP Measurement Plane (ii) Melt Ratio Distribution at MW Probe Measurement Plane. Test Run 485 155

8.7 (i) TWC Distribution at CIKP Measurement Plane (ii) Melt Ratio Distribution at MW Probe Measurement Plane. Test Run 495 156

8.8 Quad cell face extrusion using trapezoidal volume correction method along cell node normals. 157

8.9 (i) Nusselt number vs Normalised streamwise extent (-ve is suction surface) (ii) coefficient of pressure plot vs chordwise extent over stator surface for Test Run 485. 159

8.10 (i) Nusselt number vs Normalised streamwise extent (-ve is suction surface) (ii) coefficient of pressure plot vs chordwise extent over stator surface for Test Run 495. 159

8.11 Ice and Water thickness on left y axis, Stefan and Substrate temperature on right y axisvs exposure time for (i) Adiabatic Wall - Recovery Wet Bulb (ii) Thin Film Equation with Wall Conduction. B is ice thickness, h,i is inner water film thickness and h,o is outer water film thickness. . . 160

8.12 Thermocouple (TC) response from experiments channel 1 and 2, are embedded at the mid-chord at the centreline location, these are compared to predicted substrate temperature in EMM simulation for Test Run 495. (Thermocouple data is from a different test run as 495 was not available, gas conditions are matched however TWC is $3.79 g/m^3$ compared to $4.28 g/m^3$ for TR495.) 161

8.13 Total, Ice and Water thicknesses vs exposure time for infinite thermal capacity and 1D steady conduction. 161

8.14 Normalised Accretion Thickness results for Stator Vane test case with (i) T_{wall} fixed to recovery temperature T_r and (ii) T_{wall} determined by conduction and experimental initial conditions. 162

8.15 Heat flux components at surface for (i) Adiabatic Wall and (ii)Thin Film Equation with Wall Conduction 162

8.16 (i) TR854 leading edge accretion (ii) coefficient of pressure plot vs chordwise extent over stator surface for Test Run 854 with accretion minimum adhesion pressure coefficient shown(Bottom image in (i)). . . 163

8.17 (i) Tangential Velocity component at the edge of boundary layer for TR495 stator test case. +ve U_z will concentrate accretion towards the centreline due to tip leakage effects. (ii) Stator test article looking towards the pressure surface from slightly upstream. (Equivalent to plot) Inset image: Top down view. 164

8.18 Comparison of simulated ice accretion in ICICLE 3D for periodic (infinite-span, 2D flowfield representation) and full 3D numerical flowfield. This is plotted against experimental shadow-graph data from TR 842 0° AoA Small PSD. 166

8.19 (i) Comparison of simulated ice accretion in ICICLE 3D and experimental shadow-graph data from TR 842 0° AoA Small PSD. (ii) Experimental test images at 50% and 100% test times. Top 2 images are side on - shadowgraph plane, Bottom 2 images are top down view. Note these images are not to scale. 167

8.20 Accretion Thickness normalised by axial chord length (i) 50% Test Time (ii) 100% Test Time Test Run 842 167

8.21 (i) Comparison of simulated ice accretion in ICICLE 3D and experimental shadow-graph data from TR 854 $+10^\circ$ AoA Small PSD. (ii) Experimental test images at 50% and 100% test times. Top 2 images are side on - shadowgraph plane, Bottom 2 images are top down view. Note these images are not to scale. 168

8.22 Accretion Thickness normalised by axial chord length (i) 50% Test Time (ii) 100% Test Time Test Run 854 169

8.23 DIC measurement area overlaid with ice thickness (i) spanwise distribution and (ii) chordwise distribution for TR 485 at 100% test time. 170

8.24 Comparison of simulated ice accretion in ICICLE 3D and experimental shadow-graph data from TR 485 -1.5° AoA Small PSD. ICICLE Simulation results for TR485 overlaid with shadowgraph and spatially averaged DIC measurements in (i) Chordwise distribution and (ii) Spanwise distribution 171

8.25 Test Case 485 -1.5° AoA Small PSD. Experimental test images at (a) 50% and (b) 100% test times. Left 2 images are side on - shadowgraph plane, Right 2 images are top down view. Note these images are not to scale. 172

8.26 Accretion Thickness normalised by axial chord length (i) 50% Test Time (ii) 100% Test Time Test Run 495 172

8.27 Comparison of simulated ice accretion in ICICLE 3D and experimental shadow-graph data from TR 495 $+1.5^{\circ}$ AoA Small PSD. ICICLE Simulation results for TR495 overlaid with shadowgraph and spatially averaged DIC measurements in (i) Chordwise distribution and (ii) Spanwise distribution 173

8.28 Test Case 495 $+1.5^{\circ}$ AoA Small PSD. Experimental test images at (a) 50% and (b) 100% test times. Left 2 images are side on - shadowgraph plane, Right 2 images are top down view. Note these images are not to scale. 174

8.29 Accretion Thickness normalised by axial chord length (i) 50% Test Time (ii) 100% Test Time Test Run 495 174

A.1 Total Water Content Traverse CIKP Probe Trace for Calibration Test Run 644. Measurement positions 0-4 correspond to each measurement interval. 197

A.2 Total Water Content Traverse CIKP Probe Trace for Calibration Test Run 649. Measurement positions 0-4 correspond to each measurement interval. 197

A.3 Test Run 644: Two-Way Coupling Simulation results for (i) TWC and (ii) MR at probe measurement positions. Blue and red lines in (i) represent a slice through measurement positions. 198

A.4 Test Run 649: Two-Way Coupling Simulation results for (i) TWC and (ii) MR at probe measurement positions. Blue and red lines in (i) represent a slice through measurement positions. 198

A.5 Test Run 644: Two-Way Coupling Simulation results for (i) TWC and (ii) MR at probe measurement positions. Experimental readings have been overlaid. 199

A.6 Test Run 649: Two-Way Coupling Simulation results for (i) TWC and (ii) MR at probe measurement positions. Experimental readings have been overlaid. 199

B.1 NASA PSL-3 Altitude icing wind tunnel facility, with ALF502 R5 LF01 installed [103]. 201

B.2 National Research Council of Canada - Research Altitude Test Facility icing wind tunnel [130]. 202

B.3 (i) Lycoming ALF502 - R5 LF01 Flight Test Engine used to recreate ICI conditions causing un-commanded rollback [104]. (ii) Ice Crystal Icing observed on the outer shroud downstream of the ALF502 EGV's [49]. . 204

B.4 N1 and thermocouple readings for a range of TWC settings indicating engine rollback and corresponding EGV and shroud cooling [49]. . . . 205

B.5 (i) RATFac tunnel cross section with sensors and ALF502 vane segment displayed. (ii) Lycoming ALF502 - R5 LF01 LP compressor booster stage EGV segment [54]. 205

List of Tables

1.1 Ultrafan Turbofan Schematic Labels and Descriptions 3

2.1 Existing Two-Dimensional Numerical Icing Software 42
2.2 Existing Three-Dimensional Numerical Icing Software 42

3.1 Ice Crystal Icing ComputationaL Environment Model Updates 52
3.2 K-D Tree Fluid Cell Search Algorithm 54

4.1 Saturation Vapour Pressure for Ice, Polynomial coefficients 91
4.2 Saturation Vapour Pressure for Water, Polynomial coefficients 91

5.1 Oxford Icing Experiments [21, 23, 24, 31–33] 99
5.2 Calibration Tests: RATFac Test Campaign Data 107
5.3 Cone Test Article: RATFac Test Campaign Data 108
5.4 Stator Test Article: RATFac Test Campaign 108

6.1 RATFac Turbulence Intensity Measurements from [81] 113
6.2 Particle Size Distribution Statistics for Convergence Study 115
6.3 Mach Number Study: Gas Properties 119
6.4 Particle Injection Statistics for Validation Study 136

8.1 Summary of mesh characteristics for prismatic stator test cases. 152
8.2 Particle Injection Statistics for Stator Test Cases 155
8.3 Heat Transfer Correlations 158
8.4 Two Dimensional Comparison: Gas Properties 165
8.5 Three-Dimensional Validation Study: Gas Properties 170

B.1 Ice Crystal Icing Experimental Facilities [11, 31, 50, 81, 102, 121, 126, 131] 203

A Experimental Conditions

A.1 Experimental Readings

Test runs 644, 649 and 651 form the basis for validation of the ICICLE 3D particle transport model. The following summarises the TWC measurements conducted through tunnel measurement plane traverse readings. Figure A.1 and A.2 are the processed TWC data for the CIKP probe surveys conducted for the calibration data set in Chapter 5.

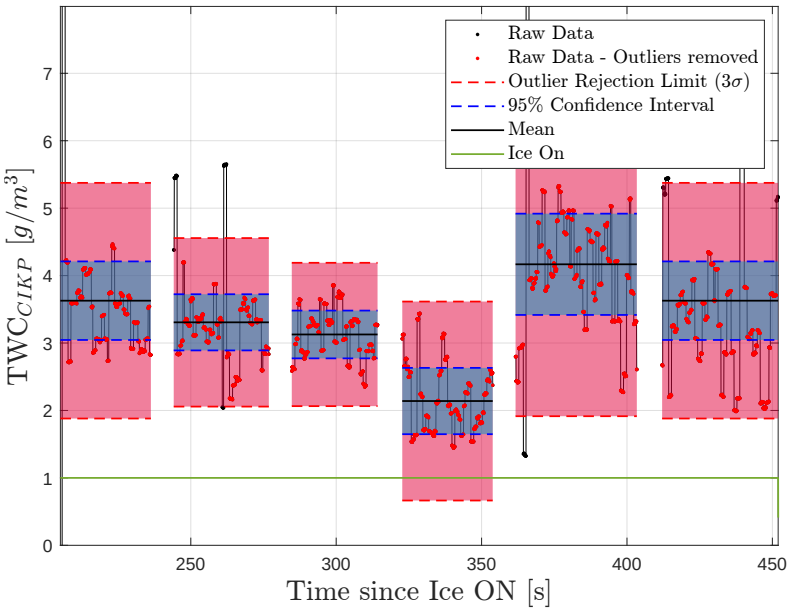

Figure A.1: Total Water Content Traverse CIKP Probe Trace for Calibration Test Run 644. Measurement positions 0-4 correspond to each measurement interval.

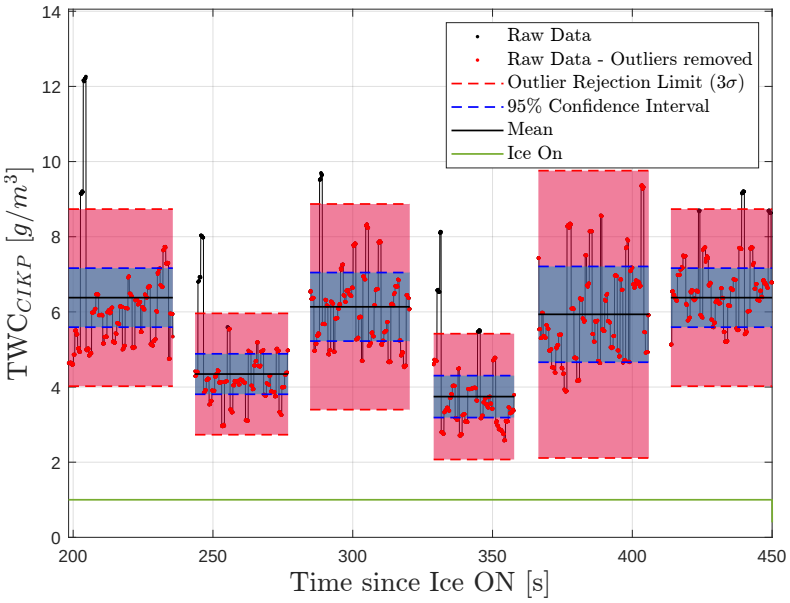

Figure A.2: Total Water Content Traverse CIKP Probe Trace for Calibration Test Run 649. Measurement positions 0-4 correspond to each measurement interval.

A.1.1 Spatial Distributions of TWC and MR

Additional ICICLE 3D simulation results for Test Runs 644 and 649 are reported below for completeness. These are the output TWC and MR results from simulations of the RATFac inlet, contraction and working section through to the measurement plane.

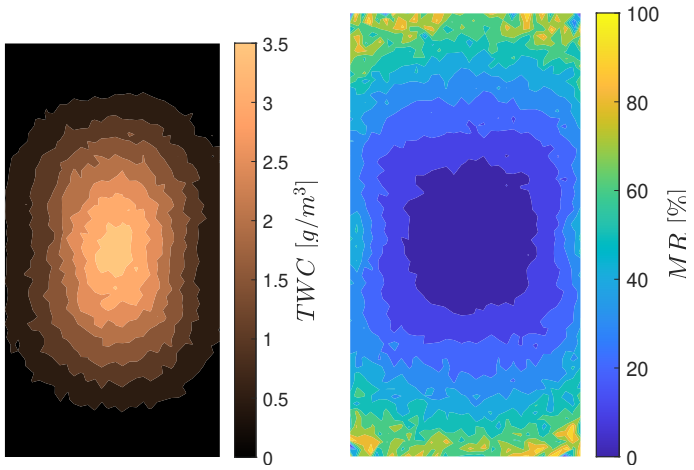

Figure A.3: Test Run 644: Two-Way Coupling Simulation results for (i) TWC and (ii) MR at probe measurement positions. Blue and red lines in (i) represent a slice through measurement positions.

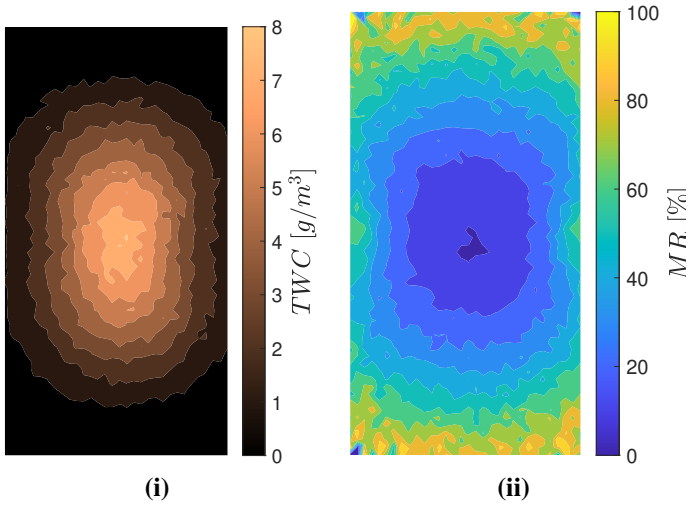

Figure A.4: Test Run 649: Two-Way Coupling Simulation results for (i) TWC and (ii) MR at probe measurement positions. Blue and red lines in (i) represent a slice through measurement positions.

A.2 Centreline Distributions of TWC and MR

The following are 2D slices through the spatial distributions of TWC and MR in Figure A.3 and A.4. Figure A.5 and A.6 are specifically the 0ne-way and two-way coupling comparison at conditions for Test Case 644 and 649 respectively.

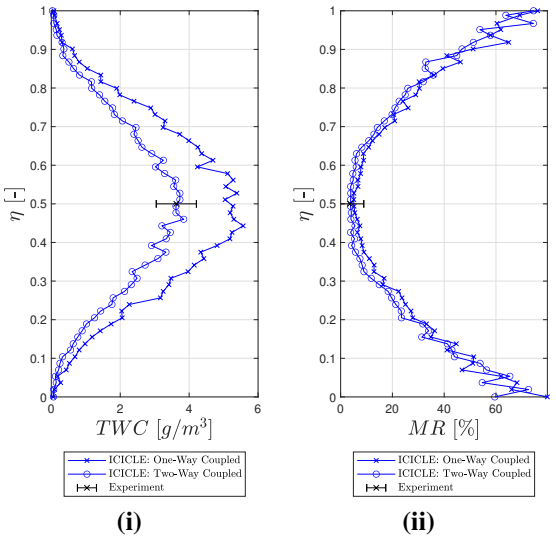

Figure A.5: Test Run 644: Two-Way Coupling Simulation results for (i) TWC and (ii) MR at probe measurement positions. Experimental readings have been overlaid.

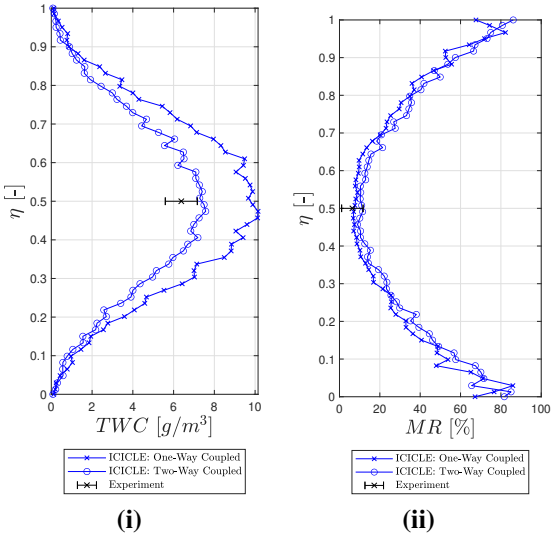

Figure A.6: Test Run 649: Two-Way Coupling Simulation results for (i) TWC and (ii) MR at probe measurement positions. Experimental readings have been overlaid.

B

Ice Crystal Icing Experiments

B.1 Ice Crystal Icing Experiments

Simulating ICI cloud conditions experienced during flight tests and in-service requires IWT facilities which can simulate P, T and Mach numbers experienced at altitudes above 22,000ft. These tunnel facilities simulate glaciated or mixed phase conditions measured at the fan or within the compressor stages. IWT facilities come in varying size and capability. From pressurised full engine IWT facilities used to test full engines or stages, to pressurised subsystem / component wind tunnels providing enough volume to test probes and engine components, to fundamental, non pressurised experimental facilities used to investigate specific icing physics.

B.1.1 Altitude Icing Wind Tunnel Facilities

B.1.1.1 NASA PSL-3

The NASA Propulsion Systems Laboratory (PSL-3) is a pressurised altitude wind tunnel, sufficient to mount a small turbofan ducted within the tunnel facility capable of Mach 3 and 90,000ft. Ice crystals are simulated using a water freeze out spray-bar system within the duct, meaning ice particles are fully glaciated at the inlet. Particle melt is therefore achieved naturally as expected during ingestion, however liquid water freeze-out will not

achieve the same random ice shapes as expected within clouds [67]. This provides an IWT which can match ICI conditions measured externally from the engine. Testing of the ALF502 R-5 LF01 small high bypass turbofan simulated engine rollback in known ICI atmospheric conditions of TWC, P, T, Mach and T_{wb} as measured from previous flight test campaigns. This provided a basis for identifying locations and inlet conditions leading to ice accretion in the LP compressor and booster stage [104].

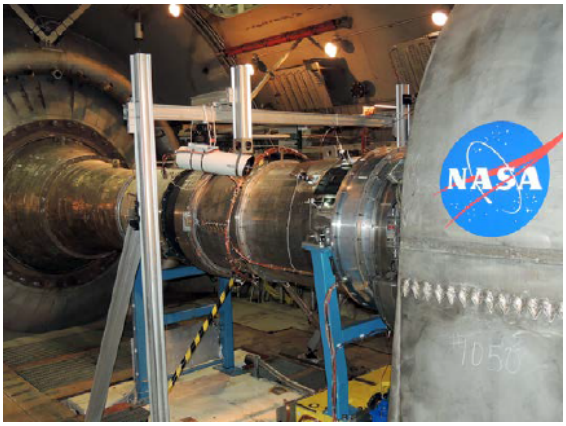

Figure B.1: NASA PSL-3 Altitude icing wind tunnel facility, with ALF502 R5 LF01 installed [103].

B.1.1.2 NRC RATFac & AIWT

The National Research Council in Canada houses altitude wind tunnels for engine sub-stages and components, shown in Figure B.2. RATFac is an open loop altitude IWT which operates up to Mach 0.5 and 15kPa (45,000ft), preventing any ice crystals from recirculating [81]. This facility unlike NASA PSL3, introduces ice to the flow using a grinder and steam system to create ice crystals and a mixed jet of warmer air, simulated relative humidity and liquid water content. This therefore can operate in set mixed phase and glaciated conditions, matching those found in the warmer compressor sections. Unlike the NASA facility, the measurement plane is within the test section. Probes measuring LWC, TWC, IWC, humidity and total temperature enable specific mixed phase ICI conditions to be generated, reproducing conditions within the LP and IP compressor [40, 41]. The Altitude Icing Wind Tunnel (AIWT) is similarly capable to RATFac, with a narrower operating range and a water spray freezeout system as implemented at NASA PSL-3.

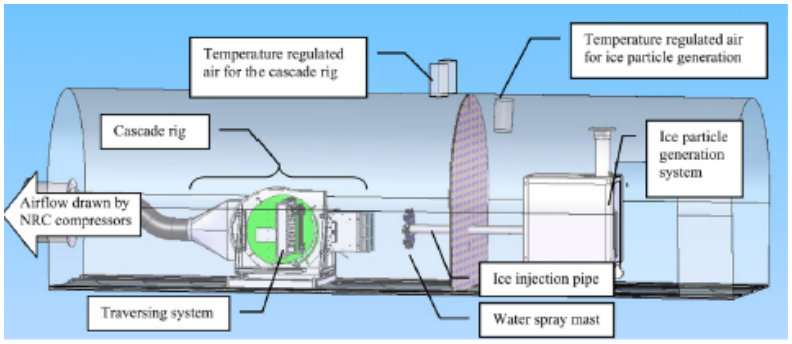

Figure B.2: National Research Council of Canada - Research Altitude Test Facility icing wind tunnel [130].

B.1.2 Unpressurised Icing Wind Tunnel Facilities

B.1.2.1 Braunschweig Icing Wind Tunnel

The IWT at TU Braunschweig is designed to generate icing conditions at sea level in a closed loop wind tunnel using a water spray system similar to the NASA PSL-3 facility, which is limited by this facility to air temperatures of -20°, above the homogenous nucleation limit of water. An ice crystal cloud generator using pressurised air and atomized water was also used to feed ice crystals into the tunnel, this offers an accurate ice crystal production system, but lacks the altitude matching needed to recreate internal compressor conditions (P,T, Mach, MR, T_{wb}, RH) [11].

B.1.2.2 USQ Icing Wind Tunnel

Similar to the Braunschweig facility, USQ IWT has been developed as a smaller scale, open loop wind tunnel without an altitude capability. This facility utilises a droplet freeze-out technique using liquid N_2. This facility provides a means to perform simple experiments investigating icing and data acquisition without the large costs associated with altitude facilities such as NASA PSL-3 and NRC RATFac [121].

Table B.1: Ice Crystal Icing Experimental Facilities [11, 31, 50, 81, 102, 121, 126, 131]

Facility	**Operator**	**Mach**	T_0 $(°C)$	**Altitude** (ft)	**Ice Generation**	**TWC** (g/m^3)	**Dimensions** (m)
PSL-3	NASA	0.0 to 3.0	-51 to -9.4	5000 - 90000	Freeze-out	0.5 to 8.0	11.8ϕ x 7.3
RATFac	NRCC	0.15 to 0.8	-40 to -35	0 - 40000	Grinder	2.0 to 14.0	0.254 x 0.132 x 1.83
AIWT	NRCC	0.0 to 3.0	-30 to 45	0 - 40000	Freeze-out	0.1 to 2.5	0.57 x 0.57 x 1.83
USQ	USQ	0.0 to 0.08	-9 to 10	0	Freeze-out	0.0 to 12.0	0.3 x 0.3
Braunchschweig	TU Braunchsweig	0.0 to 0.11	-20 to 20	0	Freeze-out	0.0 to 20.0	0.5 x 0.5

B.1.3 Ice Crystal Icing Test Campaigns

B.1.3.1 Full Engine Tests

A series of full engine rig tests at the NASA Propulsion Systems Laboratory (PSL-3) altitude icing wind tunnel were conducted to reproduce and record the ICI with a minimally and high instrumented version of the ALF502 engine [49, 104].

(i) **(ii)**

Figure B.3: (i) Lycoming ALF502 - R5 LF01 Flight Test Engine used to recreate ICI conditions causing un-commanded rollback [104]. (ii) Ice Crystal Icing observed on the outer shroud downstream of the ALF502 EGV's [49].

Evaporative cooling of the outer shroud due to runback water was observed in thermo-couple readings as shown in Figure B.4 during a rollback event. This aids in accretion initiation as centrifuging forces smaller particles to the shroud and sufficient mass flux achieves a local metal temperature low enough for accretion. The sawtooth patterns observed in Figure B.3 (ii) detail the complex ice shape distributions forming within the duct downstream of the EGVs. This highlights the highly coupled and non-linear, 3D nature of ice accretion and the impact water runback has on accretion and initiation. Despite the periodicity of the EGV stage, ice growth is distributed in the wake region and through the vane passage indicating the necessity to understand ICI accretion in 3D.

These studies were succeeded by a test campaign focusing on a sub-stage component annular section of the ALF502 EGV section. This investigated the effects of ICI cloud and atmospheric conditions (PSD, MR, Mach, P, T, T_{wb}) at the RATFac NRC facility on accretion severity.

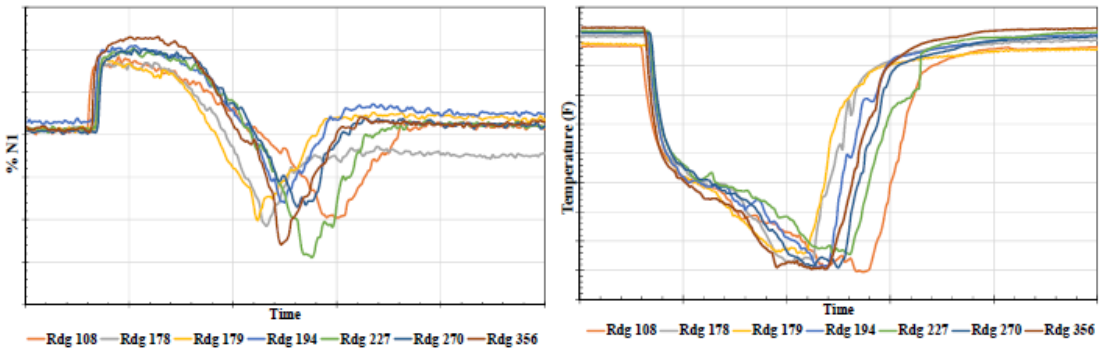

Figure B.4: N1 and thermocouple readings for a range of TWC settings indicating engine rollback and corresponding EGV and shroud cooling [49].

B.1.3.2 Stage and Subsystem Tests

Full engine testing led to a focus of the Ice Crystal Consortium (ICC) on the ALF502 LP compressor booster stage. The EGV's and downstream duct connecting to the first LP stage were known to be a primary ICI accretion location and a source of rollback initiation. An experimental campaign was conducted at RATFac to reproduce conditions at the LP compressor as identified with the Honeywell in-house engine flow simulation software and the NASA ICI particle tracking, heat transfer and ice accretion software LEWICE3D [14].

An investigation into the effects of local MR, humidity, T_{wb} and engine aerodynamic conditions was conducted on an annular EGV segment. The tunnel flow is axial in the facility and therefore did not provide an exact match of dynamic flow properties across the annular vane segment [54].

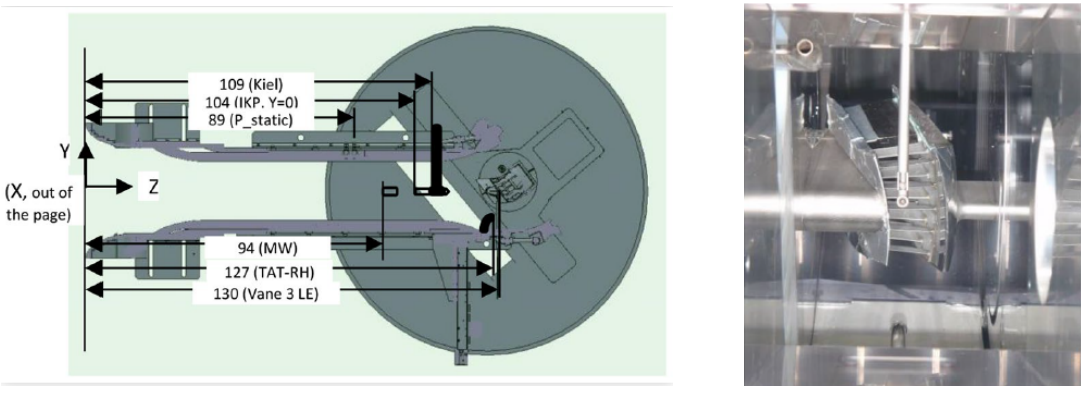

(i) **(ii)**

Figure B.5: (i) RATFac tunnel cross section with sensors and ALF502 vane segment displayed. (ii) Lycoming ALF502 - R5 LF01 LP compressor booster stage EGV segment [54].

This study also employed an ice crystal grinder configuration with a minimum $D_{v10} = 20\mu m$. This is more representative of particle sizes present within the LP compressor due to milling by the fan and upstream rotor stages [54].

References

[1] Maarten Alderliesten. “Mean Particle Diameters. Part VII. The Rosin-Rammler Size Distribution: Physical and Mathematical Properties and Relationships to Moment-Ratio Defined Mean Particle Diameters”. In: *Particle & Particle Systems Characterization* 30.3 (Mar. 2013), pp. 244–257. DOI: 10.1002/PPSC.201200021.

[2] David N. Anderson, Daniel B. Hentsche, and Gary A. Ruff. “Measurement and correlation of ice accretion roughness”. In: *36th AIAA Aerospace Sciences Meeting and Exhibit* (1998). DOI: 10.2514/6.1998-486.

[3] David N. Anderson and Jaiwon Shin. “Characterization of ice roughness from simulated icing encounters”. In: *35th Aerospace Sciences Meeting and Exhibit* (1997). DOI: 10.2514/6.1997-52.

[4] ANSYS Inc. *ANSYS FLUENT Theory Guide*. Tech. rep. 2021.

[5] Gilles Aouizerate, Virgile Charton, Morgan Balland, Jean Mathieu Senoner, Pierre Trontin, Claire Laurent, Ghislain Blanchard, and Philippe Villedieu. “Ice crystals trajectory calculations in a turbofan engine”. In: *2018 Atmospheric and Space Environments Conference* (2018). DOI: 10.2514/6.2018-4130.

[6] Hamid Arastoopour, Dimitri Gidaspow, and Robert W. Lyczkowski. *Transport Phenomena in Multiphase Systems*. Mechanical Engineering Series. Cham: Springer International Publishing, 2022. DOI: 10.1007/978-3-030-68578-2.

[7] E Ayan and SERKAN Özgen. “In-flight ice accretion simulation in mixed-phase conditions”. In: *The Aeronautical Journal* 122.1249 (2018), pp. 409–441. DOI: doi:10.1017/aer.2017.127.

[8] Erdem Ayan and Serkan Ozgen. “Modification of the Extended Messinger Model for Mixed Phase Icing and Industrial Applications with TAICE”. In: *9th AIAA Atmospheric and Space Environments Conference*. 2017, p. 3759. DOI: 10.2514/6.2017-3759.

[9] Erdem Ayan and Serkan Özgen. “In-Flight Mixed Phase Ice Accretion Prediction on Finite, Wings with TAICE-3D”. In: *7th European Conference For Aeronautics And Aerospace Sciences (Eucass)*. 2017. DOI: 10.13009/EUCASS2017-339.

[10] Gholamhossein Bagheri and Costanza Bonadonna. “On the drag of freely falling non-spherical particles”. In: *Powder Technology* 301 (2016), pp. 526–544. DOI: 10.1016/j.powtec.2016.06.015.

[11] Stephan E. Bansmer, Arne Baumert, Stephan Sattler, Inken Knop, Delphine Leroy, Alfons Schwarzenboeck, Tina Jurkat-Witschas, Christiane Voigt, Hugo Pervier, and Biagio Esposito. “Design, construction and commissioning of the Braunschweig Icing Wind Tunnel”. In: *Atmospheric Measurement Techniques* 11.6 (June 2018), pp. 3221–3249. DOI: 10.5194/amt-11-3221-2018.

[12] A Baumert, S Bansmer, P Trontin, and P Villedieu. “Experimental and numerical investigations on aircraft icing at mixed phase conditions”. In: *International Journal of Heat and Mass Transfer* 123 (2018), pp. 957–978. DOI: 10.1016/j.ijheatmasstransfer.2018.02.008.

[13] Héloïse Beaugendre, François Morency, and Wagdi G. Habashi. “FENSAP-ICE’s three-dimensional in-flight ice accretion module: ICE3D”. In: *Journal of Aircraft* 40.2 (2003), pp. 239–247. DOI: 10.2514/2.3113.

[14] Colin Bidwell and David Rigby. *Ice Particle Analysis of the Honeywell ALF502 Engine Booster*. Tech. rep. SAE Technical Paper, 2015. DOI: 10.4271/2015-01-2131.

[15] Colin S Bidwell. “Icing Analysis of a Swept NACA 0012 Wing Using LEWICE3D Version 3.48”. In: *6th AIAA Atmospheric and Space Environments Conference*. 2014, p. 2200. DOI: 10.2514/6.2014-2200.

[16] Stanislav Borodin. “Numerical Solution of the Stefan’s Problem”. In: *Tyumen State University Herald. Physical and Mathematical Modeling. Oil, Gas, Energy* 1.3 (Nov. 2015), pp. 164–175. DOI: 10.21684/2411-7978-2015-1-3-164-175.

[17] Melissa Bravin and J Walter Strapp. “A continuing investigation of diurnal and location trends in an ice crystal icing engine event database”. In: *SAE International Journal of Advances and Current Practices in Mobility* 2.2019-01-1964 (2019), pp. 90–105. DOI: 10.4271/2019-01-1964.

[18] Melissa Bravin, J Walter Strapp, and Jeanne Mason. “An investigation into location and convective lifecycle trends in an ice crystal icing engine event database”. In: *SAE 2015 International Conference on Icing of Aircraft, Engines, and Structures*. 2015. DOI: 10.4271/2015-01-2130.

[19] Christopher E. Brennen. “Fundamentals of Multiphase Flow”. In: *Fundamentals of Multiphase Flow* 9780521848046 (Jan. 2005), pp. 1–345. DOI: 10.1017/CBO9780511807169.

[20] Alexander Bucknell. “Ice crystal icing in gas turbine engines”. PhD thesis. University of Oxford, 2018.

[21] Alexander Bucknell, Matthew McGilvray, David Gillespie, Liam Parker, Peter Forsyth, Hassan Saad Ifti, Geoffrey Jones, Benjamin Collier, and Alasdair Reed. “Experimental Study and Analysis of Ice Crystal Accretion on a Gas Turbine Compressor Stator Vane”. In: *SAE Technical Papers* 2019-June.June (June 2019). DOI: 10.4271/2019-01-1927.

[22] Alexander Bucknell, Matthew McGilvray, David Gillespie, Xin Yang, Geoffrey Jones, and Benjamin Collier. “ICICLE: A Model for Glaciated & Mixed Phase Icing for Application to Aircraft Engines”. In: *SAE Technical Papers* 2019-June.June (June 2019). DOI: 10.4271/2019-01-1969.

[23] Alexander Bucknell, Matthew McGilvray, David R. H. Gillespie, Geoff Jones, Alasdair Reed, and Benjamin Collier. “Experimental Studies of Ice Crystal Accretion on Axisymmetric Bodies at Aeroengine Conditions”. In: *Journal of Propulsion and Power* 36.6 (Nov. 2020), pp. 836–850. DOI: 10.2514/1.B37635.

[24] Alexander Bucknell, Matthew McGilvray, David R.H. Gillespie, Geoff Jones, Alasdair Reed, and David R. Buttsworth. “Heat transfer in the core compressor under ice crystal icing conditions”. In: *Journal of Engineering for Gas Turbines and Power* 140.7 (July 2018). DOI: 10.1115/1.4038460/372311.

[25] Alexander Bucknell, Matthew McGilvray, David R.H. Gillespie, Geoffrey Jones, and Benjamin Collier. "A thermodynamic model for ice crystal accretion in aircraft engines: EMM-C". In: *International Journal of Heat and Mass Transfer* 174 (Aug. 2021), p. 121270. DOI: 10.1016/J.IJHEATMASSTRANSFER.2021.121270.

[26] *Cambridge Flow Solutions - BOXERmesh*. URL: https://www.cambridgeflowsolutions.com/en/products/boxer-mesh/.

[27] M. Caporaloni, F. Tampieri, F. Trombetti, and O. Vittori. "Transfer of Particles in Nonisotropic Air Turbulence." In: *JAtS* 32.3 (1975), pp. 565–568. DOI: 10.1175/1520-0469(1975)032.

[28] Yunus A Çengel. *Introduction to thermodynamics and heat transfer: Engineering*. 2008.

[29] Virgile Charton, Jean-Mathieu Senoner, Pierre Trontin, and Philippe Villedieu. "Semi-empirical Erosion Model with Particle Size and Liquid Water Content Effects for Ice Crystal Icing Simulations". In: *AIAA AVIATION 2020 FORUM*. 2020, p. 2827. DOI: 10.2514/6.2020-2827.

[30] Virgile Charton, Pierre Trontin, Gilles Aouizerate, and Philippe Villedieu. "Semi-Empirical Modelling of Erosion Phenomena for Ice Crystal Icing Numerical Simulation". In: *SAE International journal of advances and current practices in mobility* (2019). DOI: 10.4271/2019-01-1967.

[31] Jonathan Connolly. "Ice Crystal Icing in Gas Turbine Engines". PhD thesis. University of Oxford, Mar. 2022.

[32] Jonathan Connolly, Myeonggeun Choi, Xin Yang, Luke J Doherty, Matthew McGilvray, David R Gillespie, Benjamin Collier, and Geoff Jones. "Ice crystal accretion in a combined linear cascade and swan neck duct". In: *AIAA AVIATION 2020 FORUM*. 2020, p. 2828. DOI: 10.2514/6.2020-2828.

[33] Jonathan Connolly, Matthew McGilvray, David R Gillespie, Geoff Jones, and Benjamin Collier. "Digital Image Projection for 3D Ice Crystal Icing Accretion Measurements". In: *AIAA AVIATION 2020 FORUM*. 2020, p. 2812. DOI: 10.2514/6.2020-2812.

[34] Jonathan Paul Connolly, Matthew McGilvray, David Gillespie, Alex Bucknell, Liam Parker, Geoffrey Jones, and Benjamin Collier. "Two-Way Flow Coupling in Ice Crystal Icing Simulation". In: *SAE Technical Papers* June (June 2019). DOI: 10.4271/2019-01-1966.

[35] Pierre Coutris, Alfons Schwarzenboeck, Delphine Leroy, Alice Grandin, Fabien Dezitter, and J Walter Strapp. "Uncertainty of the Ice Particles Median Mass Diameters Retrieved from the HAIC-HIWC Dataset: A Study of the Influence of the Mass Retrieval Method". In: *SAE International Journal of Advances and Current Practices in Mobility* 2.2019-01-1983 (2019), pp. 140–150.

[36] Tom Currie. *Event-Driven Simulation of Particle-Particle and Particle-Surface Collisions in Ice Crystal Icing*. Tech. rep. SAE Technical Paper, 2019. DOI: 10.4271/2019-01-2014.

[37] Tom Currie. "A Physics-Based Model for Predicting Warm Surface Cool-down Resulting from Particle Impingement in Ice Crystal Icing". In: *AIAA AVIATION 2020 FORUM*. 2020, p. 2829.

[38] Tom Currie, Dan Fuleki, and Craig Davison. “Simulation of Ice Particle Melting in the NRCC RATFac Mixed-Phase Icing Tunnel”. In: *SAE Technical Papers* June (June 2015). DOI: 10.4271/2015-01-2107. URL: https://www.sae.org/publications/technical-papers/content/2015-01-2107/.

[39] Tom Currie, Dan Fuleki, and Ali Mahallati. “Experimental studies of mixed-phase sticking efficiency for ice crystal accretion in jet engines”. In: *6th AIAA Atmospheric and Space Environments Conference*. 2014, p. 3049.

[40] Tom Currie, Peter Struk, Jen-Ching Tsao, Dan Fuleki, and Daniel Knezevici. “Fundamental study of mixed-phase icing with application to ice crystal accretion in aircraft jet engines”. In: *4th AIAA Atmospheric and Space Environments Conference*. 2012, p. 3035.

[41] Tom C. Currie, Dan Fuleki, Daniel C. Knezevici, and James D. MacLeod. “Altitude scaling of ice crystal accretion”. In: *5th AIAA Atmospheric and Space Environments Conference*. 2013. DOI: 10.2514/6.2013-2677.

[42] Fabien Dezitter, Alice Grandin, Jean-Louis Brenguier, Franck Hervy, Hans Schlager, Philippe Villedieu, and Gilles Zalamansky. “HAIC-High Altitude Ice Crystals”. In: *5th AIAA Atmospheric and Space Environments Conference*. 2013, p. 2674.

[43] Bastiaan van Diedenhoven, Ann M Fridlind, Brian Cairns, and Andrew S Ackerman. “Variation of ice crystal size, shape, and asymmetry parameter in tops of tropical deep convective clouds”. In: *Journal of Geophysical Research: Atmospheres* 119.20 (2014).

[44] Ri Qiang Duan, Seiichi Koshizuka, and Yoshiaki Oka. “Numerical and theoretical investigation of effect of density ratio on the critical weber number of droplet breakup”. In: *Journal of Nuclear Science and Technology* 40.7 (2003), pp. 501–508. DOI: 10.1080/18811248.2003.9715384. URL: https://www.tandfonline.com/action/journalInformation?journalCode=tnst20.

[45] S. Elghobashi. “On predicting particle-laden turbulent flows”. In: *Applied Scientific Research* 52.4 (June 1994), pp. 309–329. DOI: 10.1007/BF00936835.

[46] Engineering Toolbox. *U.S. Standard Atmosphere vs. Altitude*. URL: https://www.engineeringtoolbox.com/standard-atmosphere-d_604.html.

[47] Jorge R. Espinosa, Carlos Vega, and Eduardo Sanz. “Homogeneous Ice Nucleation Rate in Water Droplets”. In: *Journal of Physical Chemistry C* 122.40 (Oct. 2018), pp. 22892–22896. DOI: 10.1021/ACS.JPCC.8B04788. URL: https://pubs.acs.org/sharingguidelines.

[48] FAA. *Appendix D to Part 33—Mixed Phase and Ice Crystal Icing Envelope (Deep Convective Clouds) - Aviation Regulations*. URL: https://aviation-regulations.com/part/33/appendix/D.

[49] Ashlie B Flegel and Michael J Oliver. “Preliminary Results from a Heavily Instrumented Engine Ice Crystal Icing Test in a Ground Based Altitude Test Facility”. In: *8th AIAA Atmospheric and Space Environments Conference*. 2016, p. 3894.

[50] Ashlie B. Flegel. “Ice crystal icing research at NASA”. In: *9th AIAA Atmospheric and Space Environments Conference, 2017*. American Institute of Aeronautics and Astronautics Inc, AIAA, 2017. DOI: 10.2514/6.2017-4085.

[51] I Fluent. “Fluent 14.5 user guide”. In: *Fluent Inc., Lebanon. NH-03766* (2002).

[52] Peter Forsyth. “High temperature particle deposition with gas turbine applications”. In: (2017).

[53] Dan Fuleki, Jennifer L.Y. Chalmers, and Brian Galeote. “Technique for Ice Crystal Particle Size Measurements and Results for the National Research Council of Canada Altitude Ice Crystal Test System”. In: *SAE Technical Papers* 2015-June.June (June 2015). DOI: 10.4271/2015-01-2125.

[54] Dan Fuleki, Martin Neuteboom, and Jennifer Chalmers. “Ice Crystal Icing Test Design and Execution for the ALF502 Vane Segment in the NRC RATFac Cascade Rig”. In: *SAE International Journal of Advances and Current Practices in Mobility* 2.2019-01-1925 (2019), pp. 4–14. DOI: 10.4271/2019-01-1925.

[55] Franziska Greifzu, Christoph Kratzsch, Thomas Forgber, Friederike Lindner, and Rüdiger Schwarze. “Assessment of particle-tracking models for dispersed particle-laden flows implemented in OpenFOAM and ANSYS FLUENT”. In: *Engineering Applications of Computational Fluid Mechanics* 10.1 (Jan. 2016), pp. 30–43. DOI: 10.1080/19942060.2015.1104266.

[56] Abhijit Guha. “Transport and deposition of particles in turbulent and laminar flow”. In: *Annual Review of Fluid Mechanics* 40 (2008), pp. 311–341. DOI: 10.1146/ANNUREV.FLUID.40.111406.102220.

[57] ANSYS FLUENT User Guide. “Release 14.0, ANSYS”. In: *Inc., USA, November* (2011).

[58] Avani Gupta. “Application of Extended Messinger Model for Ice Accretion on Complex Geometries”. PhD thesis. Georgia Institute of Technology, 2021. URL: http://hdl.handle.net/1853/66084.

[59] Avani Gupta, Lakshmi Sankar, Richard Kreeger, Avani Gupta, Lakshmi Sankar, and Richard Kreeger. “Application of Extended Messinger Models to Complex Geometries”. In: *SAE Technical Papers* 2020-March.March (Mar. 2020). DOI: 10.4271/2020-01-0022.

[60] A Haider and O Levenspiel. “Drag coefficient and terminal velocity of spherical and nonspherical particles”. In: *Powder technology* 58.1 (1989), pp. 63–70.

[61] Yiqiang Han and Jose Palacios. “Transient heat transfer measurements of surface roughness due to ice accretion”. In: *Transactions of Japanese Society for Medical and Biological Engineering* 51.SUPPL. (2013). DOI: 10.2514/6.2014-2464.

[62] Yiqiang Han and Jose Palacios. “Heat transfer evaluation on ice-roughened cylinders”. In: *AIAA Journal* 55.3 (2017), pp. 1070–1074. DOI: 10.2514/1.J055218/ASSET/IMAGES/MEDIUM/FIGURE8.GIF.

[63] Yiqiang Han and Jose Palacios. “Surface roughness & heat transfer improved predictions for aircraft ice-Accretion modeling”. In: *AIAA Journal*. Vol. 55. 4. American Institute of Aeronautics and Astronautics Inc., 2017, pp. 1318–1331. DOI: 10.2514/1.J055217.

[64] Philip H. Handle, Thomas Loerting, and Francesco Sciortino. “Supercooled and glassy water: Metastable liquid(s), amorphous solid(s), and a no-man’s land”. In: *Proceedings of the National Academy of Sciences* 114.51 (2017), pp. 13336–13344. DOI: 10.1073/pnas.1700103114.

[65] K. Hanjalić and B. E. Launder. "A Reynolds stress model of turbulence and its application to thin shear flows". In: *Journal of Fluid Mechanics* 52.4 (Apr. 1972), pp. 609–638. DOI: 10.1017/S002211207200268X.

[66] T Hauk, E Bonaccurso, IV Roisman, and C Tropea. "Ice crystal impact onto a dry solid wall. Particle fragmentation". In: *Proceedings of the Royal Society A: Mathematical, Physical and Engineering Sciences* 471.2181 (2015), p. 20150399.

[67] Tobias Hauk. "Investigation of the impact and melting process of ice particles". PhD thesis. Technische Universität Darmstadt, 2016.

[68] Tobias Hauk, Elmar Bonaccurso, Philippe Villedieu, and Pierre Trontin. "Theoretical and experimental investigation of the melting process of ice particles". In: *Journal of Thermophysics and Heat Transfer* 30.4 (2016), pp. 946–954. DOI: 10.2514/1.T4886.

[69] Tobias Hauk, Ilia V Roisman, and Cameron D Tropea. "Investigation of the impact behaviour of ice particles". In: *6th AIAA Atmospheric and Space Environments Conference*. 2014, p. 3046.

[70] Andrew J Heymsfield, Aaron Bansemer, Paul R Field, Stephen L Durden, Jeffrey L Stith, James E Dye, William Hall, and Cedric A Grainger. "Observations and parameterizations of particle size distributions in deep tropical cirrus and stratiform precipitating clouds: Results from in situ observations in TRMM field campaigns". In: *Journal of the atmospheric sciences* 59.24 (2002), pp. 3457–3491. DOI: 10.1175/1520-0469(2002)059<3457:OAPOPS>2.0.CO;2.

[71] Andreas Hölzer and Martin Sommerfeld. "New simple correlation formula for the drag coefficient of non-spherical particles". In: *Powder Technology* 184.3 (2008), pp. 361–365. DOI: 10.1016/j.powtec.2007.08.021.

[72] R. Hyland and A. Wexler. "FORMULATIONS FOR THE THERMODYNAMIC PROPERTIES OF THE SATURATED PHASES OF H2O FROM 173.15 TO 473.15 K." In: *Ashrae Transactions* (1983).

[73] E Iuliano, E Montreuil, Ellen Norde, Edwin Theodorus Antonius van der Weide, and Hendrik Willem Marie Hoeijmakers. "Modelling of non-spherical particle evolution for ice crystals simulation with an Eulerian approach". In: *SAE 2015 International Conference on Icing of Aircrafts, Engine, and Structures*. SAE. 2015, pp. 1–13.

[74] Xiangmin Jiao. "Volume and feature preservation in surface mesh optimization". In: *Proceedings of the 15th International Meshing Roundtable*. Springer. 2006, pp. 359–373. DOI: 10.1007/978-3-540-34958-7_21.

[75] Perry L. Johnson, Maxime Bassenne, and Parviz Moin. "Turbophoresis of small inertial particles: theoretical considerations and application to wall-modelled large-eddy simulations". In: *Journal of Fluid Mechanics* 883 (2020), A27. DOI: 10.1017/JFM.2019.865.

[76] Kamel Al-Khalil, Eddie Irani, and Dean Miller. "Mixed phase icing simulation and testing at the Cox icing wind tunnel". In: *41st Aerospace Sciences Meeting and Exhibit*. 2003, p. 903.

[77] Jeewoong Kim, LN Sankar, and Richard E Kreeger. "Assessment of classifcal and extended Messinger models for modeling rotorcraft icing phenomena". In: *European Rotorcraft Forum* (2014). DOI: 10.13140/2.1.2356.5763.

[78] Michael C. King, William D. Bachalo, Dwayne Bell, and Laura E. King-Steen. "Weber number tests in the NASA icing research tunnel". In: *2018 Atmospheric and Space Environments Conference* (2018). DOI: 10.2514/6.2018-3184.

[79] Daniel C. Knezevici, Dan Fuleki, Tom C. Currie, Brian Galeote, Jennifer Chalmers, and James MacLeod. "Particle size effects on ice crystal accretion - Part II". In: *5th AIAA Atmospheric and Space Environments Conference* (2013). DOI: 10.2514/6.2013-2676.

[80] Daniel C. Knezevici, Dan Fuleki, Tom C. Currie, and James D. MacLeod. "Particle size effects on ice crystal accretion". In: *4th AIAA Atmospheric and Space Environments Conference 2012* (2012). DOI: 10.2514/6.2012-3039.

[81] Daniel C. Knezevici, Dan Fuleki, and James MacLeod. "Development and commissioning of a linear compressor cascade rig for ice crystal research". In: *SAE Technical Papers*. SAE International, 2011. DOI: 10.4271/2011-38-0079.

[82] N. A. Konan, O. Kannengieser, and O. Simonin. "Stochastic modeling of the multiple rebound effects for particle–rough wall collisions". In: *International Journal of Multiphase Flow* 35.10 (Oct. 2009), pp. 933–945. DOI: 10.1016/J.IJMULTIPHASEFLOW.2009.05.006.

[83] N. A. Konan, O. Simonin, and K. D. Squires. "Rough Wall Boundary Condition Derivation for Particle Continuum Equations: Validation From LES/DPS of Gas-Solid Turbulent Channel Flow". In: *Proceedings of ASME Fluids Engineering Division Summer Meeting 2006, FEDSM2006* 1 SYPMOSIA (Sept. 2008), pp. 1723–1732. DOI: 10.1115/FEDSM2006-98267.

[84] Joachim Kurzke. "Fundamental differences between conventional and geared turbofans". In: *Turbo Expo: Power for Land, Sea, and Air*. Vol. 48821. 2009, pp. 145–153.

[85] R. Paul Lawson, Leigh J. Angus, and Andrew J. Heymsfield. "Cloud particle measurements in thunderstorm anvils and possible weather threat to aviation". In: *Journal of Aircraft* 35.1 (1998), pp. 113–121. DOI: 10.2514/2.2268.

[86] D Leroy, E Fontaine, A Schwarzenboeck, and JW Strapp. "Ice crystal sizes in high ice water content clouds. Part I: On the computation of median mass diameter from in situ measurements". In: *Journal of Atmospheric and Oceanic Technology* 33.11 (2016), pp. 2461–2476. DOI: 10.1175/JTECH-D-15-0151.1.

[87] Delphine Leroy, Emmanuel Fontaine, Alfons Schwarzenboeck, J Walter Strapp, Lyle Lilie, Julien Delanoë, Alain Protat, Fabien Dezitter, and Alice Grandin. *HAIC/HIWC field campaign-specific findings on PSD microphysics in high IWC regions from in situ measurements: Median mass diameters, particle size distribution characteristics and ice crystal shapes*. Tech. rep. SAE Technical Paper, 2015. DOI: 10.4271/2015-01-2087.

[88] Delphine Leroy et al. "Ice Crystal Sizes in High Ice Water Content Clouds. Part II: Statistics of Mass Diameter Percentiles in Tropical Convection Observed during the HAIC/HIWC Project". In: *Journal of Atmospheric and Oceanic Technology* 34.1 (Jan. 2017), pp. 117–136. DOI: 10.1175/JTECH-D-15-0246.1.

[89] Tianshu Li, Davide Donadio, Giovanna Russo, and Giulia Galli. "Homogeneous ice nucleation from supercooled water". In: *Physical Chemistry Chemical Physics* 13.44 (Nov. 2011), pp. 19807–19813. DOI: 10.1039/C1CP22167A.

[90] Benjamin Y.H. Liu and Jugal K. Agarwal. "Experimental observation of aerosol deposition in turbulent flow". In: *Journal of Aerosol Science* 5.2 (Mar. 1974), pp. 145–155. DOI: 10.1016/0021-8502(74)90046-9.

[91] Decang Lou and David W. Hammond. "Heat and mass transfer for ice particle ingestion inside aero-engine". In: *Journal of Turbomachinery* 133.3 (2011). DOI: 10.1115/1.4002419.

[92] S. E. Mahgoub. "Forced convection heat transfer over a flat plate in a porous medium". In: *Ain Shams Engineering Journal* 4.4 (2013), pp. 605–613. DOI: 10.1016/j.asej.2013.01.002.

[93] JE Martin and E Meiburg. "The accumulation and dispersion of heavy particles in forced two-dimensional mixing layers. I. The fundamental and subharmonic cases". In: *Physics of Fluids* 6.3 (1994), pp. 1116–1132. DOI: 10.1063/1.868283.

[94] BJ Mason. "On the melting of hailstones". In: *Quarterly Journal of the Royal Meteorological Society* 82.352 (1956), pp. 209–216. DOI: 10.1002/qj.49708235207.

[95] Jeanne Mason, Walter Strapp, and Philip Chow. "The ice particle threat to engines in flight". In: *44th AIAA Aerospace Sciences Meeting and Exhibit*. 2006, p. 206. DOI: 10.2514/6.2006-206.

[96] Bernard L Messinger. "Equilibrium Temperature of an Unheated Icing Surface as a Function of Air Speed". In: *Journal of the Aeronautical Sciences* 20.1 (Jan. 1953), pp. 29–42. DOI: 10.2514/8.2520.

[97] Dragoslav Milojević. "Lagrangian Stochastic-Deterministic (LSD) Predictions of Particle Dispersion in Turbulence". In: *Particle & Particle Systems Characterization* 7.1-4 (1990), pp. 181–190. DOI: 10.1002/PPSC.19900070132.

[98] R. A. Minzner. "The 1976 Standard Atmosphere and its relationship to earlier standards". In: *Reviews of Geophysics* 15.3 (1977), pp. 375–384. DOI: 10.1029/RG015I003P00375.

[99] Amir A. Mofakham and Goodarz Ahmadi. "On random walk models for simulation of particle-laden turbulent flows". In: *International Journal of Multiphase Flow* 122 (Jan. 2020), p. 103157. DOI: 10.1016/J.IJMULTIPHASEFLOW.2019.103157.

[100] D. G. Motwani, U. N. Gaitonde, and S. P. Sukhatme. "Heat Transfer From Rectangular Plates Inclined at Different Angles of Attack and Yaw to an Air Stream". In: *Journal of Heat Transfer* 107.2 (May 1985), pp. 307–312. DOI: 10.1115/1.3247415.

[101] Tim G Myers. "Extension to the Messinger model for aircraft icing". In: *AIAA journal* 39.2 (2001), pp. 211–218.

[102] Myron Oleskiw, Fred Hyde, and Paul Penna. "In-flight icing simulation capabilities of NRC's altitude icing wind tunnel". In: *39th Aerospace Sciences Meeting and Exhibit*. 2001, p. 94.

[103] Michael Oliver and Michael Oliver. "Ice Crystal Icing Engine Testing in the NASA Glenn Research Center's Propulsion Systems Laboratory: Altitude Investigation". In: *SAE International Journal of Aerospace* 8.1 (June 2015), pp. 33–37. DOI: 10.4271/2015-01-2156.

[104] Michael J. Oliver. "Validation Ice Crystal Icing Engine Test in the Propulsion Systems Laboratory at NASA Glenn Research Center". In: *6th AIAA Atmospheric and Space Environments Conference*. Reston, Virginia: American Institute of Aeronautics and Astronautics, June 2014. DOI: 10.2514/6.2014-2898.

[105] SERKAN Özgen and M Canıbek. "Ice accretion simulation on multi-element airfoils using extended Messinger model". In: *Heat and Mass Transfer* 45.3 (2009), pp. 305–322. DOI: 10.1007/s00231-008-0430-4.

[106] Ryan Palmer, Ian Roberts, Richard Moser, Colin Hatch, and Frank Smith. "Non-Spherical Particle Trajectory Modelling for Ice Crystal Conditions". In: *SAE Technical Papers*. Vol. 2019-June. June. SAE International, June 2019. DOI: 10.4271/2019-01-1961.

[107] Liam Parker, Matthew McGilvray, and David Gillespie. "Modelling and Simulation of Mixed Phase Ice Crystal Icing in Three-Dimensions". In: *SAE Technical Paper Series* 1 (June 2023). DOI: 10.4271/2023-01-1475.

[108] Liam Parker, Matthew McGilvray, David R. H. Gillespie, and Geoffrey Jones. "Numerical Simulations of Ice Particle Transport at Representative Turbofan Compressor Conditions". In: *ASME Turbo Expo 2024, Turbomachinery Conference and Exposition* (Aug. 2024). DOI: 10.1115/GT2024-121461.

[109] Liam Parker, Matthew McGilvray, David R.H. Gillespie, and Geoffrey Jones. "Numerical simulations of ice particle transport at representative turbofan compressor conditions". In: *Journal of Turbomachinery* (Apr. 2025), pp. 1–14. DOI: 10.1115/1.4068485.

[110] Christopher E Porter and David L Rigby. "Three Dimensional Surface Redefinition Method for Computational Ice Accretion Solvers". In: *AIAA AVIATION 2020 FORUM*. 2020, p. 2831.

[111] Emmanuel Radenac. "Validation of a 3D ice accretion tool on swept wings of the SUNSET2 program". In: *8th AIAA Atmospheric and Space Environments Conference*. 2016, p. 3735. DOI: 10.2514/6.2016-3735.

[112] Emmanuel Radenac, Helene Gaible, Herve Bezard, and Philippe Reulet. *IGLOO3D Computations of the Ice Accretion on Swept-Wings of the SUNSET2 Database*. Tech. rep. SAE Technical Paper, 2019. DOI: 10.4271/2019-01-1935.

[113] Darko Radenkovic and Olivier Simonin. "Stochastic modelling of three-dimensional particle rebound from isotropic rough wall surface". In: *International Journal of Multiphase Flow* 109 (Dec. 2018), pp. 35–50. DOI: 10.1016/j.ijmultiphaseflow.2018.07.013.

[114] Darko Radenkovic and Olivier Simonin. "Stochastic modelling of three-dimensional particle rebound from isotropic rough wall surface". In: *International Journal of Multiphase Flow* 109 (2018), pp. 35–50.

[115] Darko Radenkovic and Olivier Simonin. "Modelling of three-dimensional particle rebound from an anisotropic rough wall". In: *Powder Technology* 393 (Nov. 2021), pp. 165–183. DOI: 10.1016/j.powtec.2021.07.055.

[116] Thomas Ratvasky et al. "Summary of the High Ice Water Content (HIWC) RADAR Flight Campaigns". In: *SAE Technical Papers*. Vol. 2019-June. June. SAE International, June 2019. DOI: 10.4271/2019-01-2027.

[117] M. W. Reeks. “The transport of discrete particles in inhomogeneous turbulence”. In: *Journal of Aerosol Science* 14.6 (Jan. 1983), pp. 729–739. DOI: 10.1016/0021-8502(83)90055-1.

[118] Andrew Richards. *Advanced Research Computing*. DOI: 10.5281/ZENODO.22558. URL: https://zenodo.org/records/22558.

[119] Rolls Royce plc. *Ultrafan- Full shot*. 2019.

[120] R. Rorato, M. Arroyo, E. Andò, and A. Gens. “Sphericity measures of sand grains”. In: *Engineering Geology* 254 (May 2019), pp. 43–53. DOI: 10.1016/j.enggeo.2019.04.006.

[121] Ramiz Saeed, David Buttsworth, and Khalid Saleh. “A New Wind Tunnel Facility for Ice Crystal Icing Experiments”. In: *International Conference on Icing of Aircraft, Engines, and Structures*. SAE International, June 2019. DOI: https://doi.org/10.4271/2019-01-1926.

[122] SAFFMAN PG. “MODEL FOR INHOMOGENEOUS TURBULENT FLOW”. In: 317.1530 (1970), pp. 417–433. DOI: 10.1098/RSPA.1970.0125.

[123] Hermann Schlichting and Klaus Gersten. “Boundary-Layer Theory”. In: *Boundary-Layer Theory* (Oct. 2016), pp. 1–799. DOI: 10.1007/978-3-662-52919-5.

[124] A. El-shamy, R. Sakr, and N. S. Berbish. “EXPERIMENTAL AND NUMERICAL STUDY OF FORCED CONVECTION HEAT TRANSFER FROM AN INCLINED HEATED PLATE PLACED BENEATH A POROUS MEDIUM”. In: (2007).

[125] Jaiwon Shin. “Characteristics of surface roughness associated with leading-edge ice accretion”. In: *Journal of Aircraft* 33.2 (1996), pp. 316–321. DOI: 10.2514/3.46940. URL: http://arc.aiaa.org.

[126] Ronald H. Soeder. *NASA Lewis Propulsion Systems Laboratory Customer Guide Manual*. 1994.

[127] M. Sommerfeld. “Modelling of particle-wall collisions in confined gas-particle flows”. In: *International Journal of Multiphase Flow* 18.6 (1992), pp. 905–926. DOI: 10.1016/0301-9322(92)90067-Q.

[128] M. Sommerfeld and N. Huber. “Experimental analysis of modelling of particle-wall collisions”. In: *International Journal of Multiphase Flow* 25.6-7 (Sept. 1999), pp. 1457–1489. DOI: 10.1016/S0301-9322(99)00047-6.

[129] Peter Struk, Tadas Bartkus, Jen Ching Tsao, Tom Currie, and Dan Fuleki. “Ice Accretion Measurements on an Airfoil and Wedge in Mixed-Phase Conditions”. In: *SAE Technical Papers* 2015-June.June (June 2015). DOI: 10.4271/2015-01-2116.

[130] Peter M Struk, Andy P Broeren, Jen-Ching Tsao, Mario Vargas, William B Wright, Tom Currie, Danny Knezevici, and Dan Fuleki. “Fundamental ice crystal accretion physics studies”. In: (2012).

[131] Peter M. Struk, Timothy Bencic, Jen Ching Tsao, Dan Fuleki, and Daniel C. Knezevici. “Preparation for scaling studies of ice-crystal icing at the NRC research altitude test facility”. In: *5th AIAA Atmospheric and Space Environments Conference* (2013). DOI: 10.2514/6.2013-2675.

[132] L Tang, F Wen, Y Yang, CT Crowe, JN Chung, and TR Troutt. “Self-organizing particle dispersion mechanism in a plane wake”. In: *Physics of Fluids A: Fluid Dynamics* 4.10 (1992), pp. 2244–2251. DOI: 10.1063/1.858465.

[133] C.M. Thompson and L. Shure. *MATLAB: Mathematics [User Guide]*. MathWorks, 2022.

[134] Xialoing Tong, David Thompson, Qiuhan Arnoldus, Eric Collins, and Edward Luke. "Three-dimensional surface evolution and mesh deformation for aircraft icing applications". In: *Journal of Aircraft* 54.3 (2017), pp. 1047–1063. DOI: 10.2514/1.C033949.

[135] P. Trontin, A. Kontogiannis, G. Blanchard, and P. Villedieu. "Description and assessment of the new ONERA 2D icing suite IGLOO2D". In: *9th AIAA Atmospheric and Space Environments Conference, 2017*. American Institute of Aeronautics and Astronautics Inc, AIAA, 2017. DOI: 10.2514/6.2017-3417.

[136] P. Trontin and P. Villedieu. "A comprehensive accretion model for glaciated icing conditions". In: *International Journal of Multiphase Flow* 108 (Nov. 2018), pp. 105–123. DOI: 10.1016/j.ijmultiphaseflow.2018.06.023.

[137] Pierre Trontin, Ghislain Blanchard, Alexandros Kontogiannis, and Philippe Villedieu. "Description and assessment of the new ONERA 2D icing suite IGLOO2D". In: *9th AIAA Atmospheric and Space Environments Conference*. 2017, p. 3417.

[138] Pierre Trontin, Ghislain Blanchard, and Philippe Villedieu. "A comprehensive numerical model for mixed-phase and glaciated icing conditions". In: *8th AIAA Atmospheric and Space Environments Conference*. American Institute of Aeronautics and Astronautics Inc, AIAA, 2016. DOI: 10.2514/6.2016-3742.

[139] Mario F Trujillo and Alex E Parkhill. "A local lagrangian analysis of passive particle advection in a gas flow field". In: *International journal of multiphase flow* 37.9 (2011), pp. 1201–1208. DOI: 10.1016/j.ijmultiphaseflow.2011.06.003.

[140] Jen-Ching Tsao. "Preliminary Evaluation of Altitude Scaling for Turbofan Engine Ice Crystal Icing". In: *9th AIAA Atmospheric and Space Environments Conference*. 2017, p. 4086. DOI: 10.2514/6.2017-4086.

[141] Jen-Ching Tsao. *Scaling Evaluation of Ice-Crystal Icing on a Modern Turbofan Engine in PSL Using the COMDES-MELT Code*. Tech. rep. SAE Technical Paper, 2019. DOI: 10.4271/2019-01-1920.

[142] Jen-Ching Tsao and Sam Lee. *Evaluation of Icing Scaling on Swept NACA 0012 Airfoil Models*. Tech. rep. SAE Technical Paper, 2011. DOI: 10.4271/2011-38-0081.

[143] Y. Tsuji, Y. Morikawa, T. Tanaka, N. Nakatsukasa, and M. Nakatani. "Numerical simulation of gas-solid two-phase flow in a two-dimensional horizontal channel". In: *International Journal of Multiphase Flow* 13.5 (Sept. 1987), pp. 671–684. DOI: 10.1016/0301-9322(87)90044-9.

[144] X Veillard, W G Habashi, M S Aubé, and G S Baruzzi. *FENSAP-ICE: Ice Accretion in Multi-stage Jet Engines*. Tech. rep. 2009.

[145] Joseph P Veres, Philip Jorgenson, and Scott M Jones. "Modeling of Highly Instrumented Honeywell Turbofan Engine Tested with Ice Crystal Ingestion in the NASA Propulsion System Laboratory". In: *8th AIAA Atmospheric and Space Environments Conference*. 2016, p. 3895.

[146] German Vidaurre and John Hallett. "Particle impact and breakup in aircraft measurement". In: *Journal of Atmospheric and Oceanic Technology* 26.5 (2009), pp. 972–983. DOI: 10.1175/2008JTECHA1147.1.

[147] Philippe Villedieu, Pierre Trontin, Gilles Aouizerate, Stephan Bansmer, Paolo Vanacore, Ilia Roisman, and Cameron Tropea. "MUSIC-haic: 3D Multidisciplinary Tools for the Simulation of In-Flight Icing due to High Altitude Ice Crystals". In: *SAE International Journal of Advances and Current Practices in Mobility* 2.2019-01-1962 (2019), pp. 78–89.

[148] Philippe Villedieu, Pierre Trontin, and Rémi Chauvin. "Glaciated and mixed phase ice accretion modeling using ONERA 2D icing suite". In: *6th AIAA Atmospheric and Space Environments Conference*. Reston, Virginia: American Institute of Aeronautics and Astronautics, June 2014. DOI: 10.2514/6.2014-2199.

[149] Bernhard Vowinckel. "Incorporating grain-scale processes in macroscopic sediment transport models: A review and perspectives for environmental and geophysical applications". In: *Acta Mechanica* 232.6 (June 2021), pp. 2023–2050. DOI: 10.1007/S00707-021-02951-4.

[150] P. B. Whalley. "Boiling, condensation, and gas-liquid flow". In: (1987), p. 291.

[151] Frank M White. "Fluid mechanics. 5th". In: *Boston: McGraw-Hill Book Company* (2003).

[152] William Wright. "User's manual for LEWICE version 3.2". In: (2008).

[153] William B Wright. *User manual for the NASA Glenn ice accretion code LEWICE*. 2002.

[154] William B. Wright, Philip C E Jorgenson, and Joseph P. Veres. "Mixed phase modeling in GlennICE with application to engine icing". In: *AIAA Atmospheric and Space Environments Conference 2010*. 2010. DOI: 10.2514/6.2010-7674.

[155] William B. Wright, Peter Struk, Tadas Bartkus, and Gene Addy. "Recent Advances in the LEWICE Icing Model". In: *SAE Technical Papers* 2015-June.June (June 2015). DOI: 10.4271/2015-01-2094.

[156] Xin Yang, Matthew McGilvray, and David Gillespie. "Numerical modeling and parametric study of the melting behavior of ice crystal particles". In: *AIAA Journal* 59.11 (2021), pp. 4660–4668. DOI: 10.2514/1.J060351.

[157] Xin Yang, Matthew McGilvray, and David Gillespie. "Sticking–Erosion Model for Ice Crystal Icing Using Particle Size Distribution". In: *AIAA Journal* 61.11 (Nov. 2023), pp. 4976–4989. DOI: 10.2514/1.J062811.

[158] Xin Yang, Matthew McGilvray, and David R.H. Gillespie. "Modelling the particle trajectory and melting behaviour of non-spherical ice crystal particles". In: *International Journal of Multiphase Flow* 148 (Mar. 2022). DOI: 10.1016/j.ijmultiphaseflow.2021.103949.

[159] John Young and Angus Leeming. "A theory of particle deposition in turbulent pipe flow". In: *Journal of Fluid Mechanics* 340 (June 1997), pp. 129–159. DOI: 10.1017/S0022112097005284.

[160] Natan Zawadzki, Thomas Cross, Liam Parker, James Farmborough, Matthew McGilvray, and David Gillespie. "Wall Heat Transfer Measurements in a Turbomachinery Environment Subject to Ice Crystal Icing". In: *AIAA AVIATION FORUM AND ASCEND 2024*. Reston, Virginia: American Institute of Aeronautics and Astronautics, July 2024. DOI: 10.2514/6.2024-3848.